

# Magneto-optical transport studies on ultra-low disordered semiconductor quantum wells grown by MOVPE

*By*

SUBHOMOY HALDAR

Enrolment No: PHYS03201404012

Raja Ramanna Centre for Advanced Technology,

Indore - 452013, India

*A thesis submitted to the*

*Board of Studies in Physical Sciences*

*In partial fulfillment of requirements*

*for the Degree of*

DOCTOR OF PHILOSOPHY

*of*

HOMI BHABHA NATIONAL INSTITUTE



July, 2020

# Homi Bhabha National Institute<sup>1</sup>

## Recommendations of the Viva Voce Committee

As members of the Viva Voce Committee, we certify that we have read the dissertation prepared by Subhomoy Halder entitled “Magneto-optical transport studies on ultra-low disordered semiconductor quantum wells grown by MOVPE” and recommend that it may be accepted as fulfilling the thesis requirement for the award of Degree of Doctor of Philosophy.

Chairman - Dr. Aparna Chakrabarti

Aparna Chakrabarti  
2.7.20

Guide / Convener - Dr. Vijay Kumar Dixit

Vijay Kumar Dixit  
02/07/2020

Examiner - Dr. Sandip Ghosh

Attended via Video Conference

Member 1- Dr. Anil Kumar Sinha

Anil Kumar Sinha 02/07/2020

Member 2- Dr. Tarun Kumar Sharma

Tarun Kumar Sharma

Member 3- Dr. Maulindu Kumar Chattopadhyay

Maulindu Kumar Chattopadhyay 02/07/2020

Member 3- Dr. Rajeev Rawat

Attended via Video Conference

Final approval and acceptance of this thesis is contingent upon the candidate's submission of the final copies of the thesis to HBNI.

I/We hereby certify that I/we have read this thesis prepared under my/our direction and recommend that it may be accepted as fulfilling the thesis requirement.

Date: 02/07/2020

Place: RRCAT, Indore

Signature

Guide

Vijay Kumar Dixit  
02/07/2020

<sup>1</sup> This page is to be included only for final submission after successful completion of viva voce.

# Homi Bhabha National Institute<sup>1</sup>

## Recommendations of the Viva Voce Committee

As members of the Viva Voce Committee, we certify that we have read the dissertation prepared by Subhomoy Halder entitled "Magneto-optical transport studies on ultra-low disordered semiconductor quantum wells grown by MOVPE" and recommend that it may be accepted as fulfilling the thesis requirement for the award of Degree of Doctor of Philosophy.

Chairman - Dr. Aparna Chakrabarti

Aparna Chakrabarti  
2.7.20

Guide / Convener - Dr. Vijay Kumar Dixit

Vijay Kumar Dixit  
02/07/2020

Examiner - Dr. Sandip Ghosh

Attended via Video Conference

Member 1- Dr. Anil Kumar Sinha

Anil Kumar Sinha 02/07/2020

Member 2- Dr. Tarun Kumar Sharma

Tarun Kumar Sharma

Member 3- Dr. Maulindu Kumar Chattopadhyay

Maulindu Kumar Chattopadhyay 02/07/2020

Member 3- Dr. Rajeev Rawat

Attended via Video Conference

Final approval and acceptance of this thesis is contingent upon the candidate's submission of the final copies of the thesis to HBNI.

I/We hereby certify that I/we have read this thesis prepared under my/our direction and recommend that it may be accepted as fulfilling the thesis requirement.

Date: 02/07/2020

Place: RRCAT, Indore

Signature

Guide

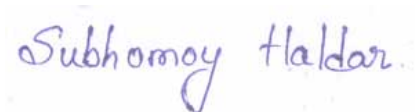
Vijay Kumar Dixit  
02/07/2020

<sup>1</sup> This page is to be included only for final submission after successful completion of viva voce.

## STATEMENT BY AUTHOR

This dissertation has been submitted in partial fulfillment of requirements for an advanced degree at Homi Bhabha National Institute (HBNI) and is deposited in the Library to be made available to borrowers under rules of the HBNI.

Brief quotations from this dissertation are allowable without special permission, provided that accurate acknowledgement of source is made. Requests for permission for extended quotation from or reproduction of this manuscript in whole or in part may be granted by the Competent Authority of HBNI when in his or her judgment the proposed use of the material is in the interests of scholarship. In all other instances, however, permission must be obtained from the author.

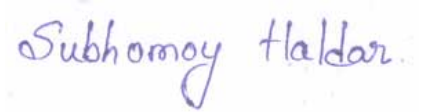


Subhomoy Haldar



## DECLARATION

I, hereby declare that the investigation presented in the thesis has been carried out by me. The work is original and has not been submitted earlier as a whole or in part for a degree / diploma at this or any other Institution / University.



Subhomoy Haldar

# List of Publications arising from the thesis

## Publications in Peer-reviewed Journals:

1. “Effect of carrier confinement on effective mass of excitons and estimation of ultralow disorder in  $\text{Al}_x\text{Ga}_{1-x}\text{As}/\text{GaAs}$  quantum wells by magneto-photoluminescence”, **S. Haldar**, V.K. Dixit, G. Vashisht, S.K. Khamari, S. Porwal, T.K. Sharma, and S.M. Oak, *Scientific Reports*, **2017**, 7, 4905(12).
2. “Effect of magnetic field on free and bound exciton luminescence in  $\text{GaAs}/\text{AlGaAs}$  multiple quantum well structure: A quantitative study on the estimation of ultralow disorder”, **S. Haldar**, V.K. Dixit, G. Vashisht, S. Porwal, and T.K. Sharma, *Journal of Physics D: Applied Physics*, **2017**, 50, 335107(10).
3. “Radiative recombination efficiency and effective mass of thermally activated magneto-excitons probed by quasi-simultaneous magneto-photoluminescence and magneto-surface photovoltage spectroscopy”, **S. Haldar**, V.K. Dixit, G. Vashisht, S. Porwal, and T.K. Sharma, *Journal of Applied Physics*, **2018**, 124, 055704(10).
4. “A parallel magnetic field driven confinement versus separation of charges in  $\text{GaAs}$  quantum well investigated by magneto-photovoltage and magneto-photoluminescence spectroscopy”, **S. Haldar**, A. Banerjee, G. Vashisht, S. Porwal, T.K. Sharma, and V.K. Dixit, *Journal of Luminescence*, **2019**, 206, 342(6).
5. “Simultaneous magneto-electro-optical measurements in modulation-doped quantum well: an investigation on magneto-photoluminescence intensity oscillations”, **S. Haldar**, G. Vashisht, S. Porwal, T.K. Sharma, and V.K. Dixit, *Journal of Applied Physics*, **2019**, 125, 205701(10).

6. “Development of a simple and cost effective maskless photolithography system”,  
**S. Haldar**, G. Vashisht, U.K. Ghosh, A.K. Jaiswal, S. Porwal, A. Khakha, T.K. Sharma, and V.K. Dixit, *AIP Conf. Proc.*, **2019**, 2115, 030219(4).
7. “Anisotropic magnetic properties of excitons in GaAs multiple quantum wells”,  
**S. Haldar**, A. Banerjee, K. Kumar, R. Kumar, G. Vashisht, T.K. Sharma, and V.K. Dixit, *Superlattices and Microstructures* **2020**, 137, 106332(7).

Communicated in Peer-reviewed Journal:

1. “Photovoltaic response and charge redistribution processes in GaAs/AlGaAs multiple-quantum wells structure”,  
**S. Haldar**, S. Kumar, R. Roychowdhury, and V.K. Dixit *physica status solidi b* (submitted).

Presented in Conferences:

1. “Role of disorder and multi-valley scattering on the dynamics and effective mass of excitons in  $\text{Al}_x\text{Ga}_{1-x}\text{As}/\text{GaAs}$  quantum wells investigated by magneto-photoluminescence”,  
**S. Haldar**, G. Vashisht, S. Parwal, S.K. Khamari, V.K. Dixit, T.K. Sharma, and S.M. Oak, *Condensed Matter Physics under Extreme Conditions*, **April 2016**, Bhabha Atomic Research Centre, Mumbai, India [Oral presentation].
2. “Effect of barrier layer on the effective mass of excitons in  $\text{GaAs}/\text{Al}_x\text{Ga}_{1-x}\text{As}$  QWs investigated via Magneto-PL spectroscopy”,  
**S. Haldar**, G. Vashisht, S. Porwal, T.K. Sharma and V.K. Dixit *19<sup>th</sup> International Workshop on The Physics of Semiconductor Device*, **December 2017**, Delhi, India [Oral presentation].
3. “Effect of magnetic field on the radiative recombination efficiency of excitons and trions in  $\text{GaAs}/\text{AlGaAs}$  quantum well”,  
**S. Haldar**, G. Vashisht, S. Porwal, T.K. Sharma, and V. K. Dixit, *27<sup>th</sup> DAE-BRNS National Laser Symposium*, **December 2018**, Indore, India.

4. “Development of a simple and cost effective maskless photolithography system”,  
**S. Haldar**, G. Vashisht, U.K. Ghosh, A.K. Jaiswal, S. Porwal, A. Khakha, T.K. Sharma, and V.K. Dixit, *63<sup>rd</sup> DAE-Solid State Physics Symposium*, **December 2018**, Haryana, India [Oral presentation].
5. “Interdependence of magneto-photoluminescence and quantum Hall effect in modulation doped GaAs/AlGaAs quantum well”,  
**S. Haldar**, G. Vashisht, S. Porwal, T.K. Sharma, and V.K. Dixit, *UK Semiconductors*, **July 2019**, Sheffield, United Kingdom [Oral presentation].

Awards:

1. Best Paper Award: Role of disorder and multi-valley scattering on the dynamics and effective mass of excitons in  $\text{Al}_x\text{Ga}_{1-x}\text{As}/\text{GaAs}$  quantum wells investigated by magneto-photoluminescence.  
**S. Haldar**, G. Vashisht, S. Parwal, S.K. Khamari, V.K. Dixit, T.K. Sharma, and S.M. Oak. *Condensed Matter Physics under Extreme Conditions*, **April 2016**, BARC, India.
2. Young Scientist Award: “Indigenous and inexpensive maskless-photolithography system for semiconductor devices development”,  
**S. Haldar** *34<sup>th</sup> M.P. Young Scientist Congress*, **March 2019**, Bhopal, India.

*Subhomoy Haldar*

Subhomoy Haldar

*Dedicated to all my well-wishers...*

## Acknowledgements

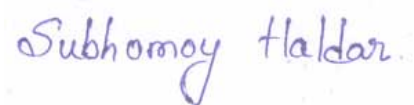
First and foremost, I would like to express my sincere gratitude to my Ph.D. supervisor Dr. Vijay Kumar Dixit for his guidance, support, suggestions, and motivations. I thank him for giving me the opportunity to discuss each and every query related to the work and beyond. His activeness towards new scientific discoveries encouraged me to think more about the subject. The frequent discussions we had during many a time helped me to think deeper and grow as an independent researcher. Besides the scientific discussion, his fatherly advice on honesty, ethics, patience, and dedication for work helped me to find joy. He was always there to support every aspect of my life during my Ph.D.

I am sincerely thankful to my doctoral committee members: Dr. S.M. Oak, Dr. P.A. Naik, Dr. H.S. Rawat, Dr. K.S. Bindra, Dr. Aparna Chakrabarti, Dr. R. Chari, Dr. A.K. Sinha, Dr. S.M. Gupta, Dr. T. Ganguli, Dr. T.K. Sharma, Dr. M.K. Chattopadhyay, Dr. M.H. Modi, and Dr. Rajeev Rawat for their valuable time to evaluate my research progress. Their comments helped me to improve my research work.

I would like to thank Dr. Dipankar Jana, Dr. S.K. Khamari, Dr. R. Kumar, Mr. A. Chatterjee, Ms. P. Taya, Mr. P. Mudi, Dr. N. Sharma, Mr. A. Khakha, Mr. V. Agnihotri and Mr. G. Jayaprakash for fruitful scientific discussions. I am highly thankful to Ms. Geetanjali Vashisht and Mr. Rijul Roychowdhury for scientific discussions and experimental support. I gratefully acknowledge their friendly support and motivation during each and every hard phase. I am thankful to Mr. S. Porwal, Mr. U.K. Ghosh, Mr. A.K. Jaiswal, and A. Khakha for the experimental skills that I have received from them. I am also grateful to Dr. Shailendra Kumar for scientific discussions and motivations. I would like to express my sincere gratitude to Dr. T.K. Sharma, Head, Materials Science Sec., for his guidance and support during the entire work.

I am thankful to Mr. P.K. Kush and all the members of the cryogenic department, RRCAT, for providing adequate liquid helium to perform low-temperature measurements, Dr. Alok Banerjee and Mr. K. Kumar for magnetization measurements at UGC-DAE-CSR, Dr. S.D. Singh for Matlab programming to solve Schrödinger equation, Dr. A.K. Srivastava and Dr. P. Das for TEM measurements, Dr. Aparna Chakrabarti and Dr. C. Kamal for DFT band calculations, Dr. Suparna Pal and Dr. C. Mukherjee for providing high-reflectivity Ag-mirrors for magneto-PL experiments. Very special gratitude goes to Homi Bhabha National Institute-Mumbai for providing me the financial assistance, and faculty and staff members of HBNI-RRCAT cell for their support. I am thankful to Dr. Arup Banerjee, Dean Academics, Dr. C.P. Paul, Dean Student Affairs, and Dr. Aparna Chakraborti, Chairman Doctoral Committee, for their guidance and support on academic and administrative fronts. I would like to thank Dr. Arup Banerjee for his valuable time in conducting my thesis review. I am also thankful to Mr. Debashis Das, Director, RRCAT and Dr. S.V. Nakhe, Group director, Materials Science Group for their kind support during the entire work.

Above all, it would not have possible for me to achieve this milestone without the sacrifices, encouragement, and support from my father, mother, and grand-parents. I am thankful to all my family members for their love, prayer, and support. I would like to express my gratitude to Mrs. Alka Dixit for her care and blessings. I am thankful to Ms. Meholi Chatterjee for her support and understanding during this hard phase of my life. I would also like to thank my Ph.D. batch mates for making this journey colorful, and all my M.Sc., B.Sc., and school friends, who motivated me to come this far. At the end, I express my sincere gratitude to all my teachers who taught me, guided me, and showed me the way.



Subhomoy Haldar

# Contents

<b>Summary</b>	<b>xiv</b>
<b>List of Tables</b>	<b>xvi</b>
<b>List of Figures</b>	<b>xxv</b>
<b>1 Introduction</b>	<b>1</b>
1.1 Crystal structure . . . . .	2
1.2 Electronic interactions and band-structure . . . . .	3
1.3 Excitons and excitonic-complexes . . . . .	8
1.4 Semiconductor quantum structures . . . . .	11
1.5 Oscillator strength . . . . .	13
1.6 External perturbations on the carriers in semiconductors . . . . .	14
1.7 Motivation and layout of the present study . . . . .	15
<b>2 Growth and Experimental Techniques</b>	<b>17</b>
2.1 Introduction . . . . .	17
2.2 Metal-organic vapor phase epitaxy growth . . . . .	18
2.3 Structural Characterization . . . . .	21
2.3.1 High-resolution x-ray diffraction measurements . . . . .	21
2.3.2 Cross-sectional transmission electron microscopy . . . . .	22
2.4 Spectroscopic characterization techniques . . . . .	24
2.4.1 Photoluminescence spectroscopy . . . . .	24



2.4.2	Surface photovoltage spectroscopy . . . . .	27
2.4.3	Magneto-optical spectroscopy . . . . .	29
2.5	Charge transport measurements . . . . .	31
2.5.1	Capacitance-voltage measurements . . . . .	31
2.5.2	Electro-chemical capacitance-voltage measurements . . . . .	34
2.5.3	Classical Hall effect . . . . .	35
2.5.4	Quantum Hall effect . . . . .	37
2.6	Photolithography techniques . . . . .	40
2.6.1	Mask-based optical projection photolithography . . . . .	40
2.6.2	Concepts of maskless-photolithography technique . . . . .	41
2.6.3	A simple and inexpensive maskless-photolithography system . . . . .	42
2.7	Semiconductor device development . . . . .	46
2.7.1	Laser diode arrays . . . . .	46
2.7.2	Photo-detectors . . . . .	47
<b>3</b>	<b>Effect of quantum confinement on optical properties and effective mass of excitons</b>	<b>49</b>
3.1	Introduction and background . . . . .	49
3.2	Sample details and experimental procedure . . . . .	50
3.3	Photoluminescence spectroscopy . . . . .	52
3.3.1	Quantification of QW thickness fluctuation . . . . .	55
3.3.2	Excitation power-dependent PL spectroscopy . . . . .	58
3.4	Surface photovoltage spectroscopy . . . . .	59
3.4.1	Charge redistribution processes with temperature . . . . .	59
3.4.2	Impact of carrier-carrier interaction on charge redistribution process	65
3.4.3	Response time of charge redistribution process . . . . .	66
3.5	Magneto-PL spectroscopy . . . . .	68
3.5.1	Effective mass of excitons and non-parabolicity of bands . . . . .	68
3.6	Conclusion . . . . .	75

<b>4</b>	<b>Optical properties of excitons under a magnetic field and estimation of defect density in QWs</b>	<b>76</b>
4.1	Introduction and background . . . . .	76
4.2	Experimental procedure . . . . .	77
4.3	Magneto-excitons in semiconductor QWs at a low-temperature . . . . .	78
4.3.1	Quantitative estimation of point defects in QWs . . . . .	79
4.3.2	Impact of magnetic field on free-exciton recombination . . . . .	81
4.4	Electro-optical properties of thermally activated magneto-excitons . . . . .	84
4.4.1	Magneto-PL at 100 K . . . . .	85
4.4.2	Magneto-SPV at 100 K . . . . .	90
4.4.3	Effective mass of heavy and light hole excitons . . . . .	92
4.5	Conclusion . . . . .	94
<b>5</b>	<b>Anisotropic properties of excitons and parallel magnetic field induced separation of charges</b>	<b>96</b>
5.1	Introduction and background . . . . .	96
5.2	Sample details and experimental procedure . . . . .	98
5.3	Theoretical background . . . . .	99
5.3.1	Magnetic field perpendicular to the QW plane . . . . .	100
5.3.2	Magnetic field parallel to the QW plane . . . . .	101
5.4	Anisotropic effective mass of exciton in QWs . . . . .	103
5.5	Magnetic field driven confinement versus separation of charges . . . . .	106
5.6	Anisotropic magnetic behavior of charge carriers in GaAs QWs . . . . .	110
5.7	Conclusion . . . . .	115
<b>6</b>	<b>Magneto-optical spectroscopy in quantum Hall regime</b>	<b>116</b>
6.1	Introduction and background . . . . .	116
6.2	Sample details and experimental procedure . . . . .	117
6.3	Impact of photo-excitation on the transport property of electrons . . . . .	118
6.3.1	Estimation of electrical transport parameters . . . . .	119

6.3.2	Impact of laser-illumination on the scattering process . . . . .	122
6.4	Magneto-PL spectroscopy in quantum Hall regime . . . . .	123
6.4.1	Estimation of carrier density in the QW . . . . .	126
6.4.2	Recombination time as a function of magnetic field . . . . .	127
6.4.3	Carrier density in Landau states . . . . .	128
6.4.4	Fermi energy as a function of magnetic field . . . . .	128
6.4.5	Effective mass of charge carrier . . . . .	129
6.4.6	Magneto-PL intensity oscillations . . . . .	131
6.5	Conclusion . . . . .	133
<b>7</b>	<b>Semiconductor device operation under a high magnetic field</b>	<b>135</b>
7.1	Introduction . . . . .	135
7.2	Sample details and experimental procedure . . . . .	137
7.3	Edge-emitting diode lasers . . . . .	138
7.4	Photo-detectors . . . . .	141
7.4.1	Magneto-PL of the detector sample . . . . .	143
7.5	Conclusion . . . . .	145
<b>8</b>	<b>Conclusion and Future work</b>	<b>146</b>
8.1	Summary of the Thesis work . . . . .	146
8.2	Suggested Future work . . . . .	150
	<b>Bibliography</b>	<b>151</b>
	<b>Appendices</b>	<b>169</b>

# List of Tables

3.1	Probability of finding an electron-hole pair in QW ( $f$ ) and barrier layers ( $1-f$ ). PL line-broadening originated by different mechanisms are tabulated. . . . .	57
3.2	Time constants of charge redistribution process in different thicknesses of QW. . . . .	67
3.3	The reduced effective mass and binding energy of excitons with a variation in QW thickness are summarized, where the free-electron mass is denoted by $m_0$ . . . . .	69
3.4	The increase in effective mass due to the wave function penetration. The PL peak energy, ground state energy of heavy-hole, and energy eigenstate of electrons in the non-parabolic band are summarized. Subsequently, the non-parabolicity factor is estimated by using $\varepsilon'_{e1}$ and Eq. 3.15 . . . . .	72
4.1	The spatial extent of electron and hole wave functions along the $z$ -direction and the estimated defect density in four QWs are tabulated. .	81
4.2	The reduced mass of heavy and light hole excitons estimated by magneto-PL and magneto-SPV spectra at 100 K. . . . .	93
6.1	The transport parameters estimated by using $R_{xx}$ and $R_H$ under dark and laser illumination are summarized. . . . .	122
7.1	The estimated responsivity, specific detectivity, and quantum efficiency of the detector at 4.2 K. . . . .	143

# List of Figures

1.1	The zinc-blende structure of GaAs and basic-physical parameters of GaAs, AlAs, and InAs material systems at room temperature. . . . .	2
1.2	(a) Formation of bands due to the overlap of atomic orbitals followed by the hybridization of energy states and (b) band-structure of GaAs in different crystallographic orientations are schematically illustrated. . . .	6
1.3	Schematic diagrams showing the band-dispersion and recombination of electron-hole pairs in (a) direct and (b) indirect bandgap semiconductors.	7
1.4	Spatial extent of (a) tightly-bound Frankel-excitons in insulators and (b) weakly-bound Wannier-excitons in semiconductors. . . . .	8
1.5	(a) Schematic of a QW-structure and one-dimensional confinement of charge carriers leading to the (b) discretization of energy states and (c) modification of DOS. . . . .	11
2.1	(a) Schematic and (b) photograph of the MOVPE system for the III-V semiconductor growth. . . . .	18
2.2	Schematic diagram showing the growth rate as a function of temperature in the MOVPE technique. . . . .	19
2.3	(a) Schematic of the instrumental configuration for HRXRD measurements and (b) goniometer rotation for different modes of x-ray scan. . .	21
2.4	Results of HRXRD measurement and simulated profile of a GaAs/AlGaAs QW sample. . . . .	22

2.5	(a) Schematic diagram of a transmission electron microscope and (b) steps involved in preparing samples for cross-sectional TEM measurements.	23
2.6	(a) Excitation of charge carriers by photons followed by the relaxation and recombination of electron-hole pairs. (b) PL line-shape contributed by the band-to-band recombination and defect-assisted radiative recombination of a 190 Å thick GaAs/AlGaAs QW at 4.2 K. . . . .	25
2.7	Schematic of the photoluminescence experimental setup. . . . .	26
2.8	(a) Generation of photo-voltage by charge redistribution processes is schematically illustrated and (b) SPV amplitude and phase of a semi-insulating GaAs substrate at room temperature. . . . .	27
2.9	Schematic of the experimental setup for SPV measurement. . . . .	28
2.10	(a) Schematic and (b) photographs of the experimental setup for magneto-PL measurements. . . . .	30
2.11	Metal-semiconductor junction in the case of (a) $\Phi_m < \Phi_s$ and (b) $\Phi_m > \Phi_s$ resulting Ohmic and rectifying-nature of the junction, where E.A. stands for the electron affinity of the semiconductor. . . . .	32
2.12	(a) Schematic diagram showing the sample prepared for C-V measurements and (b) carrier density estimated by C-V measurements on a QW.	33
2.13	Schematic of the (a) semiconductor-electrolyte Helmholtz contact formation and (b) cross-sectional view of electrochemical-cell for ECV measurements. . . . .	34
2.14	Experimental configuration to measure the classical Hall effect in the van-der Pauw method. The flow of charge current and equipotential lines (a) in the absence and (b) under $B_z$ are shown. . . . .	36
2.15	(a) Magnetic field-driven discretization of energy state in the form of Landau states and sweeping of Landau states across $\varepsilon_f$ . Under this condition, resistance in the direction of current oscillates with increasing the magnetic field (b), and resistance perpendicular to the current flow exhibits a quantized variation (c). . . . .	38

2.16 (a) Hall-bar sample for longitudinal and transverse magneto-resistance measurements and (b) schematic of the quantum Hall experimental setup.	40
2.17 Flow diagram showing the main steps involved in the photolithography technique. . . . .	41
2.18 (a) Schematic and (b) photograph of a simple maskless-photolithography system based on a projector and an optical microscope. (c) The emission spectrum of the projector corresponding to the white light is also shown.	43
2.19 Photographic images of various patterns developed by the maskless-photolithography system. . . . .	45
2.20 Schematic of a QW-based p-i-n laser diode. . . . .	46
2.21 Schematic flow diagram showing the steps for the development of semiconductor laser diode arrays. . . . .	47
2.22 Schematic diagram showing the steps involved to develop photo-detectors.	48
3.1 (a) Schematic diagram of a GaAs/AlGaAs MQW sample and (b) simulated result of HRXRD data to estimate the structural details of the sample. . . . .	51
3.2 (a) Temperature-dependent PL spectra of the GaAs/AlGaAs MQW sample and (b) shift in PL peak energy as a function of temperature. . . .	52
3.3 4.2 K PL spectra of the MQW sample and PL line-shape fitting by Gaussian along with Lorentz distribution function. . . . .	53
3.4 (a) Schematic illustration of charge carriers' confinement in a QW and (b) cross-sectional TEM image of a GaAs/AlGaAs MQWs showing the quality of the hetero-interfaces. . . . .	54
3.5 The broadening of PL peak ( $P_1$ ) as a function of QW width. The inset shows that the excitons in a narrow QW experience thickness fluctuations due to the atomic irregularities at the hetero-junctions. . . . .	55

3.6	The spatial extent of electron-hole wave functions in different thicknesses of QWs, which is estimated by solving the 1-dimensional Schrödinger equation. . . . .	56
3.7	(a) Power dependent PL spectra and intensity of $P_1$ (b) and $P_2$ (c) peaks as a function of the excitation power density of laser light. . . . .	58
3.8	(a) Schematic of the GaAs/AlGaAs MQW layer structure and (b) sample stage for SPV measurements. (c) The SPV amplitude and (d) phase spectra of the MQW sample in the temperature range of 92 - 300 K. Maxima of heavy and light hole related (e) SPV amplitude $\times h\nu$ and (f) phase are plotted as a function of temperature. . . . .	60
3.9	The energy band profile of the MQW structure is estimated by solving the one-dimensional Schrödinger-Poisson equation without considering the contribution of interface defect states. The potential barrier of electrons ( $V_e$ ) and heavy holes ( $V_{hh}$ ) in QWs are shown in the unit of meV. . . .	62
3.10	The recombination (cyan arrow), capture by point defects (magenta arrows), thermal activation (black arrows), and electron-electron repulsion followed by carrier localization at heterointerfaces (purple arrows) are schematically illustrated. In a high-temperature regime, a significant number of electrons escape from the QW and drift/diffuse in barrier layers. In this process of charge migration, electrons are captured and re-escape from the defect states in barrier layers or other QWs in the MQW structure. . . . .	63
3.11	Excitation power-dependent SPV (a) amplitude and (b) phase maxima related to QW transitions at 300 K. . . . .	65
3.12	(a) The SPV amplitude and (b) phase maxima are plotted as a function of chopping frequency at 300 K. . . . .	67
3.13	(a) 4.2 K magneto-PL spectra under the magnetic field up to 8 T. The magnetic field-driven blue-shift in PL peaks are plotted in (b)-(e) . . .	68



3.14	Non-parabolic band dispersion for different thickness of QWs. A parabolic dispersion curve for bulk GaAs is also shown by the red dashed line. The maximum $k'_e$ value up to which the dispersion curve is valid is marked by green dots. . . . .	73
3.15	Theoretically calculated band-structure of (a) 20 MLs GaAs, (b) 10 MLs GaAs sandwiched between 5 MLs of $\text{Al}_{0.5}\text{Ga}_{0.5}\text{As}$ barrier, and (c) 10 MLs GaAs sandwiched between 5 MLs of AlAs barrier. . . . .	74
4.1	4.2 K magneto-PL spectra under a magnetic field perpendicular to the QW plane. . . . .	78
4.2	Magneto-PL lineshape fitting by Gaussian with Lorentz functions to decouple FX and BX transitions in the case of QW-1. . . . .	79
4.3	Integrated PL intensity of (a) $P_2$ and (b) $P_1$ peaks plotted as a function of a magnetic field, and (c) schematic illustration of excitonic confinement by an applied magnetic field, where the number of in-plane defects (red dots) experienced by excitons decrease under a high field. . . . .	80
4.4	(a) Formation of Landau states, inter-subband relaxation and inter-band radiative recombination of charge carriers are schematically illustrated. The carrier occupancy in Landau states with increasing the magnetic field is numerically estimated for three different electron-hole pair generation rates (b) $G_E$ , (c) $10G_E$ , and (d) $100G_E$ . . . . .	83
4.5	Schematic of the experimental setup for the simultaneous measurement of magneto-PL and magneto-SPV. . . . .	84
4.6	Magneto-PL spectra of the MQW sample at 100 K. An enhancement of the HH PL signal is observed for QW-1, where the asymmetry in the PL peak remains invariant under the magnetic perturbation. . . . .	85

4.7	PL intensity of HH and LH transitions at 100 K as a function of the magnetic field for (a) QW-1, (b) QW-2, (c) QW-3, and (d) QW-4. The variation of HH PL intensity with the external magnetic field at 4.2 K is also shown. The diamagnetic blue-shift of HH and LH transitions for the four QWs at 100 K is plotted (e-h). . . . .	86
4.8	The rate of radiative recombination of heavy and light holes, and carrier escape from QWs are estimated by solving Eq. 4.9 for (a) QW-1 and (b) QW-4. The $G_E$ for this analysis is considered as $3 \times 10^{23} \text{ m}^{-2}\text{s}^{-1}$ . The results obtained by this calculation are schematically described for a (c) thick and (d) narrow QW. . . . .	89
4.9	(a) Magneto-SPV spectra of the MQW sample at 100 K. The energy separation between HH and LH transitions is indicated for the QWs. (b) Fundamental processes that are responsible for the generation of SPV are schematically shown. . . . .	91
4.10	SPV amplitude at 100 K is plotted as a function of the magnetic field for (a) QW-1, (b) QW-2, (c) QW-3, and (d) QW-4. Diamagnetic blue-shift of HH and LH transitions are also plotted as a function of field (e-f). . . . .	92
5.1	Schematic of the sample mounting stage design for magneto-PL measurements in (a) Faraday and (b) Voigt configurations. . . . .	98
5.2	Magneto-PL spectra of sample $S_1$ under (a) perpendicular and (b) parallel magnetic field orientations. The Landau-diamagnetic shift in PL peaks as a function of magnetic fields are plotted (c - f). . . . .	104
5.3	In-plane and out-of-plane effective mass of excitons as a function of QW thickness are estimated by magneto-PL spectroscopy. Solid lines are shown to guide the eye. . . . .	105
5.4	(a) Schematic and (b) photograph of the spatially patterned sample for the in-plane magneto-PV measurements. The width of each parallel strip, containing the QW regions, is kept as $80 \mu\text{m}$ . . . . .	106

5.5	Magneto-PL and magneto-PV spectra of sample $S_2$ under parallel (a) & (b), and perpendicular (c) & (d) field configurations. An increase in lateral PV signal is recorded under strong $B_y$ , which indicates the in-plane charge separation process within the QW. . . . .	107
5.6	(a) Intensity and (b) linewidth of PL peak as a function of $B_y$ for sample $S_2$ . . . . .	108
5.7	Results obtained by (a) HRXRD and (b) cross-sectional TEM measurements to estimate the structural parameter of sample $S_3$ . (c) Carrier distribution in the 50-period MQW sample as a function of the depth is estimated by ECV measurements. . . . .	110
5.8	(a) Experimentally estimated magnetic susceptibility of sample $S_3$ at 300 and 2 K by a magnetic field perpendicular to the QW plane, $\chi_\perp$ . (b) Theoretically calculated magnetic susceptibility of carriers in the valence/conduction band for the two temperatures. . . . .	111
5.9	(a) Experimentally and (b) theoretically estimated magnetic susceptibility of charge carriers in Sample $S_3$ under two different magnetic field configurations, at 2 K. . . . .	113
5.10	The magnetic susceptibility of empty straws that are used to hold the sample and measured magnetic-susceptibility of carriers in Sample $S_3$ . .	114
6.1	(a) Schematic of the GaAs/AlGaAs modulation-doped QW structure. Theoretically estimated (b) band-diagram and (c) carrier accumulation in different layers of the sample. . . . .	118
6.2	(a) Simultaneous measurements of quantum Hall and magneto-PL spectroscopy on a Hall bar device is schematically illustrated. (b) The longitudinal magneto-resistance and Hall resistance as a function of magnetic field up to 8 T. . . . .	119

6.3	The oscillatory part of longitudinal magneto-resistance in (a) dark and (b) laser-illuminated condition is extracted. The SdH amplitude at three different temperatures (c), FFT amplitude of SdH-oscillations (d), and the Hall coefficient as a function of the magnetic field are plotted. . . .	120
6.4	The representative magneto-PL line-shape fitting at four different magnetic fields at 4.2 K (a-d). PL spectra are fitted by the use of multiple Gaussian functions to de-convolute the Landau PL transitions, PL intensity, and the linewidth of Landau states. . . . .	124
6.5	(a) Integrated PL intensity of FX and BX transitions, (b) PL intensity related to different Landau states, (c) linewidth of Landau transitions, and (d) Landau-diamagnetic shift as a function of field. Solid-lines denote the fitted curves, and dotted-lines are used to guide the eye. . . . .	125
6.6	(a) The density of electron-hole pair in the QW, (b) radiative recombination time, (c) carrier density in Landau states, and (d) Fermi energy as a function of the magnetic field are estimated by the magneto-PL spectra. In figure (d), the dash-dotted lines are showing the magnetic field-driven shift in Landau states, which is calculated by $\Delta\varepsilon_{j,z}(B) = (j + 1/2)\hbar eB/\mu_{x,y}^* - (1/2)g_{\perp}^*\mu_B B$ . . . . .	127
6.7	(a) Magneto-PL spectra of the same modulation doped QW sample in Voigt configuration at 4.2 K and (b) diamagnetic shift in PL peak under $B_y \leq 8$ T. . . . .	130
6.8	(a) Sweeping of Landau PL transition across $\varepsilon_k$ is schematically depicted. Under this condition, an oscillatory variation in PL intensity can be recorded by increasing the magnetic field. (b) Magneto-PL intensity oscillation curves which are recorded at different probe energies at 4.2 K.	131
7.1	(a) Schematic and (b) energy band-profile of the InGaAs/GaAs laser structure. (c) Layer details and (d) band-profile of a GaAs/AlGaAs p-i-n detector structure. . . . .	137

7.2	(a) light output power-current characteristics, (b) emission spectra of the laser at room temperature, and (c) schematic diagram showing the band-to-band and defect-related recombination in the active layer. The inset of figure (a) shows the photograph of the laser diode array. . . . .	139
7.3	(a) Sample stage design for the operation of laser under a high magnetic field, (b) the emission spectra of the diode laser, and (c) laser intensity as a function of the magnetic field at 4.2 K. . . . .	140
7.4	(a) Photograph of the photo-detector, (b) current-voltage characteristics under different excitation powers, and (c) spectral-response as a function of magnetic field. . . . .	142
7.5	(a) Magneto-PL spectra of the p-i-n detector structure, (b) schematic diagram showing the direct and indirect excitonic transitions, and (c) energy separation between IX - FX peaks and PL intensity of IX transition as a function of magnetic field. (d) Magnetic field driven in-plane confinement of charges and their drift due to the structural electric field are schematically illustrated. . . . .	144

Table 1: Symbols and abbreviation.

$A$	Area
$A_s$	Atomic mass
$a$	Lattice constant
$\alpha$	Entropy of the system
$\alpha^*$	Absorption coefficient
$\alpha_i$	Variational parameter in wave function
$\mathbf{B}$	Magnetic field
$B_c$	Critical magnetic field
$b_{1,2}$	Coulomb interaction
$\beta$	Debye temperature
$C$	Capacitance
$C_A$	Auger coefficient
$c$	Velocity of light
$\chi$	Magnetic susceptibility
$\chi_V^{para}$	van Vleck Paramagnetic susceptibility
$D$	Area of the QW
$\delta_1$	QW thickness fluctuation
$\delta_2$	Point defect density
$\delta^D$	Dirac delta function
$d_{h,k,l}$	Inter-planar spacing
$\Delta\varepsilon_v$	Valence band offset
$\Delta\varepsilon_c$	Conduction band offset
$\mathbf{E}$	Electric field
$\mathbf{E}_i$	Interface-electric field
$\mathbf{E}_s$	Surface electric field
$e$	Electronic charge ( $1.6 \times 10^{-19}$ coulomb)
$\eta_1$	Normalized free-exciton PL
$\eta_2$	Normalized bound-exciton PL
$\eta^*$	Quantum efficiency
$\varepsilon$	Energy
$\varepsilon_g$	Bandgap
$\varepsilon_g^*$	Bandgap of quantum well
$\varepsilon_e$	Confinement energy of electron in QW
$\varepsilon_h$	Confinement energy of hole in QW
$\varepsilon_b$	Binding energy of exciton
$\varepsilon_f$	Fermi energy
$\varepsilon_{esc}$	Energy required for carrier escape
$\epsilon_0$	Permittivity of free space
$\epsilon_r$	Permittivity of a medium
$F_e$	Fermi function
$F_a$	Faraday constant

$f_\nu$	Frequency
$f$	Probability of electron/hole occupancy in QW
$G$	Carrier generation rate
$\Gamma$	Broadening of energy state
$g_\perp^*$	Lande-g factor under $B_z$
$g_\parallel^*$	Lande-g factor under $B_y$
$g$	Gain of laser
$g_{modal}$	Modal gain
$h$	Plank's constant ( $6.626 \times 10^{-34}$ m <sup>2</sup> kg/s)
$\hbar$	Reduced Plank's constant ( $h/2\pi$ )
$i$	Current
$I$	PL intensity
$I_{FX}$	PL intensity related to FX recombination
$I_j$	Intensity of $j^{th}$ Landau state transition
<b>J</b>	Current density
$j$	Index of the Landau state
$J$	Total angular momentum
$K$	Momentum of excitons
$k$	Momentum of electron/hole
$k_B$	Boltzmann constant ( $1.38 \times 10^{-23}$ m <sup>2</sup> kg s <sup>-2</sup> K <sup>-1</sup> )
$\kappa$	The fraction of total defects which is radiatively active
$L$	Width of the Hall bar
$L_\phi$	Phase coherence length
$l_w$	Quantum well thickness
$l_w^*$	Effective quantum well thickness
$l_d$	Depletion width
$\lambda$	Wavelength of electro-magnetic radiation
$\Lambda$	Variational parameter in Coulomb energy
$M^*$	Total effective mass of exciton
$M_a$	Molecular weight
$[M]$	Transition Matrix
$\mathcal{M}$	Magnetization
$m_e^*$	Effective mass of electron
$m_{hh}^*$	Effective mass of heavy hole
$m_{lh}^*$	Effective mass of light hole
$m_j$	Quantum number of J
$\mu^*$	Reduced mass of exciton
$\mu_{lh}^*$	Reduced mass of light hole exciton
$\mu_{hh}^*$	Reduced mass of heavy hole exciton
$\Delta m_{penetration}$	Increase in mass due to wave function penetration
$\mu$	Mobility of charge carriers
$N$	Degeneracy of Landau state
$n$	Carrier density

$n_{2D}$	Two-dimensional carrier density
$n_j$	Carrier density in $j^{th}$ Landau state
$\nu$	Filling ratio of Landau state ( $n \times h/2eB$ )
$p'$	Power of the incident light
$p_{exc}$	Power density of incident light ( $p'/A$ )
$\mathbf{p}$	Momentum
$P_1$	Intensity of FX PL
$P_2$	Intensity of BX PL
$P_\Gamma$	Pulse-width of current
$\psi$	Wave function
$\Phi_m$	Work-function in metals
$\Phi_s$	Work-function of semiconductors
$\Phi_0$	Photon flux
$q$	Order of x-ray diffraction
$Q$	Ideality factor of rectifying contact
$R$	Rate of carrier recombination
$R_H$	Hall coefficient
$\rho_s$	Density of solids
$\rho$	Resistivity
$R$	Resistance
$R_{xx}$	Longitudinal magneto-resistance
$R_{xy}$	Transverse magneto-resistance
$\Delta R_{xx}$	Oscillatory part of $R_{xx}$
$\delta R_{xx}$	Magnitude of $R_{xx}$ oscillations
$r$	Coordinate in relative frame of reference
$\varrho$	Oscillator strength
$s$	Index of QW energy eigenstate
$\sigma$	Conductivity of charge carriers
$\sigma_{ee}$	Conductivity correction due to electron-electron interaction
$\sigma_{WL}$	Conductivity correction due to weak localization
$T$	Temperature
$t$	Thickness of a film
$\tau_r$	Radiative recombination time
$\tau_c$	Carrier capture time
$\tau_0$	Inter-subband relaxation time
$\tau_{nr}$	Non-radiative decay time
$\tau_q$	Quantum scattering time
$\tau_t$	Transport scattering time
$\xi$	Magnetic length ( $\sqrt{\hbar/eB}$ )
$U$	Rate of thermal escape
$V$	Voltage or potential
$V_H$	Hall voltage
$V_s^{dark}$	Surface potential in dark



$V_s^{light}$	Surface potential in light
$V_z$	Barrier height in QW
$v_d$	Drift velocity
w	Width of the Hall channel
x	Aluminum composition in AlGaAs layer
y	Exponent of power-law relation
Z	Atomic number
$z_s$	Atomic mass
$Z_p$	Partition function
AlGaAs	Aluminium gallium arsenide
BX	Bound exciton
CM	Center of mass
CV	Capacitance voltage
DOS	Density of state
ECV	Electrochemical capacitance voltage
FX	Free exciton
FFT	Fast Fourier transformation
GaAs	Gallium Arsenide
HH	Electron-heavy hole transition
HRXRD	High resolution x-ray diffraction
InGaAs	Indium gallium arsenide
ITO	Indium tin oxide
LHe	Liquid helium
LH	Electron-light hole transition
MQW	Multiple quantum well
MOVPE	Metal-organic vapor phase epitaxy
MPL	Magneto-photoluminescence
MIS	Metal-insulator-semiconductor
PL	Photoluminescence
PV	Photovoltage
PRI	Pulse repetition interval
QW	Quantum well
QWR	Quantum wire
QD	Quantum dot
QTH	Quartz tungsten halogen lamp
RM	Relative motion
SdH	Shubnikov de Haas
SPV	Surface photovoltage
SQUID	Superconducting quantum interference device
TEM	Transmission electron microscope

---

# Chapter 8

## Conclusion and Future work

### 8.1 Summary of the Thesis work

In the present thesis, optical and electrical transport properties of ultra-low disordered semiconductor QWs have been investigated under a strong magnetic field. The nearly-lattice matched GaAs-based single, multiple and modulation-doped QWs, and their laser and detector structures for this investigation are grown by the MOVPE technique. The structural parameters of the grown samples are estimated by HRXRD and cross-sectional TEM measurements, and the doping density of an epitaxial layer is evaluated by classical Hall, C-V, and ECV measurements. In the beginning, carrier localization in QWs and the role of thermal energy on the radiative and non-radiative processes in QWs are investigated by two complementary spectroscopic techniques, i.e., PL and SPV. It is shown that atomic irregularities at the hetero-junctions causing fluctuations in QW thickness can be estimated by modeling the PL linewidth as a function of QW thickness. On the other hand, thermionic escape followed drift/diffusion of charges in a multiple-QWs structure is investigated by temperature, excitation power, and chopping frequency-dependent SPV measurements. A careful study of SPV-amplitude and phase spectra under external perturbations has provided crucial information on carrier-carrier interaction in QWs. The various thicknesses of QW that are grown under identical growth conditions, i.e., the MQW structure, is found to be the key recipe in this work. Also, the impact of quantum confinement on the effective mass of excitons

is investigated by PL spectroscopy under a high magnetic field. It is observed that the effective mass of electrons significantly increases with a decrease in QW thickness, which can not be explained by the penetration of wave functions into barrier layers. The estimated effective mass as a function of QW-thickness is then used to evaluate the non-parabolicity factor of bands when the energy eigenstate is at different  $(\varepsilon, k)$  in the band dispersion.

It is observed that the asymmetric tail in PL spectra, which is contributed by disorder bound-excitons, decreases under a strong magnetic field. Such an effect is explained by the magnetic field-driven spatial confinement of excitons, and therefore, charge carriers in the QW experience a small number of defects. A phenomenological model of magneto-excitons is developed where the magnetic field-driven reduction in bound-exciton PL helps in evaluating the point defect-density in QWs. In addition to this, the role of magnetic perturbation on the radiative and non-radiative processes of thermally activated excitons are probed by magneto-PL and magneto-SPV measurements. In particular, the emission-based PL spectra helped to realize the impact of magnetic perturbation on the radiative recombination efficiency of excitons at an elevated temperature. At the same time, carrier escape from QWs, followed by the drift or diffusion of charges, is probed by magneto-SPV measurements. Although the recombination-rate of thermally activated electron-hole pairs in a thick QW increases under a strong magnetic field, a large number of electron and hole may escape from a narrow QW under this magnetic perturbation. A comprehensive understanding of the magnetic field-assisted relaxation, recombination, and carrier escape mechanisms for a quantum structure is developed by a rate equation model. Considering the above processes, the requirement of a minimum QW-width is suggested that would be essential for the magnetic field-driven advanced optoelectronic device operation.

After that, anisotropic properties of excitons in GaAs QWs are investigated by magneto-optical spectroscopy and magnetization measurements in perpendicular and parallel magnetic field configurations. A dramatic reduction in the diamagnetic energy of excitons is observed under a magnetic field parallel to the QW-plane. It is found

that the existing theoretical models could not explain the feeble diamagnetic-energy of excitons and a decrease in PL intensity under a parallel magnetic field in the case of a narrow QW. We have derived an analytical relation of diamagnetic energy by considering (a) the coupling of quantum confinement with the diamagnetic energy of excitons, and (b) inter-play between the center of mass and relative motion of charge carriers. The analytical relation, along with the diamagnetic energy in perpendicular and parallel field configurations, is used to evaluate the in-plane and out-of-plane reduced mass of excitons in various thicknesses of QW. According to the theoretical framework, it is proposed that the in-plane separation between electron and hole may increase under a parallel magnetic field, which may cause a chiral charge transport across the hetero-interfaces of the QW. As a result of this, charge carriers in a QW become more susceptible for in-plane motion that gives rise to enhancement of photovoltage signal and reduction in PL intensity. On the contrary, a magnetic field perpendicular to the QW plane emphatically confines the exciton and causes substantial enhancement of PL intensity and reduction in lateral photovoltage signal. Furthermore, it is found that a magnetic field along different orientations can control the paramagnetic and diamagnetic behavior of excitons. Therefore, a unique method to control the recombination, transport, and magnetic properties of charge carriers is shown by the strength and orientation of an external magnetic field.

In order to correlate the optical and transport parameters of low-dimensional systems, magneto-PL spectroscopy is performed in the quantum Hall regime. The results obtained by magneto-resistance measurements under dark and laser-illuminated conditions helped in realizing the carrier-carrier interactions in a modulation-doped QW, which forces the electrons to move at the hetero-interfaces and scattered by the interface-roughness. It is found that photo-generated holes screen this electron-electron interaction, which enhances the mobility of charge carriers. During the quantum Hall measurements, relaxation of charges among the Landau states and their recombination is probed by magneto-PL spectroscopy on the Hall bar device. The correlation of PL intensity with a rate equation model helped to estimate carrier density in each Landau

states, recombination time of excitons, and Fermi energy as a function of the magnetic field. A novel method to investigate magneto-PL intensity oscillations is also presented, which is conceptually similar to the Shubnikov-de Haas oscillations. This new method can be exploited in evaluating the magneto-optical parameters in semiconductor quantum structures without a line-shape fitting procedure.

Finally, the role of magnetic perturbation on the electro-optical processes in semiconductor devices is investigated. To fabricate these devices, a simple and inexpensive maskless-photolithography system is developed, which is found to be beneficial to pattern various structures with a minimum feature size of  $\sim 20 \mu\text{m}$ . In order to validate our above findings on QWs, diode lasers, and photo-detectors with QWs are developed. The role of carrier localization on the performance of these devices is understood by operating these devices at a low-temperature and high magnetic field conditions. It is observed that the lasing emission related to defect states decreases under a magnetic field. At the same time, the free-excitonic laser peak increases with the strength of the applied field. Such effects can be explained by the understanding developed in the context of magneto-PL spectroscopy of QWs. On the other hand, the QW embedded in a p-i-n structure of the photodetector traps the background charge carriers, which acts as an artificial localization center to minimize the dark current. Under a high magnetic field, the in-plane diffusion of photo-generated charge carriers is restricted, and therefore, the in-plane migration followed by the carrier localization becomes feeble. As a result of this, the photo-generated charge carriers can only move along the growth direction of the p-i-n structure, which increases the spectral response of the photodetector under a high magnetic field. It is therefore observed that the magnetic field can be used to suppress the impact of defects on the lasing emission and offers a tunability in lasing wavelength, whereas in the case of photo-detectors, magnetic perturbation enhances the spectral response.

In conclusion, the optical, magnetic, and transport properties of charge carriers in ultra-low disordered QWs, with variations in QW-thickness, doping-density, and barrier-composition, are investigated. The results obtained by magneto-optical,

magneto-transport, and magnetization measurements helped to develop a detailed understanding of the impact of charge carrier confinement on the electro-optical processes and fundamental parameters of the material system. The magneto-optical measurement is found to be an efficient tool for the quantitative estimation of point defect density in a truly non-invasive manner. A unique method to control recombination, electrical transport, and magnetic behavior of charge carriers by the strength and orientations of a magnetic field is demonstrated by magneto-PL, magneto-PV, and magnetization measurements. The magnetic field induced non-radiative processes that may deteriorate the efficiency of quantum devices is investigated, and a critical dimension of quantum structures that would be essential to suppress those effects is proposed. The results obtained by magneto-transport measurements are correlated with the magneto-optical spectroscopy, which would be beneficial in estimating the electro-optical parameters of quantum structures, especially when a contact-based measurement is not feasible. Therefore, in addition to the fundamental physics of magneto-excitons, the present thesis provides clear guidelines for the magnetic field-assisted advanced electro-optical devices development.

## 8.2 Suggested Future work

The understanding developed in the present thesis would be beneficial to study the fundamental mechanisms underlying the superfluidity of excitons in bi-layers or two-dimensional systems. In particular, the unique property of dark-excitons (forbidden for radiative transitions) and their role in the above process can be investigated. Here, an expected extraordinarily long recombination time of dark-carriers would be beneficial in realizing the excitonic superfluidity even at room temperature. The impact of barrier layers on the carrier localization and capture of charge carriers at the hetero-interfaces can be investigated by combining spectroscopic and electrical transport measurements. Experimental setup of scanning surface-photovoltage measurements can also be developed to probe the formation of dark-excitons in semiconductors. In addition to

this, an external magnetic field along different directions would be applied to control the recombination, transport, and magnetic behavior of excitons to achieve excitonic superfluidity. For this purpose, excitons can also be coupled with photons in micro-cavity structures in the form of polariton. On the other hand, the impact of magnetic perturbation on the inter-subband electronic transition can be investigated by THz spectroscopy, and the role of magnetic perturbation on the threshold current of diode lasers/vertical-cavity surface-emitting lasers can be probed. This would be beneficial to achieve further insights towards the high-efficiency wavelength-tunable light-source and single-photon/electron devices.

## Summary

Research on the electro-optical properties of III-V semiconductors has provided unprecedented opportunity to develop numerous optoelectronic devices. An ultra-low disordered semiconductor, with extremely high mobility and very high radiative recombination efficiency, is widely used in light-emitting diodes, lasers, and ultrafast communication devices. Also, the electro-optical properties of the material system can be enriched by confining the charges in a low-dimensional system. Although the optical and transport properties of semiconductors can be enriched by quantum confinement, penetration of wave function in surrounding mediums upsurges with a reduction in quantum well (QW) thickness. Therefore, charge carriers become localized by interface defects, and their properties get modified due to penetration effects. To probe these effects, photoluminescence (PL) and surface photovoltage (SPV) measurements are performed on GaAs QWs. The PL linewidth as a function of QW thickness is modeled for the quantitative estimation of atomic-irregularities at the hetero-junctions. The impact of quantum confinement on the effective mass of excitons is also investigated by PL measurements under a high magnetic field. It is observed that the effective mass of electrons significantly increases with a reduction in QW thickness. The estimated effective mass is then used to determine the non-parabolicity factor of bands for different thicknesses of QW. In addition, PL intensity related to the disorder bound-excitons is found to be suppressed under a strong magnetic field. A phenomenological model of magneto-excitons is developed where this magnetic field-driven reduction in disorder related PL helps in evaluating the point defect-density. Although the unique properties of magneto-excitons are beneficial for optical-emitters, a short recombination time of excitons is detrimental for photovoltaics and quantum information processing. A novel method to control the recombination, transportation, and magnetic properties of excitons is demonstrated by an external magnetic field along different orientations. It is observed that the Landau-diamagnetic shift of energy states dramatically reduces when the mag-



netic field is parallel to the QW-plane. Moreover, the magnetic field parallel to the QW plane induces a chiral charge transport across the hetero-interfaces of the QW, without applying an electric field. As a result of this, recombination time under parallel field increases. With this understanding, a simultaneous measurement of quantum Hall and magneto-PL spectroscopy is performed to correlate optical and transport parameters. Results obtained by magneto-transport measurements in laser-illuminated condition helped to identify the sources of scattering mechanism. It is found that photo-generated holes screen the interface roughness assisted scattering of electrons, which enhances the mobility of electrons. Under this condition, recombination time of magneto-excitons, the carrier density in Landau states, and Fermi energy as a function of a magnetic field are estimated by magneto-PL spectroscopy. Such an investigation would be beneficial to probe the magneto-electro-optical processes, especially when a contact-based measurement is not feasible. A simple maskless-photolithography system is also developed to pattern various structures for contact-based transport measurements and semiconductor devices development. The system is developed by a commercial projector, a low-cost stereo-zoom optical microscope, an x-y-z controlled stage, and a computer, which can pattern a minimum feature size of  $\sim 20 \mu\text{m}$ . In order to validate the experimental findings of magneto-optical processes in QWs, QW-based semiconductor diode lasers and photo-detectors are developed and operated at low-temperature and high-magnetic field. It is observed that the contribution of defect states on laser emission can be suppressed by an external magnetic field. On the other hand, the localization of charges within a QW in the p-i-n photo-detector helps in reducing the dark current of the device. Under a high magnetic field, in-plane diffusion of photo-generated charges followed by their localization by point-defects is reduced. Hence, carriers are efficiently flown along the growth direction of the p-i-n structure to enhance the spectral response of a detector. Besides the physics of magneto-excitons, present thesis provides clear guidelines for magnetic field controlled advanced electro-optical devices development.

# Chapter 1

## Introduction

The development of optoelectronic and photonic devices by semiconductors is one of the remarkable technology that has evolved over the past few decades. An extensive amount of research has been performed to utilize III-V compound semiconductors in numerous types of light-emitting devices, photovoltaics, and high-mobility transistors.[1, 2, 3, 4, 5] The exciting electro-optical property and feasibility to grow high crystalline quality quantum structures are some of the key aspects, which make III-V semiconductors a unique choice for fundamental-research and technological advancement. In particular, a highly lattice-matched GaAs/AlGaAs hetero or quantum structure is often used in realizing innovative proof of concepts, let it be the induced-superconductivity, excitonic superfluidity, exciton-polariton coupling, spin-lasers, etc.[6, 7, 8] Added to this, recent investigations on the emerging technologies related to the quantum computer have significantly renewed the importance of ultra-low disordered quantum structures.[9, 10] A precise control on the recombination, relaxation, and transport properties of charge carriers is found to be essential for novel devices, like single-photon emitters, single-electron transistors, spin-qubit devices, etc.[11, 12, 13, 14] In the present scenario, in-depth knowledge of the quantum mechanical interactions in semiconductors, and their effects on microscopic and mesoscopic scales are crucial. The ever-increasing need to understand the complex interactions in low-dimensional systems can be realized by inter-correlating advanced spectroscopic and electrical-transport measurements that are sensitive to probe the above effects. The electro-optical processes in solids

can also be controlled by an external perturbation, e.g., electric field, magnetic field, pressure, etc.[15, 16, 17] Moreover, the response against these applied perturbations can be used to evaluate the optical and charge-transport parameters of the material system.[18, 19, 20] In this introductory chapter, the fundamental concepts of semiconductor physics that are relevant to the present thesis are briefly discussed.

## 1.1 Crystal structure

In general, III-V semiconductors crystallize into a zinc-blende structure, where two interpenetrating face-centered cubic lattices of group-III and V elements occupy  $(0, 0, 0)$  and  $(1/4, 1/4, 1/4)$  atomic positions. Schematic of GaAs zinc-blende structure, and the basic physical properties of GaAs, AlAs, InAs crystals are shown in Fig. 1.1.[21, 22] In this particular class of semiconductors, atomic bonds are formed by an  $sp^3$  hybridization process, and being cubic in structure, their crystals are described by a single lattice-constant,  $a$ . The compound semiconductors with two elements ‘A’ and ‘B’ are also known as a binary system, (e.g., gallium-arsenide), which possess  $F\bar{4}3m$  space group symmetry. Incorporation of a third element ‘C’ either by substituting ‘A’ or ‘B’ elements may alter the physical properties of the semiconductor, which is known as alloying. The alloying has great technological importance to tailor the physical and optoelectronic properties of semiconductors. For example, when the x-fraction of Al

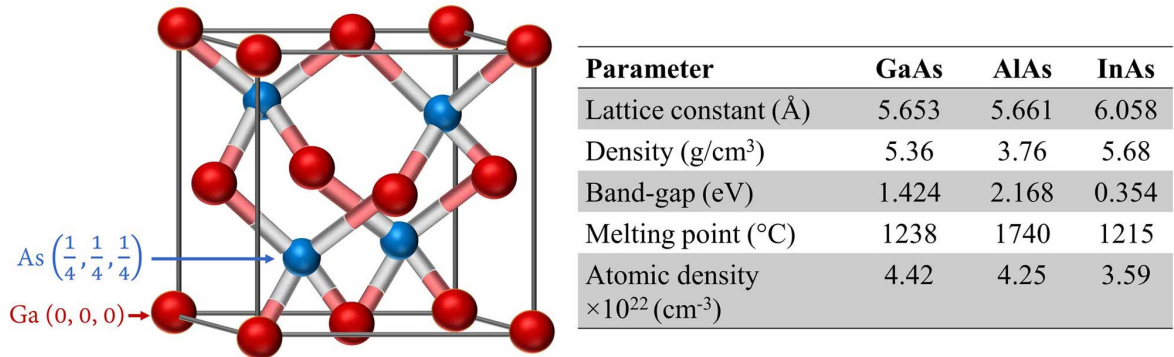


Figure 1.1: The zinc-blende structure of GaAs and basic-physical parameters of GaAs, AlAs, and InAs material systems at room temperature.

substitutes Ga atoms in GaAs crystal, the lattice constant of  $\text{Al}_x\text{Ga}_{1-x}\text{As}$  alloy becomes,  $a_{\text{Al}_x\text{Ga}_{1-x}\text{As}} = xa_{\text{AlAs}} + (1-x)a_{\text{GaAs}}$  (Vegard's law). The difference in lattice constant between GaAs and AlGaAs being feeble, with lattice mismatch at room temperature  $(a_{\text{GaAs}} - a_{\text{AlAs}})/a_{\text{GaAs}} \lesssim 0.14\%$ , high-crystalline quality GaAs/AlGaAs hetero and quantum structures can be grown without introducing a considerable amount of strain. Notably, under special circumstances, III-V semiconductors can also be grown in the wurtzite phase with a different lattice constant, packing density, and band-structure than that of the zinc-blende structure.

## 1.2 Electronic interactions and band-structure

A comprehensive understanding of the band structure in different crystallographic orientations is of utmost importance in semiconductor physics, where the curvature of band and forbidden-gaps determine the optical and transport properties of the material. The formation of bands and electro-optical properties of a solid, with a large number of interacting atomic orbitals, can be explained by the Schrödinger equation in a many-body framework. The Hamiltonian energy operator of the above system can be described by considering the electron-electron and electron-nuclei interactions. The estimation of energy eigenstate  $\psi(r_1, r_2, \dots, r_n; x_1, x_2, \dots, x_n)$  and eigenvalue ( $\varepsilon$ ) of the Schrödinger equation is possible under Born-Oppenheimer approximation, where the resultant wave function is expressed as the product of electronic and nuclear counterparts,  $\psi(r_1, r_2, \dots, r_n; x_1, x_2, \dots, x_n) \approx \psi_e(r_1, r_2, \dots, r_n)\psi_n(x_1, x_2, \dots, x_n)$ . Here,  $r_n$  and  $x_n$  symbolize the position co-ordinate of  $n^{\text{th}}$  electron and nuclei, respectively. In an equilibrium condition, the separation between nuclei remains invariant, and therefore, the contribution of nuclei-nuclei and nuclei-electron interactions can be added as an effective potential  $[V(r, x)]$  in the Schrödinger equation.[23, 24]

$$\left[ -\sum_i \frac{\hbar^2 \nabla_i^2}{2m_e^*} + \sum_n V(r, x) - \sum_p \sum_{q \neq p} \frac{Ze^2}{8\pi\epsilon_0 |r_p - r_q|} + H_s \right] \psi_e(r_1, r_2, \dots, r_p, r_q) = \varepsilon \psi_e(r_1, r_2, \dots, r_p, r_q) \quad (1.1)$$

where

$$\sum_n V(r, x) = + \frac{1}{4\pi\epsilon_0} \left[ \sum_{i \neq n} \frac{Z^2 e^2}{2|x_n - x_i|} - \sum_p \frac{Ze^2}{|r_p - x_n|} \right]$$

where  $m_e$  denotes the mass of electrons and  $Z$  represents the atomic-number of nuclei. The permittivity of free-space and spin-orbit interaction are symbolized by  $\epsilon_0$  and  $H_s$ . The first and third terms of Eq. 1.1 signify the kinetic and potential energy of electrons that are interacting with each other. In the idealized model presented in Eq. 1.1, ‘nuclei’ is often considered as ‘core electrons’ that is surrounded by a valence electron cloud. The solution of Eq. 1.1 is tedious for real-crystals with a large number of interacting atoms ( $\sim 10^{22} \text{ cm}^{-3}$ ). Therefore, a further simplification can be performed by considering the electrons are independent of each other, which can be expressed by:

$$\psi_e(r_1, r_2, \dots, r_n) = A' \phi_{1,\sigma}(r_1) \phi_{1,\sigma'}(r_1) \phi_{2,\sigma}(r_2) \phi_{2,\sigma'}(r_2) \dots \phi_{n,\sigma}(r_n) \phi_{n,\sigma'}(r_n) \quad (1.2)$$

where  $A' = (n!)^{1/2} \sum_P (-1)^{\check{p}} P$  is an anti-symmetrizing operator, with  $\check{p}$  is it's parity and  $P$  is one of the  $n!$  permutations of  $n$  objects.[23] The symbols  $\sigma$  and  $\sigma'$  denote the spin quantum numbers that are summed from  $+1/2$  to  $-1/2$ . The wavevector  $\phi_{n,\sigma}(r_n)$  is best represented by the Hartree-Fock solution of the entire system with the ground energy eigenstate,[23]

$$\begin{aligned} \varepsilon_0 = \sum_{i,\sigma} \int \phi_{i,\sigma}^*(r) \left[ -\frac{\hbar^2 \nabla^2}{2m_e} + V(n, r) \right] \phi_{i,\sigma} d^3r \\ + \frac{1}{2} \left[ \sum_{i,\sigma,j,\sigma'} \int \phi_{i,\sigma}^*(r_1) \phi_{j,\sigma'}^*(r_2) b_{1,2} \phi_{i,\sigma}(r_1) \phi_{j,\sigma'}(r_2) d^3r_1 d^3r_2 \right. \\ \left. - \int \phi_{i,\sigma}^*(r_1) \phi_{j,\sigma}^*(r_2) b_{1,2} \phi_{j,\sigma'}(r_1) \phi_{i,\sigma}(r_2) d^3r_1 d^3r_2 \right] \end{aligned} \quad (1.3)$$

where  $b_{1,2} = e^2/4\pi\epsilon_0|r_1 - r_2|$  denotes the Coulomb interaction. The last two-terms of Eq. 1.3 signify the Coulomb and exchange interaction between the charge carriers. In the crystalline solid, electrons experience the periodic potential of nuclei (or core electrons) having the periodicity of lattice constant  $a$ , i.e.,  $V_0(r) = V_0(r + a)$ , and the

wavevector is represented by Bloch function,

$$\phi(r) = \frac{\sigma_{\pm 1/2}}{a^{3/2}} u_k(r) \exp(i\mathbf{k} \cdot \mathbf{r}) \quad (1.4)$$

where  $u_k(r)$  is a periodic function,  $a^3$  is the crystal volume, and  $\sigma_{\pm 1/2}$  symbolizes the eigenvector of the spin operator. The Schrödinger equation with the above approximations can be solved to estimate allowed energy states that are separated by the forbidden energy gap,  $\varepsilon_g$ . In a simplified model, the Schrödinger equation and energy eigenvalue at the band-edge are expressed by,

$$\left[ \frac{\mathbf{p}^2}{2m_e^*} + \frac{\hbar^2 k^2}{2m_e^*} + \frac{\hbar}{m_e^*} \mathbf{k} \cdot \mathbf{p} + V(r) - \frac{e^2}{4\pi\epsilon_0\epsilon_r|r|} \right] u_k(r) = \varepsilon(k) u_k(r) \quad (1.5)$$

$$\varepsilon_{k \rightarrow 0} = \frac{\hbar^2 k^2}{2m_e^*} \quad (1.6)$$

Here, the impact of crystal potential is considered by the effective mass of electrons and the dielectric constant of the medium ( $\epsilon_r$ ). The curvature of the band defines the effective mass  $m_e^* = \hbar^2 / [\partial^2 \varepsilon / \partial k^2]$ . The symbols  $\mathbf{p}$  and  $\mathbf{k}$  denote the momentum and wave vector of electrons, respectively. The third term of Eq. 1.5 signifies the  $\mathbf{k} \cdot \mathbf{p}$  perturbation, which is the origin of  $\mathbf{k} \cdot \mathbf{p}$  perturbation theory of bands.[25] Notably, the carriers with sufficient kinetic or potential energy ( $k \gg 0$ ) may experience the non-parabolicity of band dispersion. This non-parabolicity in bands arises due to the electronic interactions, electron-nuclei interactions, anharmonic crystal potential of lattice, etc. (Eq. 1.1). Because of this, the effective mass is an important parameter that provides a measure of band-curvature and crucial information related to electronic interactions in solids. In the literature, various analytical relations were proposed to describe the non-parabolicity of bands, which are often used in describing the anisotropic effective mass and non-linear property of charge carriers.[26, 27, 28, 29]

A phenomenological description of band formation can also be provided by the interaction of a large number of atomic orbitals, which causes splitting of energy states with infinitesimally small energy separation.[30, 31] The electrons occupied in the out-

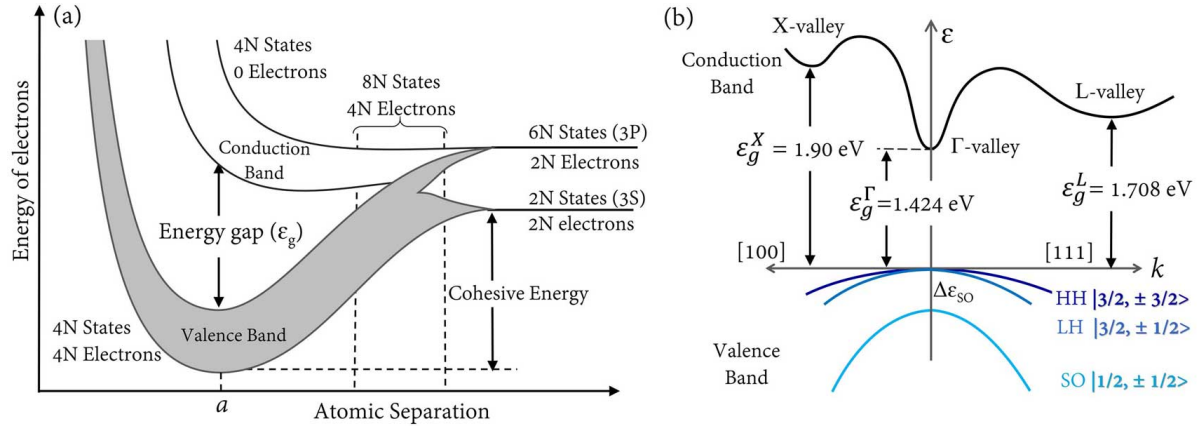


Figure 1.2: (a) Formation of bands due to the overlap of atomic orbitals followed by the hybridization of energy states and (b) band-structure of GaAs in different crystallographic orientations are schematically illustrated.

ermost orbitals minimize their energy due to a hybridization process, and the corresponding branch of energy-states is known as the valence band, Fig. 1.2a. The valence band gets separated from the upper energy states (conduction band) having an energy gap of  $\epsilon_g$ . The materials with moderate  $\epsilon_g$ , with respect to the thermal energy of charge carriers, exhibit the most striking electro-optical behavior that is applicable in electronic and optical devices. In this class of materials, known as semiconductors, electronic transport and optical properties can be easily controlled by an external perturbation or doping the films with impurity atoms of different valencies. The flexibility to modify bandgap and control of free-carrier density in the conduction/valence bands by doping, alloying, and induced strain make semiconductors superior to others.

According to the convention, the center of the Brillouin zone in the reciprocal lattice is defined as  $\Gamma$ -point. The valence band with the nature of p-orbitals can split into three sub-bands, which are known as heavy hole  $|J = 3/2, m_j = \pm 3/2\rangle$ , light hole  $|3/2, \pm 1/2\rangle$ , and split-off band  $|1/2, \pm 1/2\rangle$ . The symbol  $J$  denotes the total angular momentum (orbital + spin) and  $m_j$  symbolizes the corresponding quantum number. In bulk semiconductors, heavy-hole and light hole bands are degenerate at  $\Gamma$ -point, where the names heavy and light are originated from to the fact that effective mass of holes is higher in heavy hole band (i.e.,  $m_{hh}^* > m_{lh}^*$ ). Due to the spin-orbit interaction between  $J$

$= 3/2$  and  $J = 1/2$  states, the split-off band is separated by  $\Delta\varepsilon_{SO}$  energy from the heavy and light hole bands at  $\Gamma$ -point. The structure of bands along the other symmetry axes, for example, X and L valleys in  $[100]$  and  $[111]$  crystallographic directions (Fig. 1.2b), are of importance in understanding multi-valley scattering and hot carrier relaxation processes. A schematic of valence-subbands and  $\Gamma$ , X, and L-valleys in the conduction band of GaAs is depicted in Fig. 1.2b. Depending on the band structure and optical-property, semiconductors are broadly classified into the following two categories,

1. **Direct bandgap material** (GaAs, InGaAs, InP, etc.): In this type of semiconductor, the minimum of the conduction band and maximum of the valence band are positioned at the same  $k$  ( $\Gamma$ -point). The excitation or recombination of electrons between the two bands is possible by the absorption or emission of photons with suitable energy (Fig. 1.3a). These materials are important because of their very-high radiative recombination efficiency and large-mobility of charge carriers.
2. **Indirect bandgap material** (Si, Ge, AlAs, GaP, etc.): In this class of semiconductors, the conduction band minimum does not position at the same  $k$ -value of the valence band maximum. As a result of this, the inter-band electronic transition is not-possible by the involvement of photons only. This is because the substantial change in momentum ( $\hbar\Delta k$ ) during the electronic transition between two indirect bands can not be conserved by the small momentum of photons, which

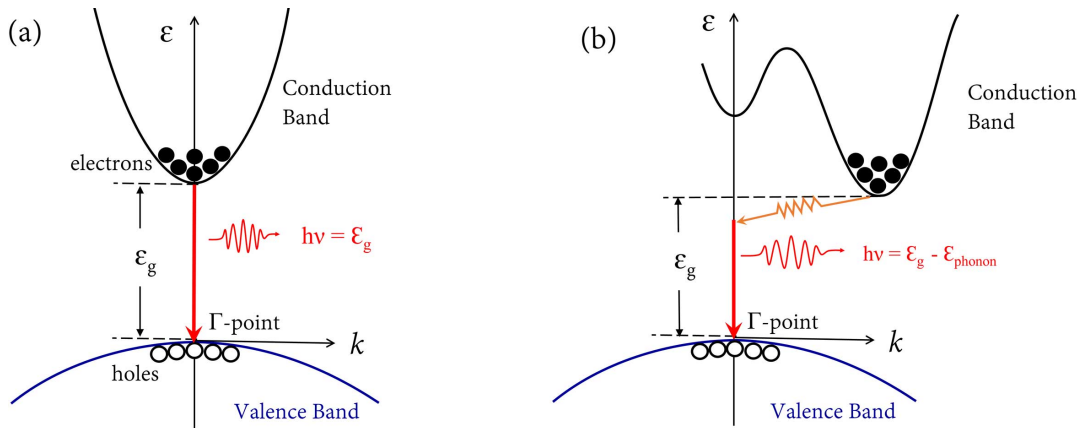


Figure 1.3: Schematic diagrams showing the band-dispersion and recombination of electron-hole pairs in (a) direct and (b) indirect bandgap semiconductors.



requires the emission or absorption of phonons: the quanta of lattice-vibration (Fig. 1.3b). Due to the involvement of phonon, it is challenging to use these materials in emission-based devices.

### 1.3 Excitons and excitonic-complexes

Absorption of photons in semiconductors or insulators can excite electrons from the valence band to conduction band, with the creation of positive charge vacancies in the valence band (holes). An attractive Coulomb interaction binds the electron and hole in the form of a neutral quasi-particle, which is known as an exciton. The theory of excitons was formulated by Frenkel, Peierls, and Wannier in explaining the light absorption mechanism in insulating solids.[32, 33] The difference between the excitons in semiconductors (Wannier-Mott) and insulator (Frenkel) is merely the radius, which is governed by their different dielectric constant and effective mass of charge carriers. The excitons in lattice carry a momentum which is the vector sum of the electron and hole-momenta,  $\hbar\mathbf{K} = \hbar\mathbf{k}_e - \hbar\mathbf{k}_h$ . Here, the wave vector of the electron ( $\mathbf{k}_e$ ) and hole ( $\mathbf{k}_h$ ) depends on the extrinsic and intrinsic perturbations on the charge carriers. The Wannier excitons with relatively large separation of electron-hole pairs can move in periodic potential of semiconductors are also known as free-excitons (FX). With the excitons being stable under the Coulomb interaction, the energy eigenstate of excitons is analogous to that of a hydrogen atom. However, the major difference between the hydrogen atom and

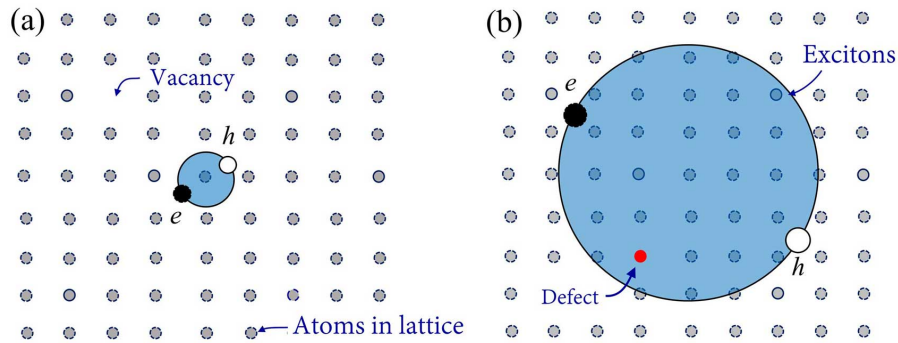


Figure 1.4: Spatial extent of (a) tightly-bound Frenkel-excitons in insulators and (b) weakly-bound Wannier-excitons in semiconductors.

exciton arises because:  $m_{proton} > m_h^*$  and the contribution of dielectric constant in the case of excitons. Therefore, unlike the hydrogen atom, both the electron and hole in an exciton move across a center of mass, and their Hamiltonian energy operator can be sub-divided into the center of mass motion and relative motion of charge carriers.

In the theoretical framework, the formation of excitons is described by an elementary excitation that removes a Bloch electron from the valence band (m-state) and creates another Bloch electron in the conduction band (n-state). The energy of the composite system is in-general expressed by the following relation,[23, 24]

$$\begin{aligned} \langle \phi_{mn\mathbf{k}_e\mathbf{k}_h} | H_{e-h} | \phi_{m'n'\mathbf{k}'_e\mathbf{k}'_h} \rangle &= \delta_{\mathbf{k}_h,\mathbf{k}'_h}^D \delta_{\mathbf{k}_e,\mathbf{k}'_e}^D [\varepsilon_0 + \varepsilon_n(\mathbf{k}_e) + \varepsilon_m(\mathbf{k}_h)] + \delta_{\mathbf{k}_e,\mathbf{k}_h}^D \delta_{\mathbf{k}'_e,\mathbf{k}'_h}^D \\ &\quad [2D_M \langle \phi_{n\mathbf{k}_em\mathbf{k}'_h} | b_{1,2} | \phi_{m\mathbf{k}_hn\mathbf{k}'_e} \rangle - \langle \phi_{n\mathbf{k}_em\mathbf{k}'_h} | b_{1,2} | \phi_{n\mathbf{k}'_em\mathbf{k}_h} \rangle] \end{aligned} \quad (1.7)$$

where  $\varepsilon_n(\mathbf{k}_e)$  [ $\varepsilon_m(\mathbf{k}_h)$ ] signifies the energy of an electron in the conduction band [valence electron] considering the Coulomb and exchange interactions. The last two terms of Eq. 1.7 have the interpretations in the diagonal elements (i.e.,  $\mathbf{k}_h = \mathbf{k}'_h$  and  $\mathbf{k}_e = \mathbf{k}'_e$ ), which represent the Coulomb and exchange interactions between electron and holes. The symbol  $\delta^D$  represents the Dirac-delta function. The magnitude of  $D_M$  is unity for a pure singlet state and zero for a triplet state, because exchange interaction vanishes for electron-hole with parallel spins. In the case of large radius Wannier excitons, all other many-body interaction terms, except the electron and hole Coulomb interaction, can be neglected. Under this approximation, the Schrödinger equation and binding energy of excitons ( $\varepsilon_b$ ) are expressed by,

$$\left[ -\frac{\hbar^2 \nabla_e^2}{2m_e^*} - \frac{\hbar^2 \nabla_h^2}{2m_h^*} - \frac{e^2}{4\pi\epsilon_0\epsilon_r|r_b|} \right] \phi_{m,n,\mathbf{k}_e,\mathbf{k}_h} = \varepsilon \phi_{m,n,\mathbf{k}_e,\mathbf{k}_h} \quad (1.8)$$

$$\varepsilon_b(\mathbf{K}) = \frac{\mu^* e^4}{32\pi^2 \epsilon_0^2 \epsilon_r^2 n^2 \hbar^2} + \frac{\hbar^2 \mathbf{K}^2}{2M^*} \quad (1.9)$$

where  $\mu^* = (1/m_e^* + 1/m_h^*)^{-1}$ ,  $M^* = (m_e^* + m_h^*)$  and  $r_b$  denote the reduced mass, total effective mass, and Bohr radius of excitons, respectively. The second term of Eq. 1.9 signifies the energy of excitons in the center of mass frame of reference, which is often

neglected because  $M^* \gg \mu^*$ . A detailed description of excitons in the center of mass frame and its constituent electron-hole in the relative frame of reference is discussed in the forthcoming chapters of the thesis.

The Coulomb attraction between two oppositely charged particles enhances the electron-hole wave function overlap, which causes a decrease in radiative recombination time of excitons. Therefore, the radiative recombination efficiency  $[1/(1+\tau_r/\tau_{nr})]$  of the material system increases, which may also influence the inter-subband relaxation process. Here,  $\tau_r$  and  $\tau_{nr}$  represent the radiative and non-radiative recombination time of charge carriers, respectively. Such effects of Coulomb interaction are often used to develop high-efficiency light-emitters, photonic devices, excitonic switches, etc.[34, 35, 36] Depending on the optical property of excitons and their coupling with the dipole electric field, excitons are classified into ‘bright’ and ‘dark-excitons’. The excitons with total angular momentum  $\pm 1$  are dipole allowed and possess high radiative recombination efficiency are known as bright-excitons. On the contrary, when the electron and hole spin become parallel, i.e.,  $J = \pm 2$ , excitons may not couple to dipole electric field; they can not be created by optical excitation and forbidden for radiative recombination.[37, 38] Because of the extra-ordinary long recombination time, dark-excitons are being exploited in spintronic devices and quantum information processing.[39, 40] More than two-charged particles can also be bound by the Coulomb interaction to form trions (three-particle state), bi-excitons (four-particle state), and so on, which are known as excitonic-complexes. For example, an additional electron (or hole) can be bound with an exciton to form negatively (positively) charged-exciton or trion. In general, these excitonic-complexes are highly unstable and can be observed in high-quality quantum structures at a fairly low temperature. In addition to their novel electro-optical properties, investigation on the excitonic-complexes can provide valuable information about the many-body interactions in solids.[41]

## 1.4 Semiconductor quantum structures

Charge carriers in a solid exhibit quantum mechanical behavior when the physical size of the system becomes comparable with the characteristic wavelength of electron and hole ( $\lambda_{deBroglie} = h/\sqrt{2m^*k_B T}$ ). The confinement of electron-hole in one, two, and three-dimensions are technically known as the quantum well (QW), quantum wire (QWR), and quantum dot (QD) respectively. The reduction in dimensionality causes a dramatic change in electronic behavior, known as quantum size-effects, which is widely used in various types of lasers, photo-detectors, and high-mobility devices. The QW structure is constructed when a small bandgap material having a thickness of  $l_w \leq \lambda_{deBroglie}$  or  $r_b$ , is sandwiched between a high-bandgap material (barriers). Therefore, the motion of charge carriers is forbidden along the growth direction, where the band offset in conduction and valence band acts as the barrier potential ( $\Delta\epsilon_c$  and  $\Delta\epsilon_v$ ), Figs. 1.5a and 1.5b. Moreover, the degeneracy of heavy and light hole states is lifted due to the breaking of translational symmetry along the z-direction. The high crystalline quality QW and barrier layers are grown by advanced epitaxial growth techniques, such as metal-organic vapor phase epitaxy (MOVPE) and molecular beam epitaxy (MBE). The energy eigenstates of an infinite potential well can be easily estimated by solving the Schrödinger equation which is given by,

$$\epsilon_s(l_w) = \epsilon_s(z) + \epsilon(x, y) = \frac{s^2 \pi^2 \hbar^2}{2m_{e/h}^* l_w^2} + \frac{\hbar^2}{2m_{e/h}^*} (k_x^2 + k_y^2) \quad (1.10)$$

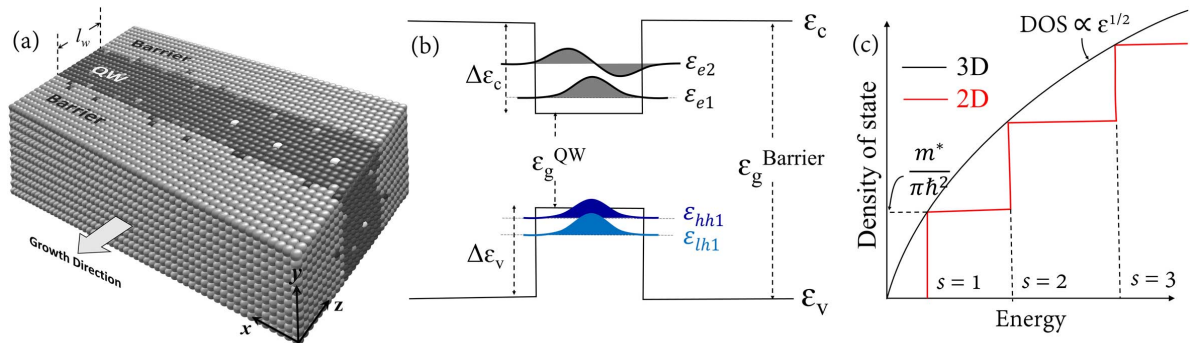


Figure 1.5: (a) Schematic of a QW-structure and one-dimensional confinement of charge carriers leading to the (b) discretization of energy states and (c) modification of DOS.

where,  $\varepsilon_s(l_w)$  represents the  $s^{th}$  quantized energy state of electrons/hole. Equation 1.10 has great importance which shows that the effective bandgap of the material  $[\varepsilon_g^* = \varepsilon_g + \varepsilon_e(l_w) + \varepsilon_h(l_w)]$  varies with QW thickness. In the case of finite barrier ( $V_z$ ) potential well, a significant amount of wave function penetrates into barrier layers. Therefore, an effective QW thickness ( $l_w^*$ ) can be introduced in Eq. 1.10 to consider the penetration effects, where  $l_w^* \geq l_w$ . According to the previous reports, one such correction factor in  $l_w$  is given by,[42]

$$l_w^* = l_w + \frac{2}{k_b} \quad (1.11)$$

The wave vector ( $k_b$ ) can be estimated by the following transcendental equations,

$$k_w l_w = s\pi - 2 \arcsin \left[ \frac{k_w/m_w^*}{k_w^2/m_w^{*2} + k_b^2/m_b^{*2}} \right] \quad (1.12)$$

where,

$$k_w = \frac{\sqrt{2m_w^*\varepsilon_s}}{\hbar} \quad k_b = \frac{\sqrt{2m_b^*(V_z - \varepsilon_s)}}{\hbar} \quad (1.13)$$

The symbols  $m_w^*$  and  $m_b^*$  signify the effective mass of charge carriers in the QW and barrier layer, respectively. Notably, one can numerically solve the Schrödinger equation for finite barrier QW using a self-consistent finite element/difference method by commonly used software programming (Matlab, Python, and COMSOL), or by the use of transcendental equations.[43]

The density of state (DOS), which defines the number of electronic states per unit energy interval in a unit volume, is another important factor that gets modified in quantum structures. As compared to a bulk semiconductor where DOS continuously varies with energy  $[\text{DOS}(3\text{D}) \propto \varepsilon^{1/2}]$ , the DOS for a QW remains invariant with energy  $\text{DOS}(2\text{D}) = m^*/\pi\hbar^2$ . Nonetheless,  $\text{DOS}(2\text{D})$  exhibits a step-like increase when the next energy level of the QW is introduced (Fig. 1.5c). This sharp increase in  $\text{DOS}(2\text{D})$  helps in accumulating a large number of charge carriers at the band-edges. The carrier

occupancy in the QW can be explained by the following relation,

$$n_{2D} = \int [\text{DOS}(2D) \times F_e(\varepsilon_f)] d\varepsilon = \frac{m^*}{\pi \hbar^2} \ln \left[ 1 + \exp(\varepsilon_c - \varepsilon_f)/k_B T \right] \quad (1.14)$$

where  $F_e(\varepsilon_f) = 1/[1 + \exp(\varepsilon - \varepsilon_f)/k_B T]$  is the Fermi-Dirac distribution function, which signifies the probability of electron occupancy in the conduction band. Similar to this, the confinement of charge carriers in QWRs and QDs further quantizes the energy state and modifies the DOS. A detailed discussion on the impact of charge carrier confinement in quantum structures may be found in Refs. [44, 45].

## 1.5 Oscillator strength

The confinement of charges in a low-dimensional system enhances the electron-hole wave-function overlap, which can be described by the oscillator strength,  $\varrho$ . During the electronic transition, oscillating dipole must be induced by the interaction of electron-hole pairs with electromagnetic radiation. Therefore, the oscillator strength of electron-hole pairs having the dipole moment of  $-\hat{\mathbf{E}} \cdot \mathbf{r}$  is often used in explaining the absorption and emission properties of semiconductors. For the light propagation along the  $z$ -direction, the oscillator strength of excitons is given by,[46, 47]

$$\varrho = \frac{2}{\mu^* \varepsilon_g} \left| \Phi(0) \hat{x} \cdot [M]_{n \rightarrow m} \right|^2 \quad (1.15)$$

where  $|\Phi(0)|^2$  is the probability of finding electron and hole at the same position, and  $[M]_{n \rightarrow m}$  denotes the transition matrix element corresponding to the optical transition. In the case of excitons confined in a QW, Eq. 1.15 is given by,[48]

$$\varrho = \frac{2}{\mu^* \varepsilon_g D} \times \left[ \frac{1}{\sqrt{D}} \int e^{ik_x y r} \Phi_{ex}(r) d^2 r \right]^2 \left| \langle u_c | \hat{\mathbf{E}} \cdot \mathbf{p} | u_v \rangle \langle \phi_{e,p}(z) | \phi_{h,p}(z) \rangle \right|^2 \quad (1.16)$$

where  $D$  is the area of the QW. An extensive amount of research is performed to estimate  $\varrho$  as a function of QW thickness, which in-general increases with decreasing

the QW thickness. This increase in  $\rho$  for a low-dimensional system is therefore desirable for high-efficiency emission and absorption based devices. However, in the case of a very thin QW, a significant amount of electron-hole wave function penetrates into the barrier layer, which causes a reduction of  $\rho$ .<sup>[49]</sup>

## 1.6 External perturbations on the carriers in semiconductors

The electro-optical properties of semiconductors are highly sensitive to external perturbations, such as temperature, pressure, electric field, magnetic field, etc. For example, with an increase in temperature, most of the semiconductors exhibit a reduction in the bandgap, which can be explained by the thermal expansion of lattice and electron-phonon interactions in the solid.<sup>[50, 51]</sup> Moreover, the thermal energy may excite electrons into the conduction band, which can alter the conductivity of charge transport. Therefore, the recombination of electron-hole and charge-transport in the medium are affected by the involvement of phonons, which may lead to non-radiative decay of charge carriers. At a sufficiently high temperature ( $\varepsilon_b < k_B T$ ), excitons get dissociated where the constituent electron and hole may overcome the potential barrier of the quantum structure. On the contrary, a magnetic perturbation can be desirable in confining electron-hole pairs in a given plane, which enhances the oscillator strength and binding energy of excitons. Similar to the structural confinement, strong magnetic confinement causes discretization of energy state and modifies the DOS.<sup>[52, 53]</sup> Notably, the carriers in a QW are confined in all the three-directions when a magnetic field is applied perpendicular to the QW-plane. Therefore, the system becomes conceptually similar to a QD. Moreover, the magnetic confinement does not introduce additional surfaces or interface-states that helps to overcome the common problem of surface charge recombination in QDs and QWRs. In view of this, the impact of the magnetic field on the inter-band excitonic recombination and inter-subband carrier relaxation can be utilized in advanced optoelectronic and photonic devices.<sup>[54, 55]</sup> Since the discovery of

quantum Hall by Klaus von Klitzing and even before, the magnetic field has been extensively used in realizing the fundamental aspects of physics and scattering-free chiral charge transport in solids.[56, 57, 58] A natural extension of these investigations under a high magnetic field helped in explaining novel concepts of condensed matter physics (e.g., topological state) and development of quantum devices.

## 1.7 Motivation and layout of the present study

Confinement of charge carriers in a low-dimensional semiconductor may cause an enhancement of carrier-carrier interaction, which is responsible for the stability of excitonic quasi-particles under an external perturbation. Investigation on the unique properties of excitons in quantum structures and their coupling with electro-magnetic radiation is of great importance in optoelectronic and photonic devices. However, with an increase in carrier confinement, a significant amount of wave function penetrations into the surrounding medium. As a result of this, charge carriers become localized at the hetero-interfaces, and their decay life increases due to the non-radiative process. Therefore, to develop highly efficient advanced optoelectronic devices, critical factors that can control the radiative and non-radiative processes need to be understood by combining advanced techniques that are sensitive to probe the ultra-low defect density. Application of a magnetic field during spectroscopic or charge transport measurement is one such perturbation, which can provide critical information related to the above processes and fundamental properties of the material system. Moreover, a sufficiently strong magnetic perturbation can be desirable for surmounting the disorders' influence on electro-optical processes. Besides the magnetic field-driven charge carrier confinement, magnetic perturbation along different planes can be utilized for precise control of the recombination and transport property of excitons. The motivation of the present thesis is to utilize the 'magnetic field' as a unique tool to control charge carriers' localization, recombination, and their transport property. The present thesis deals with novel methodologies for spectroscopic and charge-transport measurements on ultra-low disordered QWs. The usefulness of magnetic perturbation in evaluating the defect



density and its role in the device performance are also presented.

The thesis is organized into eight chapters. In Chapter 2, a brief description of the MOVPE technique to grow III-V semiconductors and experimental techniques to characterize the basic properties of the grown samples are discussed. The details of a maskless-photolithography system, which is developed to fabricate semiconductor devices, are also described. In Chapter 3, carrier-carrier interaction leading to the localization of charges at the hetero-interfaces and broadening of energy state for various thicknesses of QW are investigated by PL and SPV measurements. An experimental investigation to realize the impact of quantum confinement on the effective mass of excitons is also presented. Chapter 4 describes the magnetic field-driven in-plane confinement of electron-hole pairs to control the recombination efficiency of free and disorder-bound excitons. A phenomenological model to estimate defect density in quantum structures with the help of magneto-PL spectroscopy is presented. After that, the role of thermal energy on the magneto-optical processes is investigated by combining magneto-PL and magneto-SPV. In Chapter 5, the anisotropic property of excitons in QWs is probed by magneto-optical and magnetic-susceptibility measurements with a magnetic field perpendicular or parallel to the QW-plane. A unique method to control the recombination, transport, and magnetic behavior of charges by an external magnetic field along different orientations is demonstrated. Chapter 6 presents the correlation between the optical and transport properties of charge carriers by the simultaneous measurements of magneto-PL and magneto-resistance. It is shown that magneto-PL spectroscopy in the quantum Hall regime can provide detailed information on magneto-electro-optical processes in quantum structures. With this understanding, QW-based semiconductor laser diode and photo-detectors are tested, and their results are described in Chapter 7. To validate the above findings on the QW structures, QW-based diode lasers and photo-detectors are operated under low-temperature and high magnetic field conditions. Finally, in Chapter 8, the results of the entire thesis are summarized with a proposal for future research directions.

# Chapter 2

## Growth and Experimental Techniques

### 2.1 Introduction

This chapter briefly describes the metal-organic vapor phase epitaxy (MOVPE) growth of semiconductor hetero and quantum structures. Growth conditions in the MOVPE reactor chamber and precursors used to grow GaAs-based quantum structures are also described. Thereafter, the conventional and advanced characterization techniques which are used to study optical, electronic, and structural parameters of the grown samples are discussed. In order to pattern samples for magnetotransport measurements and to fabricate optoelectronic devices, a simple and inexpensive maskless-photolithography system is developed. In this chapter, details of the maskless-photolithography system and its advantages over a conventional mask-based photolithography technique are described. Finally, the development of edge-emitting semiconductor laser diodes and near-infrared photo-detectors by the use of the maskless-photolithography system are discussed.

## 2.2 Metal-organic vapor phase epitaxy growth

The MOVPE technique has evolved as a major technique for the epitaxial growth of III-V semiconductor quantum structures for optoelectronic devices. In particular, the ability of large-scale production, high throughput, and feasibility to grow ultra-low disordered quantum structures are some of the key features of MOVPE growth.[59] In this technique, metal-organic precursors are kept in a bubbler-bath at a low temperature, between the range of -10 to 17 °C. The vapor of the desired element is then transported into the growth chamber by carrier gases (hydrogen), Fig. 2.1a. The flow-rate of the precursor molecules is controlled by mass flow controllers. The gas flow pattern in the reactor chamber is controlled by the velocity of the gas molecules at the desired pressure and temperature. The schematic diagram and photograph of the horizontal reactor MOVPE are shown in Figs. 2.1a and 2.1b. In the reactor chamber, the substrate is kept on a silicon carbide coated graphite susceptor, which is heated by the absorption of infrared radiation, and the substrate is rotated at 20 Hz. The metal-organic precursor molecules and hydrides in close vicinity of the heated substrate are pyrolyzed by the thermal energy and then adsorbed on the surface of the substrate. The thermal energy of the substrate helps in migrating the adsorbed atoms in the energetically favorable site to grow a high-quality epitaxial layer. The adsorption and migration of atoms on the substrate also depend on the surface energy of the sub-

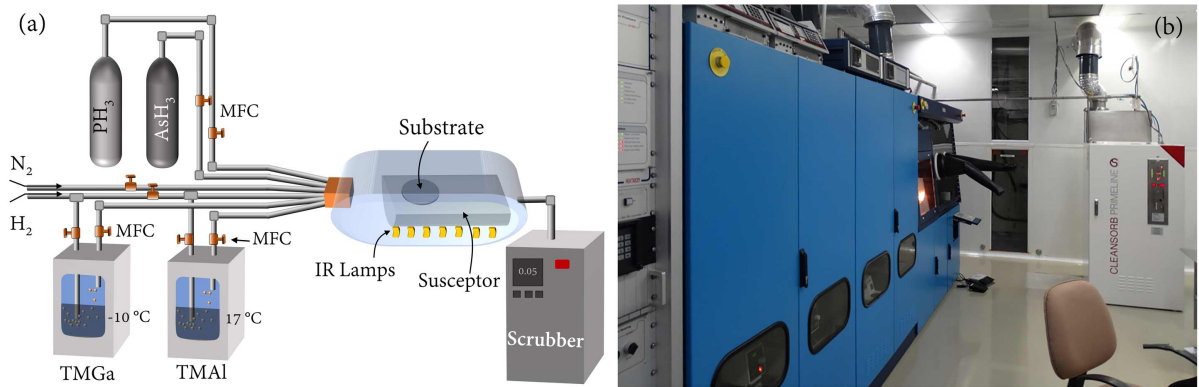


Figure 2.1: (a) Schematic and (b) photograph of the MOVPE system for the III-V semiconductor growth.

strate. The reaction by-products and non-reacted precursor molecules are then safely removed and converted into non-toxic complex oxide salts of phosphate and arsenate by a scrubber. The temperature, pressure, and surface energy of the substrate plays a vital role in determining the growth rate and quality of the grown epilayers. Depending on the growth rate and temperature-dependent processes, MOVPE growth can be subdivided into three different regimes, which are schematically depicted in Fig. 2.2. In a low-temperature regime ( $< 550\text{ }^{\circ}\text{C}$ ), the growth rate is constrained by the kinetics of the gas-phase reaction, which is mainly because the group-III precursors remain non-pyrolyzed in close vicinity of the substrate. Moreover, with the less kinetic energy of the adsorbed molecules, they can not move at the energetically favorable site on the substrate at this lower-temperature. On the other hand, the growth rate again decreases at  $T > 770\text{ }^{\circ}\text{C}$  due to the thermal desorption of deposited materials. Therefore, an intermediate temperature regime ( $550 - 770\text{ }^{\circ}\text{C}$ ), where the growth rate is independent of temperature, is preferred for high-quality epitaxial growth, which is known as mass transport region. Chemical properties of the precursors are also crucial in the MOVPE growth, which should contain the following key properties: low-pyrolysis temperature, high vapor-pressure, less-sensitive for parasitic gas-phase reaction, availability in high purity condition and less-toxic.

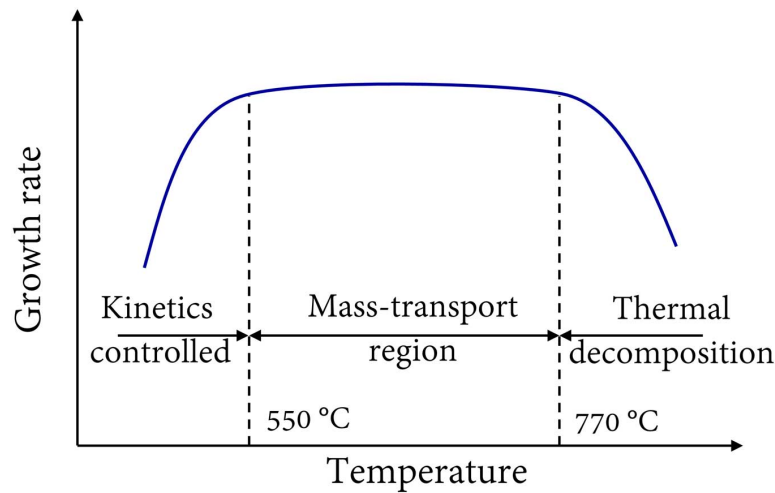
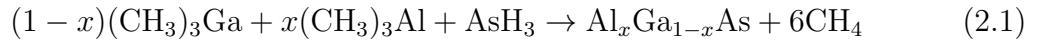


Figure 2.2: Schematic diagram showing the growth rate as a function of temperature in the MOVPE technique.

The MOVPE growth of GaAs, AlGaAs and InGaAs based hetero and quantum structures are performed by trimethyl gallium  $[(\text{CH}_3)_3\text{Ga}]$ , trimethyl aluminum  $[(\text{CH}_3)_3\text{Al}]$ , trimethyl indium  $[(\text{CH}_3)_3\text{In}]$  and arsine ( $\text{AsH}_3$ ) precursors in the AIX-200 machine. The alloying of compound semiconductors (e.g., AlGaAs, InGaAs) is achieved by mixing different metal-organic constituents in an appropriate vapor-phase ratio. The chemical process for the epitaxial growth of  $\text{Al}_x\text{Ga}_{1-x}\text{As}$  material (ternary compound) is given by,



The samples are grown on (100) oriented GaAs substrates at 670 - 770 °C temperature under 50 mbar pressure. In order to dope the epitaxial films with silicon (zinc) atoms, silane (diethyl zinc) precursor molecules are introduced into the reactor chamber during growth.

**Safety aspects:** The primary risk in MOVPE growth arises due to the highly toxic nature of hydride precursors, e.g., arsine, phosphine, silane, etc. In addition to this, hydrogen and phosphine gases are flammable, where special attention is required to prevent gas leakage from the transfer lines and reactor. Metal-organic precursors are also pyrophoric in nature. The hazard management section of MOVPE-machine ensures the safety aspects by utilizing the toxic-gas monitoring system, ventilation system, neutralization systems, and automatic process control system. Toxic gas monitoring systems (particularly for arsine and phosphine) are used to provide early detection and shut-down of the machine before the dangerous exposure occurs. Automatic process control system alarms under an accidental situation (due to the restriction of gas flow, early leak-detection, blockage in a valve and problem in the cooling system) and initiate the necessary steps to protect the loss of property and ensure the human safety. The handling of III-V semiconductors with arsenic contents also requires special attention.

## 2.3 Structural Characterization

### 2.3.1 High-resolution x-ray diffraction measurements

High-resolution x-ray diffraction (HRXRD) measurement is a powerful technique to realize the crystalline quality of epitaxial thin films. The HRXRD is a necessary tool to estimate the thickness and composition of nearly lattice-matched epitaxial layers. In this setup, x-rays generated from a copper anode ( $\lambda = 1.5405 \text{ \AA}$ ) is passed through a four bounce monochromator by Ge(2 2 0) and (4 4 0) reflection to achieve a collimated and highly monochromatic x-ray beam ( $\Delta\varepsilon/\varepsilon \geq 10^{-3}$ ), Fig. 2.3a. The beam is allowed to diffract by the sample that is kept on a goniometer stage to control the linear (x-y-z) and angular motion ( $\omega, \phi, \chi$ ) of the sample (Fig. 2.3b). The diffracted x-rays are then recorded by a Xenon filled proportional counter, where the atoms of the noble gas are ionized in an avalanche process by the high-energy x-rays. The electrons generated in the ionization process are collected by an anode-wire with 1-3 kV potential, where the number of electrons collected in the wire becomes a measure of x-ray intensity. The diffraction peak occurs when the periodic atoms in a given plane constructively interfere with the incident x-rays, which can be expressed by the well-known Bragg's law.

$$2d_{h,k,l} \sin \theta = q\lambda \quad (2.2)$$

where  $\lambda$  is the wavelength of the incident x-rays,  $d_{h,k,l}$  is the inter-planar spacing of the lattice, and  $q$  denotes the order of diffraction. In  $(\omega - 2\theta)$  scan mode, the position of the

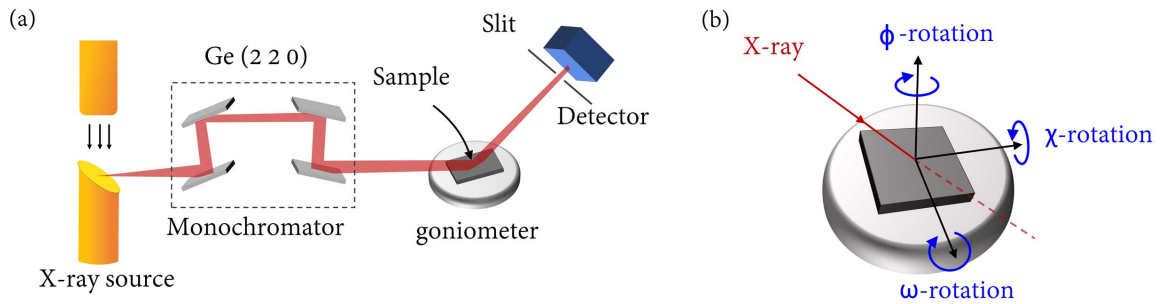


Figure 2.3: (a) Schematic of the instrumental configuration for HRXRD measurements and (b) goniometer rotation for different modes of x-ray scan.

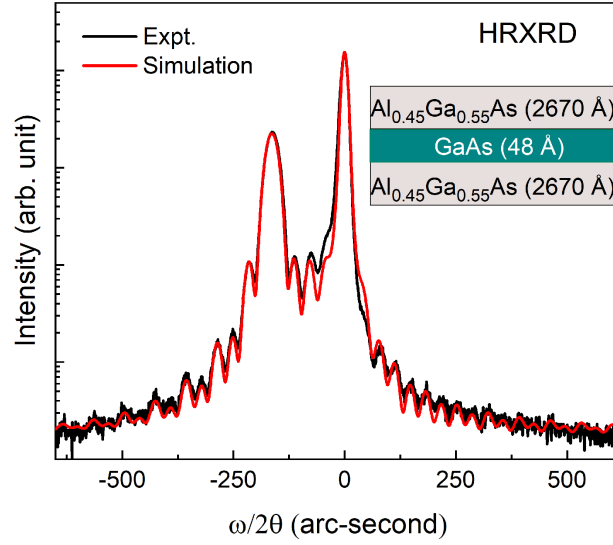


Figure 2.4: Results of HRXRD measurement and simulated profile of a GaAs/AlGaAs QW sample.

main peak provides the information of d-spacing, where the broadening of the peak is a measure of the crystalline quality of the sample. Around the central peak, fringes may arise due to the interference of x-rays by multiple layers of the sample. The thickness of an epitaxial layer can be estimated by the separation between two successive maxima in the interference fringe ( $\Delta\theta$ ), which is given by the Scherrer equation,[60]

$$t = \frac{(q_1 - q_2) \times \lambda}{2\Delta\theta \cos \theta} \quad (2.3)$$

In this thesis, the PANalytical X'Pert diffractometer is used to record the HRXRD profile, which is then simulated to estimate layer thickness and composition of the grown films. Figure 2.4 shows the HRXRD data of a GaAs QW sample, where the distinct fringes on either side of GaAs and AlGaAs peaks suggest the high crystalline quality of epitaxial thin-films. The result obtained by HRXRD measurement is also matched with a simulated-profile to estimate the layer details (shown in the inset).

### 2.3.2 Cross-sectional transmission electron microscopy

Cross-sectional transmission electron microscopy (TEM) provides direct imaging of solids with resolution down to few nanometers. This is beneficial in realizing the crys-

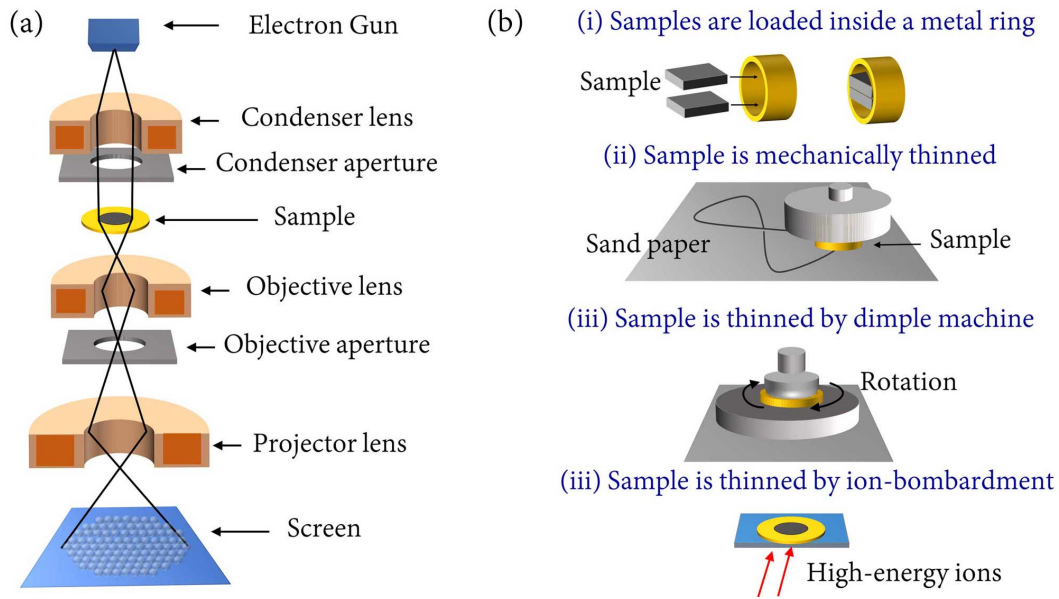


Figure 2.5: (a) Schematic diagram of a transmission electron microscope and (b) steps involved in preparing samples for cross-sectional TEM measurements.

talline quality of bulk/hetero-junctions, layer thickness, sample non-uniformity, etc. In this technique, a high energy electron beam (100 - 300 keV) with very small de-Broglie wavelength is transmitted or diffracted by solids to achieve magnification up to 10,00,000X. In order to transmit the electron beam across the sample, the thickness of the specimen is reduced to a few tens of nanometers. The transmitted or scattered electrons are then projected on a fluorescent screen to image the sample. The contrast between two adjacent portions of a TEM image is originated due to a variation in atomic-density or non-uniformity in sample thickness. Figure 2.5a shows the schematic diagram of a transmission electron microscope in imaging mode, which consists of electron-gun, electro-magnetic lenses, apertures, and an image screen. The energetic electrons emitted from an electron-gun, either by thermionic emission or field emission process, are passed through a condenser lens, which collimates the e-beam. After that, the electrons are passed through the sample, and an objective lens collects the scattered electrons. An objective aperture is also used to define the collection angle of the scattered electrons, which is then magnified and focused on a phosphor screen by a projector lens. Depending on the position of the objective aperture and electromagnetic lenses, the sample can be probed in imaging mode or diffraction mode.



Other than the instrumentation, the most difficult part of this technique is the sample preparation to probe a cross-sectional interface, which is schematically illustrated in Fig. 2.5b. First, two small pieces of a sample (thickness  $\sim 300 \mu\text{m}$ ) are loaded inside a metal ring with a cross-sectional edge towards the open faces of the metal ring (inner diameter  $\sim 2 \text{ mm}$ ). The ring with the sample is mechanically thinned up to  $\sim 100 \mu\text{m}$ , and then put inside a dimpling machine to reduce the thickness ( $\sim 20 \mu\text{m}$ ) using a diamond paste. Finally, an ion-bombardment technique is used to thin the sample up to a few nanometers, which is then imaged by TEM. In this thesis work, cross-sectional TEM measurements are performed by Philips CM200 instrument, which is operated at 200 kV.

## 2.4 Spectroscopic characterization techniques

### 2.4.1 Photoluminescence spectroscopy

Photoluminescence (PL) spectroscopy is a powerful tool to investigate the optical properties of semiconductors (particularly for direct-bandgap materials), which is widely used because of its simplicity and non-invasive characteristics. In this technique, electrons in the valence band are excited into the conduction band by electromagnetic radiation (i.e., photons) with energy  $h\nu > \varepsilon_g$ . The photo-excited electron and hole quickly relax ( $\lesssim \text{ps}$ ) to their respective band-edges, and recombine either by the radiative or non-radiative process. The photons emitted due to the radiative recombination of electron-hole pairs are dispersed in energy to record the PL spectrum, Fig. 2.6a. In general, the intensity of PL ( $I$ ) is expressed by the recombination rate of charge carriers ( $R_r$ ), which depends on the carrier density in the respective bands (n and p) and radiative recombination time ( $\tau_r$ ), i.e.,  $I = [M]_{n,m} \times R_r = [M]_{n,m} \times (n \times p / \tau_r)$ . The carrier occupancy in the conduction/valence band under a steady-state condition can

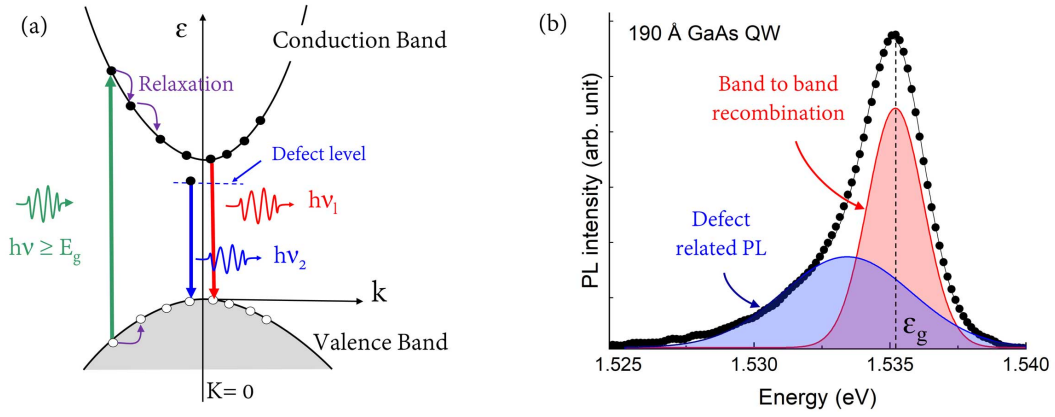


Figure 2.6: (a) Excitation of charge carriers by photons followed by the relaxation and recombination of electron-hole pairs. (b) PL line-shape contributed by the band-to-band recombination and defect-assisted radiative recombination of a 190 Å thick GaAs/AlGaAs QW at 4.2 K.

be expressed by,

$$n = \int_{\epsilon_c}^{\infty} \text{DOS}_e F_e(\epsilon_{fn}) d\epsilon \quad (2.4)$$

$$p = \int_0^{\infty} \text{DOS}_h [1 - F_e(\epsilon_{fn})] d\epsilon \quad (2.5)$$

where  $\epsilon_{fn}$  denotes the quasi-Fermi energy of electrons under light illumination. At a low-temperature, Coulomb interaction between electron and hole becomes dominant as compared to their thermal energy, which results in a formation of excitons and causes a decrease in  $\tau_r$  (ns - ps). [61] On the other hand, photo-excited carriers in the band can be captured by defects, impurities, and localization potentials due to shallow defects. The recombination of carriers via radiatively active defect-centers may cause asymmetry in the PL line-shape. Figure 2.6b shows the PL spectra of a 190 Å thick GaAs/AlGaAs QW, where the asymmetric peak due to the carrier localization can be clearly observed. Because of this, PL spectroscopy under an external perturbation (such as temperature, pressure, electric field, magnetic field, etc.) is often desirable in realizing the optical response, carrier localization, and quality of semiconductors.

The experimental setup for PL measurement is schematically shown in Fig. 2.7. Here, a laser light illuminates the sample over a circular spot diameter  $\leq 1$  mm, with

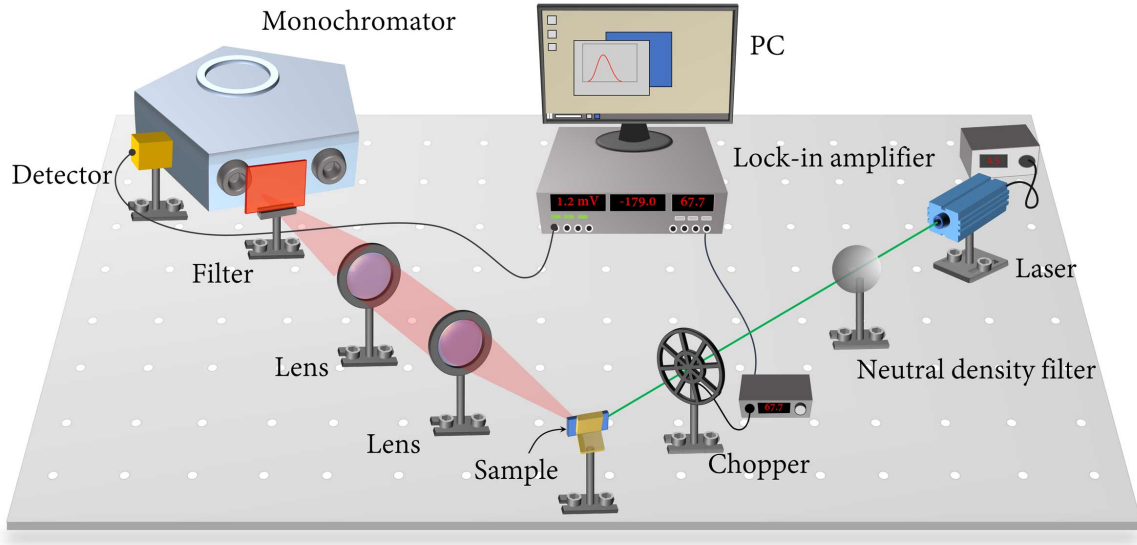


Figure 2.7: Schematic of the photoluminescence experimental setup.

a typical laser power density  $\leq 2.5 \text{ W/cm}^2$ . A circularly gradient neutral density filter is used to control the excitation power of the laser light for a power-dependent PL measurement. This low level of excitation power helps in minimizing the saturation of energy levels, broadening of energy states, and temperature rise effects within the sample. In general, the above effects become dominant for the excitation power density greater than  $10 - 12 \text{ W/cm}^2$ .<sup>[62]</sup> The PL spectra are recorded by using the second harmonics of Nd: YAG laser (532 nm) and diode lasers (640, 690, and 808 nm) for the excitation of charge carriers in the QW or barrier layers. The PL is collected by a pair of lenses, which is then transmitted through a long-pass filter to remove the reflected laser light. The long-pass filters that are mainly used in this thesis have the cutoff wavelengths of 560, 450, and 880 nm. A spectrometer (*i*HR320) with 1200 lines/mm grating is used to disperse the PL signal, which is then measured by a p-i-n silicon photo-diode. To reduce the contribution of noise, PL spectra are recorded by using a lock-in amplifier (SR830) with a reference from a mechanical chopper (mostly at 67 Hz). The chopping frequency is ascertained from where the contribution of noise in PL spectra is minimized.

### 2.4.2 Surface photovoltage spectroscopy

Surface photovoltage (SPV) spectroscopy is an efficient technique to probe absorption and redistribution of charge carriers in bulk, hetero, and quantum structures of semiconductors. In general, bands at the surface or interface of semiconductors bend due to the localization of charges by surface and interface defect states. These localization/defect centers are originated due to the breaking of crystal periodicity, which creates unsaturated dangling bonds and causes the transfer of charges from bulk to the surface. Under this condition, photo-excited charge carriers spatially migrate according to the surface/interface electric field or due to a non-uniform carrier generation in the sample. These charge redistribution processes under light illumination may change the surface potential ( $V_s^{dark} - V_s^{light}$ ), which is a measure of the SPV signal.[63, 64] On the other hand, a relative change in SPV-phase can be understood either by evolution or dominance of a charge distribution that may oppose an existing process. Generation of SPV due to drift and diffusion of charges is schematically illustrated in Fig. 2.8a for a sample with upward band-bending. Charge carriers that are excited within the depletion width ( $l_d$ ), drift according to this surface band-bending. The spatial separation of electron and holes due to this drift develops an electric field ( $\mathbf{E}_s^*$ ), which is in the opposite direction of the surface electric field ( $\mathbf{E}_s$ ), hence band-bending is re-

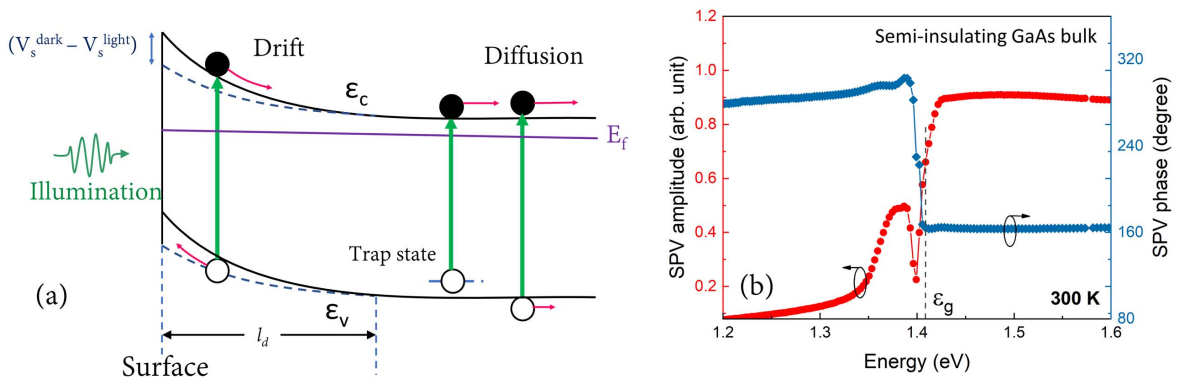


Figure 2.8: (a) Generation of photo-voltage by charge redistribution processes is schematically illustrated and (b) SPV amplitude and phase of a semi-insulating GaAs substrate at room temperature.

duced. On the other hand, both the electron and hole in the field-free region (deep in the sample) diffuse away from the surface. This is because the photo-excited carrier density decreases with the depth from the surface,  $n(w) \sim n(0) \times \exp(-\alpha^*w)$  where  $\alpha^*$  denotes the absorption coefficient. Although the electron and hole diffuse in the same direction, they become spatially separated due to their different mobility and diffusion constant. The SPV signal, which is generated by this difference in electron and hole mobility, is known as Dember voltage.[65] Figure 2.8b shows the SPV amplitude and phase spectra of a semi-insulating GaAs substrate, where an enhancement of SPV-amplitude and sharp-change in SPV-phase can be observed at the band-edge (1.42 eV). In particular, when the energy of the incident photons is higher than  $\varepsilon_g$ , a large number of electrons are photo-excited and the spatial redistribution of these charge carriers causes an enhancement of SPV amplitude. Here, the capture of charge carriers by defects plays a vital role in determining the amplitude and phase spectra. Similar to this, SPV of a p-doped semiconductor with downward band-bending can be found in literature reports.[63]. Further, discussion on the charge redistribution processes and contribution of carrier localization in the SPV of QWs can be found in Chapter 3.

SPV measurements are performed in metal-insulator-semiconductor (MIS) configuration, which is depicted in Fig. 2.9.[66] For the excitation of electrons, a broad spectrum

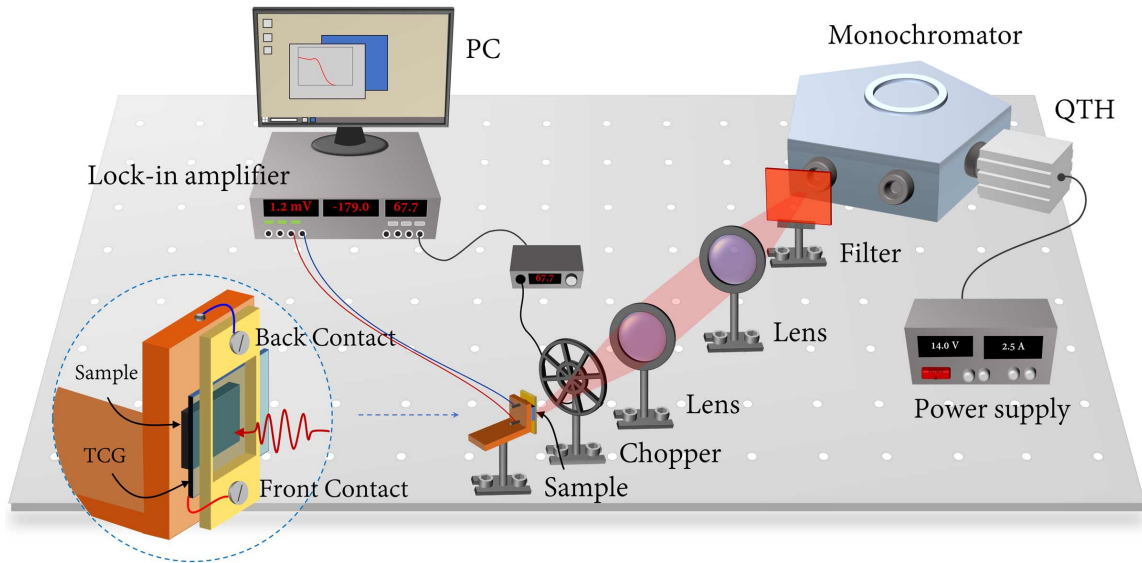


Figure 2.9: Schematic of the experimental setup for SPV measurement.

of quartz-tungsten-halogen (QTH) lamp is monochromatized by *i*HR-320 monochromator, which is then passed through a long-pass filter to remove higher harmonics originated from the grating. An indium-tin-oxide (ITO) coated transparent conducting glass (TCG) plate is kept in a soft contact mode with the sample surface.[66] The sample is illuminated through the TCG plate, which measures the change in surface potential during the photo-excitation (Fig. 2.9). The SPV is recorded by a lock-in amplifier (SR830) with mechanical chopper arrangements (chopping frequency range 20 Hz - 3 kHz). In particular, SPV measurements at a higher chopping frequency is beneficial to probe the carrier redistribution process with relatively small response time (i.e., fast process), whereas the SPV at a low-chopping frequency can be contributed by both the fast and slow processes.

### 2.4.3 Magneto-optical spectroscopy

Detailed information on the optoelectronic properties and fundamental parameters of semiconductors can be acquired by spectroscopic measurements under a magnetic perturbation. Under a strong magnetic field, charge carriers are confined in a very small radius, which causes the discretization of energy state in the form of Landau states. The energy eigenvalue of charge carriers under an applied magnetic field [ $\varepsilon(B_z)$ ] can be estimated by solving the Schrödinger equation using a magnetic vector potential  $\mathbf{A} = -1/2(\mathbf{r} \times \mathbf{B})$ . [52]

$$\Delta\varepsilon(B_z) = \left(j + \frac{1}{2}\right) \frac{\hbar e B_z}{\mu^*} \pm \frac{1}{2} g^* \mu_B B_z - \frac{e^2}{4\pi\epsilon_0\epsilon_r |r_b(B_z)|} \quad (2.6)$$

The first term of Eq. 2.6 represents the Landau diamagnetic energy, where  $j$  is the index of the Landau state (for ground state  $j = 0$ ), and  $\hbar$  is the reduced Plank's constant. Subsequent terms in Eq. 2.6 signify the Zeeman splitting and Coulomb energy between electron-hole pairs with  $g^*$  being the Lande-g factor. The effective mass estimated by Eq. 2.6 with the help of magneto-optical spectroscopy can also be used in deducing the curvature of bands [ $m^* = \hbar^2/(\partial^2\varepsilon/\partial k^2)$ ], the binding energy of excitons ( $\varepsilon_b =$



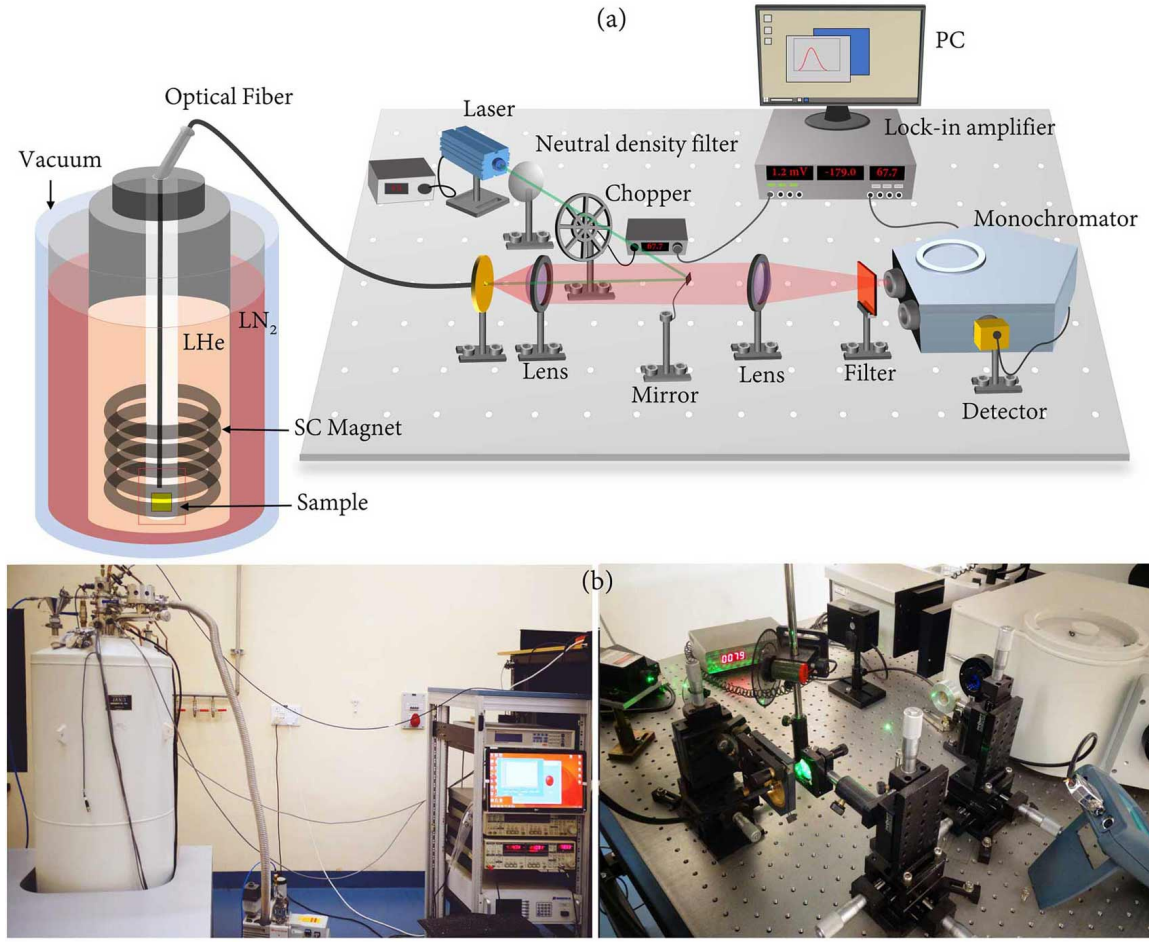


Figure 2.10: (a) Schematic and (b) photographs of the experimental setup for magneto-PL measurements.

$\mu^*e^4/32\pi^2\epsilon_0^2\epsilon_r^2\hbar^2)$  and exciton Bohr radius ( $r_b = 4\pi\epsilon_0\epsilon_r\hbar^2/\mu^*e^2$ ).[52]

The schematic and photograph of the experimental setup for magneto-PL spectroscopy are shown in Figs. 2.10a and 2.10b. The sample is kept inside liquid helium (LHe) Dewar of the thermostat (Janis SVT-2513 DMI), which is surrounded by a helically shaped niobium-titanium (NbTi) superconducting magnet. The critical magnetic field of the superconducting magnet is  $\sim 9.8$  T at 4.2 K temperature. The LHe space with the superconducting solenoid is surrounded by liquid nitrogen and vacuum chambers ( $1 \times 10^{-6}$  mbar) to provide thermal isolation from the surrounding environment. To maintain a steady-state temperature during the experiment, a needle valve that is kept between the sample-space and LHe chamber allows the transfer of LHe into the sample-space. For the spectroscopic measurements, laser light is transported by an

optical fiber with a core diameter 400  $\mu\text{m}$ , which illuminates the sample over a circular spot area  $\sim 1 \text{ mm}^2$ . The same optical fiber is used to take-out the PL signal, which is then dispersed by a spectrometer and detected by a photo-diode. Magneto-optical measurements are performed under a magnetic field up to 8 T at  $T \geq 1.8 \text{ K}$ . The experiments below 4.2 K are performed by reducing the vapor pressure on LHe, which is achieved by continuous evacuation of the sample-space by a low-power dry rotary pump.

## 2.5 Charge transport measurements

The Ohmic and rectifying nature of metal-semiconductor junction or semiconductor hetero-junctions often plays an important role in determining the transport properties of charge carriers. Specifically, when the work function of the metal is lower than the work function of semiconductor (i.e.,  $\Phi_m < \Phi_s$ ), electrons flow from metal to semiconductor to align the Fermi level. Under a steady-state condition, the band alignment for the given metal-semiconductor junction is schematically depicted in Fig. 2.11a. In this band-profile, current ( $i$ ) can easily flow across the junction, which is known as Ohmic contact,  $V = i \times R$ , where  $R$  is the resistance against current flow. On the contrary, when  $\Phi_m > \Phi_s$ , the flow of electrons from semiconductor to metal results in a Schottky-barrier ( $V_s$ ) at the interface, Fig. 2.11b. Here, the current-voltage relation in forward bias condition can be expressed by,  $i = i_0 \times \exp(-eV_S/Qk_B T)$ , which is known as a rectifying contact. The deviation of ideal rectifying characteristics of the contact is denoted by  $Q$ , known as the ideality factor, which might be contributed by the recombination of charges.[67]

### 2.5.1 Capacitance-voltage measurements

In the case of metal-semiconductor Schottky junction, charge carriers are depleted due to the bending of bands and the corresponding junction capacitance can be ex-



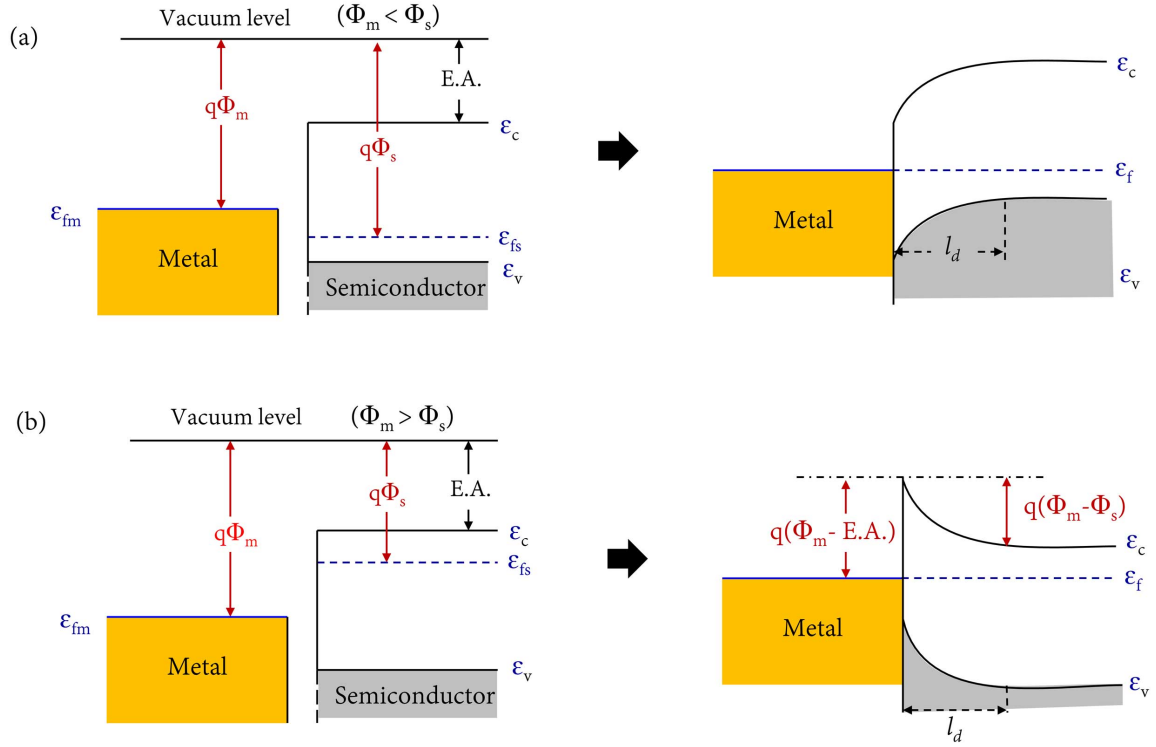


Figure 2.11: Metal-semiconductor junction in the case of (a)  $\Phi_m < \Phi_s$  and (b)  $\Phi_m > \Phi_s$  resulting Ohmic and rectifying-nature of the junction, where E.A. stands for the electron affinity of the semiconductor.

pressed by,

$$C = \frac{\epsilon_0 \epsilon_r A_e}{l_d} = \frac{de}{dV} \quad (2.7)$$

where  $A_e$  denotes the electrical area of contact. Let an applied reverse bias  $dV$  increases the depletion width by  $dl_d$ , and therefore junction capacitance can be written as,

$$C = \frac{dq}{dV} = en_w \frac{dl_w}{dV} \quad (2.8)$$

Now, using Eqs. 2.8 and 2.7, carrier density as a function of depth  $[n(w)]$  can be estimated by plotting  $1/C^2$  as a function of applied bias  $V$ .

$$n(w) = \frac{2}{e\epsilon_0\epsilon_r A_e [d(1/C^2)/dV]} \quad (2.9)$$

In order to perform the C-V measurements, an Ohmic (rectifying) contact is made at the back (front) side of the sample, Fig. 2.12a. Generally, the Ohmic contact on an n-doped (p-doped) GaAs substrate is made by Au-Ge/Ni/Au (Ti/Pt/Au) multi-layer

evaporation followed by rapid thermal annealing (RTA) at  $\sim 400$  °C. This is because, at an elevated temperature, inter-diffusion of Ge (or atoms with high diffusion coefficient) causes alloying of the semiconductor in close vicinity of the metal-semiconductor junction, which reduces any sharp-rise of interface-potential. On the contrary, deposition of Au without annealing may form a rectifying contact. Before the C-V measurements, metal-semiconductor junction characteristics and its break-down voltage in the reverse bias condition are checked by current-voltage analysis using a Keithley 236 source measuring unit (SMU). C-V measurements are then performed in a constant current region (when current is independent of applied bias) by using Keithley 590 C-V analyzer at 0.1 and 1 MHz frequencies. The frequency-dependent C-V measurement is beneficial to probe the contribution of surface states and mid-gap states on the electronic processes. In general, the response time of mid-gap states is relatively large, and hence, their contribution can be eliminated under a high-frequency C-V measurement.[68, 69] Figure 2.12b shows the temperature-dependent carrier accumulation in a 110 Å thick InGaAs/GaAs QW, which is estimated by C-V measurements at 100 kHz.[70] The results obtained in Fig. 2.12b shows that the carrier accumulation in the QW increases at low-temperature, where a decrease in carrier density at a high-temperature can be explained by the thermal escape of charge carriers from QW to barrier layers.

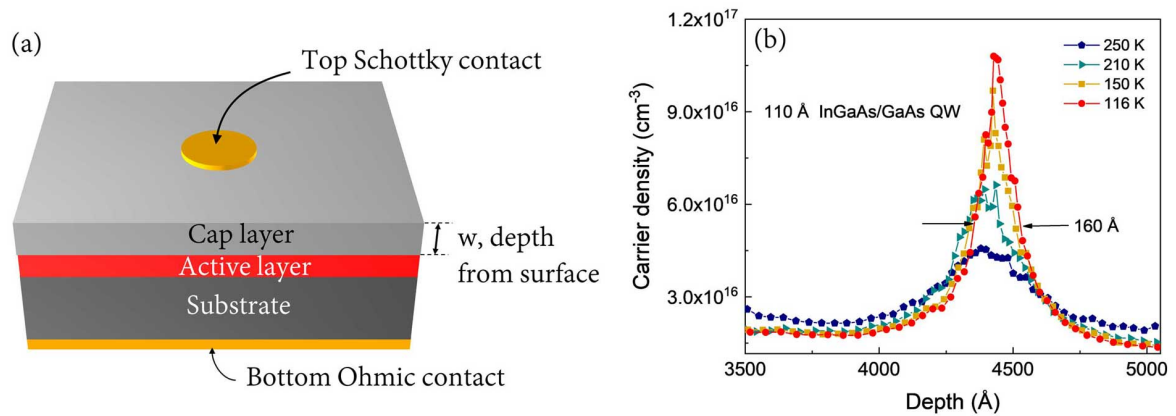


Figure 2.12: (a) Schematic diagram showing the sample prepared for C-V measurements and (b) carrier density estimated by C-V measurements on a QW.

### 2.5.2 Electro-chemical capacitance-voltage measurements

Although the conventional C-V measurement is an efficient tool to estimate carrier density as a function of depth, major limitations of this technique arise due to the break-down potential of the metal-semiconductor junction and leakage current due to the trap states at the semiconductor surface. Therefore, the hetero-junction or quantum structures deeply buried inside the sample ( $\gtrsim 100$  nm from the surface) is extremely difficult to be probed by C-V measurement. To overcome these limitations, electro-chemical capacitance-voltage (ECV) measurement can be performed.[71, 72] In this technique, an electrolyte-semiconductor junction acts as the depletion region, which is formed by the Coulomb interaction between carriers in semiconductors and ions in the electrolyte solution (Helmholtz-layer), as shown for an n-type material in Fig. 2.13a. The depth profiling of carrier density is achieved by electrochemical etching, followed by the  $dC/dV$  measurements at a fixed bias condition (Eq. 2.9). The amount of current flow ( $i_{dis}$ ) due to the dissolution of semiconductor ions in chemical solution provides a measure of etch depth, which is expressed by Faraday's law,[72]

$$W_r = \frac{M_a}{z_a F_a \rho_s A} \int i_{dis} dt \quad (2.10)$$

where  $M_a$ ,  $z_a$ ,  $F_a$  and  $\rho_s$  represent the molecular weight of the semiconductor, dissolution valency (number of carriers required to dissolve an atom), Faraday constant, and density of the semiconductor, respectively. The dissolution of ions and their separation

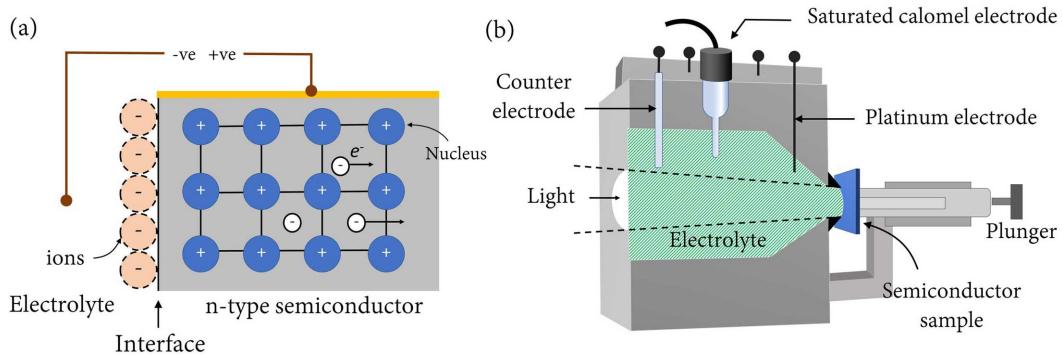


Figure 2.13: Schematic of the (a) semiconductor-electrolyte Helmholtz contact formation and (b) cross-sectional view of electrochemical-cell for ECV measurements.

in electrolyte solution depend on the presence of holes at the semiconductor-surface. In the case of a p-type semiconductor, holes are already present in the sample, which help in the above process. Therefore, etching can be performed in forward bias condition even in the absence of light. On the contrary, for an n-type sample, electrochemical etching requires a reverse bias condition with above bandgap light illumination to generate sufficient numbers of holes.

ECV measurements are performed by Accent PN4300PC ECV profiler, where a 1 M  $\text{H}_2\text{SO}_4$  is used as the electrolyte solution for etching and 1 M KOH solution as the second electrolyte. Figure 2.13b shows the cross-sectional view of an electrochemical cell, where the semiconductor is loaded by a mechanical force that experiences the electrolyte solution through a circular aperture of diameter, either 1 or 3 mm. The area of the semiconductor-electrolyte solution for ECV measurements is decided by the impedance of the sample. In order to probe the contribution of defect states and their time response in electronic processes, frequency-dependent ECV measurements can be performed in the range of 0.3 - 25 kHz.

### 2.5.3 Classical Hall effect

Classical Hall measurement is a very important tool to study the transport properties of charge carriers. In a semiconductor laboratory, four-probe Hall measurements are routinely performed to estimate carrier density, resistivity, mobility as a function of temperature, which also helps to understand scattering mechanisms in the material system. The technique relies on the measurement of the magnetic field-driven deflection of charges that are in drift motion. According to the Drude model, the equation of motion for the electrons under electric ( $\mathbf{E}$ ) and magnetic field ( $\mathbf{B}$ ) is given by,

$$m_e^* \frac{d\mathbf{v}}{dt} = -e\mathbf{E} - e\mathbf{v} \times \mathbf{B} - \frac{m_e^* \mathbf{v}}{\tau_t} \quad (2.11)$$

The first two terms of Eq. 2.11 symbolize the force exerted on the electrons by the electric  $\mathbf{E} = (E_x, 0, 0)$  and magnetic field  $\mathbf{B} = (0, 0, B_z)$ . The last term signifies the

scattering of charges, where  $\tau_t$  symbolizes the average time between two-successive collisions, which is also known as transport scattering time. In an equilibrium condition, it can be considered that  $d\mathbf{v}/dt = 0$  and current density  $\mathbf{J} = ne\mathbf{v}$ . Now, using these two relations, Eq. 2.11 can be expressed as the following matrix form,

$$0 = \begin{pmatrix} 1 & \omega_c \\ \omega_c & 1 \end{pmatrix} \mathbf{J} - \frac{ne^2\tau_t}{m_e^*} \mathbf{E} \quad (2.12)$$

where  $\omega_c = (eB/m_e^*)$  is the cyclotron frequency under the magnetic field. Equation 2.12, can be written in the form of  $\mathbf{E} = [\rho]\mathbf{J}$ , where  $[\rho]$  is the resistivity tensor which is the inverse of conductivity  $[\sigma] = [\rho]^{-1}$ .

$$[\rho] = \frac{m_e^*}{ne^2\tau_t} \begin{pmatrix} 1 & eB/m_e^* \\ eB/m_e^* & 1 \end{pmatrix} \quad (2.13)$$

Equation 2.13 readily shows that the resistivity in the direction of the current is independent of  $B$  and inversely related to the scattering time ( $\rho_{xx} = m_e^*/ne^2\tau_t$ ), whereas perpendicular resistivity is independent of scattering processes ( $\rho_{xy} = B/ne$ ). The rate of increase in  $\rho_{x,y}$  as a function of  $B$  is known as the Hall coefficient ( $R_H = 1/ne$ ), which contains the information of carrier density in the solid.

In general, classical Hall measurements are performed by a four-probe technique

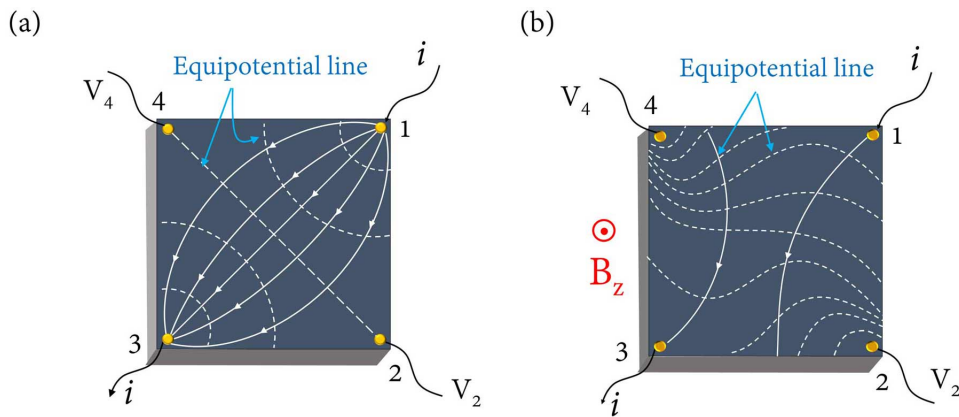


Figure 2.14: Experimental configuration to measure the classical Hall effect in the van der Pauw method. The flow of charge current and equipotential lines (a) in the absence and (b) under  $B_z$  are shown.

in the van-der Pauw method. The Ohmic contacts are made at the corners of a square-shaped sample by using indium balls. Current is passed through the diagonal contacts (1 and 3), and voltage is measured across the other two probes by Keithley 236 SMUs, Fig. 2.14a. Contacts 2 and 4 being situated on the same equipotential line, the voltage measured across the two probes is ideally becomes zero. However, the deflection of carriers by  $B_z$  distorts the equipotential lines (Fig. 2.14b), and a potential difference ( $V_H$ ) is generated at the voltage probes. In ven der Pauw geometry, contacts should be very small and situated at the boundary of the sample, where the sample thickness is much lower than the lateral dimension. Moreover, transportation of carriers in a thin or non-inform sample requires a correction factor  $[f(R_{12,34}/R_{23,41})]$ . Rather than the spherical distribution of charges, here a cylindrical symmetry is considered and a conformal mapping procedure is employed to express resistivity and mobility of thin samples by the following relations,[73]

$$\rho_{xx} = \frac{\pi d}{\ln 2} \left[ \frac{R_{12,34}(0) + R_{23,41}(0)}{2} \right] f \left( \frac{R_{12,34}(0)}{R_{23,41}(0)} \right) \quad (2.14)$$

$$\mu = \frac{d}{B} \left[ \frac{R_{24,13}(0) - R_{24,13}(B)}{\rho} \right] \quad (2.15)$$

where  $R_{12,34}(B)$  is the measured resistance when current is passed through 1-2 terminal, and voltage is measured across 3-4 terminal under a magnetic field.

#### 2.5.4 Quantum Hall effect

The quantum mechanical effect in Hall measurement arises when charge carriers with drift velocity are strongly confined by a magnetic field. With increasing the magnetic field, Landau states shift towards high energy  $[\Delta\varepsilon_j \approx (j + 1/2)\hbar eB/m^*]$  and sequentially swept across  $\varepsilon_f$ . Once a Landau state crosses the Fermi level, the charge carriers occupied in that state either relax to lower energy states or recombine radiatively/non-radiatively. Under this condition, the electrical resistance in the direction of the current (longitudinal magneto-resistance,  $R_{xx}$ ) exhibits an oscillatory variation. This is because, a partially filled Landau state is mainly responsible for the

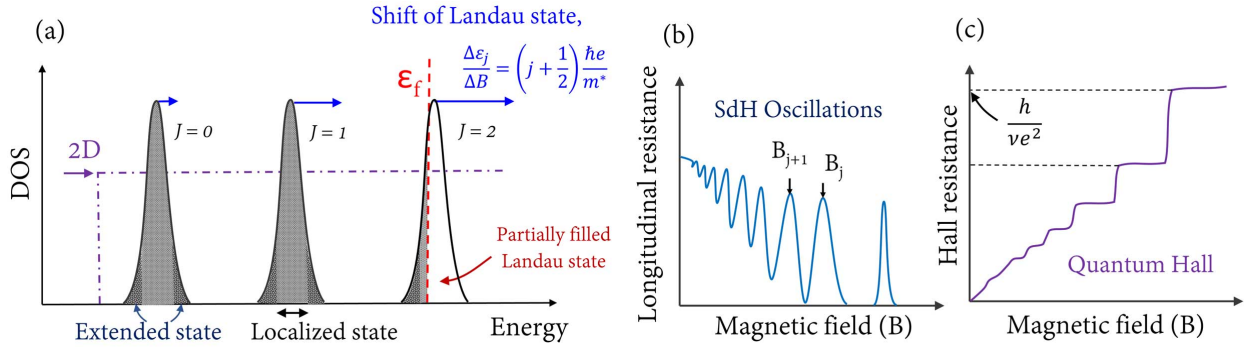


Figure 2.15: (a) Magnetic field-driven discretization of energy state in the form of Landau states and sweeping of Landau states across  $\varepsilon_f$ . Under this condition, resistance in the direction of current oscillates with increasing the magnetic field (b), and resistance perpendicular to the current flow exhibits a quantized variation (c).

transportation of charges, i.e., when  $\varepsilon_f$  is located on the localized states of a Landau-level, resistivity shows a minimum (Fig. 2.15a). The magnetic field-driven oscillatory variation of  $R_{xx}$  is known as Shubnikov-de Haas (SdH) oscillation (Fig. 2.15b). Using the Boltzmann transport equation, the longitudinal conductivity of charge carrier can be expressed by,

$$\sigma_{xx} = \frac{e^2}{m_e^*} n \tau_t = \frac{2e^2}{m_e^* h^2} \int \frac{\varepsilon}{\Gamma} \left( -\frac{dF_e}{d\varepsilon} \right) d^2 p \quad (2.16)$$

where  $\Gamma$  denotes the broadening of Landau states. Using the above relation and Dingle factor of charge transport, the oscillatory variation in resistivity can be expressed by,[74, 75, 76]

$$\rho_{xx} = \left( \frac{\sigma_{xx}}{\sigma_{xx}^2 + \sigma_{xy}^2} \right) \sim \frac{1}{\sqrt{B}} \frac{\exp(\pi m_e^*/eB\tau_q) \times \cos(2\pi\varepsilon_f m_e^*/\hbar eB)}{\sinh(2\pi^2 m_e^* k_B T/\hbar eB)} \quad (2.17)$$

Here,  $\tau_q$  signifies the quantum scattering time: average time an electron spends in a definite momentum eigenstate, which is different from the transport scattering time  $\tau_t$  ( $= \mu m_e^*/e$ ). At the same time, Hall resistivity (perpendicular to current,  $\rho_{xy}$ ) exhibits a quantized variation with an accuracy up to few parts in 10 million (Fig. 2.15c).[77]

$$\rho_{xy} = \frac{h}{\nu e^2} \quad (2.18)$$

It is noteworthy to mention that charge carriers in a bulk-medium perform closed orbit motion under a high magnetic field, which hardly contributes to current flow. However, the carriers near the boundary of the sample cannot complete their orbit and perform a chiral motion across the edges, which is known as the edge state motion.

The energy eigenvalue of Landau states in the quantum Hall regime can be estimated by solving the Schrödinger equation with  $\mathbf{B}$  and  $\mathbf{E}$  oriented along  $z$  and  $x$ -directions, respectively. The magnetic vector potential of the above system can be expressed by Landau gauge,  $\mathbf{A} = (0, xB_z, 0)$  and the corresponding energy eigenvalue can be estimated by neglecting the carrier-carrier interaction,[52]

$$\Delta\varepsilon(B_z, E_x) = \left(j + \frac{1}{2}\right) \frac{\hbar e B_z}{m_e^*} - e E_x k_y \xi - \frac{m_e^* E_x^2}{2 B_z^2} \quad (2.19)$$

where  $\xi = \sqrt{\hbar/eB}$  represents the magnetic length of charge carriers. In the case of a current-carrying device, the contribution of  $\mathbf{E}$  in Eq. 2.19 becomes feeble as compared to the first term. Therefore, the magnetic field that would be required to sweep the  $j^{\text{th}}$  Landau state across the Fermi level becomes  $B_j = 2\varepsilon_f m_e^* / \hbar e (2j + 1)$ . Now, the carrier density  $n_{2D}$  can be expressed by the product of DOS and  $\varepsilon_f$ ,  $n_{2D} = 2m^* / \pi \hbar^2 \times \varepsilon_f$ . Here, this parabolic band approximation remains valid for wide-QWs with  $k \approx 0$ . Now, using the above two relations, the magnetic field corresponding to the successive maxima in SdH oscillations can be used to estimate  $n_{2D}$  by the following relationship:

$$n_{2D} = \frac{2e}{h} \left[ \frac{1}{1/B_{j+1} - 1/B_j} \right] \quad (2.20)$$

Also, the transverse conductivity in high field regime can be expressed by,[78]

$$\sigma_{xy} = -\frac{e}{hV_H} \int \frac{dp}{2\pi} v_y(k) = \frac{e}{2\pi\xi^2} \int dx \frac{1}{eB} \frac{\partial V}{\partial x} = \frac{\nu e^2}{h} \quad (2.21)$$

where  $\nu$  is the filling ratio of Landau states that is signifying the fraction of a Landau state which is occupied by charge carriers,  $\nu = (2j + 1) = n_{2D} \hbar / 2eB$ , where  $2eB/\hbar$  is the degeneracy of a Landau state.

In order to measure  $R_{xx}$  and  $R_{xy}$ , Hall bar devices (with length  $L$  and width



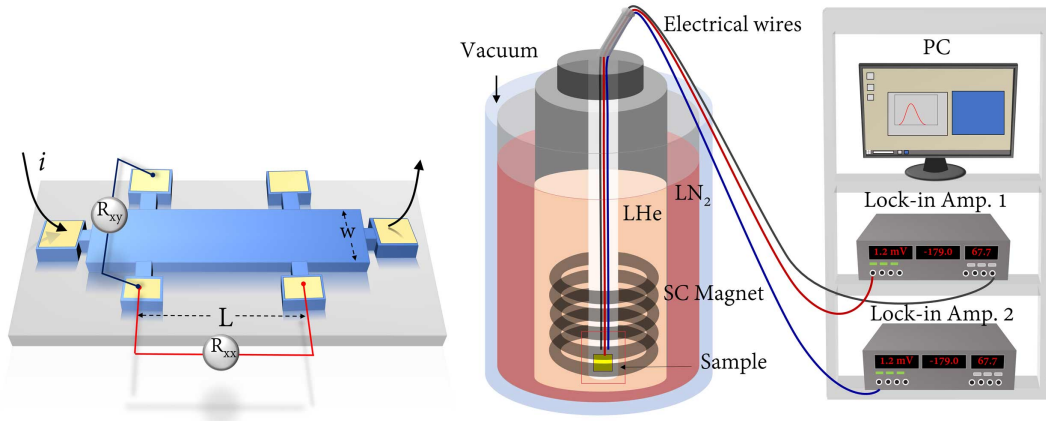


Figure 2.16: (a) Hall-bar sample for longitudinal and transverse magneto-resistance measurements and (b) schematic of the quantum Hall experimental setup.

w) are fabricated by photolithography technique followed by a selective area chemical etching to define the charge transport region (Fig. 2.16a). Ohmic contacts on the Hall bar sample are made by Au-Ge/Ni/Au multi-layers, followed by the RTA at 400 °C for 20 sec. Magneto-resistance measurements are performed inside LHe Dewar of the thermostat ( $T \geq 1.8$  K) under the magnetic field up to 8 T (Fig. 2.16b). Two lock-in amplifiers are used to measure longitudinal and Hall resistances. The quantum Hall measurements are also performed by a single channel source measuring unit under DC bias.

## 2.6 Photolithography techniques

### 2.6.1 Mask-based optical projection photolithography

The technique to transfer the desired pattern from one medium to another with the help of photons is called photolithography. In this technique, ultra-violet (UV) light is transmitted through a photo-mask to achieve a spatially patterned light beam, which is then projected on a photo-sensitive material (photoresist). The photo-mask contains the desired patterns of opaque and transparent portions on a fused silica glass plate. The photoresist is a light-sensitive organic compound or polymer. The high energy photons (wavelength  $\leq 500$  nm) break atomic bonds or re-arrange the polymer-chains to alter the stability of the photoresist. Depending on the stability after exposure, photoresists

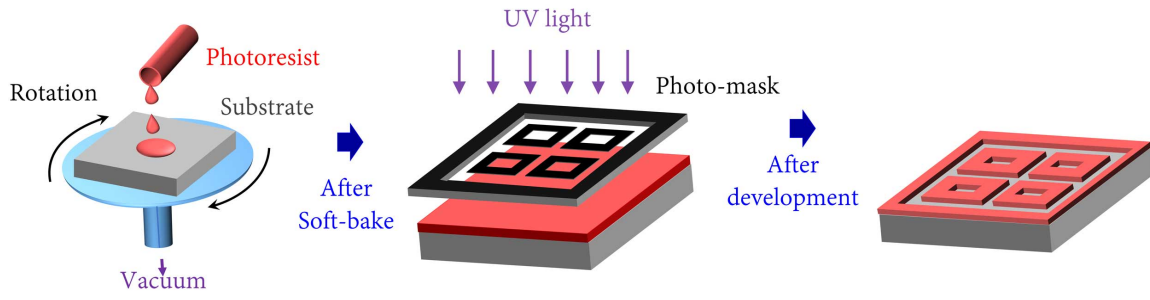


Figure 2.17: Flow diagram showing the main steps involved in the photolithography technique.

can be sub-divided into (i) positive photoresist - illuminated portions become soft and dissolve in a developer solution (used in this thesis work) and (ii) negative photoresist - unexposed regions are removed-out in a developer solution. Notably, the proper development of photoresist patterns depends on the intensity of light, time of exposure, and distance between the photo-mask and sample surface.

Figure 2.17 shows the steps involved in the photolithography technique. In the first step, a uniform thickness of photoresist (Shipley S1813) is deposited on a substrate using a spin coater method. Here, the substrate with photoresist is rotated with 3500 RPM (30 sec) to spill-out the excess photoresist by centrifugal force. Thereafter, the photoresist is soft-baked at 95 °C for 1 min to reduce the water and liquid contents. Then the photoresist is exposed to UV light through the transparent portions of the photo-mask, followed by the development in the MFCD-26 solution for 1 min. The sample is hard-baked at 120 °C for 1 min to harden the photoresist patterns.

**Safety aspects:** Photoresists are unsafe for human skin; consumption of photoresist vapor during breathing can be poisonous for the human body. Also, direct exposure to UV light is dangerous for eyes, which can cause permanent blindness.

### 2.6.2 Concepts of maskless-photolithography technique

Although mask-based photolithography is most suitable for industrial applications, cost, and time delay associated with designing and fabricating a photo-mask are some of the major limitations. Moreover, there is no scope of modification once a photo-

mask is fabricated. These limitations of a mask-based system render the concepts of maskless-photolithography technique, which is now a primary need for small-scale industry, research, and development activities. Electron-beam lithography, x-ray lithography, focused ion-beam lithography, scanning probe lithography, zone plate array lithography, interference lithography, are some of the alternative techniques developed in this category.[79, 80, 81, 82, 83] Although many of these techniques are useful in nano-meter scale patterning, fabrication of a complex or arbitrary pattern requires a raster scan by a digitally controlled x-y stage, which enhances the complexity and reduces the speed of patterning. Therefore, a simple way to avoid photo-mask can be the projection of patterned light directly on the substrate. This can be achieved by reflecting or transmitting a collimated light from a spatial light modulator (e.g., digital micromirror device, thin-film-transistor screen). Musgraves *et al.*[84, 85] developed a maskless-photolithography system using a digital-projector and an optical microscope. Here, a diverging light from a projector is focused by an optical microscope, where the exposure pattern was controlled by a computer. Using this simple system, a minimum feature size of  $\sim 15 \mu\text{m}$  over a sub-millimeter<sup>2</sup> substrate area was achieved. However, non-uniform photoresist development and feature size-dependent exposure time are some of the critical issues which need to be addressed in their setup. Lambert *et al.*[86] also developed a similar system. Using a biological microscope, a minimum feature size of  $\sim 1 \mu\text{m}$  was achieved with improved photoresist sidewalls over a very small exposure area. The inbuilt lens of the projector was reversed in this setup to achieve a converging light from the projector, and a mechanical shutter was employed to control the exposure time.

### 2.6.3 A simple and inexpensive maskless-photolithography system

In order to pattern various structures related to this thesis work, a maskless-photolithography system is developed by a digital-projector and a stereo-zoom optical-microscope using a similar concept of Musgraves *et al.*[84, 85] In this setup, highly divergent light from the projector is focused on a substrate by a 10X eyepiece and an

objective lens of a microscope. The projector is equipped with  $1920 \times 1080$ -pixel resolution, 1:13000 contrast ratio, 3500 ANSI Lumens brightness. The emission of light from the projector is configured to its highest available  $f$ -value (available 2.59 - 2.91) to obtain a relatively less divergent light. A 10X eyepiece is placed close to the projector ( $\leq 1$  cm), which collimates the light over an aperture area  $\sim 1.5 \times 1.5$  cm<sup>2</sup>. The collimated light is then coupled into the trinocular head of a stereo-zoom microscope (Figs. 2.18a and 2.18b). In order to minimize aberrations of light, eyepiece and microscope are aligned as per the axis of the light, which is coming out from the projector. The microscope is used for the following reasons- (i) objective lens helps to control exposure area on the substrate (0.6 - 5X de-magnification), and (ii) eyepiece in the binocular-

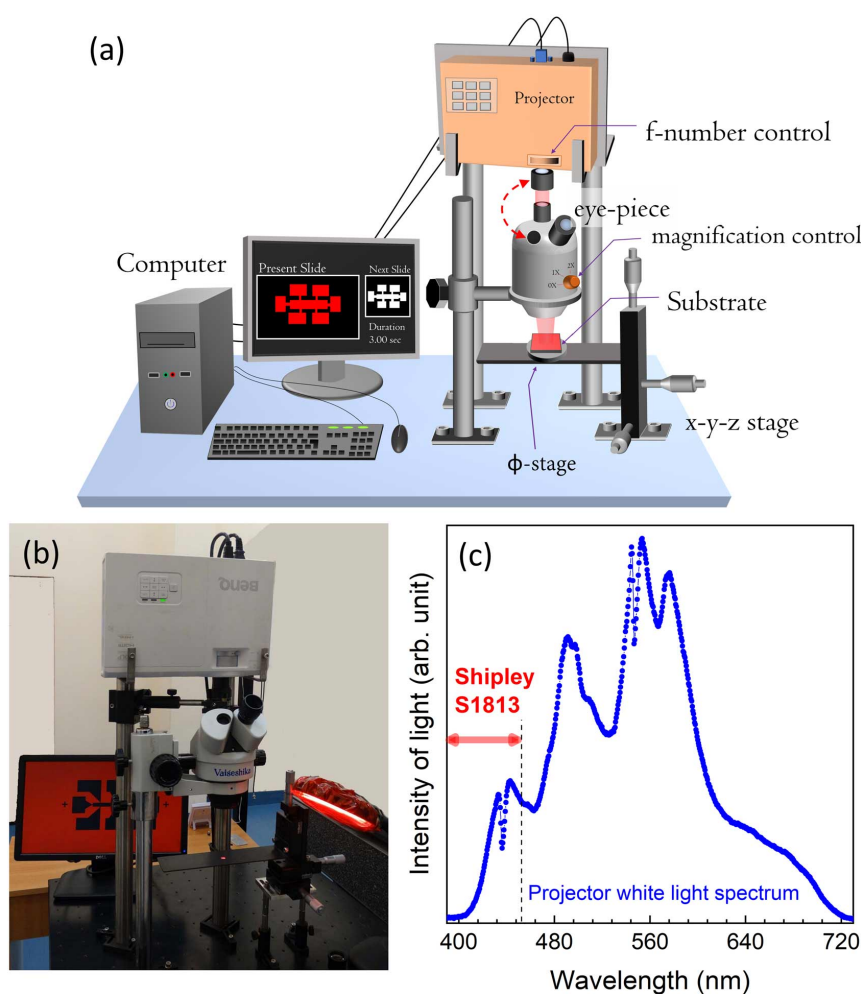


Figure 2.18: (a) Schematic and (b) photograph of a simple maskless-photolithography system based on a projector and an optical microscope. (c) The emission spectrum of the projector corresponding to the white light is also shown.

head helps to check pattern placement and focusing of incident light on the substrate (Figs. 2.18a and 2.18b). In this setup, the projector is used to achieve spatial patterning of the light, where the desired image-patterns are drawn in PowerPoint software. The computer software directly controls the intensity and duration of exposure. Note that the hardware configuration of the projector and optical microscope is not affected, and external lenses and mechanical shutters are also not required in the present setup. The wavelength of exposure is indirectly controlled by choosing a suitable color in the PowerPoint image.

A higher de-magnification in the microscope objective can be useful to expose smaller features. However, with increasing the de-magnification, the area of exposure significantly decreases, which is therefore feasible for small samples. In this experimental setup, the minimum feature size is mainly constrained by the pixel-density of the digital projector, which can be expressed by the following relation,

$$W_p = \sqrt{\frac{\text{Exposure area on the substrate}}{\text{Total number of pixels}}} \quad (2.22)$$

Therefore, an optimum de-magnification of 2X by the objective lens is used from where the area of exposure becomes  $10 \times 6 \text{ mm}^2$ , with the theoretical limit of minimum feature  $W_p \approx 5 \text{ }\mu\text{m}$ . However, in order to achieve well-defined photoresist patterns, a few pixels of incident light are found to be essential, which enhances the minimum feature size to  $\sim 20 \text{ }\mu\text{m}$ . On the other hand, the minimum feature size due to the diffraction of light can be estimated by,

$$W_d = k \times \frac{\lambda}{N.A.} \quad (2.23)$$

Here,  $\lambda$  is the wavelength of exposure ( $\sim 430 \text{ nm}$ ), N.A. stands for the numerical aperture of the system ( $\sim 0.2$ ), and  $k$  is an instrumental parameter related to the microscope and projector ( $\sim 1.5$ ). With these values, the minimum feature size due to diffraction is estimated to be  $W_d \approx 3.2 \text{ }\mu\text{m}$ . Note that the numerical aperture related to the optical components inside the projector may also influence the estimated value of  $W_d$ , which is not considered in the above calculation. This is because the dismantling

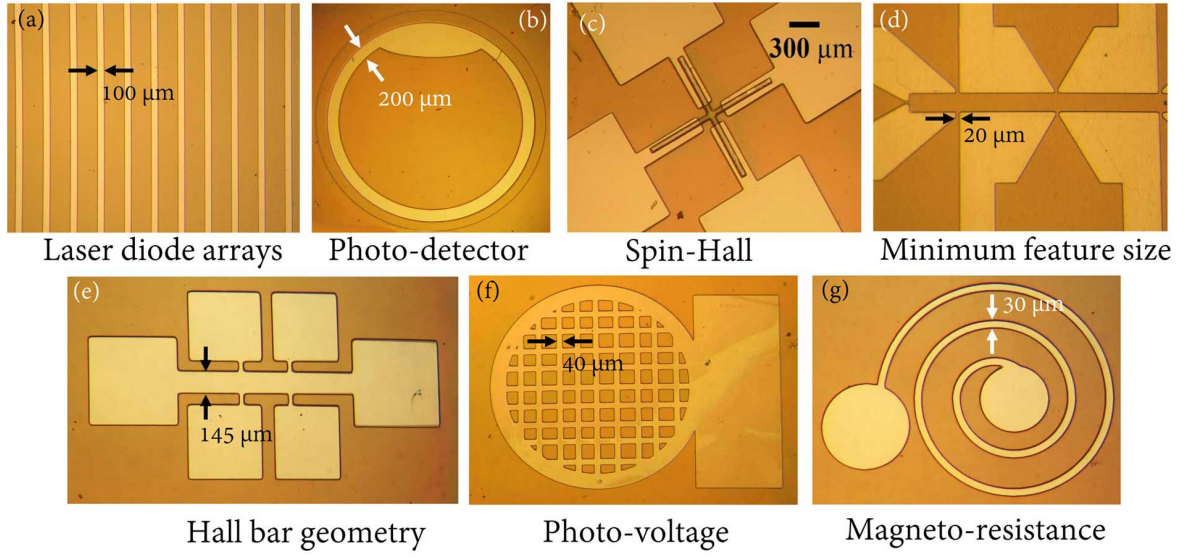


Figure 2.19: Photographic images of various patterns developed by the maskless-photolithography system.

of the projector for optical measurements may cause serious damage to the system.

The photoresist (Shipley-S1813) coated substrate is kept on an  $x$ - $y$ - $z$ - $\phi$  controlled stage (Fig. 2.18a), where  $x$ - $y$  motion and  $\phi$  rotation of the stage are used to ensure the pattern placement, and  $z$ -motion confirms the focusing of incident light on the substrate (Figs. 2.18a and 2.18b). Initial alignments are performed by a red patterned light (does not expose the photoresist), which contains an identical pattern that is to be exposed. After that, the same image but with white light is used to expose photoresist (6 sec). The intensity of projector light is controlled by introducing a semi-transparent over-layer (72 % in our case) in the PowerPoint image. The white light spectrum of the projector is shown in Fig. 2.18c, where the photons with  $\lambda < 450$  nm bleaches the photoresist. The photographic images of various structures (e.g., lasers, detector, Hall bar, etc.), which are patterned by the above system are shown in Fig. 2.19. It is found that the typical exposure time for the fabrication of various structures, having the dimension  $20 \mu\text{m} \leq W \leq 10000 \mu\text{m}$ , is invariant. This is a necessary condition for the fabrication of complex patterns that contain both small and relatively large features.

## 2.7 Semiconductor device development

### 2.7.1 Laser diode arrays

The basic operation of a diode-laser depends on the recombination of electron-hole pairs in p-i-n junction, where photon confinement is achieved by total internal reflection or Bragg-mirror. In general, a semiconductor diode-laser consists of an active medium that can be a QW or QDs (decides the emission wavelength), a cladding region having a lower-refractive index with respect to the active medium (provides photon confinement by total internal reflection) and a waveguide medium (decides the optical mode of the laser). [69, 87] The different segments of the semiconductor diode lasers are schematically illustrated in Fig. 2.20. The intensity of photon-flux decreases with the propagation of the wave in the waveguide, which can be expressed by  $I(w) = I_0 \times \exp(-\alpha^*w)$ , where  $\alpha^*$  is the absorption coefficient and  $w$  distance of wave propagation. In order to achieve the lasing, the gain of the optical medium should be equal to the absorption losses, i.e.,  $g = -\alpha^*$ . In the semiconductor lasers, only a small part of the optical-modes overlaps with the active region, which is located at the center of the waveguide. The gain factor associated with the active medium of the laser is known as modal gain ( $g_{modal}$ ), [69]

$$g_{modal} = g \times \frac{\int_{-l_w/2}^{l_w/2} I(w)dw}{\int_{-\infty}^{\infty} I(w)dw} \quad (2.24)$$

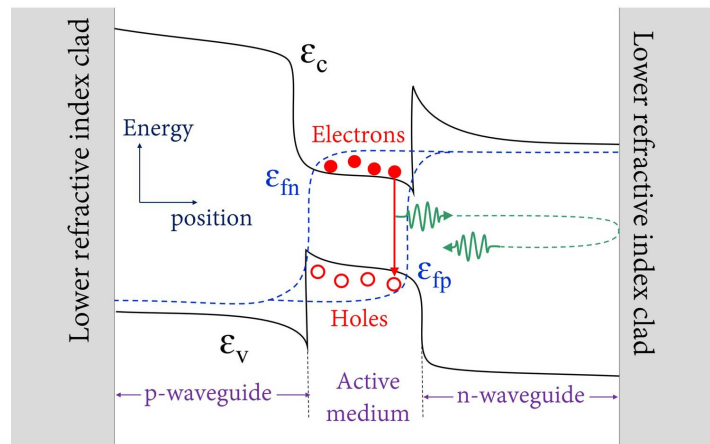


Figure 2.20: Schematic of a QW-based p-i-n laser diode.



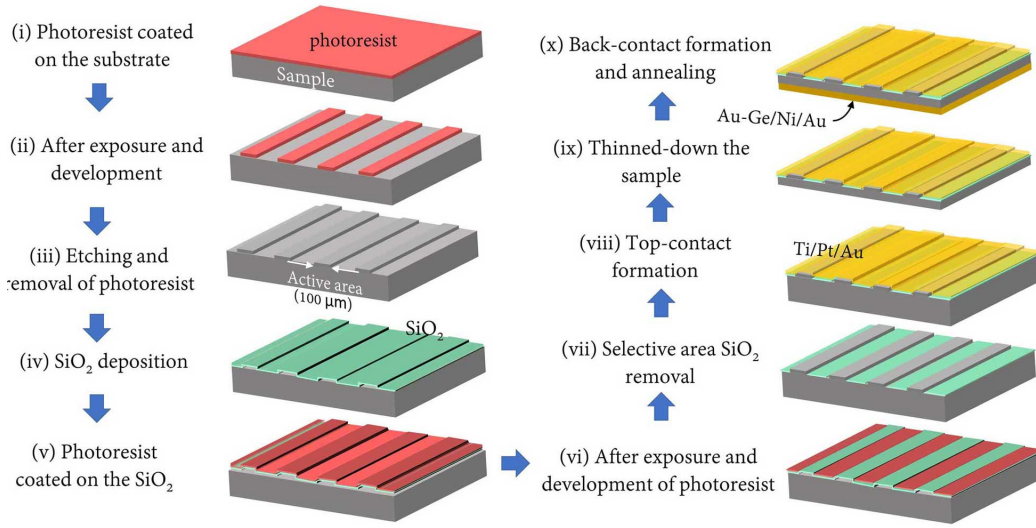


Figure 2.21: Schematic flow diagram showing the steps for the development of semiconductor laser diode arrays.

Figure 2.21 shows the steps involved in the processing of diode lasers. In the first step, the maskless photolithography system is used to pattern the sample with 100 μm thick parallel lines, which are separated by 500 μm thick regions. The unwanted areas that are surrounded by the active elements are chemically etched up to the depth of ~1.8 μm by CH<sub>3</sub>OH : H<sub>3</sub>PO<sub>4</sub> : H<sub>2</sub>O<sub>2</sub> solution, followed by a SiO<sub>2</sub> coating to passivate the surface states of the etched sidewalls. To take the top contact, the deposited SiO<sub>2</sub> is selectively removed on the active elements of the laser diode by buffer hydrofluoric acid solution (6:1) using a photolithography technique. Top contacts from the diodes are made by Ti/Pt/Au multilayer deposition. The thickness of the sample is then reduced to ~100 μm by back-side lapping and polishing method, and back-contact is made by Au-Ge/Ni/Au multi-layers. Finally, the sample is annealed at 400 °C for 20 sec to make Ohmic contacts.

### 2.7.2 Photo-detectors

Detection of photons by semiconductor materials works on the collection of photo-generated electron-hole pairs. The illumination of photons with energy more than the bandgap excites electrons in the conduction band, where the photo-generated electron-hole drift in crystal either due to an intrinsic or external electric field. The separation



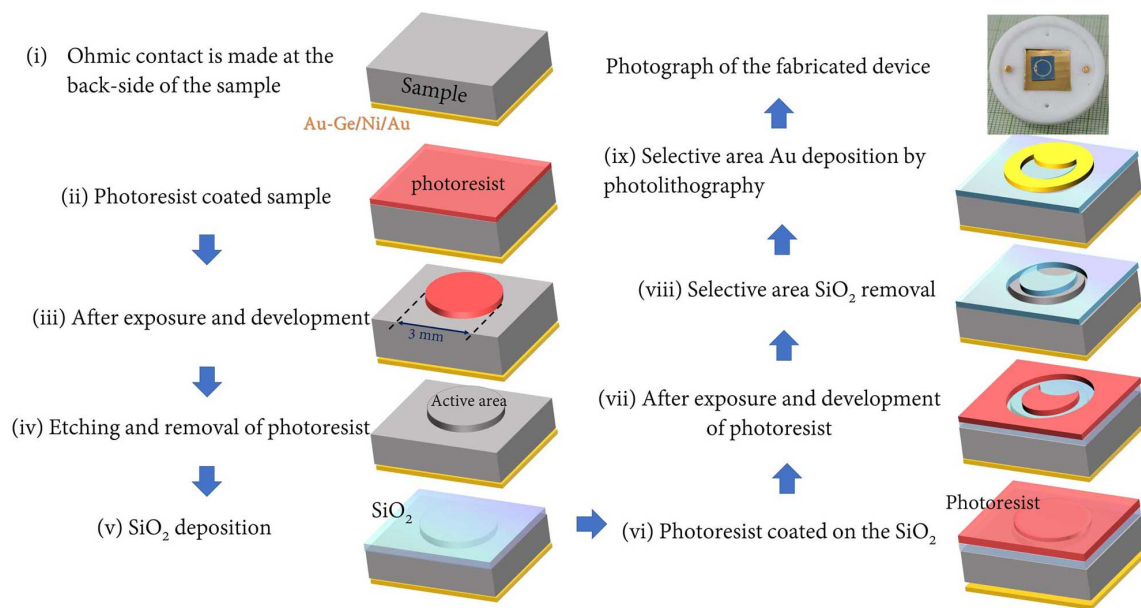


Figure 2.22: Schematic diagram showing the steps involved to develop photo-detectors.

of electron-hole by this process gives rise to current flow across the semiconductor in closed-circuit condition or alters the surface potential in the open-circuit configuration. The amount of current flow or the change in surface potential due to the light illumination depends on the intensity of photon flux, absorption coefficient, and internal quantum efficiency of the material system. The steps involved in the development of a photo-detector are shown in Fig. 2.22. In the first step, Au-Ge/Ni/Au multilayers are deposited at the back-side of the sample followed by an RTA at 400 °C for 20 sec. After that, the active area of the detector (3 mm diameter) is defined by the photolithography technique followed by a chemical etching up to the depth of active layers. In order to passivate the surface states and to reduce reflection of photons from the detector surface, a uniform thickness of SiO<sub>2</sub> (~ 120 nm) is deposited on the sample. Now, to take-out the top-contact from the detector, a selective area oxide removal is performed. After that, a ring-shaped Schottky contact is made on the top of the detector by Au evaporation and a lift-off method.

# Chapter 3

## Effect of quantum confinement on optical properties and effective mass of excitons

### 3.1 Introduction and background

The optoelectronic properties of semiconductors can be enriched by confining charge carriers in a low-dimensional system. However, with an increase in carrier confinement, a significant amount of wave function penetrates into barrier layers. As a result of this, electron and hole become localized by the atomic irregularities at the hetero-interfaces, and basic property of the material system gets modified because of quantum effects and wave function penetration. Such effects of quantum confinement are often investigated by non-invasive techniques such as PL and SPV spectroscopy.[88, 89, 90, 91] An extensive amount of research has been performed to derive a quantitative relationship between the linewidth of an emission/absorption spectrum and the inhomogeneity in semiconductors. For example, Aksenov and Oliveira *et al.* proposed a relation to express PL linewidth as a function of lateral-inhomogeneities at the hetero-junctions,[92, 93] by assuming the vertical-fluctuation of QW thickness was one monolayer of GaAs. The theory of PL line-shape to determine the interface quality of QWs was also formulated by Singh *et al.*[94, 95] With the continuous evolution of growth techniques and the advancement of device technology, it is now essential to develop a comprehen-

sive understanding on electro-optical processes that define the spectral line-shape of ultra-low disordered systems. A systematic study needs to be performed on various thicknesses of QW that are grown under identical conditions, for example, a multiple-QWs (MQWs) structure with different thicknesses of QW.[91] The effective mass ( $m^*$ ) of charge carrier is another important parameter, which can be probed to investigate interactions between charge carriers, band-curvature, and non-linear property of quantum structures.[28, 29, 96, 97] However, the estimation of  $m^*$  for an active layer in an MQW structure is difficult by electrical transport measurements due to the problem of the parallel layer conduction process. The estimation of  $m^*$  by cyclotron-resonance measurements is also not feasible when the resonance frequencies related to different QWs are closely separated, and their absorption features are merged.[98, 99] Because of this, magneto-optical spectroscopy is an attractive technique, where the values of  $m^*$  related to each QWs in an MQW structure can be easily estimated.

In this chapter, the optical properties of excitons and carrier redistribution processes in GaAs/AlGaAs QWs are investigated by temperature, excitation-power, and chopping frequency-dependent PL and SPV measurements. The impact of carrier localization on the line-shape of PL and SPV spectra of QWs are investigated. Magneto-optical measurements are performed to probe the effects of quantum confinement on the effective mass and binding energy of excitons. Also, the impact of wave function penetration into barrier layers and the role of non-parabolic bands on the effective mass of excitons are explained for various thicknesses of QW.

## 3.2 Sample details and experimental procedure

GaAs/Al<sub>0.28</sub>Ga<sub>0.72</sub>As MQW samples are grown on a (001) oriented n<sup>+</sup> GaAs substrate by the MOVPE technique. The samples are grown at 730 °C temperature and 50 mbar pressure. The MQW structure consists of four QWs, 190 (QW-1), 100 (QW-2), 50 (QW-3) and 30 Å thickness (QW-4), which are sandwiched between ~980 Å thick Al<sub>x</sub>Ga<sub>1-x</sub>As layers. This higher thickness of the barrier layer restricts the coupling of

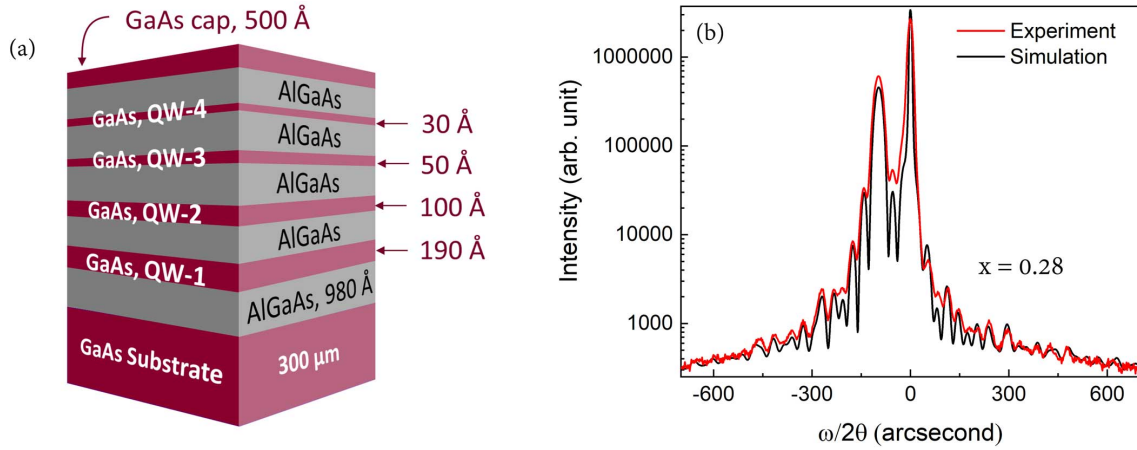


Figure 3.1: (a) Schematic diagram of a GaAs/AlGaAs MQW sample and (b) simulated result of HRXRD data to estimate the structural details of the sample.

wave function between the neighboring QWs (Fig. 3.1a). The structural parameters (e.g., composition and layer thickness) are estimated by matching the HRXRD pattern with the simulated results of X'Pert epitaxy software (Fig. 3.1b). Layer thicknesses are also confirmed by cross-sectional TEM measurements and by matching PL peak energy with the numerical solution of the Schrödinger equation. Temperature-dependent PL and SPV measurements are performed in a closed-cycle cryostat with optical window access. On the other hand, magneto-PL experiments are performed in an LHe cooled Dewar, with a magnetic field perpendicular to the sample surface. Magneto-optical measurements are performed by an optical fiber-based setup, which is described in Section 2.4.3. For the temperature and magnetic field dependent PL measurements, a 532 nm green laser is used to excite charge carriers, and the chopping frequency is kept as 67 Hz (unless otherwise specified). SPV measurements are performed in MIS geometry, where the carriers are excited by monochromatizing the broad spectrum of a QTH lamp. The spectrometer used for these measurements is equipped with 1200 lines/mm grating having the spectral resolution of  $\gtrsim 0.01$  nm. A 560 nm long-pass filter is used to block the reflected laser light during PL measurements or to restrict the higher harmonics in monochromatic light (originated from grating) during the SPV measurements. Spectra are recorded by a silicon photo-diode with the help of a lock-in amplifier. Details of the experimental setup for PL, SPV, and magneto-PL measurements can be found in

Sections 2.4.1, 2.4.2, and 2.4.3.

### 3.3 Photoluminescence spectroscopy

In the beginning, temperature-dependent PL measurements are performed on the GaAs MQW sample to study the optical properties of excitons in a low-dimensional system, Fig. 3.2a. It is observed that the PL intensity related to the excitonic transition decreases with a rise in temperature, which becomes negligible for  $T \gtrsim 180$  K. This temperature-dependent reduction in PL can be explained by the thermal dissociation of excitons followed by the escape of charge carriers from the QWs. Additionally, due to an enhancement of electron-phonon interaction, radiative recombination time of excitons increases at high temperature [ $\tau_r(T) \sim T \times \tau_r(0)$ ].[61, 100] On the other hand, with an increase in temperature, PL peaks shift towards the low-energy (Figs. 3.2a and 3.2b), which can be described by a semi-empirical Varshini's relation,  $\varepsilon_g^*(T) = \varepsilon_g^*(0) - \alpha T^2/(\beta + T)$ . [101, 102] Here,  $\alpha$  and  $\beta$  signify the entropy of charge carrier and the Debye temperature of the system, respectively. Symbol  $\varepsilon_g^*(T)$  represents the sum of fundamental band-gap [ $\varepsilon_g(T)$ ] and confinement energy of electron-hole in the QW ( $\varepsilon_0 = \varepsilon_e + \varepsilon_{hh}$ ), i.e.,  $\varepsilon_g^*(T) = \varepsilon_g(T) + \varepsilon_0$ . The experimentally estimated  $\varepsilon_g^*(T)$  is fitted by the Varshini relation with  $\alpha = 370$  K [21, 103] and  $\beta \approx 7 \times 10^{-4}$  eV-K $^{-1}$  (Fig. 3.2b). Careful observation shows that the fitted curve of Varshini's relation

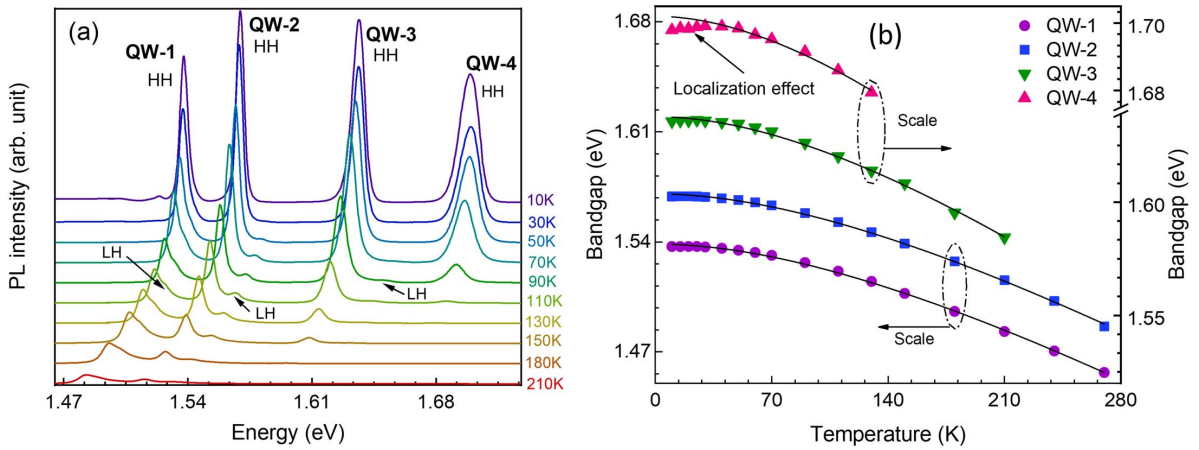


Figure 3.2: (a) Temperature-dependent PL spectra of the GaAs/AlGaAs MQW sample and (b) shift in PL peak energy as a function of temperature.

slightly deviates for QW-4 at  $T < 50$  K. Such an observation indicates that the excitons confined in a narrow QW are significantly affected by the atomic-irregularities at the hetero-junction. This anomalous variation of  $\varepsilon_g^*(T)$  in low-temperature regime can be explained by introducing a correction factor in Varshini's relation to consider carrier localization effects.[104, 105, 106]

At a fairly low-temperature, spectral line-shapes are asymmetrically broadened, where the linewidth of the PL peak increases with decreasing QW thickness (Fig. 3.3). In general, the broadening of PL peak is understood by the following factors– (1) thermal energy of charge carriers ( $\Gamma_{homogeneous}$ ), (2) impact of defect/disorders ( $\Gamma_{defect}$ ), (3) compositional variation in barrier layer ( $\Gamma_{pot.fluct.}$ ), (4) thickness fluctuation of QW ( $\Gamma_{thickness}$ ), and (5) penetration of wave function into barrier layers ( $\Gamma_{penetration}$ ), which are schematically illustrated in Fig. 3.4a. Particularly, the atomic irregularities at the hetero-junctions causes fluctuations in QW thickness ( $l_w \pm \delta_1$ ), which may cause a variation in quantum confinement energy  $\pm \Delta \varepsilon_0$ . Note that the large islands or terrace-shaped interface-roughness, which was previously reported at GaAs/AlGaAs interfaces,[107, 91] could not be observed in the cross-sectional TEM images of our MQW sample. A representative TEM image of a GaAs/AlGaAs MQWs, which is grown under identical growth conditions, is shown in Fig. 3.4b. It is observed that the fluctuation in QW thickness remains within  $1\text{-}2 \times$  mono-layer width of GaAs ( $1 \text{ ML} = 2.83 \text{ \AA}$ ). Therefore, in the case of a high-quality QW, the broadening of a PL peak can

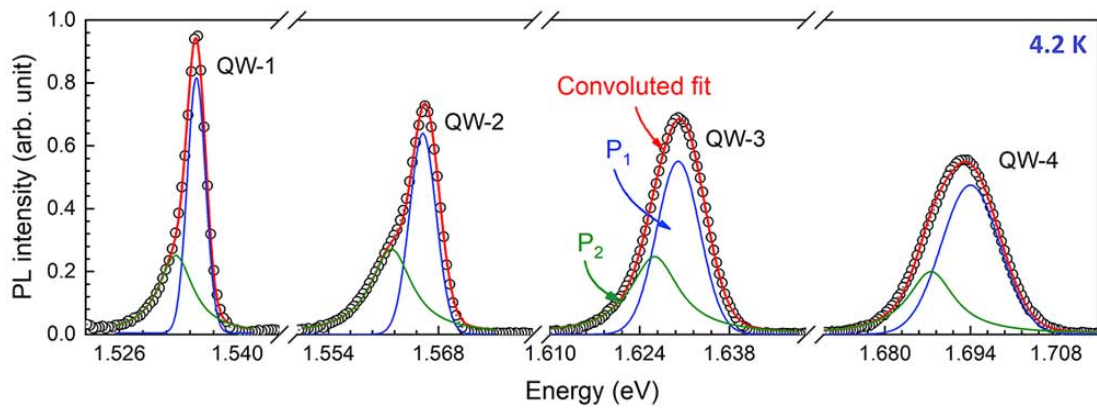


Figure 3.3: 4.2 K PL spectra of the MQW sample and PL line-shape fitting by Gaussian along with Lorentz distribution function.



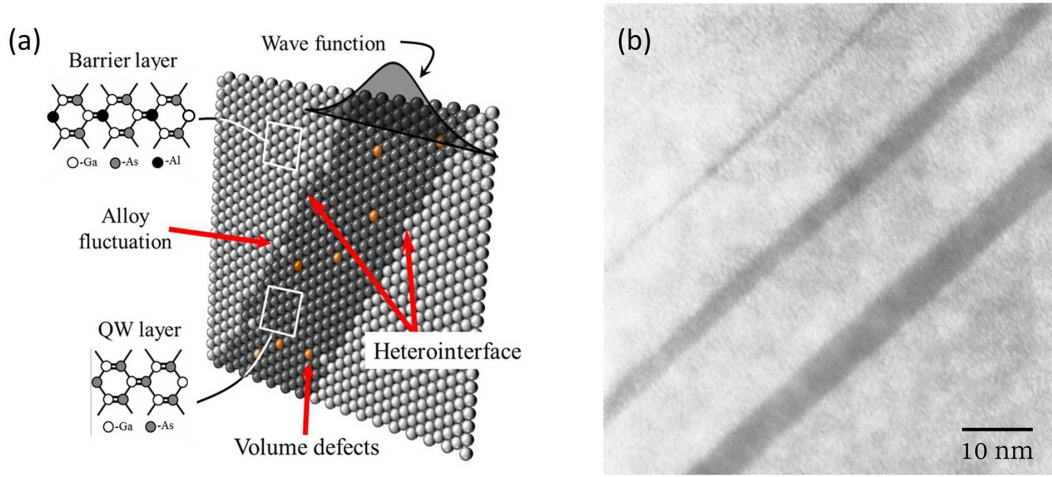


Figure 3.4: (a) Schematic illustration of charge carriers' confinement in a QW and (b) cross-sectional TEM image of a GaAs/AlGaAs MQWs showing the quality of the hetero-interfaces.

be described by the following relation,[108, 109, 110, 111]

$$\Gamma_{Total}^2 = \Gamma_{homogeneous}^2 + \Gamma_{defect}^2 + \Gamma_{pot.fluct.}^2 + \Gamma_{thickness}^2 + \Gamma_{penetration}^2 \quad (3.1)$$

The excitons which are susceptible for band-to-band recombination (free-exciton, FX) may experience the localization potentials, and their recombination at different spatial position contribute to the inhomogeneous broadening (Eq. 3.1) with Gaussian distribution.[108] Notably, strain-induced inhomogeneous line-broadening is not considered in the present study because of the very small ( $< 0.04\%$ ) lattice mismatch between GaAs and  $\text{Al}_{0.28}\text{Ga}_{0.78}\text{As}$  materials.[21] Also, the effect of spectral diffusion on the PL linewidth is negligible for GaAs QWs with highly-uniform spatial charge distribution.

In addition to the broadening in PL spectra, defects (vacancy, substitutional, interstitial atoms), impurities (Si, C, etc.), and inhomogeneity in lattice may introduce isolated localized energy states within the bandgap. The excitons that are captured by these localization potentials are known as bound-exciton (BX), which can recombine radiatively and cause asymmetry in PL spectra. With the kinetic energy of BXs being feeble, the PL line-shape of a BX transition can be approximated by Lorentz function in the case of binary semiconductors.[108] Notably, distinct PL peaks related to the donor

or acceptor bound exciton or trion are not observed in the PL spectra of the undoped QWs (Fig. 3.3). However, defect and impurity-bound excitons may have slightly donor-type nature due to the incorporation of silicon impurities in the MOVPE grown samples. In order to estimate PL intensity and linewidth of the FX and BX transitions, PL line-shape is fitted with Gaussian function along with a Lorentzian distribution. Figure 3.3 shows the PL line-shape fitting of QWs at  $T = 4.2$  K. Here, the Gaussian peak  $P_1$  with relatively large PL intensity is understood by the radiative recombination of FX, whereas the homogeneously broadened  $P_2$  is contributed by BX transition.

### 3.3.1 Quantification of QW thickness fluctuation

The linewidth of  $P_1$  transition for the four QWs at 4.2 K is plotted in Fig. 3.5. To understand the impact of wave function penetration on the broadening of PL peak, the probability distribution of electron and hole in QWs is estimated by solving the Schrödinger equation in finite difference method. The parameters used for this calculation, e.g.,  $m^*$  and  $\varepsilon_g(T)$ , and band-offsets for GaAs/ $\text{Al}_{0.28}\text{Ga}_{0.72}\text{As}$  system, are acquired from the standard literature reports.[21, 112] Figure 3.6 shows that the charge carriers in QW-1 ( $l_w = 190$  Å) are not considerably influenced by the atomic irregularities at

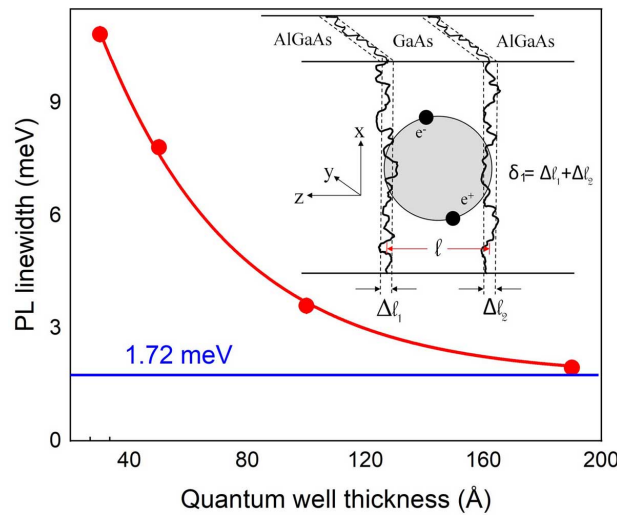


Figure 3.5: The broadening of PL peak ( $P_1$ ) as a function of QW width. The inset shows that the excitons in a narrow QW experience thickness fluctuations due to the atomic irregularities at the hetero-junctions.



the hetero-junctions. However, in the case of other QWs, the spatial extent of the electron/hole is larger than the corresponding QW thickness. Therefore, an enhancement in PL linewidth for a narrow QW can be explained by the effect of wave functions penetration with the substantial influence of hetero-interfaces. It is observed that the PL linewidth as a function of QW thickness saturates near  $(1.72 \pm 0.05)$  meV (Fig. 3.5), where this minimum value of linewidth is governed by the homogeneous broadening ( $\Gamma_{homogeneous}$ ), potential fluctuations ( $\Gamma_{pot.fluct.}$ ), and in-plane defects ( $\Gamma_{defect}$ ) in the QW layer. The probability of carrier occupancy in barrier layers ( $f$ ) is numerically calculated by using Fig. 3.6 (Table 3.1), which is then used to estimate the enhancement in PL linewidth due to the wave function penetration,

$$\Gamma_{penetration} = (1 - f) \times \Gamma_{Al_{0.28}Ga_{0.72}As} \quad (3.2)$$

The PL linewidth of  $Al_{0.28}Ga_{0.72}As$  barrier is measured independently, which is found to be 16.6 meV (data not shown). Thereafter, the broadening in PL spectra due to QW thickness fluctuation ( $l_w \pm \delta_1$ ) is estimated by subtracting the contribution of other terms in Eq. 3.1, which is summarized in Table 3.1. Finally, the amount of PL line-broadening due to the QW thickness fluctuation  $[\varepsilon_g^*(l_w - \delta_1) - \varepsilon_g^*(l_w + \delta_1)]$  is used to estimate  $\delta_1$  by the following relation,

$$\Gamma_{thickness} = \frac{\pi^2 \hbar^2}{\mu^*} \left[ \frac{2l_w \delta_1}{(l_w^2 - \delta_1^2)^2} \right] \quad (3.3)$$

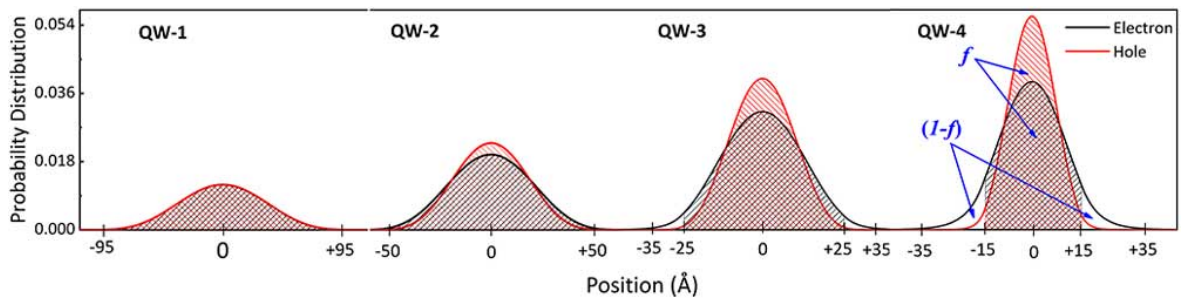


Figure 3.6: The spatial extent of electron-hole wave functions in different thicknesses of QWs, which is estimated by solving the 1-dimensional Schrödinger equation.

Table 3.1: Probability of finding an electron-hole pair in QW ( $f$ ) and barrier layers ( $1-f$ ). PL line-broadening originated by different mechanisms are tabulated.

$f$	$(1-f)$	$\Gamma_{penetration}$ (meV)	$[\Gamma_{homogeneous}^2 + \Gamma_{defect}^2 + \Gamma_{pot.fluct.}^2]^{1/2}$ (meV)	PL linewidth ( $P_1$ ) (meV)	$\Gamma_{thickness}$ (meV)
1.000	0.000	0.00	1.72	1.95	0.90
0.998	0.002	0.03	1.72	3.64	3.21
0.980	0.020	0.33	1.72	7.82	7.62
0.913	0.087	1.44	1.72	10.83	10.56

With the QWs in the MQW structure are grown under identical condition, fluctuations in QW thickness can be evaluated by averaging the estimated  $\delta_1$  of the four QWs, which is found to be  $\langle\delta_1\rangle = 2.1 \pm 0.4$  Å. The  $\mu^*$  required for this calculation is estimated by the magneto-PL spectroscopy, which is discussed in the later section of this chapter. A similar order of interface roughness was previously reported by complex and destructive techniques, like cross-sectional scanning tunneling microscopy, TEM, etc.[113, 114, 115, 116] Notably, the defects acquainted along the growth direction of the QW may contribute to the estimated  $\delta_1$ , which can be higher for a thick QW. In addition to this, the fluctuation in QW thickness in the case of a wide QW may average out over the higher exciton Bohr radius. The contribution of disorder-averaging predominantly depends on the quality of epi-layer and hetero-interfaces, the kinetics of excitons, and carrier capture mechanisms by defects.[90, 117] The above approach to estimate the fluctuations in QW thickness would be suitable for any set of QWs that are grown under identical conditions. Notably, a variation in composition and growth conditions between the QWs may lead to an erroneous result by the above technique to estimate  $\delta_1$ . This is because, in such a condition, the defect density, dopant density, and the quality of hetero-junctions may vary among QWs. In summary, the simple and contactless nature of PL measurements is really attractive to probe inhomogeneities in QWs.

### 3.3.2 Excitation power-dependent PL spectroscopy

In order to confirm the nature of  $P_1$  and  $P_2$  peaks that are partially merged in the PL spectra, excitation power-dependent PL measurement is also performed at 4.2 K (Fig. 3.7a). Figure 3.7b shows that the integrated PL intensity of  $P_1$  linearly increases with a laser power density ( $p_{exc}$ ). The variation in PL intensity with  $p_{exc}$  can be understood by a rate equation model,  $I \propto R_r = (n \times p)/\tau_r \sim p_{exc}$ . Here, each photon generates an electron-hole pair (exciton) that recombines radiatively to emit the same photon again. Therefore, the intensity of free-excitonic PL linearly increases with increasing electron-hole pair generation rate. However, a sub-linear power-dependence of  $P_2$  ( $I \propto p_{exc}^y$ , with  $y < 0.9$ ) indicates that the defect states of the high-quality QW are saturated under a high  $p_{exc}$  (Fig. 3.7c). [118] Note that the power-dependent PL intensity may exhibit a super-linear variation ( $1 < y \leq 2$ ) for free-carrier recombination, where the photo-generated carriers can be recombined with carriers that are already present in the sample. Therefore, in an ideal case of free-carrier recombination, PL intensity quadratically varies with  $p_{exc}$  [i.e.,  $I \propto (p_{exc})^2$ ], since the rate of carrier recombination depends on the product of electron and hole density. [119]

Note that the relative strength of PL emission from different thicknesses of QW, at a given excitation power, can be explained by considering the absorption of pho-

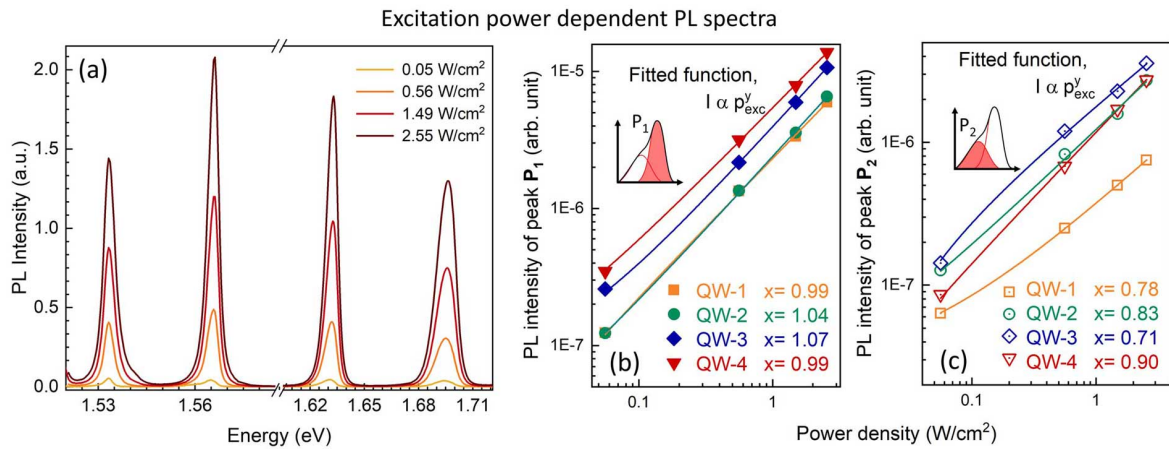


Figure 3.7: (a) Power dependent PL spectra and intensity of  $P_1$  (b) and  $P_2$  (c) peaks as a function of the excitation power density of laser light.

tons, radiative recombination of excitons, and non-radiative decay of charge carriers. The density of photo-excited carriers in a thick QW, deep inside the MQW structure (see Fig. 3.1a), is mainly constrained by the reduction of photon-flux as a function of depth [ $I \sim I_0 \times \exp(-\alpha \cdot l)$ ] and smaller joint density of state. Moreover, the oscillator strength of excitons (Eq. 1.16) decreases with an increase in QW thickness,[48, 49] which enhances the radiative recombination time and reduces the PL signal ( $I \sim n/\tau_r$ ) for the thick QW. On the contrary, charge carriers that are confined in a narrow QW experience disorders present at the hetero-interfaces and decay via a non-radiative process. As a result of the above processes, the PL intensity, at a given excitation power, gradually increases with a reduction in QW thickness (Fig. 3.7b). Notably, when a significant amount of wave function penetrates in barrier layers (for  $l_w \ll 30 \text{ \AA}$ ), the oscillator strength of exciton again decreases,[49] which may cause a reduction in the PL intensity. Also, under a very high pump power, carrier-carrier scattering, screening of Coulomb potential, and sample heating play an important role to define the relative strength of the PL peaks for different QWs.[120, 121]

## 3.4 Surface photovoltage spectroscopy

### 3.4.1 Charge redistribution processes with temperature

The absorption of photons and redistribution of photo-generated charge carriers in the MQW structure are also investigated by SPV measurements. Temperature-dependent SPV amplitude and phase spectra of the MQWs are shown in Figs. 3.8c and 3.8d. It is observed that the SPV amplitude related to QW transitions monotonically increases with an enhancement of temperature, where the heavy (HH) and light hole (LH) transitions are identified by solving the 1-D Schrödinger equation. According to literature reports, the amplitude of SPV signal can be explained by following processes: (i) thermal escape of charge carriers from the QW, (ii) electric field-assisted tunneling of charges, (iii) separation of electron-hole within the QW, and (iv) capture of charges by interface defects or disorders.[122] Electron and hole, which are escaped from a QW,

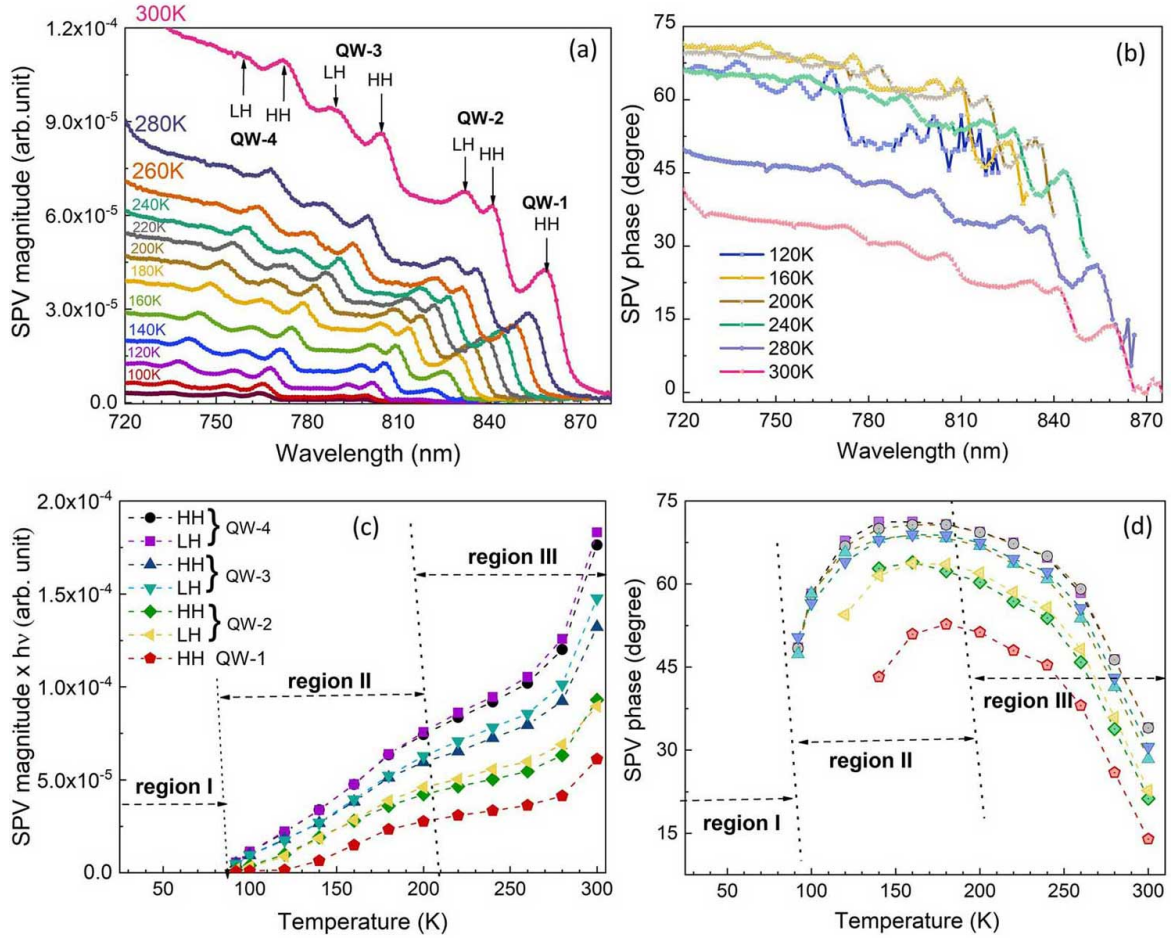


Figure 3.8: (a) Schematic of the GaAs/AlGaAs MQW layer structure and (b) sample stage for SPV measurements. (c) The SPV amplitude and (d) phase spectra of the MQW sample in the temperature range of 92 - 300 K. Maxima of heavy and light hole related (e) SPV amplitude  $\times h\nu$  and (f) phase are plotted as a function of temperature.

either by thermal energy or tunneling, drift according to the surface and interface band-bending. The thermally activated charge carriers may also diffuse in barrier layers due to a gradient in photo-generated carrier density. In general, charge redistribution processes, contributing to the SPV-amplitude, are expressed by the following relationship of algebraic sum,[123]

$$\text{SPV} = \sum_{\text{process}} \int_{l_d} \left( \frac{dV^{\text{light}}}{dz} - \frac{dV^{\text{dark}}}{dz} \right) dz \quad (3.4)$$

where  $V^{\text{light}}$  and  $V^{\text{dark}}$  represent the surface or interface potential during the light illumination and dark respectively, and  $l_d$  symbolizes the depletion width. On the contrary, a variation in SPV-phase can be explained by the emergence or dominance of a

charge redistribution process under an external perturbation, such as enhancement of temperature, photon flux, magnetic field, etc. In particular, the SPV phase may continuously vary under the presence of non-linear processes in the sample.[124] Notably, sub-bandgap SPV features in bulk and heterostructures of GaAs and similar systems are previously investigated by many authors,[125, 126] and therefore, not discussed in the present study.

It is observed that the SPV-amplitude related to QW-transitions exhibits a peak-like behavior (Fig. 3.8c), which is replicated by the phase spectra of the measured signal (Fig. 3.8d).<sup>1</sup> The origin of distinct peaks in phase spectra, which are observed exactly at the same energies when there is a peak in SPV amplitude, is not yet understood. To realize the spectral line-shape of SPV phase and temperature-dependent processes, SPV amplitude  $\times h\nu$  and phase maxima as a function of temperature are plotted in Figs. 3.8e and 3.8f. Depending on their variations, temperature-dependent processes can be divided into three regions, as marked in Figs. 3.8c and 3.8d. Also, the contribution of drift/diffusion of electron and hole in the measured SPV signal is realized by the energy band-profile of the MQW structure (Fig. 3.9), which is numerically estimated by solving the Schrödinger-Poisson equation for an intermediate temperature.[127] According to Fig. 3.9, holes that are escaped from a QW drift towards the surface, whereas electrons after the thermal escape drift away from the surface (i.e., towards the substrate). On the contrary, the photo-generated electron-hole pair density being maximum close to the surface, both the electron and hole diffuse away from the surface. Therefore, the contribution of hole-redistribution in the measured SPV signal would be feeble when drift and diffusion try to cancel the impact of each other. Moreover, with the mobility of electrons is much higher than the mobility of holes [128] and diffusion of electrons is faster than holes [129, 130], SPV signal in the present case is predominantly contributed by the thermal escape of electrons from QWs followed by their drift/diffusion towards the substrate.

---

<sup>1</sup>SPV phase in the sub-band gap region (870 nm) of GaAs at 67 Hz chopping frequency is set to zero which is used as the reference for the phase variation.



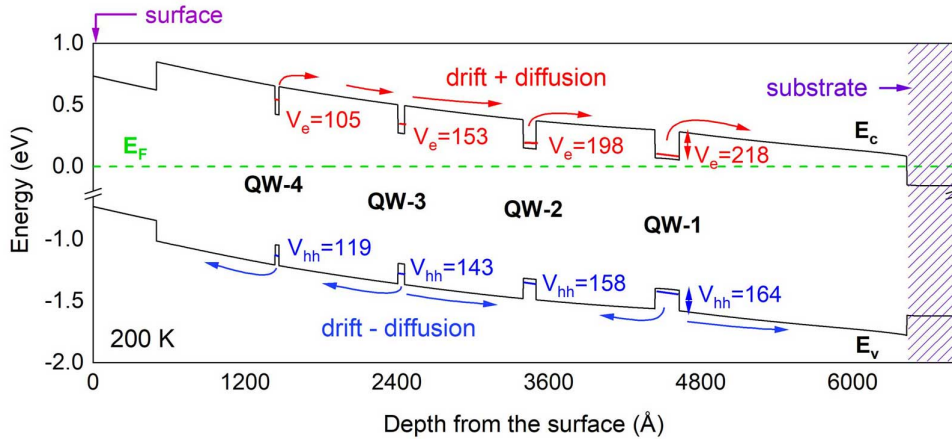


Figure 3.9: The energy band profile of the MQW structure is estimated by solving the one-dimensional Schrödinger-Poisson equation without considering the contribution of interface defect states. The potential barrier of electrons ( $V_e$ ) and heavy holes ( $V_{hh}$ ) in QWs are shown in the unit of meV.

It is observed that, in region-I ( $T \lesssim 80$  K), SPV amplitude and phase spectra related to QW transitions could not be recorded, even under the maximum photon-flux ( $\sim 1$  mW/cm<sup>2</sup>) available in our experimental setup (Figs. 3.8c-f). This is because most of the photo-excited electrons in this low-temperature regime radiatively recombine with holes, which leads to a strong luminescence signal.[131] In addition, a significant number of electrons are captured by point defects in QWs, which is shown by magenta arrows in Fig. 3.10. As a result of this, the probability of carrier redistribution within QWs or the thermal escape of electrons becomes feeble, which causes a negligibly small SPV signal in region-I.

However, with an enhancement of temperature, radiative recombination time of charge carriers increases [ $\tau_r(T) \sim T \times \tau_r(0)$ ],[61, 100] and electrons, which have been captured by point defects, are thermally activated to energy eigenstates of the QW (shown by black arrows, Fig. 3.10). A small fraction of these electrons may also escape from the QW and drift towards the substrate, leading to a gradual enhancement of the SPV amplitude. Therefore, in region II ( $80 \lesssim T \lesssim 200$  K), the free-carrier density in the conduction band increases due to thermal activation of point-defects and increase in  $\tau_r$ , which may enhance an electron-electron interaction within the QW. Under this condition, electrons are forced to move towards interfaces and increase the carrier lo-

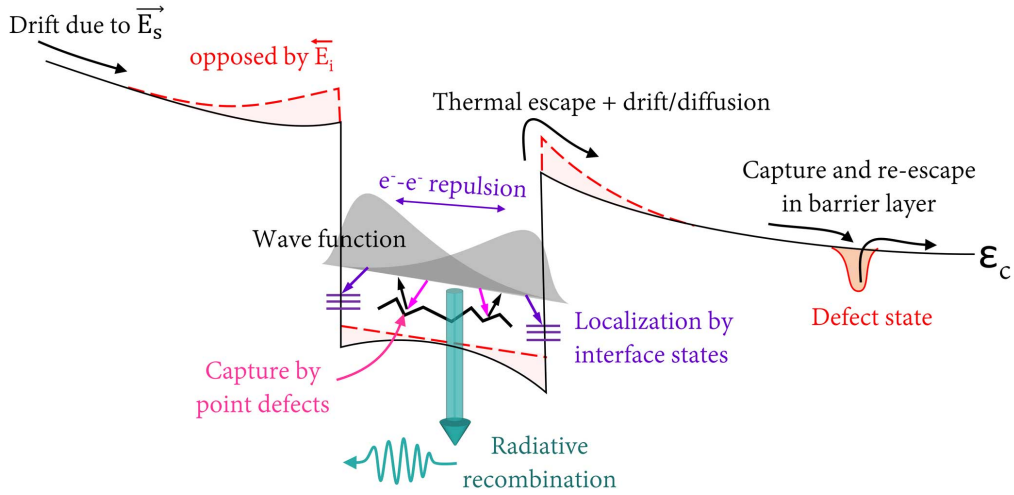


Figure 3.10: The recombination (cyan arrow), capture by point defects (magenta arrows), thermal activation (black arrows), and electron-electron repulsion followed by carrier localization at heterointerfaces (purple arrows) are schematically illustrated. In a high-temperature regime, a significant number of electrons escape from the QW and drift/diffuse in barrier layers. In this process of charge migration, electrons are captured and re-escape from the defect states in barrier layers or other QWs in the MQW structure.

calization at the QW interfaces (purple-arrows in Fig. 3.10). As a result of this, an interface electric field  $\mathbf{E}_i$  would be generated that may oppose the drift of electrons under the influence of surface electric field  $\mathbf{E}_s$ , see Fig. 3.10. This enhancement of  $\mathbf{E}_i$  due to the electron-electron interaction could be the main reason for the temperature-dependent increase in the SPV phase in region-II (Fig. 3.8f). Note that the hole-hole interaction in the valence band of QWs followed by their capture in heterointerfaces will reduce the magnitude of  $\mathbf{E}_i$ . However, since the QWs are already occupied by a considerable number of electrons that are migrated from the  $n^+$  substrate (see the Fermi level in Fig. 3.9), the electron-electron interaction would be a dominating process than the hole-hole repulsion.

Further enhancement of temperature significantly increases the thermal escape of electrons, which leads to a non-linear rise of the SPV amplitude in region-III ( $T \gtrsim 200$  K), Fig. 3.8e. In this process, the electronic density in QWs decreases, and electrons that were captured at heterointerfaces are also released by thermal energy. Therefore, the amplitude of  $\mathbf{E}_i$  at GaAs/AlGaAs heterointerfaces reduces at a high temperature,



and causes a decrease in the SPV phase (Fig. 3.8f).

In summary, an electron-electron interaction within the QW enhances the interface electric field, which may oppose drift and diffusion of charges in the QW-based structure. In this process, the relative phase of the SPV-signal increases. Therefore, when the energy of the incident photons is resonant with a QW transition, a large number of electrons are excited due to a higher absorption coefficient, which enhances the electron-electron interaction and builds up a strong  $\mathbf{E}_i$ . This could be the reason to observe a peak like variations in SPV-phase exactly at the same energy when there is a peak in SPV-amplitude. It is noteworthy to mention that since the built-in interface electric field opposes the redistribution of electrons, elimination of the above process would be beneficial to achieve a significant enhancement of photovoltaic response of the system.

The SPV amplitude related to QW transitions in region-III can be explained by the absorption of photons using the following relation,[132]

$$|\text{SPV}|_{abs} = \frac{k_B T}{e} \frac{A \eta^* e \Phi_0 (1 - R^*)}{h \nu} [1 - e^{-\alpha^* l_w}] \quad (3.5)$$

Here, an above bandgap light of photon flux  $\Phi_0$  illuminates the sample over an exposure area  $A$ , where the reflectivity of light and quantum efficiency are symbolized by  $R^*$  and  $\eta^*$  respectively. Moreover, in the case of a thin absorbing layer, the quantity  $[1 - \exp(-\alpha^* l_w)]$  can be approximated to  $\alpha^* l_w$ . Note that the absorption coefficient, which depends on the joint-density of state, may also vary with an enhancement of temperature. Equation 3.5 can be used to explain the SPV-amplitude as a function of temperature by introducing an additional term related to the thermal escape. The SPV being a complementary technique to emission spectroscopy, temperature-dependent SPV can be explained with the help of the Arrhenius equation,[133] which is often used to study temperature-dependent PL intensity  $[I(T)]$ .

$$\begin{aligned} \text{SPV}(T) &\sim [I(0) - I(T)] \\ &\sim |\text{SPV}|_{abs} \times \frac{\tau_r}{\tau_{nr}} \exp\left(-\frac{\varepsilon_{esc}}{k_B T}\right) \end{aligned} \quad (3.6)$$

The symbols  $\tau_{nr}$  and  $\varepsilon_{esc}$  represent the non-radiative decay time and the energy required for the electronic escape from the QW, where  $\varepsilon_{esc}$  signifies the sum of barrier height ( $V_e$ ) and binding energy of excitons. Unlike the present case, when both the electron and hole contribute to the SPV signal, an additional term related to holes can be incorporated in Eq. 3.6. Further simplification of Eq. 3.6 can be performed by considering  $\tau_r(T) \sim T \times \tau_r(0)$ . Therefore, Eq. 3.6 shows that the amplitude of SPV increases with rising the temperature due to the following reasons - (a) radiative recombination time of charge carrier increases due to the electron-phonon interaction, and (b) probability of thermal escape increases with raising the temperature. Besides the above formulation, the band-bending of the MQW structure and carrier localization in point defects may slightly vary with temperature in region-III, which may also contribute to temperature-dependent SPV-amplitude and phase spectra.

### 3.4.2 Impact of carrier-carrier interaction on charge redistribution process

Further insights of carrier localization at the heterointerfaces and its impact on SPV amplitude and phase are realized by excitation power ( $p_{exc}$ ) dependent SPV measurements. Results obtained in Figs. 3.11a and 3.11b show that SPV amplitude and phase of QW transitions are simultaneously increasing with an enhancement of  $p_{exc}$ . The SPV-

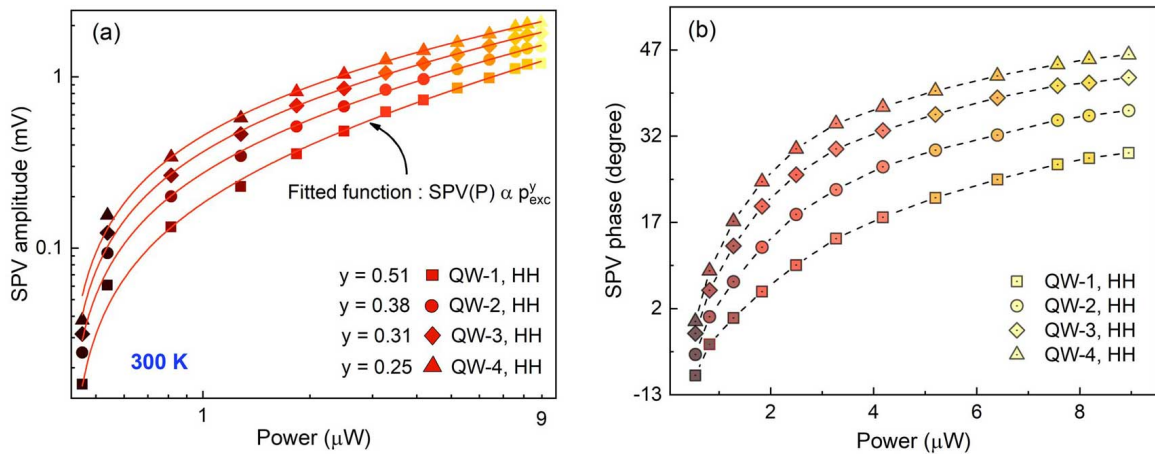


Figure 3.11: Excitation power-dependent SPV (a) amplitude and (b) phase maxima related to QW transitions at 300 K.

amplitude as a function of  $p_{exc}$  is also fitted by a power-law relation,  $SPV \propto (p_{exc})^y$ , Fig. 3.11a, where numerical values of the exponent are shown in the inset of the plot. It is found that the fitted value of  $y$  is much lower than unity for all four QWs, which indicates a large number of photo-excited electrons that are bound by defect/disorders could not contribute to SPV, especially at higher excitation power. At the same time, an increasing SPV phase suggests that the interface electric field also enhances at higher  $p_{exc}$ . This is because photo-excited electrons become highly susceptible to be localized at the heterointerfaces of the QW due to a strong electron-electron interaction under intense light illumination (Fig. 3.11b). As a result of this, the drift of electrons in the MQW structure is affected and the SPV amplitude exhibits a sublinear increase as a function of  $p_{exc}$ . A lower value of  $y$  for a narrow QW (e.g.,  $y = 0.25$  for QW-4) readily indicates that when a significant amount of wave function has penetrated in barrier layers, electron-electron interaction plays an important role on the carrier localization at the heterointerfaces. Notably, the accumulation of photo-generated charge carriers in all four QWs is different due to their different  $\alpha^*$  and  $\varepsilon_{esc}$ , which may also influence the numerical value of  $y$ .

### 3.4.3 Response time of charge redistribution process

A chopping frequency-dependent SPV measurement is also performed to probe the time response of carrier redistribution processes that are contributing to the SPV signal (Fig. 3.12). According to the previous reports, the SPV-amplitude as a function of frequency ( $f_\nu$ ) can be expressed by the following relation,[134]

$$SPV(f_\nu) = \sum_k \frac{\wp_k \tau_k}{[1 + (2\pi f_\nu \tau_k)^2]^{1/2}} \quad (3.7)$$

Equation 3.7 can be easily derived by considering the capacitance-resistance circuit of metal (TCG) - insulator (air) - semiconductor sample stage configuration. Here, the time constant associated with the process  $k$  is denoted by  $\tau_k$  and  $\wp_k$  represents the

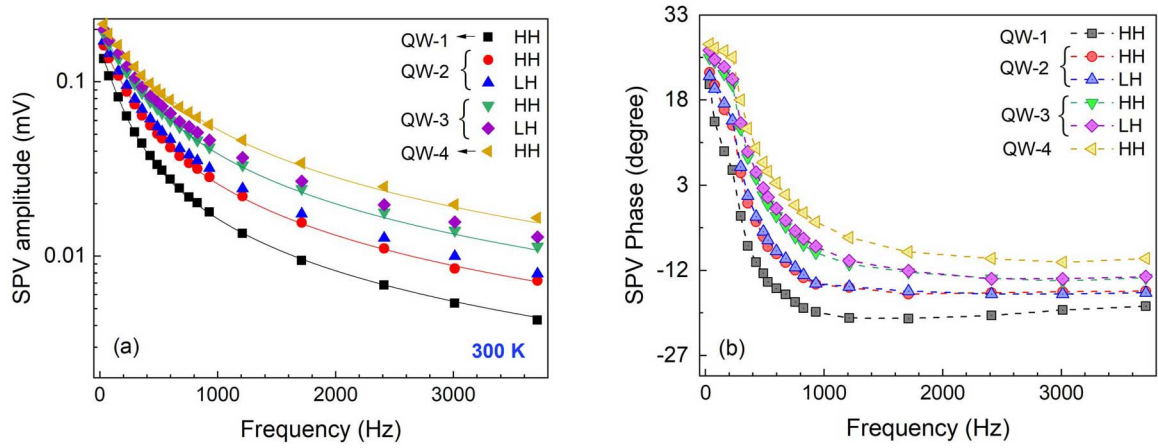


Figure 3.12: (a) The SPV amplitude and (b) phase maxima are plotted as a function of chopping frequency at 300 K.

strength of the corresponding process, which are estimated by fitting the frequency-dependent SPV amplitude as shown in Fig. 3.12a (Table 3.2). The estimated  $\tau_1$  with higher  $\phi$  could be related to the thermal escape of photo-generated electrons followed by their drift in barrier layers, whereas a higher value of  $\tau_2$  could be related to the de-localization of electrons followed by their thermal escape and drift in the MQW structure. It is noteworthy to mention that, even though the thermal escape, drift and carrier capture mechanisms are in-general ns process, the estimated  $\tau_1$  and  $\tau_2$  are found to be in the ms range. This is mainly because of the carrier localization and de-localization processes during their migration in barrier layers (see, Fig. 3.10), which enhances the effective time constant of the above processes. Note that the electrons, which are escaped from a QW, may also be localized into other QWs in the MQW structure. In addition, a sharply decreasing SPV-phase indicates that the carrier-carrier interaction followed by their capture at heterointerfaces and development of the interface electric

Table 3.2: Time constants of charge redistribution process in different thicknesses of QW.

QW thickness (Å)	$\phi_1$ (s <sup>-1</sup> )	$\tau_1 \pm 0.03$ (ms)	$\phi_2$ (s <sup>-1</sup> )	$\tau_2 \pm 0.3$ (ms)
190	1.02	1.3	0.01	5.0
100	1.50	0.75	0.16	3.9
50	2.06	0.48	0.48	2.1
30	2.62	0.31	1.03	1.3

field is also a slow process with a few ms time response.

## 3.5 Magneto-PL spectroscopy

### 3.5.1 Effective mass of excitons and non-parabolicity of bands

In this section, the impact of quantum confinement on the effective mass and binding energy of excitons is investigated by PL measurements under a high magnetic field. Figure 3.13 shows the magneto-PL spectra of the MQW sample under the magnetic field up to 8 T. With an increase in the magnetic field, a blue-shift in PL peaks is observed, which is found to be significant for a thick QW (e.g., QW-1). The magnetic field-driven blue-shift in FX transition energy ( $P_1$ ) for the QWs is plotted in Figs. 3.13(b-e). In a low field regime ( $B < B_c$ ), the diamagnetic shift of energy states can be expressed by the following relation,[52, 135]

$$\Delta\varepsilon(B) = R_D \frac{e^2 B^2 r_b^2}{4\mu^*} \quad (3.8)$$

A dimensionless parameter  $R_D$  is introduced in Eq. 3.8 to consider the role of charge carrier confinement in quantum structures. However, under a strong magnetic field when magnetic length  $<$  exciton Bohr radius,[52] energy eigenstates become discretized in the form of Landau states. In this condition, the energy eigenvalue of Landau states

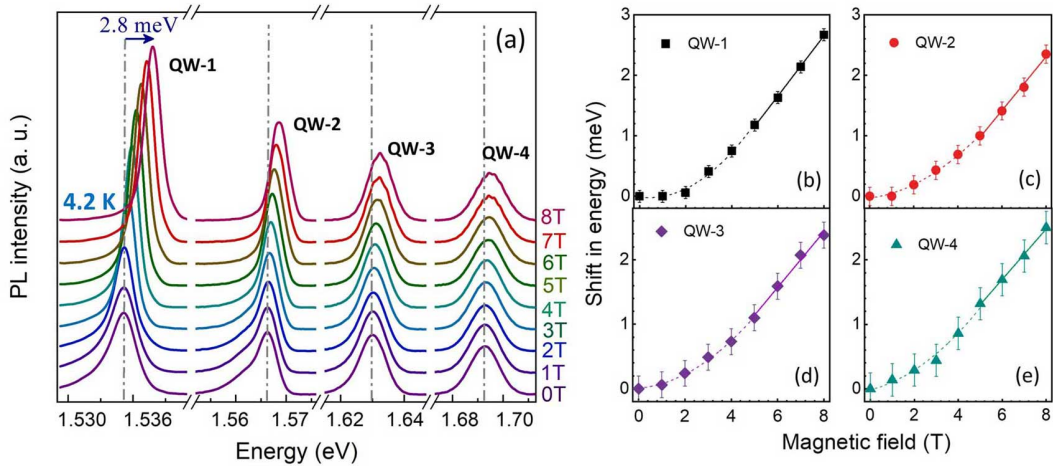


Figure 3.13: (a) 4.2 K magneto-PL spectra under the magnetic field up to 8 T. The magnetic field-driven blue-shift in PL peaks are plotted in (b)-(e)

Table 3.3: The reduced effective mass and binding energy of excitons with a variation in QW thickness are summarized, where the free-electron mass is denoted by  $m_0$ .

$l_w$ Å	$\mu^* \pm \text{error}$ ( $\times m_0$ )	$\varepsilon_b \pm \text{error}$ (meV)
190	$0.114 \pm 0.002$	$8.9 \pm 0.4$
100	$0.133 \pm 0.002$	$10.4 \pm 0.6$
50	$0.163 \pm 0.006$	$12.7 \pm 1.0$
30	$0.178 \pm 0.007$	$13.9 \pm 1.1$

can be expressed by,[52, 135]

$$\Delta\varepsilon(B) = \left(j + \frac{1}{2}\right) \frac{\hbar e B}{2\mu^*} \quad (3.9)$$

The magnetic field above which magnetic perturbation dominates over Coulomb interaction is termed as the critical magnetic field ( $B_c = \mu^{*2}e^3/16\pi^2\epsilon_0^2\epsilon_r^2\hbar^3$ ),[52] According to this expression, the critical field of bulk GaAs can be estimated to be  $\sim 4.9$  T, considering  $\epsilon_r$  of GaAs is 13.18.[21] Now, the magnetic-field dependent linear shift in PL peak energy ( $B \geq 5$  T) is used to estimate the reduced effective mass of excitons by Eq. 3.6 [Figs. 3.13(b-e)].[136, 135, 19] Subsequently, the estimated  $\mu^*$  is used to calculate the binding energy of excitons in the absence of a magnetic field by  $\varepsilon_b(B=0) \approx (\mu^*e^4/32\pi^2\epsilon_0^2\epsilon_r^2\hbar^2)$ ,[52] which is shown in Table 3.3. The binding energy estimated by this simple relation (considering spherical charge distribution) is found to be in close agreement with the literature reported  $\varepsilon_b$  that was calculated by a rigorous theoretical framework.[137, 138, 139] Such an observation indicates that the penetration of wave function into barrier layers is trying to restore the three-dimensional character of excitons in the QWs.

### Effect of wave function penetration into barrier layers

It is observed that the estimated  $\mu^*$  of the QWs (Table 3.3) is higher than the reduced mass of excitons in GaAs [ $\mu^* = 0.056m_0$ ],[140] which dramatically increases with decreasing the QW thickness. According to the existing literature reports, one plausible explanation for the increase of effective mass with decreasing QW thickness

can be the impact of wave function penetration into barrier layers. In particular, with a decrease in QW thickness, wave function penetration upsurges which may increase  $\mu^*$ . The resultant effective mass of electron and hole by considering this penetration effect can be estimated by,[141]

$$\frac{1}{m^*(\text{QW} + \text{penetration})} = \frac{f}{m_{\text{GaAs}}^*} + \frac{(1-f)}{m_{\text{AlGaAs}}^*} \quad (3.10)$$

where  $f$  and  $(1-f)$  signify the occupation probability of charge carriers in the QW and barrier layer, respectively. The effective mass of charge carriers in GaAs and AlGaAs materials is symbolized by  $m_{\text{GaAs}}^*$  and  $m_{\text{AlGaAs}}^*$ . Using Eq. 3.10, the increase in effective mass due to the above process can be estimated by,

$$\Delta m_{\text{penetration}}^* = \frac{m_{\text{GaAs}}^*(1-f)(m_{\text{AlGaAs}}^* - m_{\text{GaAs}}^*)}{f \times m_{\text{AlGaAs}}^* + (1-f) \times m_{\text{GaAs}}^*} \quad (3.11)$$

The numerical values of  $f$  for the QWs are estimated by Fig. 3.6. Subsequently, the estimated  $\Delta m_{\text{penetration}}$  is summarized in Table 3.4. It is found that the enhancement of effective mass due to wave function penetration is not sufficient to explain the experimentally observed higher values of  $\mu^*$  (Table 3.4).

### Effect of non-parabolicity of conduction band

Another factor that may influence the estimated  $\mu^*$  is the non-parabolicity of the conduction and valence bands. Many groups have theoretically investigated the role of non-parabolic conduction band in explaining a higher value of effective mass for QWs.[142, 143, 97, 144] According to these reports, the Hamiltonian of charge carriers under a magnetic field can be described by the following relation,[145, 146, 147]

$$H = \frac{\hbar^2 k^2}{2\mu^*} + \frac{1}{2}g\mu_B\sigma_p B + \Gamma_D\sigma_p\phi + a_1k^4 + \frac{a_2}{\xi_B^4} + a_3\left[\left\{k_x^2, k_y^2\right\} + \left\{k_x^2, k_z^2\right\} + \left\{k_y^2, k_z^2\right\}\right] + a_4k^2\sigma_p B + a_5(\sigma_p k, kB) + a_6k^2B\sigma_p + V_z(e) \quad (3.12)$$

Here,  $\Gamma_D$  and  $\sigma_p$  symbolize the Dresselhaus spin-orbit coupling constant and Pauli spin matrices, respectively. The quantity  $\phi$  is a vector-operator with components  $\phi_x =$

$(k_y k_x k_y - k_z k_x k_z)$ . Notably, the Lande g-factor of GaAs being very small ( $g^* \approx -0.44$  at 5 K), [145] the contribution of Zeeman splitting in Eq. 3.12 becomes feeble (0.2 meV at 8 T). Also, the contribution of the third term, in representing the spin-orbit interaction, is very small in the present case due to the negligible inversion symmetry of GaAs crystal structure. [145] The fourth term of Eq. 3.12 having quadratic dependence with the applied magnetic field (where  $\xi = \sqrt{\hbar/eB}$ ) denotes the diamagnetic energy of charge carriers. The terms containing  $a_1$  and  $a_3$  represent the non-parabolicity of bands with  $k^4$  dependency. Further details of Eq. 3.12 may be found in Refs. [145, 146] Under the above approximations for a GaAs-type system, a simplified form of Eq. 3.12 is proposed by Hiroshima and Lang to express the non-parabolicity in conduction band which is given by, [143]

$$\varepsilon'_e = \frac{\hbar^2}{2m_e^*} k_e'^2 (1 - \gamma k_e'^2) \quad (3.13)$$

where  $(\varepsilon'_e, k'_e)$  represents the energy eigenstate of electrons in non-parabolic band dispersion, which may not be same as  $(\varepsilon_e, k_e)$  corresponding to the parabolic band. The  $\gamma$  symbolizes the non-parabolicity factor of the conduction band. It is noteworthy to mention that, when QW thickness is large, energy eigenstate is positioned at the conduction band edge with wavenumber  $k'_e \rightarrow 0$  and Eq. 3.13 turns out to be a parabolic band dispersion  $\varepsilon_e = \hbar^2 k_e^2 / 2m_e^*$ . Here,  $m_e^*$  ( $= d^2\varepsilon_e / dk_e^2 = 0.067 m_0$ ) [21] is the effective mass of electrons, which is a measure of band-curvature at the conduction band edge. Therefore, a second-order derivative of Eq. 3.13 becomes,

$$\left[ \frac{\partial^2 \varepsilon'_e}{\partial k_e'^2} \right]_{\varepsilon'_{e1}} = \frac{\hbar^2}{m_e(\text{QW})} = \frac{\hbar^2}{m_e^*} - \frac{6\gamma \hbar^2 k_{e1}'^2}{m_e^*} \quad (3.14)$$

For a QW, the energy-dependent effective mass (mass as a function of QW width) and ground energy state of electrons in the non-parabolic band are represented by  $m_e(\text{QW})$  and  $(\varepsilon'_{e1}, k'_{e1})$ , respectively. Combining Eqs. 3.13 and 3.14, the non-parabolicity factor  $\gamma$  can be estimated by the following relation,

$$\gamma = \left[ \frac{m_e(\text{QW}) - m_e^*}{6m_e(\text{QW}) \times k_{e1}'^2} \right] = \frac{[m_e(\text{QW}) - m_e^*] \times [5m_e(\text{QW}) + m_e^*]}{72m_e^* [m_e(\text{QW})]^2 \varepsilon'_{e1}} \times \hbar^2 \quad (3.15)$$



Table 3.4: The increase in effective mass due to the wave function penetration. The PL peak energy, ground state energy of heavy-hole, and energy eigenstate of electrons in the non-parabolic band are summarized. Subsequently, the non-parabolicity factor is estimated by using  $\varepsilon'_{e1}$  and Eq. 3.15

$l_w$ (Å)	$\Delta m_{hh}^*$ (penet.) ( $\times m_0$ )	$\Delta m_e^*$ (penet.) ( $\times m_0$ )	$m_{hh}^*(\text{QW})$ +penet.) ( $\times m_0$ )	$m_e(\text{QW})$ ( $\times m_0$ )	$\varepsilon_g^*$ (eV)	$\varepsilon_{hh1}$ (meV)	$\varepsilon'_{e1}$ (meV)	$\gamma$ ( $\times 10^{-18}$ ) ( $m^2$ )
190	0.0000	0.0000	0.350	0.169	1.5352	2.5	22.6	2.32
100	0.0000	0.0000	0.350	0.214	1.5665	7.9	50.0	1.18
50	0.0015	0.0001	0.352	0.303	1.6304	24.0	100.1	0.62
30	0.0060	0.0026	0.356	0.356	1.6926	48.0	139.5	0.48

In order to estimate  $\gamma$  by the use of Eq. 3.15, one needs to have information about  $m_e(\text{QW})$  which can be decoupled from the estimated  $\mu^*$ , and energy eigenstates of the QW ( $\varepsilon'_e$ ) corresponding to the non-parabolic band dispersion. Here, the transition energy of the PL peak is used to estimate confinement energy ( $\varepsilon'_{e1}$ ) of electrons.

$$\varepsilon_g^* = \varepsilon_g^{\text{GaAs}} + \varepsilon'_{e1} + \varepsilon_{hh1} - \varepsilon_b \quad (3.16)$$

where  $\varepsilon_g^*$  is the energy of PL peak,  $\varepsilon_g^{\text{GaAs}} = 1.519$  eV is the bandgap of GaAs at 4.2 K,[21]  $\varepsilon_{hh1}$  is theoretically calculated, and  $\varepsilon_b$  is already estimated in Table 3.3. The estimated  $\varepsilon'_{e1}$  for the QWs is shown in Table 3.4.

Note that the heavy-hole band in-general does not interact with the conduction band edge and experience a weak interaction with the distant bands. Therefore, the impact of the non-parabolic heavy hole band on  $\mu^*$  can be neglected for the QW thickness greater than 30 Å.[97, 148, 149] Under this condition,  $m_{hh}^*$  is considered to be invariant,  $m_{hh}^* = 0.35m_0$ , [140, 150] and effective mass of electrons [ $m_e(\text{QW})$ ] is decoupled from  $\mu^*$  that is estimated by magneto-PL spectroscopy (Table 3.4).

$$\frac{1}{\mu^*} = \frac{1}{m_{hh}^*} + \frac{1}{m_e(\text{QW})} \quad (3.17)$$

The estimated  $m_e^*(\text{QW})$  as a function of QW thickness is summarized in Table 3.4. Now, Eq. 3.15 is used to deduce  $\gamma$  of the conduction band for the four QWs, by using

$m_e(\text{QW})$ ,  $m_e^*$  and  $\varepsilon'_{e1}$ . The non-parabolic  $\varepsilon$ - $k$  dispersion curves are then plotted in Fig. 3.14 highlighting the energy eigenstate of QWs by yellow dots. Here, the dispersion curves are valid within the range of  $0 \leq k'_e \leq k_{\max}$ . [151] The experimentally estimated  $\gamma$  for different thicknesses of QW can be compared with the previously reported non-parabolicity factor for GaAs QWs. [97, 152, 140, 153] In particular, the estimated  $\gamma$  for QW-4 is found to be in good agreement with the non-parabolicity factor reported by Nelson *et al.* for a narrow QW. [97]

It is noteworthy to mention that due to the non-parabolicity in bands, the effective mass of charge carriers increases when the energy eigenstate is shifted to higher  $(\varepsilon, k)$ , which can be explained by Eq. 3.14. In previous studies, it has been reported that the Landau-diamagnetic energy may exhibit a sub-linear variation when the energy eigenstates are significantly blue-shifted under a strong magnetic field. [52, 48, 154] Such an observation can be explained by the non-parabolicity in bands, where the effective mass of excitons increases due to the blue-shift in energy state under a high magnetic field. [52, 48] With this understanding, it can also be inferred that the charge carriers at higher energy sub-bands in a QW ( $s = 2, 3$ , etc.) would exhibit larger effective mass and smaller Landau-diamagnetic energy.

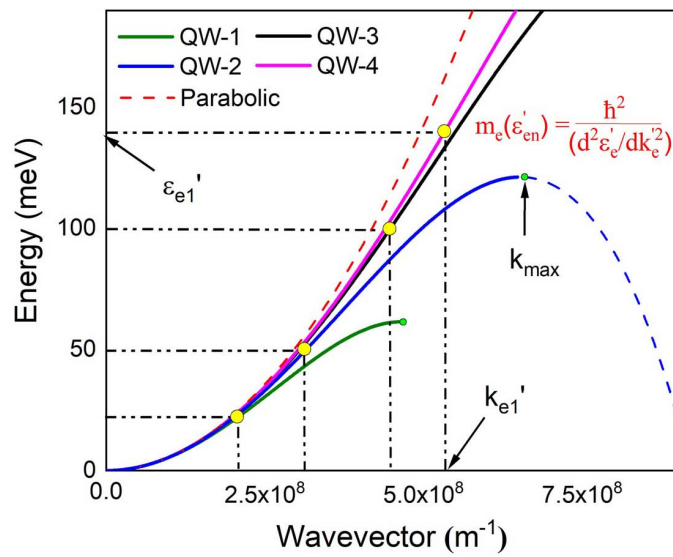


Figure 3.14: Non-parabolic band dispersion for different thickness of QWs. A parabolic dispersion curve for bulk GaAs is also shown by the red dashed line. The maximum  $k'_e$  value up to which the dispersion curve is valid is marked by green dots.

Notably, the reduced effective mass ( $\mu^*$ ) estimated by magneto-PL spectroscopy in this chapter is the in-plane counterpart of the three-dimensional mass. We have shown that the existing model of wave function penetration (using Eq. 3.10) is not sufficient to explain the higher effective mass of excitons in a narrow QW. In this analysis, the higher reduced mass of excitons is described by the spatial extent of wave functions along the out-of-plane direction. Similarly, the impact of non-parabolicity of conduction band on the effective mass primarily depends on the out-of-plane wave vector (for QWs,  $k^2 \approx k_z^2$ ). Therefore, it is evident that the effective mass estimated by magneto-PL spectroscopy can be explained by considering the out-of-plane parameters. In view of this, in-plane and out-of-plane masses are not explicitly mentioned in the above analysis. A similar convention can also be found in many reports.[141, 143, 97, 155, 156] A detailed study on the anisotropic effective mass of charge carriers in QWs can be found in Chapter 5.

In order to acquire further insights into this non-parabolicity of bands, a theoretical band calculation is also performed in collaboration with Dr. Aparna Chakrabarti and Dr. C. Kamal, RRCAT, using Vienna Ab initio Simulation Package. The calculation is performed on three different systems: (a) 20 mono-layers GaAs, (b) 5 MLs  $\text{Al}_{0.5}\text{Ga}_{0.5}\text{As}$ /10 MLs GaAs/5 MLs  $\text{Al}_{0.5}\text{Ga}_{0.5}\text{As}$ , and (c) 5 MLs AlAs/10 MLs GaAs/5 MLs AlAs. The results obtained in Fig. 3.15 show that the curvature of the conduction

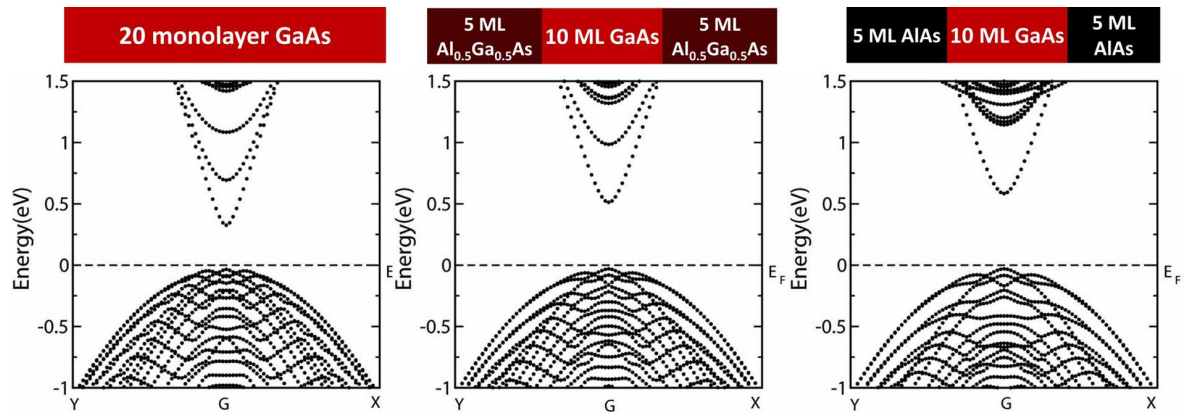


Figure 3.15: Theoretically calculated band-structure of (a) 20 MLs GaAs, (b) 10 MLs GaAs sandwiched between 5 MLs of  $\text{Al}_{0.5}\text{Ga}_{0.5}\text{As}$  barrier, and (c) 10 MLs GaAs sandwiched between 5 MLs of AlAs barrier.

band is considerably different in all three cases, whereas the curvature of the valence band edge remains nearly invariant. This indicates that the charge carriers in a QW experience an effective crystal potential due to the QW and barrier layer, which can influence the effective mass of excitons and non-parabolicity of bands.

### 3.6 Conclusion

In summary, radiative recombination and carrier redistribution processes in GaAs/AlGaAs QWs are investigated by PL and SPV measurements. The role of carrier localization on the asymmetry in PL line-shape and broadening in PL spectra is understood for various thicknesses of QW that are grown on the same substrate. The atomic irregularities at the hetero-interfaces of a QW are quantitatively estimated by modeling the PL linewidth as a function of QW width. The different thicknesses of QW with the same background parameters are found to be the key recipe for this work. Also, the localization of charge carriers in a QW leading to distinct peaks in SPV amplitude and phase spectra is realized by temperature, excitation power, and chopping frequency-dependent SPV measurements. In particular, the SPV measurement is found to be beneficial to probe carrier capture mechanisms, thermal escape of charges from QWs, and drift/diffusion in a multi-layered sample, which is also feasible for a high-temperature study. Further, the effective mass of excitons in QWs is estimated by magneto-PL spectroscopy, where the reduced mass of excitons significantly increases with decreasing QW width. It is found that the non-parabolicity of the band is an important factor that leads to a higher effective mass of charge carriers in a narrow QW.

## Chapter 4

# Optical properties of excitons under a magnetic field and estimation of defect density in QWs

### 4.1 Introduction and background

The electro-optical properties of semiconductors can be significantly affected due to the localization of charge carriers in crystalline imperfections and defects.[91, 157, 158, 90] In particular, defects acquainted in a system may reduce the radiative recombination efficiency of excitons and constrain the mobility of charge carriers.[159, 160] Therefore, the estimation of defect-density in quantum structures and their role in optoelectronic processes need to be understood. In previous, it has been proposed that a spectroscopic measurement under a high magnetic field can be beneficial for the quantitative estimation of defects.[91, 158, 161] Added to this, a magnetic perturbation can be desirous to suppress the impact of defects on the optical properties of excitons.[91, 162, 163, 164] These magneto-optical effects can be distinctly observed in GaAs-based QWs,[158, 165] because the broadening of energy states is minimum in such systems. At the same time, the magnetic field influences the radiative recombination and inter-subband relaxation of charge carriers.[166, 48, 167] With this understanding, it has been demonstrated that a magnetic perturbation can be utilized for room temperature operation of quan-

tum cascade lasers.[54, 55] At this elevated temperature, a significant number of charge carriers are excited to higher energy states, which may also escape from QWs. Therefore, the electro-optical processes at high temperatures would be different than that of a low-temperature, which requires a careful analysis by relatively high-temperature magneto-optical spectroscopy. Note that a detailed investigation of the magnetic field-driven electronic processes in QWs by considering the oscillator strength of excitons, thermal effects, and carrier redistribution in energy states has not been reported in the literature. Furthermore, in spite of having an extensive amount of research, estimation of defect-density in ultra-low disordered systems remains a challenge for most of the presently available destructive/non-destructive techniques.[168]

In the first part of this chapter, the impact of the magnetic field on optical properties of free and disorder-bound-excitons is investigated at low-temperature. A simple model of magneto-excitons is developed to estimate the defect density in QWs by magneto-PL spectroscopy. Thereafter, to probe the thermal effects on magneto-excitons, quasi-simultaneous measurements of magneto-PL and magneto-SPV are performed at 100 K. The role of the magnetic field on radiative and non-radiative processes is discussed by correlating the experimental results with a rate equation model by considering the thermal effects.

## 4.2 Experimental procedure

The growth conditions and structural details of the GaAs MQW sample that is used for this study can be found in Chapter 3. Magneto-PL and magneto-SPV measurements are performed inside LHe Dewar of the thermostat, where laser light of wavelength 532 nm excites the electrons in the QW and barrier layers. The PL and SPV measurements are quasi-simultaneously performed by the optical-fiber based setup: PL spectra is recorded when a semi-transparent ITO-plate is already kept on the sample. This ITO plate senses the change in surface band-bending under the light illumination. Therefore, the sample stage and experimental arrangements remain identical during

the two-measurements. Details of the experimental setup to record magneto-PL and magneto-SPV measurements can be found in Chapters 2 and 3.

### 4.3 Magneto-excitons in semiconductor QWs at a low-temperature

Figure 4.1 shows the magneto-PL spectra of the MQW sample at 4.2 K. It is observed that the PL spectra at a low-temperature are predominantly asymmetric, where the asymmetry in line-shape decreases under a high magnetic field (Fig. 4.1). In order to estimate the variation of BX and FX transitions with increasing the magnetic field, PL line-shapes are fitted by Gaussian ( $P_1$ ) along with Lorentz ( $P_2$ ) functions. Figure 4.2 shows the PL line-shape fitting to de-convolute BX ( $P_2$ ) and FX ( $P_1$ ) transitions in the magneto-PL spectra of QW-1. Subsequently, the intensity of  $P_2$  and  $P_1$  as a function of the magnetic field is normalized by the zero-field total PL intensity ( $P_1+P_2$ ) and then plotted in Figs. 4.3a and 4.3b. The normalized PL intensity related to BX and FX transitions is denoted by  $\eta_2$  and  $\eta_1$ , respectively.

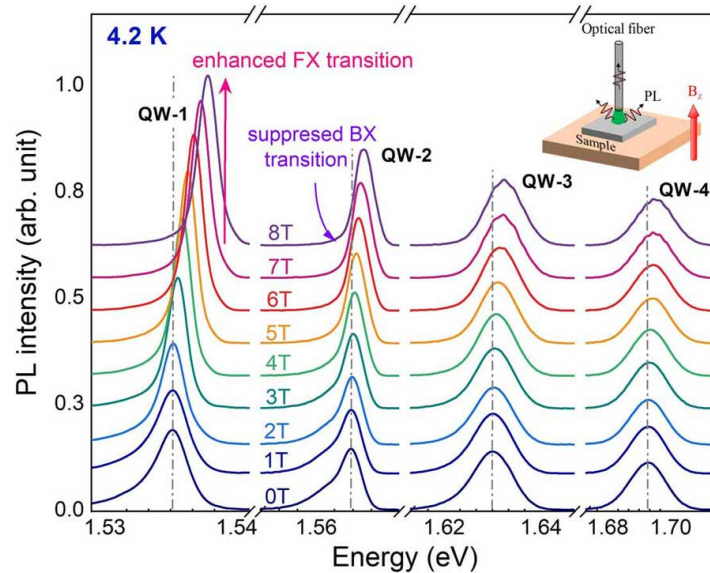


Figure 4.1: 4.2 K magneto-PL spectra under a magnetic field perpendicular to the QW plane.

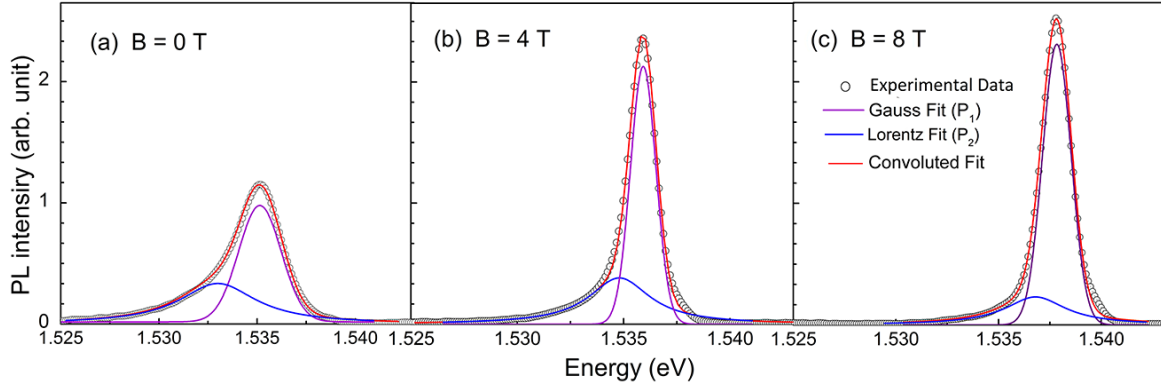


Figure 4.2: Magneto-PL lineshape fitting by Gaussian with Lorentz functions to decouple FX and BX transitions in the case of QW-1.

#### 4.3.1 Quantitative estimation of point defects in QWs

It is observed that the magnitude of  $\eta_2$  significantly decreases with the strength of a magnetic field (Fig. 4.2a). Such an observation can be explained by the magnetic field-driven spatial confinement of excitons in a smaller region of space. Under this condition, excitons in the QW experience a less number of point defects ( $\delta_2$ ), which is schematically illustrated in Fig. 4.3c. In addition to this, the PL intensity of the BX transition depends on the radiative recombination time of FX ( $\tau_r$ ) and time required to capture a free-exciton into defect states ( $\tau_c$ ).<sup>[118]</sup>

$$\eta_2 = \kappa \delta_2 \langle \Omega \rangle \times \zeta = \kappa \delta_2 \times \left[ \frac{4}{3} \pi \langle r_z \rangle \langle r_{x,y} \rangle^2 \right] \times \frac{\tau_r}{\tau_c} \quad (4.1)$$

Here,  $\langle \Omega \rangle$  represents the spatial extent of excitons, which is given by  $(4\pi/3) \times \langle r_{x,y} \rangle^2 \langle r_z \rangle$ . The symbol  $\kappa$  signifies the fraction of point defects, which is involved in the radiative recombination process ( $\kappa \leq 1$ ). In the present analysis, the numerical value of  $\kappa$  is considered as unity, since the radiatively active defects are mainly contributing to the BX transition. The symbol  $\zeta$  signifies the probability of free exciton capture into the defect states (FX to BX formation), which is expressed by the ratio of  $\tau_r$  and  $\tau_c$ . For example, a higher value of  $\tau_r/\tau_c$  for a given system suggests that excitons are more susceptible to be recombined via defect states rather than the FX transition, i.e.,  $\eta_2$  increases while decreasing the  $\eta_1$ . Note that the localization of charges at the hetero-



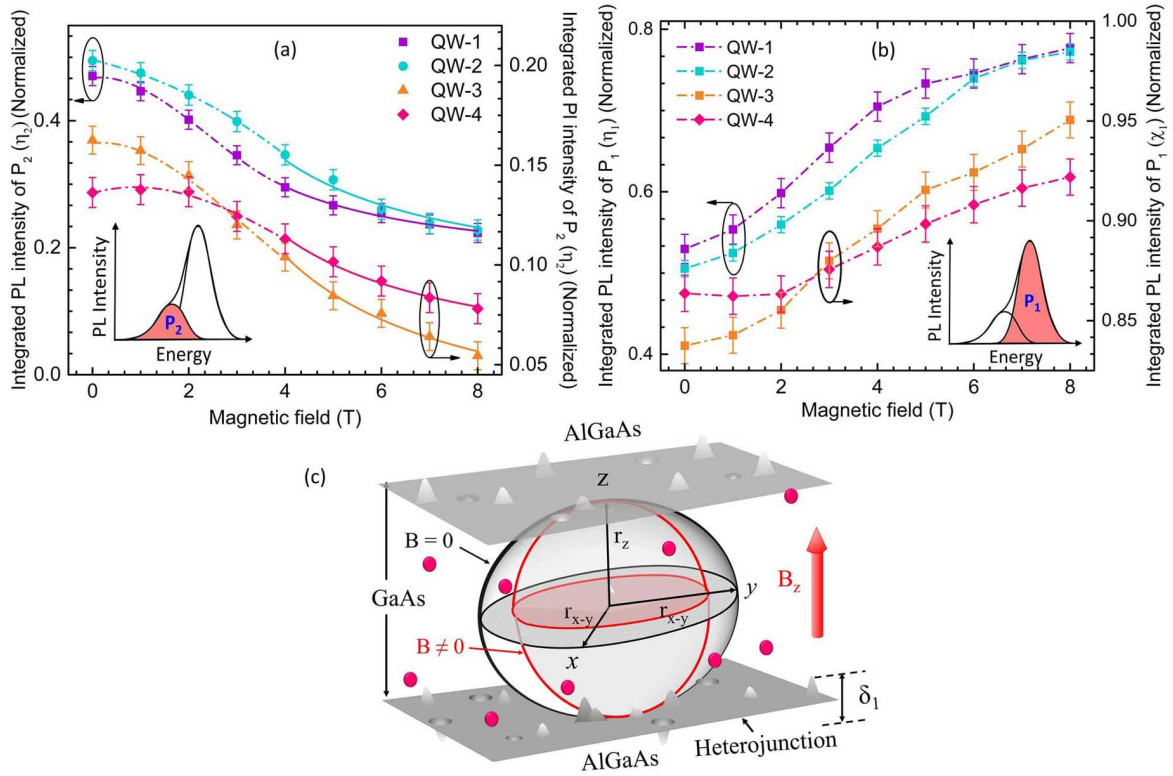


Figure 4.3: Integrated PL intensity of (a)  $P_2$  and (b)  $P_1$  peaks plotted as a function of a magnetic field, and (c) schematic illustration of excitonic confinement by an applied magnetic field, where the number of in-plane defects (red dots) experienced by excitons decrease under a high field.

interfaces of the QW (along the z-direction) is not considerably influenced under this in-plane confinement of excitons by  $B_z$  (Fig. 4.3c).[158] According to the literature reports,  $\tau_r$  and  $\tau_c$  in the case of a GaAs QW are found to be  $\sim 350$  and  $\sim 20$  ps.[169, 170, 171] On the other hand, the exciton Bohr radius in a high field regime can be approximated by,[52]

$$\langle r_{x,y} \rangle = (2j + 1)^{1/2} \xi = (2j + 1)^{1/2} \times \sqrt{\frac{\hbar}{eB}} \quad (4.2)$$

Therefore, Eq. (4.1) and (4.2) can be used to express the defect density as a function of  $\eta_2$ .

$$\eta_2 = \zeta \times \frac{2\kappa\hbar\langle r_z \rangle}{3e} \times \frac{1}{B} \times \delta_2 \quad (4.3)$$

Equation 4.3 shows that the intensity of bound exciton PL decreases with the strength of a magnetic field. The carriers in the QW being confined along the growth direction,

Table 4.1: The spatial extent of electron and hole wave functions along the z-direction and the estimated defect density in four QWs are tabulated.

$l_w$ (Å)	$l_w^*$ (Å)	$\delta_2$ $\times 10^{15}(\text{cm}^{-3})$
190	190	1.2
100	104	3.2
50	64	2.5
30	52	2.3

exciton Bohr radius in the confinement direction ( $r_z$ ) can be approximated by the effective QW thickness,  $2\langle r_z \rangle \approx l_w^*$  (where,  $l_w^* \geq l_w$ ). The numerical value of  $l_w^*$  for a given thickness of QW is estimated by solving the Schrödinger equation, Fig. 3.6 (Table 4.1), which is found to be in good agreement with the effective QW thickness estimated by Eq. 1.11.[42] Thereafter,  $\eta_2(B)$  in the range of 4 - 8 T is fitted by Eq. (4.3) to estimate  $\delta_2$  (Fig. 4.3a), which is summarized in Table 4.1. Since the QWs are grown under identical conditions, the variation in  $\delta_2$  for the four QWs can be understood by the error in the estimated parameter. In summary, a magnetic perturbation in a given plane can be utilized for surmounting the impact of defects on the optical processes in QWs. Moreover, magneto-PL spectroscopy is found to be an efficient tool to determine the point defect density in an ultra-low disordered system in a truly non-invasive manner.

#### 4.3.2 Impact of magnetic field on free-exciton recombination

On the other hand, the Coulomb interaction between two oppositely charged particles increases when excitons are confinement in the x-y plane, which increases the PL intensity related to FX transition (Fig. 4.3b).[158] In addition to this, carriers occupied in an excited state may relax to its lower Landau states under a high magnetic field. This is because, the degeneracy of Landau state increases with the strength of a magnetic field,  $N(\text{Landau state}) = 1/2\pi\xi^2 = eB/h$ , [52] and therefore, a large number of carriers can be accommodated in the ground Landau state under a high field. In a steady-state condition, electrons occupied in  $j^{\text{th}}$  Landau state is expressed by,

$$n_j = \frac{eB}{h} \int \frac{\delta^D[\varepsilon, \varepsilon_c + \varepsilon_e + (j + \frac{1}{2})\hbar\omega]}{1 + \exp\left(\frac{\varepsilon - \varepsilon_{fn}}{k_B T}\right)} d\varepsilon \quad (4.4)$$

where,  $\varepsilon_{fn}$  is the quasi-Fermi energy in the presence of  $n^*$  excess electrons in the QW. The symbol  $\delta^D(\varepsilon, \varepsilon_c + \varepsilon_e + (j + 1/2)\hbar\omega)$  signifies the Dirac delta distribution of Landau states. Such an approximation would be appropriate to study the integrated PL intensity in the case of a high-quality quantum structure with isolated Landau transitions. However, the impact of the magnetic field on the line-shape of PL spectra can be analyzed by considering the Gaussian or Lorentz distribution of Landau states.[172] Under that condition, PL linewidth would be governed by the broadening of Landau states ( $\Gamma$ ), which may also depend on  $B$ . [173, 172, 174] Additionally, the magnitude of  $\tau_r$  can vary with the magnetic perturbation, which will be discussed in the next section of this chapter.

Let,  $n_j$  be the carrier density in  $j^{th}$  energy state and  $\nu_j$  is the filling ratio of energy state,  $0 \leq \nu_j \leq 1$ . The selection rule associated with the inter-Landau state transition is  $\Delta j = \pm 1$ , [175] and the rate equations are expressed by, [91, 176, 177, 109]

$$\frac{dn_k}{dt} = G_E - (1 - \nu_{k-1})\frac{n_k}{\tau_0} - \frac{n_k}{\tau_r} \quad (4.5a)$$

$$\frac{dn_j}{dt} = (1 - \nu_j)\frac{n_{j-1}}{\tau_0} - (1 - \nu_{j-1})\frac{n_j}{\tau_0} - \frac{n_j}{\tau_r} \quad (4.5b)$$

$$\frac{dn_0}{dt} = (1 - \nu_0)\frac{n_1}{\tau_0} - \frac{n_0}{\tau_r} \quad (4.5c)$$

Here, the symbol  $k$  represents the highest Landau state that is occupied by charge carriers, and  $G_E$  denotes the electron-hole pair generation rate. To understand the carrier re-distribution among Landau states, Eqs. (4.5) are numerically solved for three different  $G_E$  values (Fig. 4.4). The  $\tau_r$  and  $\tau_0$  for this analysis is taken as 350 and 10 ps, respectively.[178] In this calculation, the numerical value of  $\tau_0$  and  $\tau_r$  are considered to be constant, as the existing reports showing the variation of  $\tau_0$  and  $\tau_r$  as a function of  $B$  is found to be inconsistent (often decreasing, increasing, or oscillatory)<sup>1</sup>. [179, 180, 181, 182] Figure 4.4b shows that, at a low excitation power, charge carriers are predominantly

---

<sup>1</sup>An analytical relation to consider magnetic field-driven variation in  $\tau_r$  is derived in the later part of this chapter, which is experimentally verified by modeling the PL intensity of magneto-excitons in Chapter 5.

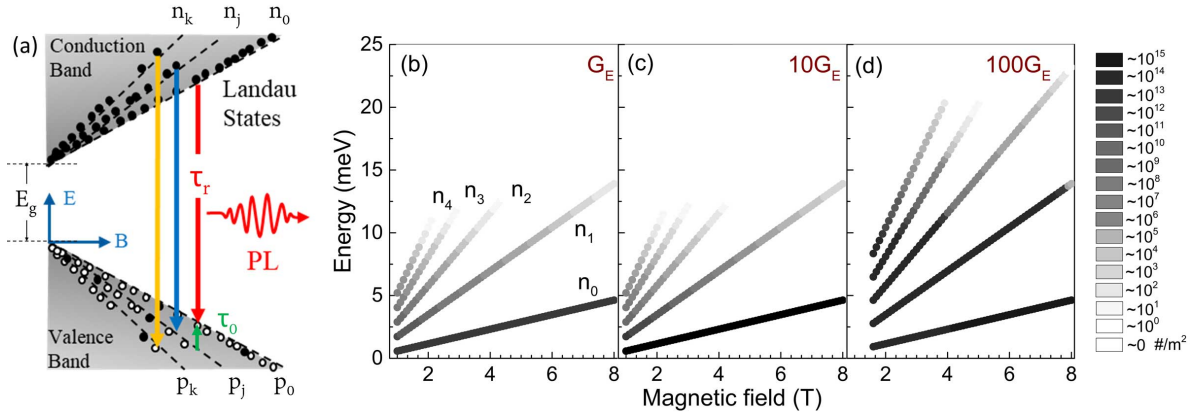


Figure 4.4: (a) Formation of Landau states, inter-subband relaxation and inter-band radiative recombination of charge carriers are schematically illustrated. The carrier occupancy in Landau states with increasing the magnetic field is numerically estimated for three different electron-hole pair generation rates (b)  $G_E$ , (c)  $10G_E$ , and (d)  $100G_E$ .

occupied in the ground state when  $\tau_0 \ll \tau_r$ . [183, 184] In this case, the carrier density in an excited state becomes feeble, i.e.,  $n_1, n_2$ , etc.  $\rightarrow 0$ ; the contribution of excited states in PL spectra is negligible. Under this limiting condition, PL intensity of FX transition can be approximated by  $I \propto R_r \approx n^*/\tau_r$  when all the photo-excited carriers ( $n^*$ ) are accommodated in the ground energy state. [176] In our experiment, the magnitude of  $p_{exc}$  is kept at low-level, and therefore, distinct PL features related to a higher Landau state is not observed. Therefore, the observed 1.3 - 2 times increase in FX PL ( $\eta_1$ ) under 0 - 8 T (Fig. 4.3b) can be correlated with a decrease in  $\tau_r$  of a similar order. Figure 4.4d also shows that, under a high-power excitation, carrier occupancy in excited Landau states can be significant even at the 8 T field. In that case, the recombination of excitons via higher Landau states can be probed by magneto-PL spectroscopy, and their contribution to the PL signal would be decreasing at a high field, Fig. 4.4d. In summary, a significant number of charge carriers from an excited state relax to the ground Landau state under a strong magnetic field, where the recombination time of excitons may also decrease by the magnetic confinement. Nonetheless, when the carrier density in excited states is feeble, the magnetic field-driven enhancement in PL signal can be correlated with the decrease in recombination time of magneto-excitons.

## 4.4 Electro-optical properties of thermally activated magneto-excitons

In Section 4.3, low-temperature (4.2 K) magneto-PL spectroscopy has been performed on GaAs QWs, and the magnetic field-driven enhancement (suppression) of FX (BX) transition is explained. At this low-temperature, PL spectra related to the light hole transition could not be probed. Moreover, with an increase in temperature, electron and hole are thermally excited to a higher energy subband, which may also escape from QWs. To realize the impact of magnetic field on recombination and carrier redistribution processes of thermally activated charge carriers, magneto-PL and magneto-SPV measurements are quasi-simultaneously performed on the same MQW sample at 100 K. The experimental setup for this measurement is schematically depicted in Fig. 4.5. The temperature of this study is ascertained from where both the PL and SPV measurements can probe HH and LH transitions of the QWs. This is because the carrier occupancy in excited states increases due to the thermal excitation of charge carriers, and therefore PL feature related to light hole transition is observed at 100 K. The thermal energy of carriers at this 100 K (8.6 meV) becomes close to the exciton binding energy of the GaAs QWs.[185, 158] Notably, even at 100 K, the HH and LH transitions in PL spectra are found to be in excitonic nature. This is con-

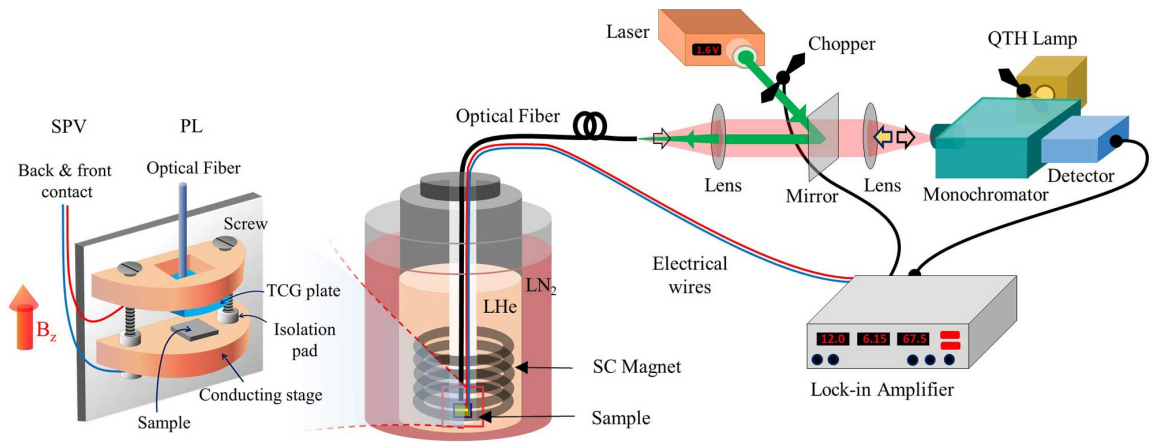


Figure 4.5: Schematic of the experimental setup for the simultaneous measurement of magneto-PL and magneto-SPV.

firmed by excitation power ( $p_{exc}$ ) dependent PL measurements, where the PL intensity linearly varies with an enhancement of  $p_{exc}$ . Therefore, excitons in QWs are influenced by two-competitive processes, (1) thermal energy of carriers or built-in electric field in the sample causes reduction of PL intensity, and 2) Coulomb interaction between two oppositely charged particles decreases  $\tau_r$  and enhances the PL signal.

#### 4.4.1 Magneto-PL at 100 K

Figure 4.6 shows the magneto-PL spectra at 100 K, and the results obtained by a detailed analysis are shown in Fig. 4.7. It is observed that the enhancement of HH PL intensity by the applied magnetic field is feeble at 100 K than that of the 4.2 K measurement (Fig. 4.7). Nevertheless, the HH PL signal corresponding to the QW-4 gradually decreases under a strong magnetic field at this 100 K (Fig. 4.7d). The magnetic field-assisted reduction of PL intensity for a narrow QW was not observed during 4.2 K (Fig. 4.7d),[166] which is also not reported in the literature. The observed variation in HH and LH PL with increasing the magnetic field can be explained by rate equations of energy states. The  $\tau_r$ , which is related to the overlap of electron-hole pairs

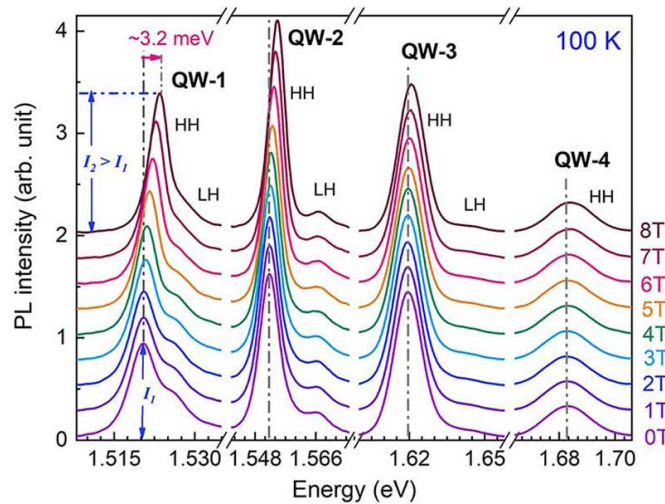


Figure 4.6: Magneto-PL spectra of the MQW sample at 100 K. An enhancement of the HH PL signal is observed for QW-1, where the asymmetry in the PL peak remains invariant under the magnetic perturbation.



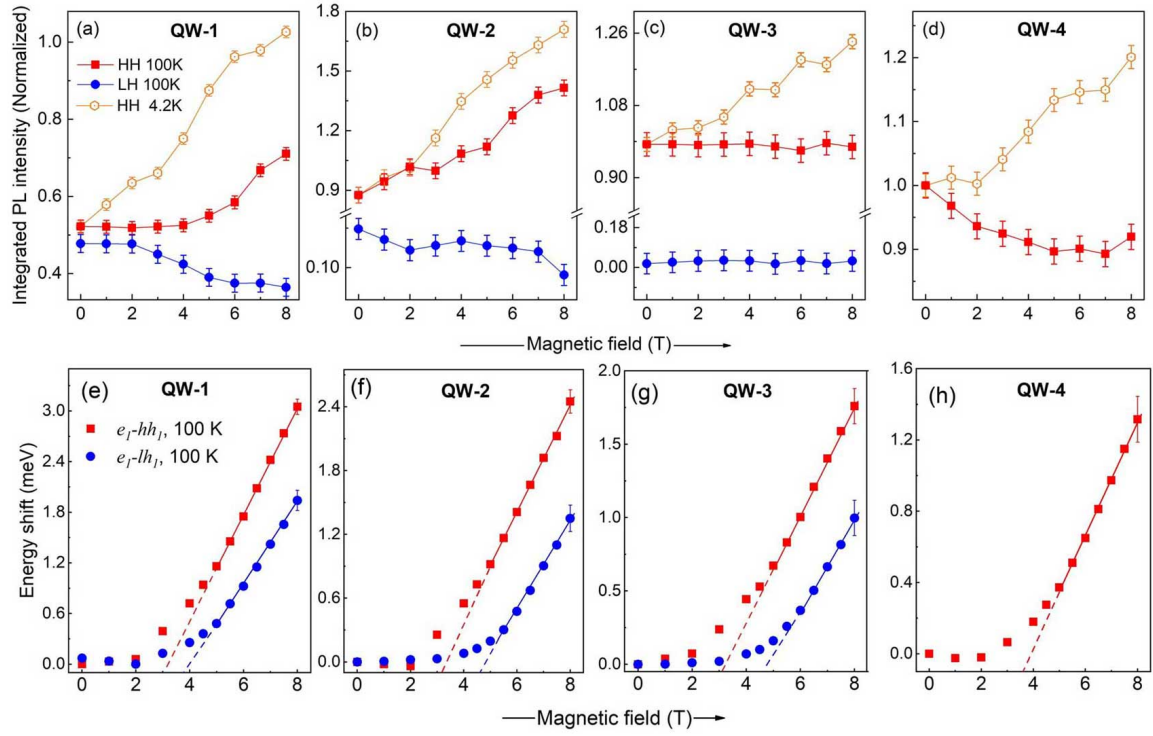


Figure 4.7: PL intensity of HH and LH transitions at 100 K as a function of the magnetic field for (a) QW-1, (b) QW-2, (c) QW-3, and (d) QW-4. The variation of HH PL intensity with the external magnetic field at 4.2 K is also shown. The diamagnetic blue-shift of HH and LH transitions for the four QWs at 100 K is plotted (e-h).

(i.e., oscillator strength  $\varrho$ ) is in-general expressed by the following relation,[186, 61]

$$\tau_r = \frac{2\pi\epsilon_0\mu^*c^3}{n_r^*e^2\omega^2\varrho} \quad (4.6)$$

where the refractive index of the medium is denoted by  $n_r^*$ , and the oscillator strength of excitons is described by,  $\varrho \propto (a^3/r_{x,y}^2r_z)$ . [186] Further, the in-plane exciton radius in high field regime can be expressed by Eq. 4.2, and the out-of-plane radius can be approximated by  $2r_z \approx l_w^*$ . [42] With these approximations, Eq. 4.6 can be expressed by,

$$\tau_r(B) \sim \frac{\pi\epsilon_0\mu^*c^3}{2n_r^*e^2\omega^2} \times \frac{l_w^*\hbar}{a^3eB} \quad (4.7)$$

Therefore, recombination time in a high magnetic field regime decreases with the strength of the external field.

Note that the barrier height for heavy and light holes in GaAs QWs is smaller than

the barrier height for electrons in the conduction band.[187] Therefore, a large number of holes overcome the barrier potential at 100 K as compared to the escape of electrons from the QW. Because of this, the rate equation analysis of holes would be important in the present investigation than the dynamics of electrons in the conduction band. Considering the Gaussian broadening of Landau states, Eq. 4.4 is used to express hole occupancy in the ground Landau state.[166]

$$p_h(B) = \frac{eB}{h} \frac{1}{\sqrt{2\pi}\Gamma^2} \int \frac{\exp[-\{\varepsilon - (\varepsilon_v + \varepsilon_h + \frac{1}{2}\hbar\omega_h)\}^2/\Gamma^2]}{1 + \exp[-(\varepsilon - \varepsilon_{fp})/k_B T]} d\varepsilon \quad (4.8)$$

where the quasi-Fermi energy of holes is denoted by  $\varepsilon_{fp}$ . At higher temperature, the rate of escape of holes from the QW can be expressed by,  $R_{esc} \sim e^{-\varepsilon_{esc}/k_B T}$ . [188, 189, 190] Under such circumstances, the rate equations of heavy and light hole transitions are expressed by,[166, 188]

$$\left| \frac{dp_{lh}}{dt} \right|_{B,T} = G_E - (1 - \nu_{hh}) \frac{p_{lh}}{\tau_0} - \frac{p_{lh}}{\tau_r(B)} + U \left[ p_{hh}(1 - \nu_{lh}) e^{-|\varepsilon_{lh} - \varepsilon_{hh}|/k_B T} - p_{lh} e^{-\varepsilon_{esc}^{lh}/k_B T} \right] = 0 \quad (4.9a)$$

$$\left| \frac{dp_{hh}}{dt} \right|_{B,T} = (1 - \nu_{hh}) \frac{p_{lh}}{\tau_0} - \frac{p_{hh}}{\tau_r(B)} - U \left[ p_{hh}(1 - \nu_{lh}) e^{-|\varepsilon_{lh} - \varepsilon_{hh}|/k_B T} + p_{hh} e^{-\varepsilon_{esc}^{hh}/k_B T} \right] = 0 \quad (4.9b)$$

Here,  $G_E$  is contributed by the photo-excited electron-hole pairs and carrier accumulation due to the thermal activation of defect states. However, at a given temperature and excitation power,  $G_E$  can be considered to be invariant with an increase in the magnetic field. Symbol  $U$  represent the rate of thermal excitation of holes and  $\nu_{hh}$  ( $\nu_{lh}$ ) is the occupation probability of charge carriers in heavy (light) hole band. In Eq. 4.9, inter-subband excitation and thermal escape of holes are considered by the terms inside the square brackets. The quantities,  $(\varepsilon_{lh} - \varepsilon_{hh})$  and  $\varepsilon_{esc}^h [= eV_z(h) - \varepsilon_h - \hbar eB/2m_{QW}^* + \hbar eB/2m_{barrier}^*]$  represent the inter-subband energy gap and activation energy required to escape a hole from the QW, respectively. With increasing the magnetic field, energy eigenstates of the QW shift towards the high energy, and



therefore, the barrier height to confine carriers in the QW decreases. As a result of magnetic field-driven lowering in barrier height, the carrier escape probability further rises. Notably, a small fraction of charge carriers that are escaped from a QW may drift or diffuse 980 Å thick AlGaAs layer (the barrier between two QWs) to be captured by another QW in the sample. However, the number of charge carriers that are accumulated due to this re-capture process would be negligible as compared to the photo-generated electron-hole pairs. Therefore, the contribution of carrier re-capture on the PL intensity is not considered in this investigation.

Now, Eq. 4.9 is numerically solved to deduce the recombination rate of heavy and light holes in QW-1 and 4 under the magnetic field up to 8 T. In this analysis,  $\varepsilon_{esc}^h$  for heavy and light holes in the absence of a magnetic field is computed by solving the Schrödinger equation, which is estimated to be  $\varepsilon_{esc}^{hh}(\text{QW-1}) = 163.4$  meV,  $\varepsilon_{esc}^{lh}(\text{QW-1}) = 157.7$  meV,  $\varepsilon_{esc}^{hh}(\text{QW-4}) = 118.6$  meV and  $\varepsilon_{esc}^{lh}(\text{QW-4}) = 74.7$  meV. For this analysis, effective mass of heavy and light holes in GaAs and  $\text{Al}_{0.28}\text{Ga}_{0.72}\text{As}$  layers is acquired from the standard literature reports.[140, 21] The thermal escape time of holes is considered as 1 ms and values of  $\tau_r(0)$  for QW-1 and 4 is acquired from the published reports.[61, 191]. The results obtained by this analysis (Fig. 4.8a) show that the recombination rate of heavy holes for QW-1 ( $R_r^{hh}$ ) increases with the magnetic field (Fig. 4.8a). Under this condition, recombination of light holes ( $R_r^{lh}$ ) decreases under a high field. It is also observed that the magnitude of  $R_{esc}$  for QW-1 is feeble, which is not influenced by the magnetic perturbation (Fig. 4.8a). In the case of QW-4, a gradual decrease in  $R_r^{hh}$  and enhancement of  $R_{esc}$  with the strength of a magnetic field is estimated. With a significant number of light holes escaped from the narrow QW,  $R_r^{lh}$  is found to be feeble for QW-4 (Fig. 4.8b), and the corresponding PL transition could not be recorded at 100 K (Fig. 4.1).

Magnetic field-driven electro-optical processes in two QWs are schematically illustrated in Figs. 4.8c and 4.8d. With increasing the magnetic field, the recombination time of excitons decreases, and a significant number of carriers in a thick QW relax to the ground energy state (Fig. 4.8c). As a result of this, the PL intensity of the heavy

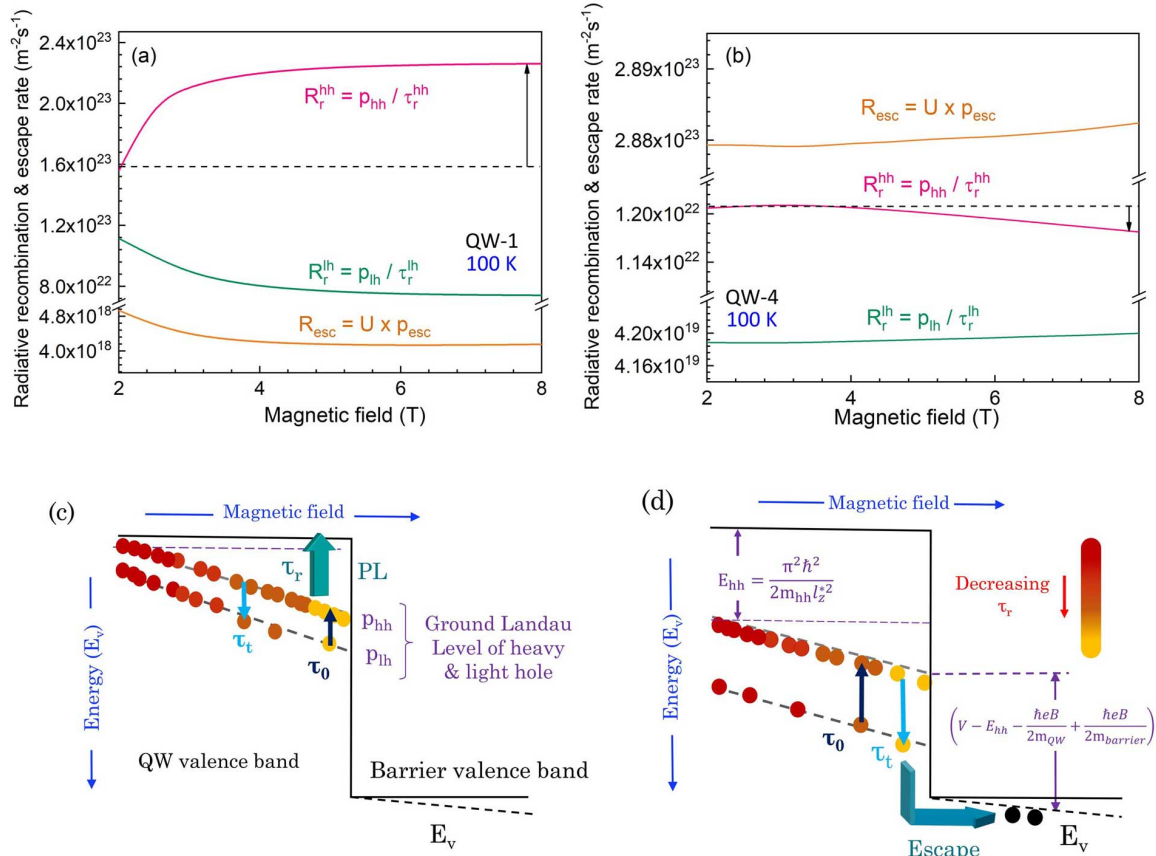


Figure 4.8: The rate of radiative recombination of heavy and light holes, and carrier escape from QWs are estimated by solving Eq. 4.9 for (a) QW-1 and (b) QW-4. The  $G_E$  for this analysis is considered as  $3 \times 10^{23} \text{ m}^{-2}\text{s}^{-1}$ . The results obtained by this calculation are schematically described for a (c) thick and (d) narrow QW.

hole transition increases under a high magnetic field. On the other hand, carriers that are confined in a narrow QW are bound by a lower barrier potential, and hence the thermal escape probability is already very high for QW-4 (Fig. 4.8d). In addition to this, the magnetic field provides an additional amount of energy ( $\sim \hbar\omega/2$ ) to the holes, which reduces the barrier height of the QW (Fig. 4.8d). This is the prime reason to observe the magnetic field-assisted reduction in PL signal in the case of QW-4 at elevated temperature. Therefore, the results obtained by the rate equation analysis (Figs. 4.8a and 4.8b) explain the enhancement or reduction of PL intensity as a function of the magnetic field (Fig. 4.6). Nevertheless, a quantitative comparison of experimental results with the rate equation solution requires an exact knowledge of  $G_E$ ,  $\tau_r$ , and  $U$  for the QWs.

Note that the contribution of the Auger recombination would be important in the above rate equation analysis for a higher injection of charge carriers,  $n^* \gtrsim 10^{19} \text{ cm}^{-3}$  (e.g., in diode lasers).[192] Under that condition, one may have to consider the Auger process in Eq. 4.9,  $R_{\text{auger}} \sim C_A \times n^3$ , where  $C_A$  denotes the Auger coefficient.[193] In the present analysis, the impact of the Auger process is not considered because magneto-PL measurements are performed under a low-power laser illumination on undoped QWs. Furthermore, the rate equations and subsequent analysis to realize carrier recombination and escape are understood for a steady-state condition, when electron and hole are thermalized. This is because the inter-sub-band relaxation of holes ( $\tau_0^h \lesssim \text{ps}$ )[194] is much faster than the radiative recombination of excitons ( $\tau_r \lesssim \text{ns}$ )[100, 191]. In view of this, the difference in the thermalization rate of electron and holes, and its impact on the PL intensity is also not considered.

Careful observation in Fig. 4.6 shows that the asymmetry in PL line-shape, associated with BX transition, remains unaffected under the magnetic field at 100 K, which was suppressed during 4.2 K measurements (see, Figs. 4.1 and 4.6). In general, the PL intensity related to the BX feature depends on the capture of charge carriers from band to defect states, which is expressed by  $\zeta \sim \tau_r/\tau_c$ .[166] Therefore, the existing BX feature at 100 K suggests that  $\tau_r/\tau_c$  ratio is not affected even under the magnetic field up to 8 T when carriers in a QW possess sufficient thermal energy to surmount the fluctuating potential of disorders.

#### 4.4.2 Magneto-SPV at 100 K

Further understanding of the magnetic field induced non-radiative processes is developed by magneto-SPV spectroscopy (Fig. 4.9a), quasi-simultaneously performed during PL measurements at 100 K. Using Fig. 4.9a, the SPV amplitude (maxima) related to HH and LH transitions as a function of the magnetic field is plotted in Fig. 4.10a. According to the previous report, processes that are responsible for the generation of SPV are discussed in Chapter 3,[122] which are schematically depicted in Fig. 4.9b).

In the MQW sample, electron and hole in a thick QW are confined by large barrier

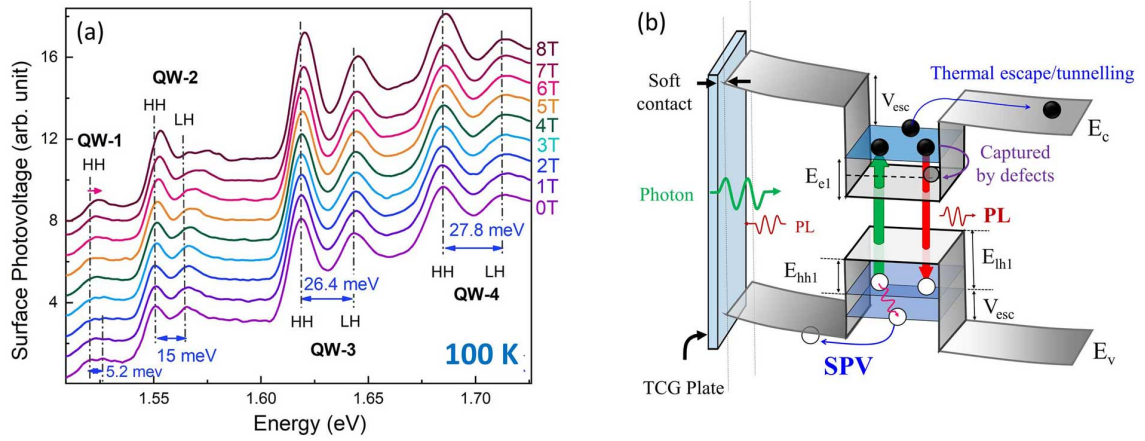


Figure 4.9: (a) Magneto-SPV spectra of the MQW sample at 100 K. The energy separation between HH and LH transitions is indicated for the QWs. (b) Fundamental processes that are responsible for the generation of SPV are schematically shown.

potential. Therefore, the probability of thermal escape is feeble for QW-1 and 2, even at 100 K. Under this condition, the SPV signal is predominately contributed by the interface-defect assisted charge separation within the QW. The SPV amplitude governed by the separation of charges within the QW generally increases with rising the carrier density in the respective energy state.[31] Note that, although the carrier occupancy in the heavy hole state of QW-1 and 2 increases at a high magnetic field (Fig. 4.8), the HH SPV of QW-1 remains invariant under a magnetic perturbation (Fig. 4.10a). This is because most of the carriers, which are relaxed from a higher energy subband at a strong magnetic field, are recombined radiatively. Hence, in QW-1, radiative recombination is a favorable process than charge separation. This also indicates that the separation of charges in a QW is a slow process as compared to the excitonic recombination, which is already confirmed by the chopping frequency-dependent SPV measurements in Chapter 3.

On the contrary, since the confinement potential due to the barrier is small for a narrow QW, a considerable number of carriers may thermally escape from QW-2 and 3. The charge carriers, thereafter, drift in AlGaAs barriers to generate a strong SPV signal. Moreover, the barrier potential height further decreases due to the Landau-diamagnetic shift of energy states, and hence the carrier escape probability from the QW increases. As a result of this, the SPV amplitude related to QW-2 and 3 increases

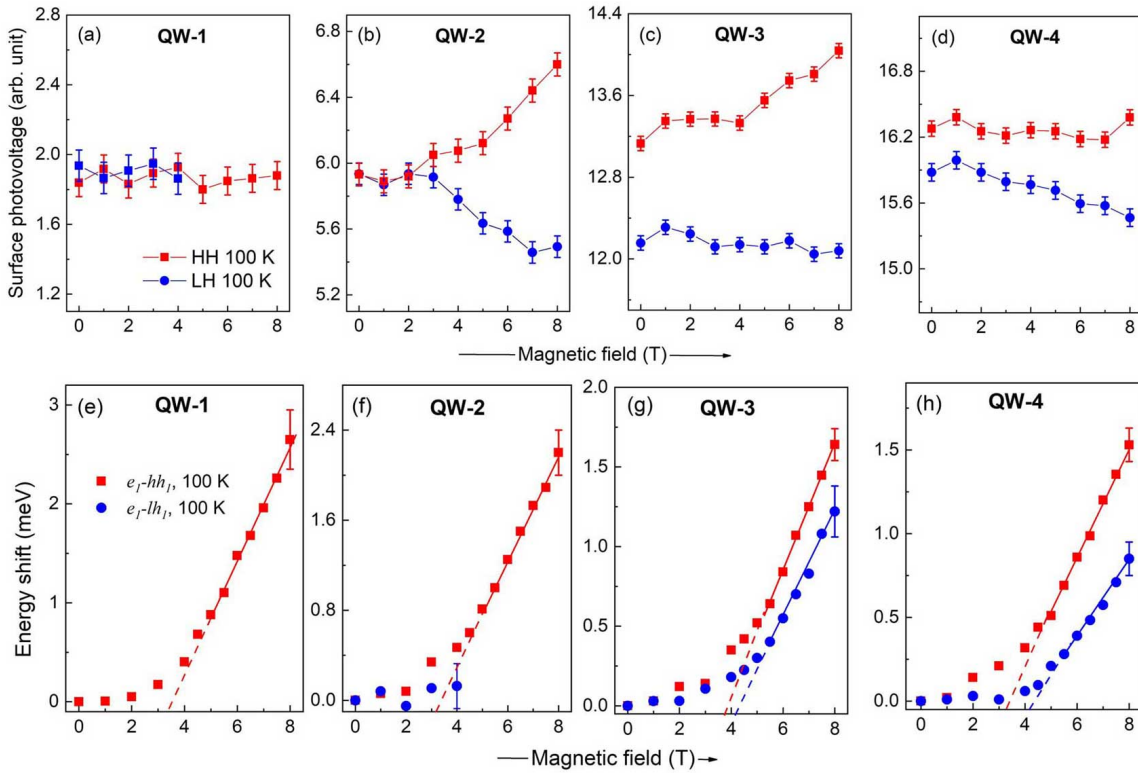


Figure 4.10: SPV amplitude at 100 K is plotted as a function of the magnetic field for (a) QW-1, (b) QW-2, (c) QW-3, and (d) QW-4. Diamagnetic blue-shift of HH and LH transitions are also plotted as a function of field (e-f).

with the magnetic field strength. Nonetheless, in the case of a very thin QW, i.e., QW-4, a significant number of charge carriers are already escaped from the QW due to the thermal energy. Under this condition, the impact of magnetic field on the carrier escape process and SPV signal are not distinctly observed for QW-4.

#### 4.4.3 Effective mass of heavy and light hole excitons

The diamagnetic shift of heavy and light hole transitions for the QWs, probed by magneto-PL and magneto-SPV spectroscopy, is plotted in Figs. 4.7(e-h) and 4.10(e-h). It is observed that the amount of Landau-diamagnetic energy under the magnetic field up to 8 T is slightly higher at 100 K than that of the 4.2 K measurements (Fig. 4.1 and 4.6). This is consistent with the existing literature reports, where a decrease in  $m^*$  at relatively high temperature is reported by many authors.[195] Figures 4.7(e-h) & 4.10(e-h) show that the blue-shift of energy states exhibits a linear magnetic field dependence under  $B \geq 5$  T, which is used to estimate heavy ( $\mu_{hh}^*$ ) and light hole exciton

Table 4.2: The reduced mass of heavy and light hole excitons estimated by magneto-PL and magneto-SPV spectra at 100 K.

	$l_w$ (Å)	$\mu_{hh}^* \pm \text{error}$ ( $\times m_0$ )	$\mu_{lh}^* \pm \text{error}$ ( $\times m_0$ )
Magneto PL	190	$0.094 \pm 0.005$	$0.11 \pm 0.01$
	100	$0.115 \pm 0.007$	$0.14 \pm 0.02$
	50	$0.163 \pm 0.008$	$0.17 \pm 0.02$
	30	$0.18 \pm 0.01$	-
Magneto SPV	190	$0.10 \pm 0.01$	-
	100	$0.12 \pm 0.01$	-
	50	$0.16 \pm 0.01$	$0.16 \pm 0.01$
	30	$0.18 \pm 0.01$	$0.24 \pm 0.02$

mass ( $\mu_{lh}^*$ ). [52, 158] The estimated effective mass (Table 4.2) by the two spectroscopic measurements (magneto-PL and magneto-SPV) is found to be in good agreement. Note that the estimation of  $\mu_{lh}^*$  is not possible for QW-4 by magneto-PL measurements due to the feeble LH PL signal. However, magneto-SPV measurements under this condition can be used to probe the excited states of a narrow QW, which is also feasible for a high-temperature measurement. On the contrary, absorption of the photon-based SPV technique is less-efficient in resolving the closely separated HH and LH transition (e.g., QW-1). Therefore, a quasi-simultaneous measurement of the two complementary techniques (magneto-PL and magneto-SPV) help in estimating both  $\mu_{hh}^*$  and  $\mu_{lh}^*$  for different thicknesses of QW.

It is found that the estimated  $\mu_{hh}^*$  and  $\mu_{lh}^*$  increases with decreasing the QW thickness. Moreover, for a given thickness of QW,  $\mu_{lh}^*$  is found to be higher than  $\mu_{hh}^*$ , i.e.,  $\mu_{lh}^* > \mu_{hh}^*$ . Such an observation of in-plane heavy and light hole mass reversal was experimentally observed by Hayne *et al.* for a 150 Å thick GaAs QW, [136] which can also be found in theoretical reports. [52, 196] The results obtained in the present study confirm that the in-plane mass reversal effect remains valid even for a narrow QW when carriers are significantly influenced by the non-parabolicity of band dispersion. In addition to this, the difference between  $\mu_{lh}^*$  and  $\mu_{hh}^*$  is found to be a minimum for QW-3. A similar anomalous trend can also be observed in the HH and LH transition energies. The SPV spectra (Fig. 4.9) shows that  $(\varepsilon_{LH} - \varepsilon_{HH})$  increases with a reduction

of QW thickness, for QW-1, 2, and 3. Nonetheless, a further increase in  $(\varepsilon_{LH} - \varepsilon_{HH})$  could not be observed for QW-4, where the separation between the two transitions is nearly the same for QW-3 and QW-4 ( $\approx 27$  meV, Fig. 4.9). Therefore, a high effective mass of heavy and light hole excitons and their transition energy can be explained by non-parabolicity of the conduction and light hole bands.

Furthermore, the impact of the magnetic field on the radiative recombination efficiency of negatively-charged excitons (i.e., trions) in GaAs/AlGaAs QWs is investigated by magneto-PL spectroscopy. A detailed discussion on magneto-PL spectroscopy of excitons and trions in a modulation-doped QW is presented in Appendix-A.

## 4.5 Conclusion

In summary, the impact of a magnetic field on the radiative recombination of free and bound-excitons is investigated by low-temperature magneto-PL measurements. It is found that the excitons in a QW experience less number of point defects under a magnetic field-driven spatial confinement of charge carriers, which eventually decreases the PL signal related to disorder bound exciton. A phenomenological model of magneto-excitons is proposed where the reduction in bound-exciton PL with increasing the magnetic field can be used to estimate disorder density. A comprehensive understanding of the recombination of magneto-excitons and inter-Landau state relaxation of carriers is developed by the rate equation analysis. Further, the impact of magnetic field on the electro-optical properties of thermally activated charge carriers is understood by simultaneous measurements of magneto-PL and magneto-SPV. In particular, emission-based PL spectroscopy helped in realizing the radiative recombination efficiency of thermally activated magneto-excitons. Under the same condition, carrier escape probability from QWs followed by the drift/diffusion of charges in barrier layers is probed by magneto-SPV measurements. It is found that although the recombination efficiency of excitons increases under a magnetic field, a significant number of carriers escape from a narrow QW due to the magnetic perturbation. Therefore, considering the

---

recombination, relaxation, thermal escape, drift, and diffusion processes, a minimum QW-width is suggested, which would be essential for the magnetic field-assisted advanced optical device operation. In conclusion, magneto-optical spectroscopy is proved to be a powerful non-invasive tool for investigating the quality of ultralow disordered systems and optoelectronic properties of magneto-excitons.



# Chapter 5

## Anisotropic properties of excitons and parallel magnetic field induced separation of charges

### 5.1 Introduction and background

In Chapter 4, the confinement of excitons by a magnetic field, and its impact on the radiative recombination and inter-subband relaxation processes are investigated. It is observed that a magnetic field perpendicular to the QW plane ( $B_z$ ) decreases the radiative recombination time of excitons. Even though the unique properties of magneto-excitons are beneficial for optical-emitters, a short decay time of charge carriers is detrimental for photovoltaic applications, transport-based devices, and quantum information processing.[197, 198, 199, 40] In a previous study, it has been reported that the tunneling of charges along the growth direction of a shallow QW [ $V_z(e, h) \lesssim 10$  meV] increases when a magnetic field is applied parallel to the QW plane ( $B_y$ ).[200] Therefore, the recombination time of excitons may increase due to this magnetic field driven charge separation process. Similarly, a parallel magnetic field-driven separation of electron and hole along the growth direction of coupled-QWs has been reported by Chang *et al.*[201] In this parallel field configuration, the diamagnetic energy of excitons is found to be feeble.[202] Recently, a phenomenological model of excitons under a parallel magnetic field is presented by Bodnar *et al.*[203] In their analysis, a significantly

high effective mass of exciton, estimated by the small diamagnetic energy, is explained by the total effective mass  $M^*$  (rather than  $\mu^*$ ). The feeble diamagnetic energy under  $B_y$ , [204, 205] and their explanation by  $M^*$  can also be found in Refs. [206, 201]. In addition to this, a parallel magnetic field-driven shift in band dispersion along the momentum space is reported by Butov *et al.* [206, 207]. From the theoretical perspective, here, the major complexities arise due to the breaking of cylindrical symmetry and coupling of  $eV_z(e, h)$  with the diamagnetic energy under  $B_y$ . [166, 208, 201] In particular, the role of  $V_z(e, h)$  and anisotropic effective mass of charge carrier have been neglected in almost all these previous reports. Besides the optical property, the magnetic behavior of excitons in a low-dimensional system is equally important for advanced optoelectronic devices. [209, 210, 211] A considerable amount of research has been performed to probe the paramagnetic and diamagnetic property of bulk-GaAs, with a variation in doping density ( $10^{15}$  -  $10^{18}$  cm $^{-3}$ ) and temperature (2 - 300 K). [212, 213, 209] It has been theoretically understood that the confinement of charge carriers in a quantum structure can control the magnetic behavior of excitons. [214, 215, 216] Nonetheless, an experimental study to probe the anisotropic magnetic property of charge carriers in a QW and its theoretical explanation could not be found in the literature.

With this in mind, an experimental study to investigate the anisotropic property of excitons in GaAs QWs is presented under perpendicular and parallel magnetic field configurations. The variation in diamagnetic energy for different thicknesses of QW is explained by a theoretical model considering the coupling of the quantum confinement and magnetic perturbation. The electro-optical processes induced by an external magnetic field with different orientations are probed by magneto-PL and magneto-photovoltage measurements. Furthermore, the magnetic behavior of charge carriers in GaAs QWs and their anisotropic variation is investigated by magnetization measurements. The experimental results obtained by magneto-PL, magneto-photovoltage, and magnetization measurements are explained by the same theoretical model, which is developed in this work.

## 5.2 Sample details and experimental procedure

For this study, three GaAs/AlGaAs QW samples ( $S_1$ ,  $S_2$  and  $S_3$ ) are grown by the MOVPE technique on  $n^+$  GaAs substrates. Sample  $S_1$  contains four GaAs QWs having the thicknesses of 190, 100, 50, and 30 Å. Sample  $S_2$  is embedded with a 48 Å thick single QW. In sample  $S_3$ , 50-periods of GaAs QWs are grown where the thickness of each QW is 75 Å that are separated by 210 Å thick AlGaAs barriers. The structural parameters of these three samples are summarized in Appendix-B. Magneto-PL measurements are performed on sample  $S_1$  in Faraday ( $B_z$ ) and Voigt configurations ( $B_y$ ) at 4.2 K. The sample inside a cylindrical bore of the LHe chamber is excited by laser light ( $\lambda = 532$  nm,  $p_{exc} = 0.5$  W/cm<sup>2</sup>) using an optical fiber-based setup. The design of the sample stages for magneto-PL spectroscopy in two configurations is depicted in Figs. 5.1a and 5.1b. Sample  $S_2$  is used for the simultaneous measurements of in-plane magneto-photovoltage (PV) and magneto-PL measurements at 4.2 K. Here, the sample is patterned in the form of parallel mesa structures (strips) by a photolithography technique, followed by chemical etching (using  $\text{CH}_3\text{OH} : \text{H}_3\text{PO}_4 : \text{H}_2\text{O}_2 = 6 : 3 : 1$ ). Au is evaporated on either side of the mesa-strips for contact formation and inter-connections. Magneto-PV measurements are performed by the same laser with  $p_{exc} \sim 0.010$  W/cm<sup>2</sup> at 67 Hz chopping frequency. Sample  $S_3$  is used for the magnetization measurements by Quantum Design: superconducting quantum interference device (SQUID).[217] The sample is mounted by transparent non-magnetic straws, where small pieces of straw

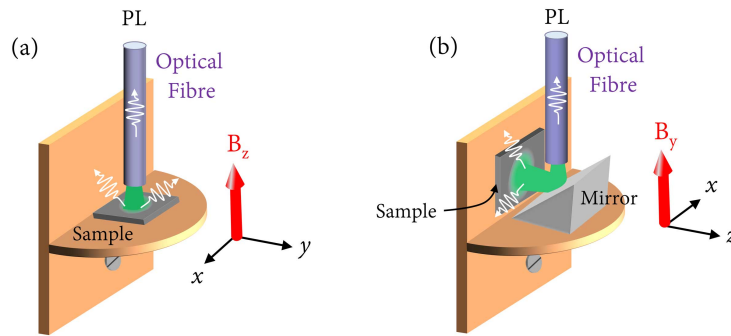


Figure 5.1: Schematic of the sample mounting stage design for magneto-PL measurements in (a) Faraday and (b) Voigt configurations.

are used for holding the sample in the desired plane.[209] To minimize the magnetic contribution from the 300  $\mu\text{m}$  thick GaAs substrate, the sample thickness is reduced to  $\sim 80 \mu\text{m}$  by back-side lapping and polishing method.

### 5.3 Theoretical background

Electro-optical property of magneto-excitons and magnetic behavior of charge carriers in a QW can be understood by the Schrödinger equation using a magnetic vector potential  $\mathbf{A}(\mathbf{r}) = -\frac{1}{2}[\mathbf{r} \times \mathbf{B}]$ .

$$\left[ \frac{(\mathbf{p}_e + e\mathbf{A}(\mathbf{r}))^2}{2m_e^*} + \frac{(\mathbf{p}_h - e\mathbf{A}(\mathbf{r}))^2}{2m_h^*} - \frac{e^2}{4\pi\epsilon_0\epsilon_r|r_b|} + eV_z(e, h) \right] \psi(r) = \varepsilon_{x,y,z} \psi(r) \quad (5.1)$$

Here, the effect of band-structure (for example, non-parabolicity of band and valence band mixing) is considered by the re-normalization of effective mass.[218, 26, 219] Thereafter, the impact of magnetic field on the center of mass (CM) motion and relative motion (RM) of charge carriers can be understood by the following transformations,[19]

$$\psi(R, r) = \exp\left(\frac{i}{\hbar}[\mathbf{P} - e\mathbf{A}(\mathbf{r})]\mathbf{R}\right) \Phi(r) \quad (5.2a)$$

$$\mathbf{R} = (m_e^*\mathbf{r}_e + m_h^*\mathbf{r}_h)/(m_e^* + m_h^*) \quad (5.2b)$$

$$\mathbf{P} = (\mathbf{p}_e - \mathbf{p}_h) \quad (5.2c)$$

where the position coordinate and momentum of excitons (i.e., carriers in CM frame) are denoted by  $\mathbf{R} = (m_e^*\mathbf{r}_e + m_h^*\mathbf{r}_h)/(m_e^* + m_h^*)$  and  $\mathbf{P} = (\mathbf{p}_e - \mathbf{p}_h)$ . Using Eqs. 5.2(a-c), the Schrödinger equation of excitons (Eq. 5.1) is expressed by,[52]

$$\left[ \frac{P^2}{2M^*} + \frac{p^2}{2\mu^*} + \frac{e^2 A(r)^2}{2\mu^*} - e \left( \frac{1}{m_e^*} - \frac{1}{m_h^*} \right) \mathbf{A}(\mathbf{r}) \cdot \mathbf{p} - \frac{2e}{M^*} \mathbf{A}(\mathbf{r}) \cdot \mathbf{P} - \frac{e^2}{4\pi\epsilon_0\epsilon_r|r_b|} + eV_z(e, h) \right] \Phi(r) = \varepsilon \Phi(r) \quad (5.3)$$

Equation 5.3 is a general expression and depending on the choice of  $\mathbf{A}(\mathbf{r})$ , this can be used to realize magneto-optical processes under perpendicular and parallel field configurations

### 5.3.1 Magnetic field perpendicular to the QW plane

In this configuration, charge carriers being confined in the x-y plane by  $B_z$ , interdependence of in-plane and out-of-plane exciton Bohr radius is expressed by,  $r_x = r_y \neq r_z$ . Therefore, the kinetic and potential energy terms in Eq. 5.3 can be described by cylindrical coordinate with symmetric vector potential,  $\mathbf{A}(\mathbf{r}) = 1/2[-yB_z, xB_z, 0]$ . Now, including the spin-splitting of energy states, the in-plane contribution of Eq. 5.3 becomes,

$$\left[ -\frac{\hbar^2}{2\mu_{x,y}^*} \left( \frac{\partial^2}{\partial \rho^2} + \frac{1}{\rho} \frac{\partial}{\partial \rho} \right) + \frac{e^2 B_z^2 \rho^2}{8\mu_{x,y}^*} + \frac{eB_z}{2\mu_{x,y}^*} (L_z + g_\perp^* s_z) - \frac{\Lambda e^2}{4\pi\epsilon_0\epsilon_r|\rho_b|} \right. \\ \left. - \frac{eB_z}{M^*} (-yP_x + xP_y) \right] \Phi(\rho) = \left( \varepsilon_{x,y} - \frac{P^2}{2M^*} \right) \Phi(\rho) \quad (5.4)$$

where  $|\rho_b| = (x^2 + y^2)^{1/2}$  symbolizes the in-plane exciton radius and  $g_\perp^* (= g_e^* + g_h^*)$  is the Landé-g factor of excitons under  $B_z$ . The orbital and spin angular momentum is denoted by  $L_z$  and  $s_z$ , respectively. In Eq. 5.4, the in-plane contribution of the spherically-symmetric Coulomb potential is isolated with the help of a variational parameter  $\Lambda$ . [152] The impact of  $B_z$  along the x and y-directions being equal, the role of CM motion in Eq. 5.4 vanishes because of  $yP_x = xP_y$ . Therefore, Eq. 5.4 can be expressed by,

$$\left[ \frac{\hbar^2}{2\mu_{x,y}^*} \left( \frac{\partial^2}{\partial \rho^2} + \frac{1}{\rho} \frac{\partial}{\partial \rho} \right) + \frac{e^2 B_z^2 \rho^2}{8\mu_{x,y}^*} + \frac{eB_z}{2\mu_{x,y}^*} (L_z + g_\perp^* s_z) - \frac{\Lambda e^2}{4\pi\epsilon_0\epsilon_r|\rho_b|} \right] \phi(\rho) = \varepsilon_{x,y} \Phi(\rho) \quad (5.5)$$

Now, the energy eigenvalue of magneto-excitons can be estimated by solving Eq. 5.5,

$$\Delta\varepsilon_{x,y}(B_z) \simeq \frac{e^2 B_z^2 \langle \rho_b \rangle^2}{8\mu_{x,y}^*} + \frac{\hbar e B_z m_\phi}{2\mu_{x,y}^*} \pm \frac{1}{2} g_\perp^* \mu_B B_z - \frac{\Lambda e^2}{4\pi\epsilon_0\epsilon_r|\rho_b|} \quad (5.6)$$

where  $\mu_{x,y}^*$  and  $\mu_B$  symbolize the in-plane reduced mass of excitons and Bohr magneton, respectively. The symbol  $m_\phi$  denotes the index of orbital angular momentum quantum number, where  $m_\phi = 0$  for the carriers occupied in s-states. In a high magnetic field regime, the energy eigenvalue of magneto-excitons can be derived as [52]

$$\Delta\varepsilon_{x,y}(B_z) \simeq \left( j + \frac{|m_\phi| + m_\phi}{2} + \frac{1}{2} \right) \frac{\hbar e B}{\mu_{x,y}^*} \pm \frac{1}{2} g_\perp^* \mu_B B_z - \frac{\Lambda e^2}{4\pi\epsilon_0\epsilon_r|\rho_b|} \quad (5.7)$$

The value of  $\Lambda$  as a function of the magnetic field can be estimated by the variational method using a trial wave function  $\Phi(\rho) \sim \exp(-2 \Lambda \rho / \alpha_1) + c \exp(-\rho^2 / 4 \alpha_2^2)$ . [152]

$$\langle \Phi(\rho, z) | H(\Lambda) | \Phi(\rho, z) \rangle = 0 \quad (5.8a)$$

$$\frac{\partial}{\partial \alpha_i} \langle \Phi(\rho) | H(\Lambda) | \Phi(\rho) \rangle = 0 \quad (5.8b)$$

where  $\alpha_i$  is the variational parameter, and  $H(\Lambda)$  is the Hamiltonian of the system, which is the sum of kinetic and potential energy terms of the Schrödinger equation. Now, the temperature-dependent magnetic behavior of carriers can be understood by defining a partition function as follows,

$$\begin{aligned} Z_p(T, B_z) &= \sum \exp[-\Delta \varepsilon_{x,y}(B_z) / k_B T] \\ &\simeq \cosh \left( \frac{g_{\perp}^* \hbar e B_z}{4 \mu_{x,y}^* k_B T} \right) \exp \left[ - \frac{e^2 B^2 \langle \rho \rangle^2}{2 \mu_{x,y}^* k_B T} + \frac{\Lambda e^2}{4 \pi \epsilon_0 \epsilon_r |\rho_b| k_B T} \right] \end{aligned} \quad (5.9)$$

The kinetic and potential energy along the z-direction being invariant with  $B_z$ , their contribution is not explicitly considered in Eq. 5.9. After that, the magnetic susceptibility of carriers in a QW can be estimated by  $\chi_{v,\perp} = \mathcal{M} / B_z = k_B T / B_z \times \partial \ln Z_p / \partial B_z$ , where the symbol  $\mathcal{M}$  denotes the magnetization.

### 5.3.2 Magnetic field parallel to the QW plane

On the contrary, cylindrical symmetry cannot be used to describe magneto-excitons under  $B_y$ . This is because, excitons in a QW being confined in the z-direction, the impact of  $B_y$  along the x and z-directions would be different. Under this condition, the Schrödinger equation of excitons (Eq. 5.3) can be expressed by the use of  $\mathbf{A}(\mathbf{r}) = 1/2[zB_y, 0, -xB_y]$ ,

$$\begin{aligned} \left[ - \frac{\hbar^2}{2 \mu_z^*} \frac{\partial^2}{\partial z^2} - \frac{\hbar^2}{2 \mu_{x,y}^*} \frac{\partial^2}{\partial x^2} + \frac{e^2 B_y^2}{8} \left( \frac{z^2}{\mu_{x,y}^*} + \frac{x^2}{\mu_z^*} \right) - \frac{e^2}{4 \pi \epsilon_0 \epsilon_r |r_b|} - \frac{e B_y}{M^*} (z P_x - x P_z) \right. \\ \left. + e V_z(e, h) \right] \Phi(x, y, z) = \left( \varepsilon_{x,y,z} - \frac{p_y^2}{2 \mu_{x,y}^*} - \frac{P^2}{2 M^*} \right) \Phi(x, y, x) \end{aligned} \quad (5.10)$$

With the electron and hole are already confined by  $V_z(e, h)$ , the CM motion of excitons is restricted along the z-direction, and therefore  $\Delta P_z(B_y) \approx 0$ . However, the CM motion in the other direction can be influenced by the parallel field, i.e.,  $P_x$  may significantly vary with  $B_y$ . Hence, the contribution of CM motion ( $eB_y z P_x / M^*$ ) cannot be neglected in Eq. 5.10, which becomes coupled with the diamagnetic energy corresponding to y-direction of confinement ( $e^2 B_y^2 z^2 / 8\mu_{x,y}^*$ ). The interplay between the CM and RM of carriers can be understood by equating the two terms ( $eB_y z P_x / M^* = e^2 B_y^2 z^2 / 8\mu_{x,y}^*$ ), which indicates that the separation between electron and hole in the direction perpendicular to  $B_y$  and  $V_z(e, h)$  increases with the magnetic field. On the other hand, with the excitons are already confined along the z-direction, the magnetic perturbation corresponding to the z-direction of confinement ( $e^2 B_y^2 z^2 / 8\mu_{x,y}^*$ ) competes with the quantum confinement energy  $\varepsilon_0$ . Now, considering  $eV_z(e, h) = \frac{1}{2}\mu_z^* \omega_z^2 z^2$ , an analytical expression of energy eigenvalue is derived by the use of Eq. 5.10,

$$\Delta\varepsilon_z(B_y) \approx \frac{1}{2} \left( \frac{e^2 B_y^2 \hbar^2}{4\mu_{x,y}^* \mu_z^*} + \varepsilon_0^2 \right)^{1/2} \pm \frac{1}{2} g_{\parallel}^* \mu_B B_y - \frac{\Lambda^* e^2}{4\pi\epsilon_0\epsilon_r \sqrt{x^2 + z^2}} \quad (5.11)$$

In Eq. 5.11, the confinement energy  $\varepsilon_0$  ( $= \hbar\omega_z$ )[136] can be directly estimated from the PL peak energy or by solving the Schrödinger equation theoretically. In this configuration, the impact of magnetic field on the Coulomb energy would be feeble. This is because, with increasing the  $B_y$ , excitons in the QW are confined in the z-direction with a spatial elongation along the x-direction, resulting  $\Delta[x^2(B_y) + z^2(B_y)] \approx 0$ . Therefore, neglecting the small variation in Coulomb energy with  $B_y$ , exciton Bohr radius along the growth direction becomes,

$$r_z^2(B_y) = \frac{p_z^2}{[\mu_z^* \times \omega_c(B_y)]^2} \simeq \left[ \frac{2\hbar}{\mu_z^* (e^2 B_y^2 / \mu_{x,y}^* \mu_z^* + 4\varepsilon_0^2 / \hbar^2)^{1/2}} \right] \quad (5.12)$$

where  $\omega_c(B_y) = (e^2 B_y^2 / 4\mu_z^* \mu_{x,y}^* + \varepsilon_0^2 / \hbar^2)^{1/2}$  denotes the cyclotron frequency of charge carriers. Using Eq. 5.11, the magnetic behavior of charge carriers under  $B_y$  can be realized by defining a partition function, as described in section 5.3.1. The typical values of diamagnetic energy [ $\Delta\varepsilon_z(B_y) - \Delta\varepsilon_z(0)$ ] and out-of-plane exciton Bohr under  $B_y = 8$

T are estimated by using Eqs. 5.11 and 5.12, which are found to be 2.4 meV and 78 Å, respectively. This is calculated for a 150 Å thick GaAs/Al<sub>0.3</sub>Ga<sub>0.7</sub>As QW, considering  $\mu_{x,y}^* = 0.061 m_0$ ,  $\mu_z^* = 0.057 m_0$ , and  $g_{||} \approx 0.37$ . [112, 220, 221] The confinement energy of electron and hole for the given thickness of the QW is estimated by solving the one-dimensional Schrödinger equation, which is found to be  $\varepsilon_0 = 21$  meV. Note that the parameters used for this analysis do not consider the impact of non-parabolicity in bands, which may largely influence the estimated values.

Note that the formation of dark-exciton under  $B_y$  which was previously proposed for coupled or super-lattice QWs, [201] can be plausible even for a single QW due to this magnetic field induced in-plane separation of charges.

## 5.4 Anisotropic effective mass of exciton in QWs

Magneto-PL spectra of sample  $S_1$  under Faraday and Voigt configurations are shown in Figs. 5.2a and 5.2b. Subsequently, the Landau-diamagnetic shift of PL peaks under the two configurations are plotted in Figs. 5.2(c-f). It is observed that the diamagnetic shift in PL peak under Faraday configuration exhibits a linear magnetic field dependence when  $B_z \gtrsim 4$  T. In this high field regime, the Landau-diamagnetic shift is fitted by the first two terms of Eq. 5.7 to estimate  $\mu_{x,y}^*$ , which is then plotted in Fig. 5.3. For this analysis, the values of  $g_{\perp}^*$  for the given thicknesses of QW are acquired from Ref. [221]. Note that the magnetic field-driven enhancement of effective mass, which can be observed under a very strong magnetic field, [222] is often neglected for  $B_z < 15$  T. [136, 223, 218, 224] Therefore, the magnetic field dependent  $\mu^*$  is not considered in our present analysis up to 8 T.

On the contrary, the diamagnetic shift in PL peak is found to be feeble in Voigt configuration [Fig. 5.2(c-f)], which becomes negligible for a narrow QW ( $\leq 50$  Å). This reduction in diamagnetic energy under the parallel field can be explained by the theoretical model presented in Section 5.3.2. According to Eq. 5.11, the impact of  $B_y$  on the shift in PL peak energy  $[\Delta\varepsilon_z(B_y)]$  becomes negligible when the quantum



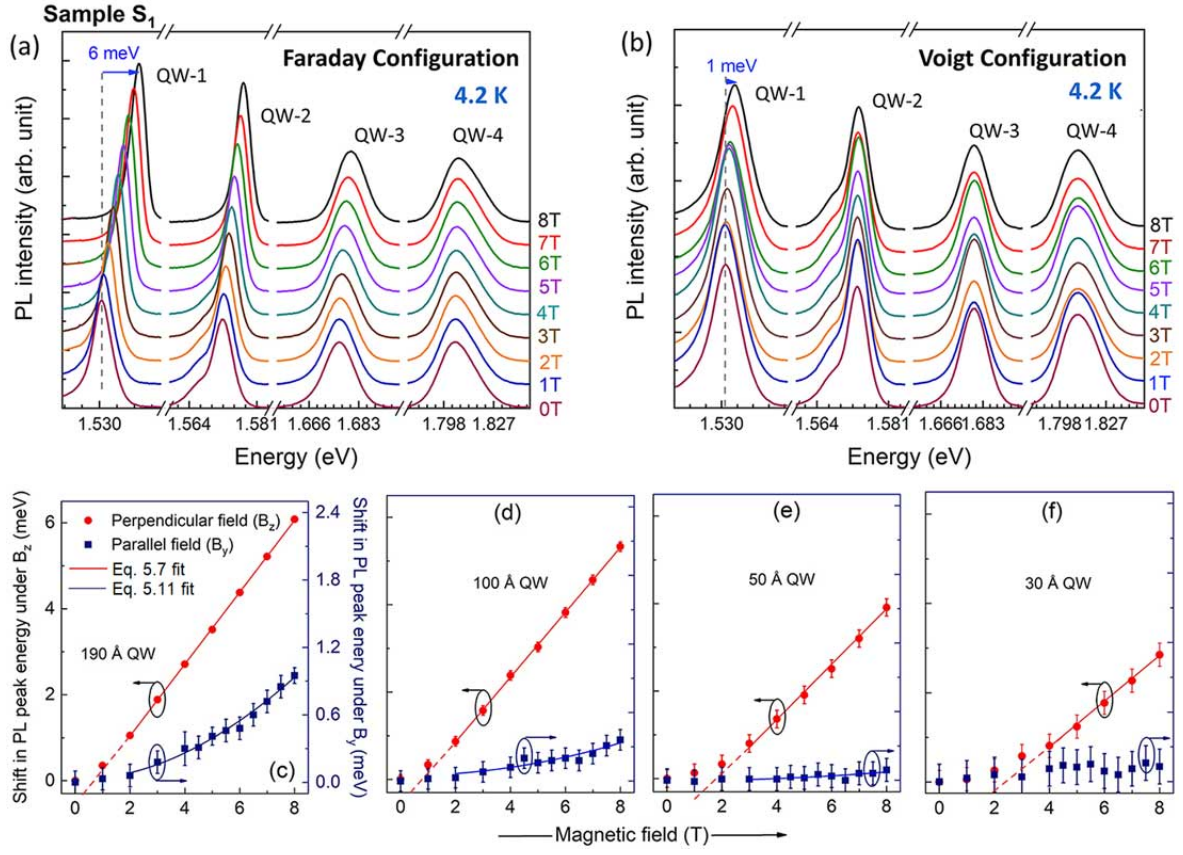


Figure 5.2: Magneto-PL spectra of sample  $S_1$  under (a) perpendicular and (b) parallel magnetic field orientations. The Landau-diamagnetic shift in PL peaks as a function of magnetic fields are plotted (c - f).

confinement is much stronger than the magnetic perturbation ( $\varepsilon_0^2 \gg e^2 B_y^2 \hbar^2 / 4\mu_{x,y}^* \mu_z^*$ ), i.e., for a narrow QW. With this understanding, the experimentally estimated PL peak energy as a function of  $B_y$  is fitted by Eq. 5.11 (Fig. 5.2). The  $\mu_{x,y}^*$  used for this fitting is already estimated by magneto-PL measurements in Faraday configuration and  $\varepsilon_0$  is deduced from the PL peak energy,  $\varepsilon_0 = \varepsilon_g^{QW} - \varepsilon_g^{GaAs} + \varepsilon_b$ . The  $\mu_z^*$  estimated by this fitting is shown in Fig. 5.3. Here, the out-of-plane mass of exciton could not be estimated for 30 Å thick QW, because of the negligibly small diamagnetic shift observed under Voigt configuration. Results obtained in Fig. 5.3 show a considerable increase in  $\mu_{x,y}^*$  with a decrease in QW thickness. This higher value of  $\mu_{x,y}^*$  for a narrow QW can be explained by the non-parabolicity of the band, which is elaborated in Chapter 3. According to the previous reports, the non-parabolicity of the band should also lead

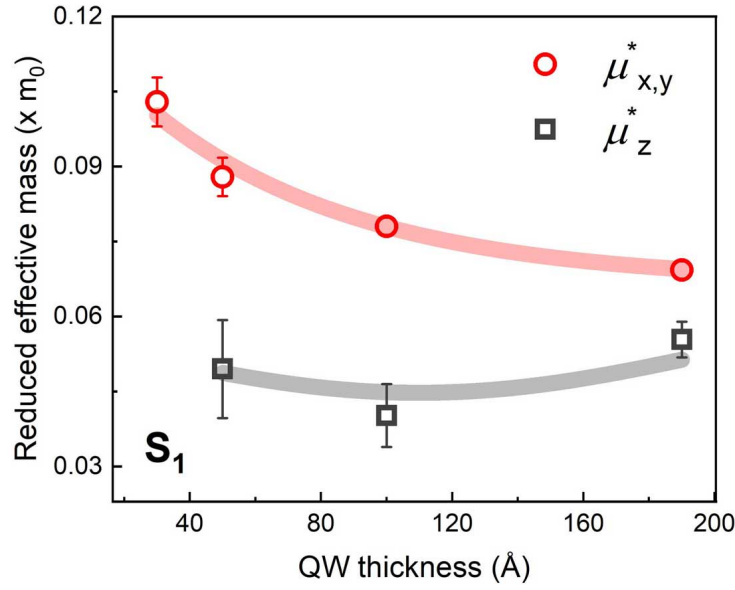


Figure 5.3: In-plane and out-of-plane effective mass of excitons as a function of QW thickness are estimated by magneto-PL spectroscopy. Solid lines are shown to guide the eye.

to an enhancement of  $\mu_z^*$  for a narrow QW.[26] However, this increase of effective mass is not distinctly observed in the experimentally estimated  $\mu_z^*$  as a function of QW thickness, Fig. 5.3. In addition to this, the total effective mass of exciton that can be estimated by  $\mu_T^* = (\mu_{x,y}^{*2} \times \mu_z^*)^{1/3}$ , is found to be 0.061, 0.061 and 0.067 $m_0$  for 190, 100, and 50 Å thick QWs, respectively. Therefore, although a significant enhancement of  $\mu_{x,y}^*$  is observed for narrow QWs, the estimated  $\mu_T^*$  remains invariant (nearly) with a variation in QW thickness. This indicates an interplay between  $\mu_{x,y}^*$  and  $\mu_z^*$ , which can be understood by complex non-parabolic dispersion of bands.[225, 26]

Note that, in a special case, when the barrier height is not sufficient to confine charge carriers in a QW (i.e., in the case of shallow QW or coupled QWs), magnetic field  $B_y$  can help the electron and hole to surmount the barrier potential. Under this condition, a variation of  $P_z$  with the applied  $B_y$  can be observed, which is neglected in Eq. 5.10. Therefore, a parallel magnetic field-driven charge separation along  $z$ -direction can be observed for QWs with very low-barrier height or in the case of coupled-QWs.[201, 206, 207]

## 5.5 Magnetic field driven confinement versus separation of charges

In sections 5.3.2, it is theoretically proposed that the electron and hole in a QW can be separated along the x-direction under the influence of  $B_y$ . As a result of this, a potential difference would be generated, in the direction perpendicular to the magnetic field and quantum confinement [i.e.,  $V_x(B_y, V_z)$ ]. The possibility to measure this voltage may depend on the crystalline quality of the GaAs/AlGaAs hetero-interface and the distance between the measuring probes,  $d$ . It is noteworthy to mention that due to the dominance of radiative recombination at a low-temperature, measurements of photovoltage (PV) signal for a GaAs QW under  $T \lesssim 50$  K is extremely difficult without applying an electric bias.[226, 227] Therefore, to record the feeble magneto-PV signal that would be generated by  $B_y$ , rectangular mesa structures (10 nos.) is developed on sample  $S_2$  (Figs. 5.4a and 5.4b). These strip-like samples are inter-connected as the series circuit of 10-voltage sources so that an appreciable amount of magneto-PV signal can be recorded even at 4.2 K.

Results obtained by the magneto-PL and lateral magneto-PV measurements under Voigt configuration are shown in Figs. 5.5a and 5.5b, respectively. It is observed that the PL intensity considerably decreases with the strength of  $B_y$ . At the same time, a gradual increase in the PV signal along the x-direction is recorded under the magnetic field parallel to the QW plane (Fig. 5.5b). These observations suggest that, under the

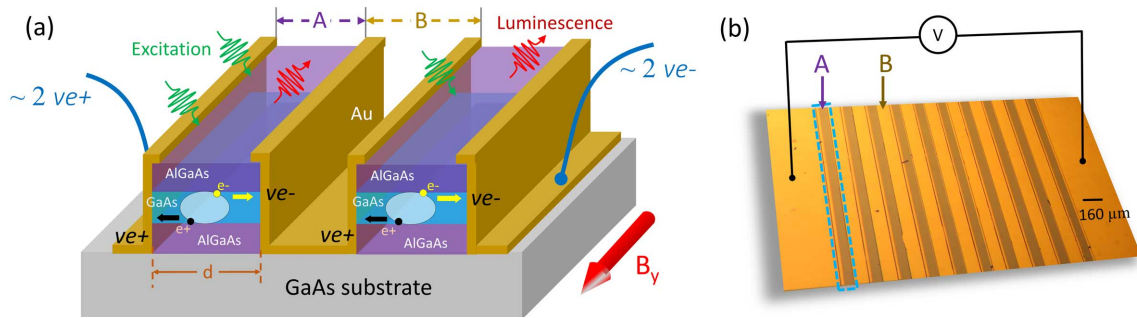


Figure 5.4: (a) Schematic and (b) photograph of the spatially patterned sample for the in-plane magneto-PV measurements. The width of each parallel strip, containing the QW regions, is kept as 80  $\mu\text{m}$ .

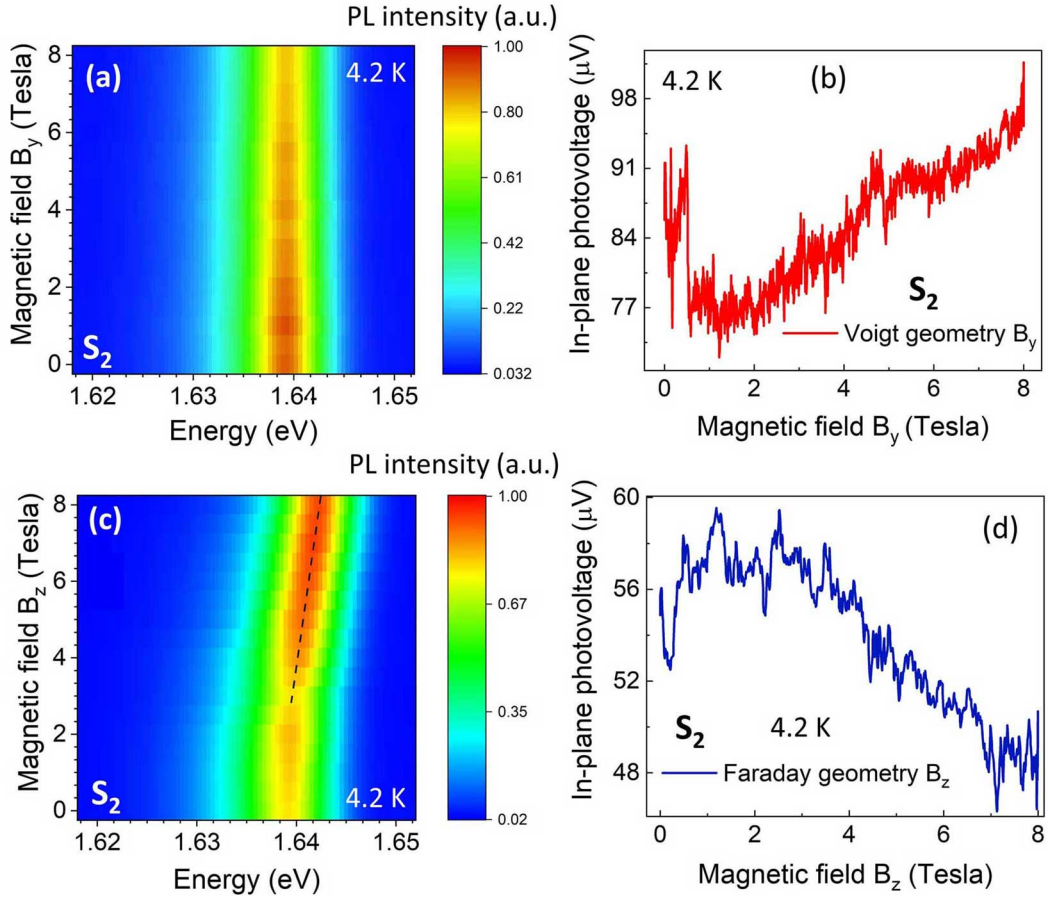


Figure 5.5: Magneto-PL and magneto-PV spectra of sample  $S_2$  under parallel (a) & (b), and perpendicular (c) & (d) field configurations. An increase in lateral PV signal is recorded under strong  $B_y$ , which indicates the in-plane charge separation process within the QW.

external field  $B_y$ , the separation of charges in the x-direction is dominant as compared to their confinement along the z-direction. As a result of this, the oscillator strength of exciton decreases, causing a reduction of PL intensity and an increase of lateral PV signal. Careful observation shows that the lateral-PV initially decreases for  $B_y \leq 1.5$  T (Fig. 5.5b), which could be due to an in-plane motion of charge carriers, followed by their localization in defect states. However, under a strong magnetic field, the momentum of charge carriers along the x-direction becomes sufficiently high to surmount the localization potentials. As a result of this, the lateral-PV monotonically increases with increasing the  $B_y$  in a high field regime. On the other hand, Figs. 5.5c and 5.5d show the results obtained by magneto-PL and lateral magneto-PV measurements in Faraday

configuration. Here, an enhancement of PL signal under  $B_z$  confirms that the applied magnetic field strongly confines excitons in the QW. With this magnetic confinement in the x-y plane, charge carriers become less susceptible to move in the plane of the QW in Faraday configuration. As a result of this, the in-plane magneto-PV signal gradually decreases with increasing the  $B_z$  (Fig. 5.5d).

Further confirmation of the parallel magnetic field induced confinement of charges along the growth direction and separation of charges within the QW-plane can be realized by magneto-PL line-shape analysis. This would be helpful to understand the impact of  $B_y$  on the electro-optical properties of excitons in a QW. Figures 5.6a and 5.6b show the integrated PL intensity and linewidth of the PL peak (sample  $S_2$ ) as a function of  $B_y$ . This is extracted from the magneto-PL spectra shown in Fig. 5.5a. The decrease in PL intensity under  $B_y$  that is observed in Fig. 5.6a, indicates a reduction in electron-hole wave function overlap in the QW, which may cause either due to –

1. Separation of electron-hole along the growth direction of the QW (which was reported for coupled or shallow QWs),[201, 205, 200] or
2. Separation of electron and hole within the QW-plane, along with their confinement in the growth direction (as described in this study).

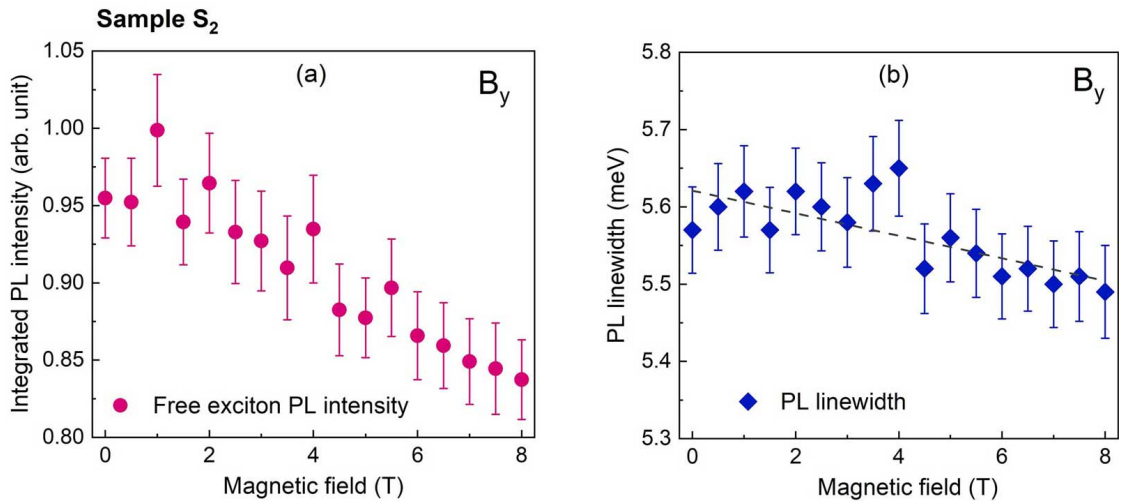


Figure 5.6: (a) Intensity and (b) linewidth of PL peak as a function of  $B_y$  for sample  $S_2$ .

Considering the first possibility, excitons in the QW would be significantly influenced by the atomic irregularities at the QW-barrier interface and alloy fluctuations of  $\text{Al}_x\text{Ga}_{1-x}\text{As}$  barrier, when they are forced to move along the  $z$ -direction. Under this condition, an enhancement in PL linewidth can be expected, which is not observed in Fig. 5.6b. According to the second possibility, when the excitons in QW are confined along the growth direction, wave function penetration into the barrier layer decreases and the impact of interface inhomogeneity/alloy fluctuations of barrier layers on the PL linewidth is suppressed under  $B_y$ . Therefore, a reduction in PL linewidth is expected in the second case, where the separation of charges in the  $x$ -direction causes a decrease in PL intensity. Moreover, with the carriers in the QW are already confined by barrier potential, magnetic field-driven confinement of charges along  $z$ -direction would be feeble. Hence, the gradual decrease in PL linewidth and PL intensity as a function of  $B_y$  (Fig. 5.6b) confirm the validity of the second possibility. In summary, under a parallel magnetic field, electron and hole in a QW are separated within the QW plane results in a decrease in PL intensity, whereas the charge carriers are confined along the growth direction, causing a gradual reduction of PL linewidth and feeble diamagnetic shift of energy states.

In this charge separation process by  $B_y$ , carriers in the QW perform a chiral motion across the GaAs/AlGaAs hetero-interfaces. Therefore, unlike a quantum Hall system, where the boundary of edge state motion is fabricated by photolithography technique (roughness  $\gtrsim 100$  nm), here the chiral charge transportation is realized via ultralow disordered GaAs/AlGaAs interfaces (interface roughness  $\lesssim 6$  Å). This may lead to an enhancement of the mean-free path and greater spin-coherence time of charge carriers. Note that the device concept demonstrated here does not require an electrical bias, where the magnetic field is solely responsible for the in-plane motion of charges within the QW. Because of this, an efficient electrical-transport across the hetero-interfaces of a QW can be realized by an applied magnetic field parallel to the QW plane.



## 5.6 Anisotropic magnetic behavior of charge carriers in GaAs QWs

In previous sections of this chapter, the anisotropic effective mass of excitons and impact of magnetic field on the electro-optical processes are investigated in Faraday and Voigt configurations. In this section, to probe the magnetic behavior of excitons in a QW, magnetization measurements are performed on a 50-period multiple-QWs sample ( $S_3$ ) under two different magnetic field orientations. The structural details of the sample are estimated by HRXRD and cross-sectional TEM (Figs. 5.7a and 5.7b).[228] The carrier accumulation in QWs is estimated by ECV measurements (Fig. 5.7c); details of the ECV measurements can be found in Section 2.5.2.[229]

Figure 5.8a shows the magnetic-susceptibility of charge carriers in sample  $S_3$  at 2 and 300 K. This is estimated by the magnetization measurements under a perpendicular magnetic field configuration ( $\chi_{\perp} = \mathcal{M}/B_z$ )[106]. The sample orientation with respect to the applied magnetic field is depicted in the inset of Fig. 5.8a. Results obtained in Fig. 5.8a show that the experimentally estimated  $\chi_{\perp}$  exhibits a paramagnetic behavior ( $\chi^{para}$ ) in a low field regime ( $B_z \lesssim 0.1$  T), which is suppressed at a low-temperature (indicated by  $\Delta\chi^{para}$ ). This paramagnetic contribution is primarily originated by a virtual magnetic-dipole-moment between the charge carriers occupied in the conduction and valence band, which is known as van Vleck paramagnetism ( $\chi_V^{para}$ ).[230, 209]

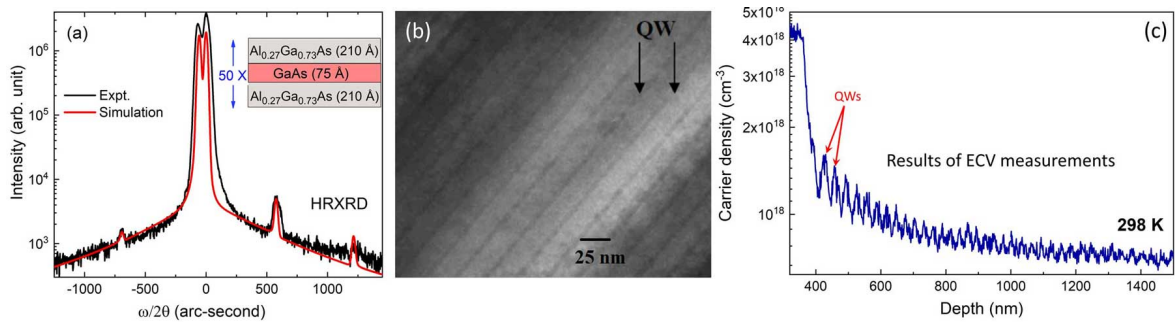


Figure 5.7: Results obtained by (a) HRXRD and (b) cross-sectional TEM measurements to estimate the structural parameter of sample  $S_3$ . (c) Carrier distribution in the 50-period MQW sample as a function of the depth is estimated by ECV measurements.

$$\chi_V^{para} = \frac{n(T)e^2}{2m^*2(\varepsilon_a - \varepsilon_b)} \sum \langle s_j | I_{ij} | b_i \rangle^2 = n(T) \frac{a}{\varepsilon_g(T)} \quad (5.13)$$

where the bandgap of the QW, carrier density in the conduction band and angular momentum operator corresponding to the carriers in conduction/valence band are denoted by  $\varepsilon_g(T) = \varepsilon_a - \varepsilon_b$ ,  $n(T)$ , and  $I_{ij}$  respectively. The bandgap of a GaAs QW generally decreases with an increase in temperature, which can be expressed by Varshini's relation.[101, 102] At the same time, the carrier density in the QW increases due to the ionization of donor atoms by thermal energy. In a steady-state condition, electronic density in the QW can be expressed by Eq. 1.16. Therefore, the increase in carrier density and decrease in bandgap can lead to a greater  $\chi_V^{para}$  at 300 K than that of at 2 K ( $\Delta\chi^{para}$ , Fig. 5.8a). Notably, the impact of carrier localization on the temperature-dependent S-shaped bandgap variation (predominant for  $T \lesssim 50$  K),[104, 105, 106] and its role on the magnetic property of charge carriers would be feeble for high-quality GaAs QWs.

Figure 5.8a shows that the diamagnetic behavior of charge carriers becomes dominant over the paramagnetic counterpart under  $B_z \geq 0.1$  T. Moreover, the diamagnetic susceptibility at 300 K is found to be higher than that of the 2 K measurements. The variation of  $\chi_{\perp}$  as a function of the magnetic field, which is observed in Fig. 5.8a, can-

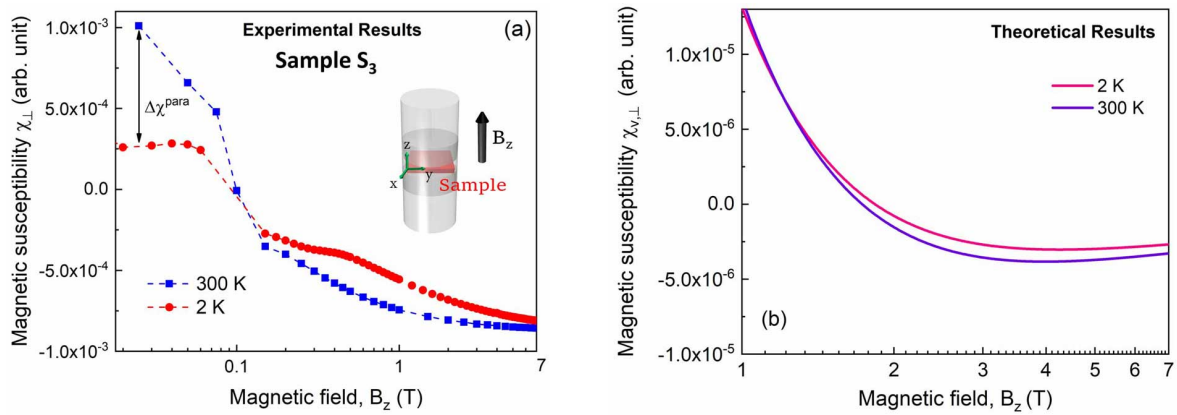


Figure 5.8: (a) Experimentally estimated magnetic susceptibility of sample  $S_3$  at 300 and 2 K by a magnetic field perpendicular to the QW plane,  $\chi_{\perp}$ . (b) Theoretically calculated magnetic susceptibility of carriers in the valence/conduction band for the two temperatures.



not be described by the simple expression of Landau-diamagnetic contribution. This is because the Landau-diamagnetic susceptibility should decrease with the strength of a magnetic field ( $|\chi^{dia}| = e^2 \rho^2 / 6m^* \epsilon_0 \epsilon_r$ ), [106, 214, 231] which is therefore inconsistent with our experimental findings. The disagreement between the theoretical and experimental results may be explained by considering the Coulomb interaction in the theoretical model, as described in Eq. 5.6. Here, an additional paramagnetic contribution arises due to the Coulomb interaction between electrons and positive charge centers or holes (contributed by acceptor-type carbon impurities). Now, the magnetic susceptibility of charge carriers is numerically estimated with the help of Eq. 5.9, and then plotted in Fig. 5.8b. In this analysis, the value of Lande-g factor for the given thickness of QW is taken from the literature ( $\approx -0.1$ ), [221, 220] and cyclotron radius in high magnetic field regime is considered as  $\langle \rho \rangle = \sqrt{\hbar / eB}$ . [52] The Coulomb separation parameter  $\Lambda$  as a function of field is estimated by the variational method (Sections 5.3.1 and 5.3.2). [232] The results obtained by this theoretical calculation (Fig. 5.8b) show that the carriers in QWs exhibit a paramagnetic behavior under a low magnetic field regime, which is governed by the Coulomb interaction and Zeeman energy. However, the net-magnetic susceptibility  $\chi_{v,\perp}$  under a strong magnetic field is mainly defined by the Landau-diamagnetic property of charge carriers. It is also found that the rate of change of  $\chi_{v,\perp}$  with the strength of the magnetic field becomes negligible for  $B_z \geq 3.5$  T. Moreover, a slight increase in diamagnetism is also computed for the high temperature. Therefore, the numerically estimated  $\chi_{v,\perp}$  by considering the Coulomb interaction is found to be in good agreement in explaining the experimentally estimated  $\chi_{\perp}$  as a function of magnetic field and temperature. In addition to this, the diamagnetic contribution of core-electrons can be added with  $\chi_{v,\perp}$  for a quantitative comparison with  $\chi_{\perp}$  estimated by SQUID magnetometer ( $\chi_{\perp} = \chi_{v,\perp} + \chi_{core,\perp}$ ). [233, 209, 230]

On the other hand, anisotropic magnetic-property of charge carriers in QWs is probed by the magnetization measurements, under Voigt configuration ( $\chi_{\parallel} = \mathcal{M} / B_y$ ). The experimentally estimated  $\chi_{\parallel}$  and  $\chi_{\perp}$  are plotted in Fig. 5.9a to compare the magnetic behavior of charges under the two configurations. The sample orientations with

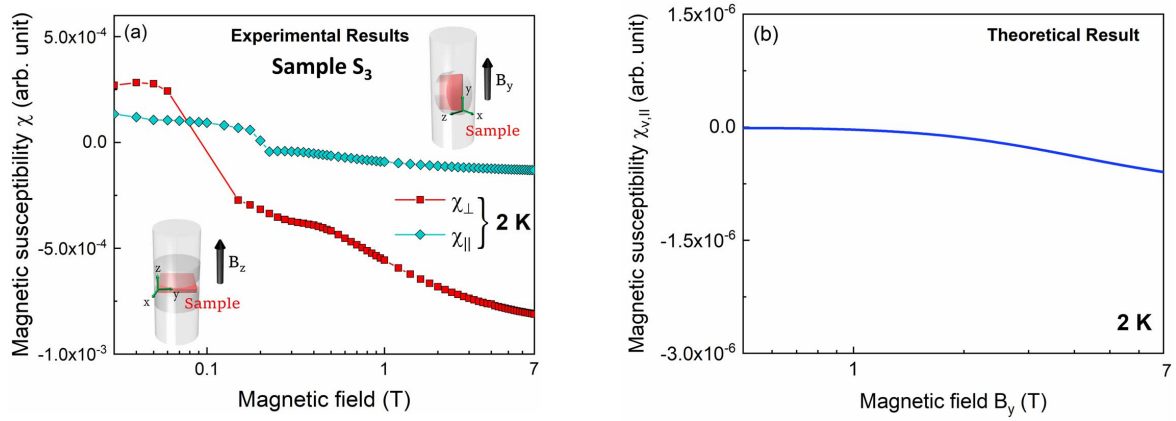


Figure 5.9: (a) Experimentally and (b) theoretically estimated magnetic susceptibility of charge carriers in Sample  $S_3$  under two different magnetic field configurations, at 2 K.

respect to the applied magnetic field are depicted in the inset of the figure. Similar to the results obtained by magneto-PL spectroscopy, it is found that the paramagnetic and diamagnetic susceptibility of charge carriers becomes feeble under this parallel field configuration. The anisotropic variation in the experimentally estimated  $\chi$  suggests that the magnetic-signal measured by SQUID is primarily contributed by the QW regions of the MQW sample. Magnetic susceptibility under the parallel field is theoretically calculated by the use of Eq. 5.11 to explain the experimental observations in Fig. 5.9a. The value of  $\varepsilon_0 = 55.7$  meV for this analysis is calculated by solving the Schrödinger equation for 75 Å thick QW. The results obtained by this theoretical calculation ( $\chi_{v,\parallel}$ , Fig. 5.9b) is found to be in good agreement in explaining the reduction of diamagnetic-susceptibility under  $B_y$ . The reason to observe this drastic suppression of magnetic behavior can be understood by the fact that charge carriers in the QW are already confined by  $V_z(e, h)$ . Hence, the parallel magnetic field-driven charge carrier confinement along the z-direction becomes feeble [ $r_z(B_y)$ ], especially when the quantum confinement is much stronger than the magnetic perturbation, Eq. 5.12.

In summary, the theoretically estimated magnetic susceptibility for the two magnetic field configurations explains the anisotropic magnetic behavior of charge carriers probed by the SQUID-magnetometer. In the theoretical framework, the contribution of core-electrons and charge screening mechanism can be added, which is beyond the scope

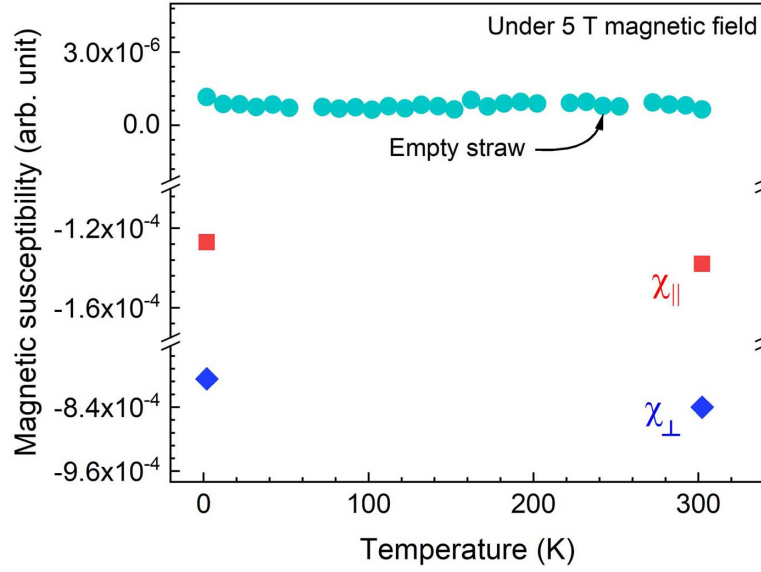


Figure 5.10: The magnetic susceptibility of empty straws that are used to hold the sample and measured magnetic-susceptibility of carriers in Sample  $S_3$ .

of our theoretical framework. In particular, this may be beneficial for a quantitative explanation of  $\chi_{\perp}$  and  $\chi_{\parallel}$  in the low magnetic field regime. The results obtained in this investigation would be helpful for spin controlled devices, where a magnetic field can control the magnetic moment of charge carriers.

Note that the accumulated magnetization signal from the 50-QWs at 7 T ( $\mathcal{M}_{MQWs} \sim 3 \times 10^{-6}$  EMU) is two orders of magnitude larger than the sensitivity of the SQUID-magnetometer ( $\sim 10^{-8}$  EMU). This confirms that the anisotropic magnetic property of charge carriers can be probed by SQUID based measurements. The magnetization signal contributed by the QW regions is calculated by,  $\mathcal{M}_{MQWs} = \chi_{GaAs} B \rho_{GaAs} \times V_{MQWs} / \mu_{GaAs}$ , where magnetic susceptibility of GaAs is denoted by  $\chi_{GaAs} \approx 3 \times 10^{-5}$  cm<sup>3</sup>/mole, density  $\rho_{GaAs} = 5.32$  gm/cm<sup>3</sup>, the volume of the 50-QWs  $V_{MQWs} = (50 \times \text{effective QW width} \times \text{sample area})$ , and  $\mu_{GaAs} = 144.6$  g/mole. Before the above analysis, it is ensured that the magnetic-susceptibility of the straw that is used for holding the sample, is feeble than that of the MQW sample. A comparison of the magnetic-susceptibility of perpendicular and parallel magnetic field of the empty straw and the sample is shown in Fig. 5.10.

## 5.7 Conclusion

In conclusion, the anisotropic property of excitons in QWs is experimentally investigated by magneto-PL measurements under perpendicular and parallel magnetic field configurations. An analytical expression of diamagnetic energy for excitons under a parallel magnetic field is derived by using the Schrödinger equation. The analytical expression, along with the results obtained by magneto-PL spectroscopy, is used to estimate the in-plane and out-of-plane mass of excitons in various thicknesses of QW. The theoretical model described in this work has suggested that the in-plane separation between electron and hole may increase with the strength of a parallel magnetic field. As a result of this, the parallel magnetic field induces chiral charge transportation across the hetero-interfaces of the QW, without applying an electric bias. Proof of this concept is demonstrated by the lateral-magneto-photovoltage measurements, where an enhancement in photovoltage signal is recorded under a strong parallel field. In this process, a reduction in PL intensity is also probed, which is due to the decrease in oscillator strength of excitons. On the contrary, the perpendicular magnetic field strongly confines electron-hole pairs, leading to an enhancement of the PL signal and a decrease in photovoltage signal. Moreover, the paramagnetic and diamagnetic behavior of charges in the QW is experimentally investigated by superconducting quantum interference device. The anisotropic magnetic property of carriers in QWs is explained by the same theoretical model, where the contribution of Coulomb interaction is found to be important for the magnetic field less than 3 T. The results obtained by this investigation suggest a unique method to control the transport, optical and magnetic property of charge carriers by a magnetic field with different orientations.

# Chapter 6

## Magneto-optical spectroscopy in quantum Hall regime

### 6.1 Introduction and background

Integer and fractional filling of Landau states and their impact on the electrical transport in semiconductors have been extensively investigated.[56, 234, 235, 236] A significant amount of research has been devoted to realize charge transport parameters and scattering mechanisms in semiconductor hetero and quantum structures.[237, 238, 239, 240, 241, 242] The impact of sample inhomogeneity or defects on the quantized Hall resistance and dissipation-less chiral charge transport was also investigated by many groups.[74, 243, 244, 245, 246] Although the transport measurements under a high magnetic field are of paramount importance, a contact-based measurement may not be feasible for undoped (insulating or semi-insulating), small (quantum dots, wire, etc.), and multi-layered samples. Moreover, being the technique is destructive, the sample after measurements can not be used for other studies or device fabrication. Therefore, magneto-optical spectroscopy, which is a non-invasive tool, has been emerged-out as an excellent alternative technique to probe magneto-electro-optical processes in quantum structures.[158, 247, 248, 166, 19, 91] In order to realize the correlation between optical and transport parameters, magneto-optical spectroscopy was performed in the quantum Hall regime on high-quality hetero-structures.[249, 250, 251, 252] It was reported that the diamagnetic shift of energy state exhibits a quantized variation at the integer or

fractional filling of Landau states.[249, 251] In particular, at the filling ratio of  $\nu = 1$ , enhancement of excitonic decay time was reported by time-resolved magneto-PL spectroscopy.[253] Nevertheless, a detailed correlation between the transport and optical property of semiconductor QWs, by the simultaneous measurements of quantum Hall and magneto-PL spectroscopy, has not been reported in the literature.

With this in mind, magneto-transport measurements and magneto-PL spectroscopy are simultaneously performed on a GaAs modulation-doped QW. In the first part of this chapter, the impact of photo-generated electron-hole pairs on the charge transport parameters is investigated. The results obtained by magneto-transport measurements under dark and illuminated conditions helped in realizing the carrier-carrier interaction and scattering mechanisms in the QW. In the quantum Hall regime, distinct Landau transitions are probed by magneto-PL spectroscopy. A rate equation model is described where PL intensity related to Landau transitions is used to investigate carrier redistribution among the Landau states and recombination time of magneto-excitons.

## 6.2 Sample details and experimental procedure

For this study, a 210 Å thick GaAs/Al<sub>0.22</sub>Ga<sub>0.78</sub>As modulation-doped QW sample is grown by the MOVPE technique. Silicon atoms are doped in AlGaAs barriers by SiH<sub>4</sub> precursor ( $\simeq 1.5 \times 10^{17} \text{ cm}^{-3}$ ), where the separation between the doped layer and QW is kept approximately 2200 Å. The electrons from the doped regions diffuse in the neighboring layers (diffusion length in Al<sub>0.22</sub>Ga<sub>0.78</sub>As is  $\sim 0.5 \text{ } \mu\text{m}$ ),[254, 255] and accumulates in the QW. The separation between the QW and doped-AlGaAs layer ensures that the ionized donors do not influence the electronic transport across the QW layer. The layer-details of the grown sample are depicted in Fig. 6.1a. The energy band diagram and carrier density in different layers are numerically evaluated by solving the Schrödinger-Poisson equation,[256, 257] which is shown in Fig. 6.1b and 6.1c. The Hall bar device having  $L \approx 600 \text{ } \mu\text{m}$  and  $w \approx 130 \text{ } \mu\text{m}$  is fabricated by the maskless photolithography system.[258] Details of the Hall bar structure fabrication can be found in Section 2.5.4.

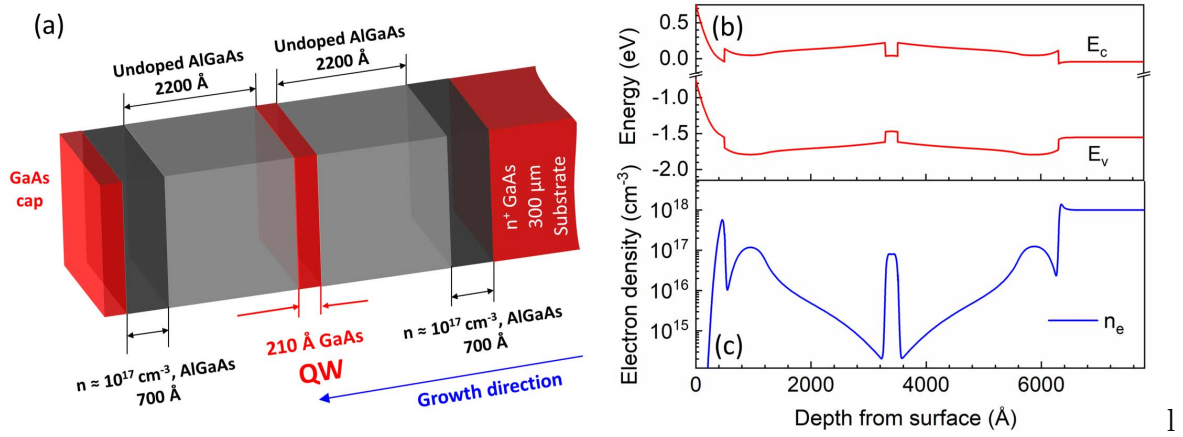


Figure 6.1: (a) Schematic of the GaAs/AlGaAs modulation-doped QW structure. Theoretically estimated (b) band-diagram and (c) carrier accumulation in different layers of the sample.

The  $R_{xx}$  and  $R_{xy}$  are measured by two lock-in amplifiers, where 52.6  $\mu\text{A}$  117 Hz AC is applied in the Hall channel. Under this applied electric bias, magneto-PL spectroscopy is performed by an optical-fiber based setup (Fig. 6.2a). The separation between the tip of the fiber and the sample surface is kept approximately 0.5 mm, which illuminates the sample over a spot diameter  $\sim 580 \mu\text{m}$  having  $p_{exc} \lesssim 1.9 \text{ W/cm}^2$ . With the laser spot diameter being greater (nearly equal) than the Hall bar width (length), uniform illumination of the Hall device is realized during the magneto-resistance measurements. Other regions of the sample being etched-out, photo-excitation in those regions, cannot contribute to the PL spectra of the QW. The magneto-resistance and magneto-PL measurements are performed in Faraday configuration unless otherwise specified.

### 6.3 Impact of photo-excitation on the transport property of electrons

Figure 6.2b shows the  $R_{xx}$  and  $R_{xy}$  of the modulation-doped QW under dark and laser-illuminated conditions. It is observed that the oscillatory behavior of  $R_{xx}$  and quantized variation in  $R_{xy}$  are damped under the photo-generated electron-hole pairs in the QW. In addition to this, the separation between two successive maxima in  $R_{xx}$  is altered, which indicates a variation in carrier density during the photo-excitation.

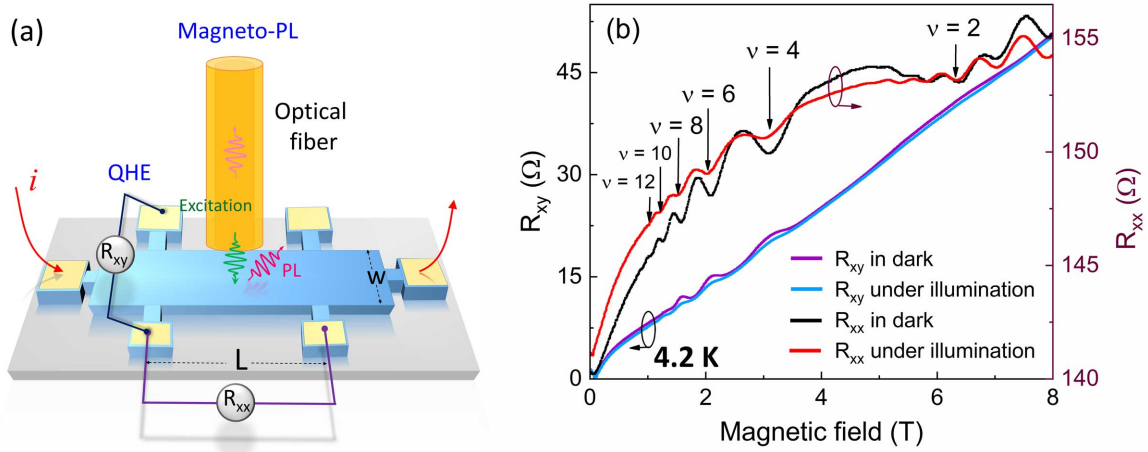


Figure 6.2: (a) Simultaneous measurements of quantum Hall and magneto-PL spectroscopy on a Hall bar device is schematically illustrated. (b) The longitudinal magneto-resistance and Hall resistance as a function of magnetic field up to 8 T.

The SdH oscillations in  $R_{xx}$  are often described by Eq. 2.17 (Chapter 2) to estimate transport parameters in low-dimensional systems.

### 6.3.1 Estimation of electrical transport parameters

In order to extract the oscillatory part of  $R_{xx}$  (i.e.,  $\Delta R_{xx}$ ), a smoothly varying background is subtracted from the longitudinal magneto-resistance, which is then plotted in Figs. 6.3a and 6.3b. Here, a quadratic background in  $R_{xx}$  can be explained by the parallel layer conduction of electrons, which is given by  $R_{xx}^b \sim (en_2\mu_2 + en_1^2/n_2\mu_2B^2)^{-1}$ . [239] In the modulation-doped QW structure, electronic transport via highly-doped AlGaAs layers (mobility  $\mu_2$ , carrier density  $n_2$ ) and GaAs QW layer (mobility  $\mu_1$ , carrier density  $n_1$ ) is mainly contributing to this parallel layer conduction process, see Fig. 6.1. After that,  $\Delta R_{xx}$  as a function of the magnetic field (Figs. 6.3a and 6.3b) is fitted by Eq. 2.17, and transport parameters under dark and laser-illuminated conditions are estimated. To reduce the uncertainty in the estimated parameters, oscillations in  $R_{xx}$  are also recorded at 2.5, 4.2 and 6 K, where the amplitude of SdH oscillations ( $\delta R_{xx}^{osc}$ ) is plotted in Fig. 6.3c. The experimental data in Fig 6.3c is then fitted by Dingle factor [ $R_d = \exp(-\pi m^*/eB\tau_q)$ ] [76] multiplied with  $\sqrt{BX}/\sinh(X)$  (where  $X = 2\pi^2 m^* k_B T / \hbar e B$ ). It is observed that the impact of laser irradiation on the esti-



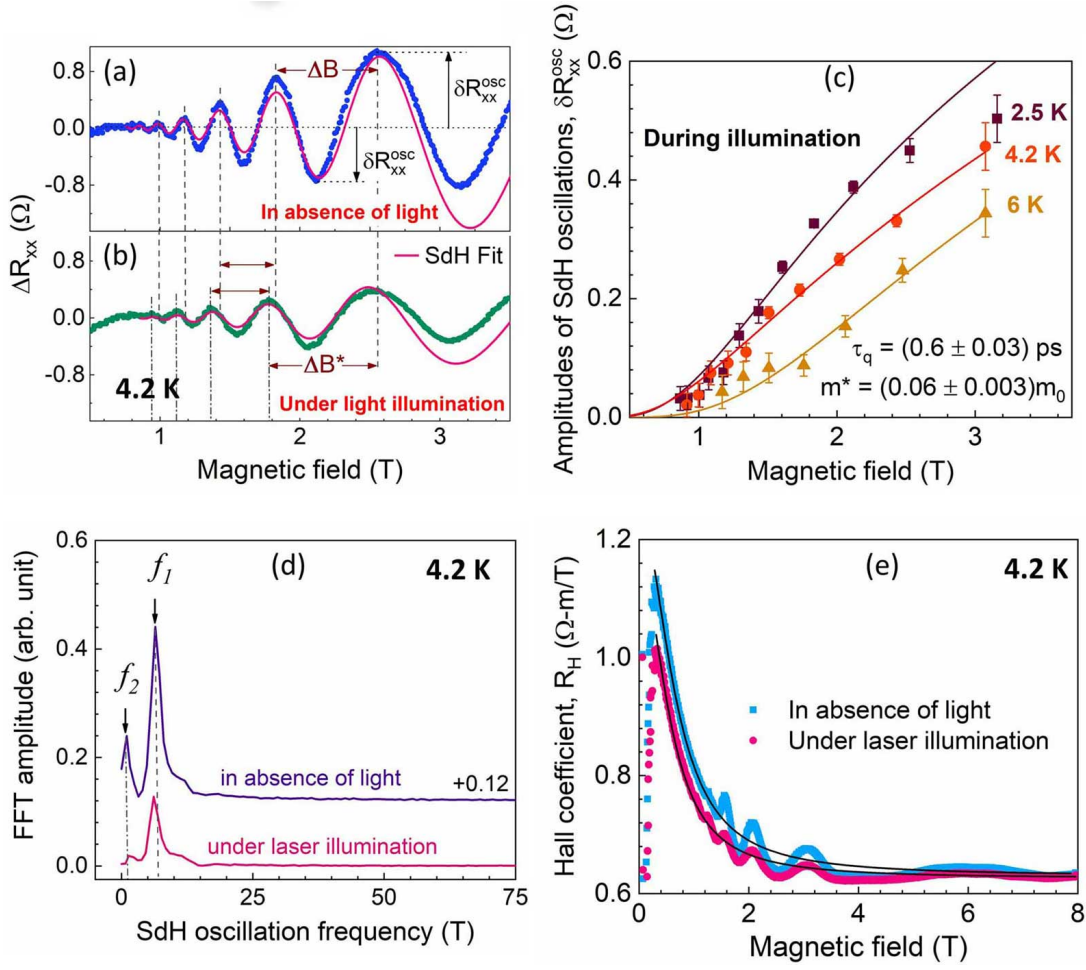


Figure 6.3: The oscillatory part of longitudinal magneto-resistance in (a) dark and (b) laser-illuminated condition is extracted. The SdH amplitude at three different temperatures (c), FFT amplitude of SdH-oscillations (d), and the Hall coefficient as a function of the magnetic field are plotted.

mated  $m^*$  ( $0.06 \pm 0.005 m_0$ ) and  $\varepsilon_f$  ( $9.5 \pm 1$  meV) is feeble, which remains within the uncertainty of the estimated value. However, a considerable decrease in  $\tau_q$  is estimated under the excess electron-hole pairs in the QW (Table 6.1).

Further insights of this light-induced variation in  $\tau_q$  is realized by a fast Fourier transformation (FFT) of  $\Delta R_{xx}$  in the magnetic field range of 0.9 - 3.5 T (Fig. 6.3d). It is found that the FFT amplitude in either condition exhibits two distinct maxima at the SdH-frequencies  $f_{\nu 1}$  and  $f_{\nu 2}$ . These SdH frequencies are then used to estimate the carrier density in two energy states of the QW,  $n_{\varepsilon i} = 2ef_{\nu i}/h$  (Table 6.1). A higher value of  $n_{\varepsilon 1}$  corresponding to  $f_{\nu 1}$  can be understood by the carrier density in the ground

state ( $\varepsilon_{e1}$ ), whereas a lower value of  $n_{e2}$  is assigned to the carrier density in the first excited state ( $\varepsilon_{e2}$ ). It is found that the carrier density in the ground state slightly decreases under laser illumination (Table 6.1). Such an observation can be explained by the recombination of charge carriers, especially, when the inter-subband relaxation of holes is faster than the relaxation of electrons (i.e.,  $\tau_0^h < \tau_0^e$ ). In the present case (210 Å QW), the energy separation between  $\varepsilon_{e1}$  and  $\varepsilon_{e2}$  [ $(f_{v1} - f_{v2})e\hbar/m^* \simeq 10$  meV][259] is lower than the longitudinal-optical phonon energy of GaAs (36.6 meV).[260, 261, 262] Therefore, the phonon-assisted quick relaxation of electrons could not be observed in the present case. Moreover, with the QW is already filled by electrons, relaxation of electrons in the conduction band is affected by the inter-subband scattering process. On the other hand, the accumulation of holes in the valence band edge increases under the laser illumination, where these photo-generated holes recombine with the electrons that are already occupied in the conduction band edge. However, being  $\tau_0 \ll \tau_r$ , most of the vacant states that are created by the electron-hole recombination are re-populated in a steady-state condition. Therefore, although a significant number of electrons in the band-edge are annihilated under a dynamic condition, only a minor decrease in  $n_{e1}$  is observed during steady-state measurements. Note that the carriers occupied in an excited state of the QW ( $\varepsilon_{e2}$ ,  $\varepsilon_{e3}$ , etc.) are highly susceptible to relax in the ground state by electron-phonon interaction, which is also influenced by the inter-subband scattering process. This can be understood by Fig. 6.3d, where the FFT amplitude ( $\sim \tau_q$ )[263] related to  $\varepsilon_{e2}$  state is found to be lower than that of  $\varepsilon_{e1}$  state. Furthermore, under the laser illumination, a significant reduction (84 %) in FFT amplitude is observed for  $\varepsilon_{e2}$  state as compared to that for  $\varepsilon_{e1}$  state (60 %). This indicates that, when the electron density in the excited state increases under the illumination, the electron-electron interaction becomes dominant which significantly affect  $\tau_q$  of an excited state.

Thereafter, the Hall coefficient ( $R_H \sim R_{xy}/B$ ) as a function of a magnetic field is deduced by the experimentally estimated  $R_{xy}$ , Fig. 6.3e. The magnetic field dependence of  $R_H$  can be explained by the parallel layer charge transport using the following relation,  $R_H \sim (en_1 + e\mu_1\mu_2n_2^2B^2/n_1)^{-1}$ . [239] Considering the parallel layer conduction

Table 6.1: The transport parameters estimated by using  $R_{xx}$  and  $R_H$  under dark and laser illumination are summarized.

	$\tau_q$ (ps)	$n_{\varepsilon 1}$ $\times 10^{11}(\text{cm}^{-2})$	$n_{\varepsilon 2}$ $\times 10^{11}(\text{cm}^{-2})$	mobility $\times 10^5(\text{cm}^2/\text{V-s})$	$\tau_t/\tau_q$
In dark	$0.9 \pm 0.03$	$3.1 \pm 0.08$	$0.7 \pm 0.1$	$1.2 \pm 0.1$	5
Under illumination	$0.6 \pm 0.03$	$2.9 \pm 0.1$	$0.7 \pm 0.2$	$1.6 \pm 0.1$	9.4

in AlGaAs and GaAs layers,[239, 245, 240, 241] the mobility of electrons is estimated by Fig. 6.3e (Table 6.1). Subsequently, the transport scattering time  $\tau_t$ , which is governed by the conductivity of electrons, is calculated by the estimated mobility,  $\tau_t = \text{mobility} \times m^*/e = 4.2$  ps (5.6 ps) in dark (illuminated) condition.

### 6.3.2 Impact of laser-illumination on the scattering process

In general, the ratio of  $\tau_t$  and  $\tau_q$  is used to identify the source of the scattering mechanism. The estimated  $\tau_t/\tau_q$  ratio in the present study is found to be 5 in the dark, which increases to 9.4 under the laser light (Table 6.1). According to the literature reports,[245, 264] a lower value of this ratio in the absence of light ( $< 10$ ) suggests that short-range scattering processes are mainly responsible for limiting the mobility of electrons in the QW. This can be governed by the atomic-irregularities at the GaAs/AlGaAs hetero-junctions or point defects acquainted in the system. Furthermore, an increase in mobility with decreasing the carrier density in the ground state (mobility  $\propto n_{\varepsilon 1}^{-|y|}$ ) confirms that the interface-roughness of the QW dominates the scattering process.[265, 245] Such a finding can be explained by the electron-electron interaction in the QW, which forces the electrons to move at the interface and scatter by high-quality GaAs/AlGaAs hetero-interfaces.[266, 267] On the contrary, an increase in  $\tau_t/\tau_q$  ratio ( $\approx 10$ ) during the laser exposure indicates that the short-range scattering by interface roughness decreases under the photo-excitation. This can be explained by the following possibilities – (a) an electron-hole Coulomb interaction reduces the impact of electron-electron repulsion and screen the scattering of electrons due to the interface-roughness, and (b) with decreasing the carrier density by the recombination process, electron-electron interaction reduces and interface-roughness experienced by

the electrons is decreased. However, the observed decrease in  $n_{\varepsilon 1}$  during the laser illumination is found to be  $\sim 6\%$ , and therefore, process (b) may not be sufficient to explain  $\sim 33\%$  enhancement in mobility (Table 6.1). Hence, the light-induced enhancement in mobility is mainly contributed by the screening of interface-potential by the electron-hole Coulomb attraction in QW. In fact, the photo-generated holes drag the electrons towards the center of the QW, and therefore, the interface-roughness experienced by electrons decreases under illumination.

Note that, although the electronic density in excited states of the QW increases under the photo-excitation, a gradual decrease in  $R_{xx}$  (at  $B = 0$ ) is observed during light illumination (Fig. 6.2b). This is because, with an increase in the carrier density, inter-subband scattering of electrons becomes dominant,[268, 269] which affects  $\tau_t$  and  $\tau_q$  related to an excited state. Moreover, an increase in electron-electron repulsion under the photo-excitation may force the excited-electrons towards the hetero-interfaces,[270, 267] leading to an enhancement of interface-scattering. Another important factor can be the higher effective mass of charge carriers when the energy eigenstate is at higher  $(\varepsilon, k)$  in the band dispersion (See, Chapter 3).[97, 158] Under this condition, the conductivity of electrons via an excited state becomes feeble ( $\sigma = ne^2\tau_t/m^* + \Delta\sigma_{ee} + \Delta\sigma_{WL}$ )[271], that may further decrease under the photo-excitation. Here, the correction factors in conductivity due to the electron-electron interaction and weak-localization (WL) are symbolized by  $\Delta\sigma_{ee} [\propto \ln(k_B T \tau_t / \hbar)]$ [271] and  $\Delta\sigma_{WL} [= -e^2/2\pi^2 \hbar \ln(L_\phi^2/l_m^2)]$ [272] respectively, where  $L_\phi$  is the phase coherence-length and  $l_m$  denotes the mean free path. Therefore, a decrease in  $R_{xx}$  at  $B = 0$  under the light illumination can be understood by the reduction in carrier density in the ground energy state ( $n_{\varepsilon 1}$ ) due to the carrier recombination process.

## 6.4 Magneto-PL spectroscopy in quantum Hall regime

In order to probe the interaction of photon and charge carriers during magneto-transport measurements, magneto-PL spectra of the Hall bar sample are recorded under

the electric bias. Measurements are performed at the magnetic fields when maxima and minima are observed in the SdH oscillations (Fig. 6.2b). Unlike the magneto-resistance measurements, variation in magneto-PL spectra in the temperature range of 2.5 - 6 K is found to be feeble, which remains within the uncertainty of the line-shape fitted parameters. In view of this, the results obtained by magneto-PL measurements at 4.2 K is only discussed here. The Landau transitions in the magneto-PL spectra are isolated by fitting the PL line-shape using multiple-Gaussian functions, which is shown in Figs. 6.4a-6.4d. Here, the Gaussian peak at the lower energy side of the spectra (purple line in Fig. 6.4a) is originated due to the radiative recombination of bound excitons, i.e., BX transition.[105, 118] The other peaks in the PL spectra are associated with the recombination of charge carriers via Landau states, where  $j = 0$  (second Gaussian, red line) denotes the ground Landau state transition,  $j = 1$  (blue line) denotes the first excited state transition, and so on.[273] Subsequently, the results obtained by PL line-shape fitting are plotted in Figs. 6.5(a-d). The PL intensity of FX recombination (contributed by all the Landau transitions) is symbolized by  $I_{FX}(B) = \sum_j I_j(B)$ , and the PL intensity of BX peak is denoted by  $I_{BX}$ , Fig. 6.5a. Here,  $I_j(B)$  symbolizes the PL intensity related to  $j^{th}$  Landau state, which is plotted in Fig. 6.5b. The experimentally observed variation in  $I_{FX}(B)$  and  $I_j(B)$  with a magnetic field can be explained by a rate equation model, where the intensity of excitonic PL for a given magnetic field is

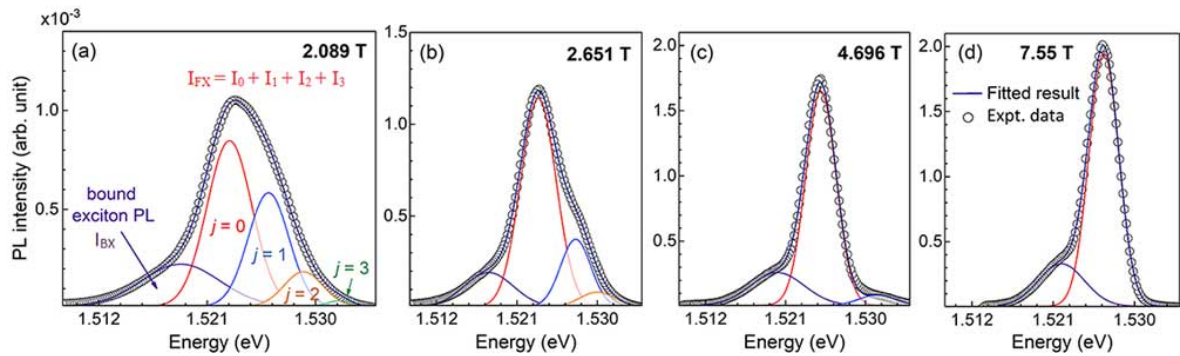


Figure 6.4: The representative magneto-PL line-shape fitting at four different magnetic fields at 4.2 K (a-d). PL spectra are fitted by the use of multiple Gaussian functions to de-convolute the Landau PL transitions, PL intensity, and the linewidth of Landau states.

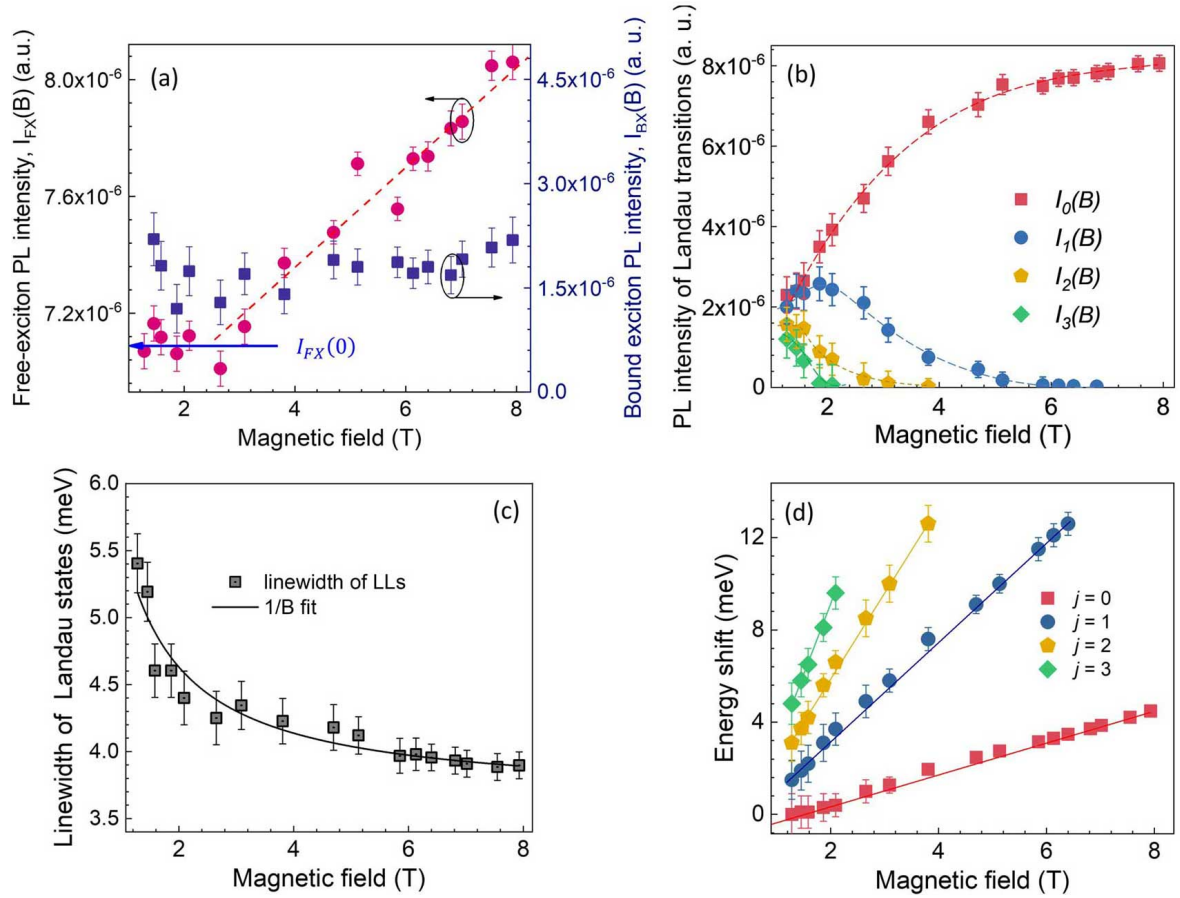


Figure 6.5: (a) Integrated PL intensity of FX and BX transitions, (b) PL intensity related to different Landau states, (c) linewidth of Landau transitions, and (d) Landau-diamagnetic shift as a function of field. Solid-lines denote the fitted curves, and dotted-lines are used to guide the eye.

expressed by,

$$\begin{aligned}
 I_{Total} &= \wp' \frac{n_{\delta_2}}{\tau_{\delta_2,r}} + \wp \frac{\sum_j n_j(B)}{\tau_r(B)} \\
 &= \wp' \frac{n_{\delta_2}}{\tau_{\delta_2,r}} + \frac{\wp}{\tau_r(B)} \sum_j \frac{2eB/h}{\sqrt{2\pi}\Gamma^2(B)} \int \frac{\exp[-\{\varepsilon_g^* - (j+1/2)\hbar eB/\mu_{x,y}^*\}^2/2\Gamma^2(B)]}{1 + \exp[(\varepsilon - \varepsilon_f)/k_B T]} d\varepsilon
 \end{aligned} \tag{6.1}$$

The first term of Eq. 6.1 signifies the intensity of BX recombination, where the carrier density in defect states and their recombination time are denoted by  $n_{\delta_2}$  and  $\tau_{\delta_2,r}$  respectively. The factor  $\wp$  is introduced to correlate the PL intensity and recombination rate of electron-hole pairs as per the following relation,  $I = \wp \times R_r$ . Notably, the magnitude of  $\wp$  remains invariant for a given set of PL spectra which are recorded by an exactly same experimental setup. Unlike the previous observation where the



magnetic field causes a reduction of BX feature (Chapters 3 and 4), the impact of magnetic field on  $I_{BX}$  is found to be feeble for the modulation-doped QW, Fig. 6.5a. This indicates that in the presence of strong electron-electron interaction, carriers are highly susceptible to be localized at the hetero-interfaces (in the z-direction). Under this condition, magnetic field-driven in-plane (x-y plane) confinement of excitons does not help in reducing the  $I_{BX}(B)$ .

### 6.4.1 Estimation of carrier density in the QW

The second term of Eq. 6.1 is signifying the PL intensity related to FX recombination,  $I_{FX}(B) = \wp \sum n_j(B)/\tau_r(B) = \wp \langle n_{e-h} \rangle / \tau_r(B)$ , where  $\langle n_{e-h} \rangle = \sum_j n_j(B)$  denotes total electron-hole pair density in all the Landau states and  $\tau_r(B)$  represents the recombination time of magneto-excitons. For a given magnetic field, the recombination time associated with different Landau levels of  $\varepsilon_1$  is considered to be the same in the present analysis.[109] At a low-temperature when  $\varepsilon_f$  is close to the excited states, PL features related to higher Landau states are distinctly observed in magneto-PL spectra. Under this condition, the ground Landau state is completely filled with charge carriers, and therefore, the carrier density in  $j = 0$  state can be equated with the degeneracy of Landau states, i.e.,  $N(\text{Landau state}) = 2eB/h = n_0$ . With this analogy, the PL intensity of the ground Landau state transition can be expressed by,  $I_0(B) = \wp \times [2eB/h\tau_r(B)]$ , and the intensity of FX transition becomes  $I_{FX}(B) = \wp \times n_{e-h}(B)/\tau_r(B)$ . The ratio of the above two relations can be used to estimate electron-hole pair density in the QW,  $n_{e-h}(B) = [2eB \times I_{FX}(B)]/[h \times I_0(B)]$ , which is then plotted in Fig. 6.6a. The average carrier density in the QW in the magnetic field range  $B \leq 4$  T is estimated to be  $\langle n_{e-h} \rangle = 1.9 \times 10^{11} \text{ cm}^{-2}$ , where the error-bar in the estimated result arises due to the uncertainties in the line-shape fitting. Here, the Landau transitions in magneto-PL spectra being merged under  $B < 2$  T, the results obtained by PL line-shape fitting are not shown for this low-field regime. Note that, when the impact of magnetic field on the BX recombination becomes significant,[158, 166] the contribution of  $I_{BX}$  (first term of Eq. 6.1) should be explicitly considered in this rate equation analysis.

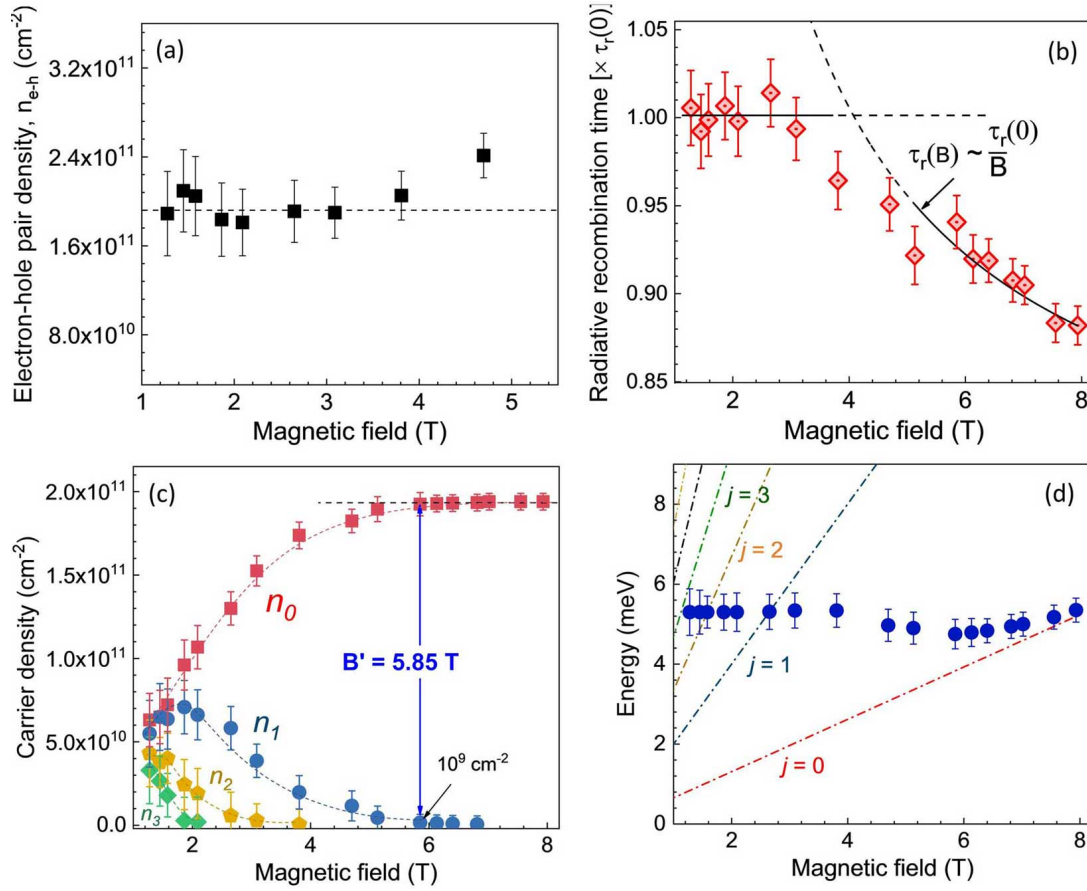


Figure 6.6: (a) The density of electron-hole pair in the QW, (b) radiative recombination time, (c) carrier density in Landau states, and (d) Fermi energy as a function of the magnetic field are estimated by the magneto-PL spectra. In figure (d), the dash-dotted lines are showing the magnetic field-driven shift in Landau states, which is calculated by  $\Delta\varepsilon_{j,z}(B) = (j + 1/2)\hbar eB/\mu_{x,y}^* - (1/2)g_{\perp}^*\mu_B B$ .

### 6.4.2 Recombination time as a function of magnetic field

After that, the radiative recombination time of magneto-excitons can be expressed in terms of the PL intensity of FX transitions,  $I_{FX}(0)/I_{FX}(B) = [n_{e-h}(0) \times \tau_r(B)]/[n_{e-h}(B) \times \tau_r(0)]$ . With  $n_{e-h}(0) \approx n_{e-h}(B)$  (Fig. 6.5a), the magnetic field-driven variation in recombination time is estimated by,  $\tau_r(B) = [I_{FX}(0)/I_{FX}(B)] \times \tau_r(0)$ . The results obtained by this analysis are plotted with a multiplication factor  $\tau_r(0)$  (Fig. 6.6b), where this  $\tau_r(0)$  can be estimated by transient PL measurements or may be taken from the literature reports. It is found that the estimated  $\tau_r(B)$  considerably decreases with the strength of the magnetic field. A theoretical expression of  $\tau_r(B)$  by considering the oscillator strength of magneto-excitons is already derived in Chapter 4. It was shown



that the confinement of excitons by an external magnetic field causes a reduction in  $\tau_r$  which can be expressed by,  $\tau_r(B) \sim 1/B$  (Eq. 4.7). The  $1/B$  dependent variation of  $\tau_r(B)$  is found to be in good agreement in explaining the experimental results under  $B \gtrsim 5$  T (Fig. 6.6b).

### 6.4.3 Carrier density in Landau states

With the quantitative estimation of  $\langle n_{e-h} \rangle$ , the carrier density in each Landau state can be estimated by  $I_{FX}(B)$  and  $I_j(B)$ , using  $n_j = [I_j(B)/I_T(B)] \times \langle n_{e-h} \rangle$ . The estimated carrier density in different Landau states (for  $j = 1, 2, 3$ ) and its variation with the magnetic field are plotted in Fig. 6.6c. Under a high magnetic field, carrier accumulation in the ground Landau state monotonically increases when the degeneracy of the Landau state has increased. In this condition, the carrier density in excited states reduces due to the relaxation of charges, and the carrier density in an excited state becomes feeble for  $B' \geq 5.87$  T. Beyond this magnetic field (5.87 T), a further enhancement in  $n_0$  is not observed. Therefore, the degeneracy of Landau state at  $B' = 5.85$  T becomes a measure of carrier density in the QW,  $n_{e-h} = 2eB/h = 2.8 \times 10^{11} \text{ cm}^{-2}$ , when most of the carriers in the QW are accommodated in  $j = 0$  state. The estimated  $n_{e-h}$  directly by this degeneracy of state is found to be in good agreement with the  $n_{e-h}$  estimated in Fig. 6.6a. It is also observed that, although the estimated  $n_0$  remains invariant under  $B' \geq 5.85$  T, the experimentally estimated  $I_0(B)$  exhibits a considerable enhancement even when  $B > B'$  (Fig. 6.5b). This further enhancement in  $I_0$  can be explained by the magnetic field-driven reduction of  $\tau_r(B)$ , which can be appreciated by Fig. 6.6b.

### 6.4.4 Fermi energy as a function of magnetic field

Considering the Gaussian distribution of Landau states, the carrier density in the QW under a steady-state condition is expressed by,

$$\langle n_{e-h} \rangle = \frac{2eB}{h} \sum_j \frac{1}{\sqrt{2\pi}\Gamma^2(B)} \int \frac{\exp[-\{\varepsilon_g^* - (j + 1/2)\hbar eB/\mu_{x,y}^*\}^2/2\Gamma^2(B)]}{1 + \exp[(\varepsilon - \varepsilon_f)/k_B T]} d\varepsilon \quad (6.2)$$

Now, using the estimated  $\langle n_{e-h} \rangle$ ,  $\Gamma(B)$ , and  $\mu_{x,y}^*$ , Eq 6.2 is graphically solved to estimate  $\varepsilon_f$  as a function of field, Fig. 6.6d. The  $\mu_{x,y}^*$  used for this analysis is deduced by the Landau-diamagnetic shift, which is elaborated in the next section. The dash-dotted line in Fig. 6.6d indicates the Landau states, which is calculated by  $\Delta\varepsilon_j(B) = (j + 1/2)\hbar eB/\mu_{x,y}^* - (1/2)g_\perp^*\mu_B B$ , considering  $\mu_{x,y}^* = 0.086m_0$  and  $g_\perp^* = 0.6$  (see, Section 6.4.5). It is observed that  $\varepsilon_f$  exhibits a gradual variation when an excited Landau state becomes empty, i.e., when the filling ratio is changed (Fig. 6.6d). Furthermore, the estimated  $\varepsilon_f$  by magneto-PL spectra is found to be smaller than the  $\varepsilon_f$  estimated by SdH oscillations, which might be due to the additional contribution of holes in magneto-PL analysis.

#### 6.4.5 Effective mass of charge carrier

The magnetic field-driven shift in Landau states that is observed in Fig 6.5d, is fitted by the following relation to estimate the in-plane reduced mass of excitons,[52]

$$\Delta\varepsilon_{j,z}(B, E) = \left(j + \frac{1}{2}\right) \frac{\hbar eB}{\mu_{x,y}^*} \pm \frac{1}{2}g_\perp^*\mu_B B - \hbar k_y \frac{E}{B} - \frac{M_{x,y}^*}{2} \left(\frac{E}{B}\right)^2 \quad (6.3)$$

The electric field applied for the magneto-resistance measurement is  $E \approx 13$  V/m, total in-plane mass of excitons is  $M_{x,y}^* \approx 0.42 m_0$ , [112] and wave vector at 4.2 K is  $k_y \sim 2 \times 10^7$  m<sup>-1</sup>. Under this condition, the contribution of the last two terms in Eq. 6.3 becomes  $\sim 10^{-4}$  meV at 4 T, which is found to be negligible as compared to the Landau-diamagnetic energy  $\sim 1$  meV at 4 T (first term). Therefore, the Landau and Zeeman terms of Eq. 6.3 are used to fit the experimental results in Fig. 6.5d. The in-plane reduced mass of exciton estimated by this fitting is found to be  $\mu_{x,y}^* = 0.086 \pm 0.002m_0$ . For this analysis, the lande-g factor of the QW is taken as 0.6.[221, 158] A careful observation shows that the shift in Landau-states slightly deviate from their linear variations, when the filling ratio of the Landau states is changed (arrow mark in Fig. 6.5d). This additional amount of shift in Landau transitions can be explained by the contribution of inter-Landau state carrier-carrier interaction.

### Magneto-PL measurements under a parallel magnetic field

Furthermore, the out-of-plane mass of excitons is estimated by magneto-PL spectroscopy under a parallel magnetic field,  $B_y$  (Fig. 6.7a). In this configuration, distinct Landau transitions in magneto-PL spectra are not observed. Moreover, the diamagnetic-shift in the PL peak is found to be feeble (Fig. 6.7b). The impact of parallel magnetic field on the optoelectronic processes and diamagnetic energy is already elaborated in Chapter 5. Using the same approach, diamagnetic shift in Voigt configuration is fitted by Eq. 5.11 to estimate  $\mu_z^*$ , which is found to be  $0.035 \pm 0.004m_0$ . The results obtained by the magneto-PL measurements under perpendicular and parallel field configurations show that the effective mass of exciton is highly anisotropic (i.e.,  $\mu_{x,y}^*(0.086m_0) \neq \mu_z^*(0.035m_0)$ ) even for 210 Å thick GaAs QW. Although none of these  $\mu_{x,y}^*$  and  $\mu_z^*$  match with the effective mass estimated by SdH oscillations, the magnitude of total effective mass  $\mu_T^* = (\mu_{x,y}^{*2} \times \mu_z^*)^{1/3} = 0.064m_0$  is found to be in close agreement with the transport mass of charge carriers. Therefore, it can be concluded that the magneto-PL spectroscopy is beneficial to investigate the anisotropic property of carriers, whereas magneto-transport measurement provides an averaged value over the entire magnetic field regime, which may also be affected by the out-of-plane property of charge carriers and more sensitive to temperature variations.

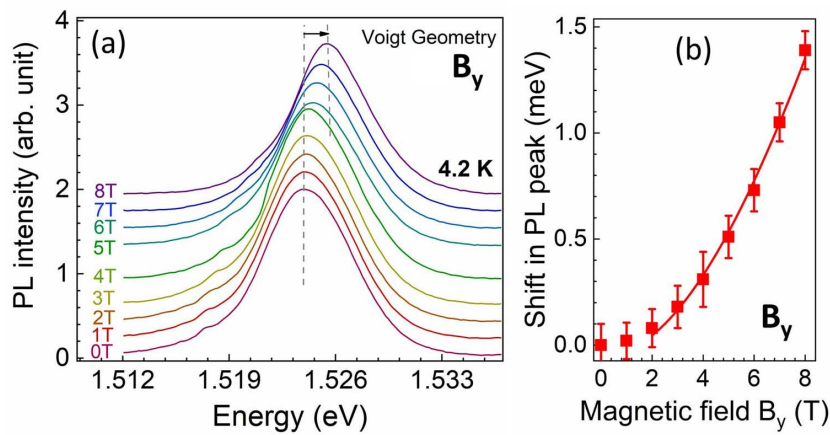


Figure 6.7: (a) Magneto-PL spectra of the same modulation doped QW sample in Voigt configuration at 4.2 K and (b) diamagnetic shift in PL peak under  $B_y \leq 8$  T.

### 6.4.6 Magneto-PL intensity oscillations

In this section, a new method to investigate magneto-PL intensity oscillations is described.[274] A schematic illustration to probe magneto-PL intensity oscillations due to the sweeping of Landau PL transitions across probe energy ( $\varepsilon_k$ ) is depicted in Fig. 6.8a. Neglecting the small contribution of Zeeman term, the magnetic field-driven blue-shift in Landau state is expressed by,  $\delta\varepsilon_j(B)/\delta B = (j + 1/2)\hbar e/\mu_{x,y}^*$ . In this condition, the strength of the magnetic field, that would be required to sweep  $j^{th}$ -Landau transition across  $\varepsilon_k$  is,  $B_j = 2\mu_{x,y}^*\varepsilon_k/[\hbar e(2j + 1)]$ , Fig. 6.8a. Due to this sequential sweeping of Landau PL transitions across the probe energy, an intensity oscillation plot can be recorded by a spectrometer. Figure 6.8b shows the experimentally estimated magneto-PL intensity oscillation plots that are probed at various energies. For a given intensity oscillation plot, the magnetic fields corresponding to the successive maxima in PL (cross-arrow in Fig. 6.8b) are used to estimate  $\mu_{x,y}^*$  by the following relation,

$$\mu_{x,y}^* = \frac{\hbar e}{\varepsilon_k} \left[ \frac{1}{1/B_{j+1} - 1/B_j} \right] \quad (6.4)$$

The estimated  $\mu_{x,y}^*$  by using Fig. 6.8b and Eq. 6.4 is found to be  $0.082 \pm 0.006m_0$ , which closely matches the  $\mu_{x,y}^*$  estimated by magneto-PL spectroscopy using Fig. 6.5d. Note that the fundamental mechanism to record this magneto-PL intensity oscillation

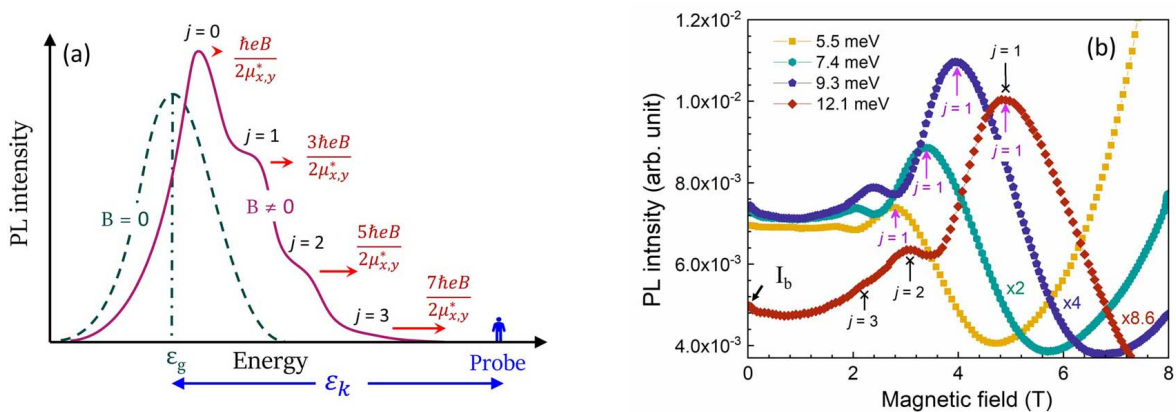


Figure 6.8: (a) Sweeping of Landau PL transition across  $\varepsilon_k$  is schematically depicted. Under this condition, an oscillatory variation in PL intensity can be recorded by increasing the magnetic field. (b) Magneto-PL intensity oscillation curves which are recorded at different probe energies at 4.2 K.

is similar to the SdH oscillations, where an oscillatory  $R_{xx}$  is recorded by sweeping the Landau states across  $\varepsilon_f$ . Unlike to magneto-resistance measurements, magneto-PL intensity oscillations can be probed at different energies ( $\varepsilon_k$ ) with the help of the spectrometer itself. In particular, with increasing the probe energy, the same Landau transition is probed at a higher magnetic field when the carrier occupancy and recombination time are altered (Fig. 6.8b). In view of this, intensity oscillation plots recorded at different probe energies would be beneficial in realizing the carrier redistribution among the Landau states. For a given magneto-PL intensity oscillation plot, the maxima in PL intensity are observed when  $\varepsilon_k = (j + 1/2)\hbar eB_j/\mu_{x,y}^*$ , and the corresponding PL intensity maximum ( $I_j^m$ ) can be expressed by using Eq. 6.1,

$$I_j^m(\varepsilon_k) = \frac{\wp}{\tau_r(B)} \frac{2eB}{h\sqrt{2\pi}\Gamma(B)^2} \left[ \frac{1 + I'_b}{\exp\left\{\frac{\Delta\varepsilon_k - \varepsilon_f}{k_B T}\right\} + 1} \right] \quad (6.5)$$

where  $I_b = I'_b \times 2eB\wp/\sqrt{2\pi}\hbar\tau_r(B)\Gamma(B)$  symbolizes the background PL intensity that might be contributed by other Landau transitions, with  $I'_b = \sum_{l \neq j} \exp[-\{\varepsilon_k - (l + 1/2)\hbar\omega\}^2/2\Gamma^2(B)]$ . A further simplification of Eq. 6.5 can be performed by considering  $\tau_r(B) \sim \tau_r(0)/B$  (Fig. 6.8b),  $\Gamma(B) \sim \Gamma(0)/B$  (Fig. 6.5d) and by setting the background PL signal ( $I_b$ ) to zero. Now,  $I_j^m(\varepsilon_1)$  and  $I_j^m(\varepsilon_2)$  being the PL intensity maxima of the  $j^{th}$  Landau transition when probed at  $\varepsilon_1$  and  $\varepsilon_2$  energies (arrow marks in Fig. 6.8b). The ratio of  $I_j^m(\varepsilon_1)$  and  $I_j^m(\varepsilon_2)$  is expressed by,

$$\left. \frac{I_j^m(\varepsilon_1)}{I_j^m(\varepsilon_2)} \right|_j = \frac{B_1^3}{B_2^3} \frac{\left[ \exp\left\{\frac{\Delta\varepsilon_2 - \varepsilon_f}{k_B T}\right\} + 1 \right]}{\left[ \exp\left\{\frac{\Delta\varepsilon_1 - \varepsilon_f}{k_B T}\right\} + 1 \right]} \quad (6.6)$$

Using the above relation, Fermi energy at the magnetic field  $[(B_1 + B_2)/2]$  is computed by the magneto-PL intensity oscillation graphs. The estimated  $\langle \varepsilon_f \rangle = 9.7 \pm 0.8$  meV by this technique can also be used to deduce the carrier density in the QW,  $\langle n \rangle = \mu_{x,y}^* \langle \varepsilon_f \rangle / \pi \hbar^2 = 3.5 \times 10^{11} \text{ cm}^{-2}$ . Therefore, investigation of magneto-PL intensity oscillations is found to be a good technique to estimate optical parameters of the material system that does not require the complete magneto-PL spectra and is also free from the line-shape fitting

procedure. Magneto-PL intensity oscillation can also be probed in the case of other high-quality materials, where isolated Landau transitions are observed in PL spectra. The PL transitions via higher Landau states are generally observed for doped materials. Nevertheless, enhancement of temperature or increase in laser excitation power can be beneficial to increase the carrier density in higher Landau states to observe the magneto-PL intensity oscillations.

Note that the magneto-resistance measurements on the Hall bar device are also performed under Voigt configuration using a DC source measuring unit. The results obtained by the magneto-resistance measurements under Faraday and Voigt configurations are compared in Appendix-C.

## 6.5 Conclusion

In conclusion, a correlation between the optical and transport property of charge carriers in a QW is realized by magneto-PL measurements in the quantum Hall regime. The results obtained by magneto-transport measurements in dark and laser-illuminated conditions helped to realize the sources of scattering mechanism and electron-electron interaction in modulation-doped QWs. It is found that the photo-generated holes screen the interface roughness assisted scattering and influences the inter-subband scattering process. Under this condition, redistribution of charges among the Landau states, recombination time of magneto-excitons, and Fermi energy as a function of the magnetic field is estimated by magneto-PL spectroscopy. The in-plane and out-of-plane effective mass of excitons are also estimated by magneto-PL measurements in Faraday and Voigt configurations, where the effective mass is found to be anisotropic even for a 210 Å thick GaAs QW. In addition to this, a novel method to investigate magneto-PL intensity oscillations, which is conceptually similar to the SdH oscillations, is described. The estimation of electro-optical parameters by this new method does not require the complete magneto-PL spectra where parametric line-shape fitting is also not required. The results obtained by combining the magneto-PL and magneto-transport measure-

ments helped to develop an in-depth understanding of the electro-optical processes. This investigation would be beneficial to investigate magneto-electro-optical processes in quantum structures, especially when a contact-based measurement is not feasible.

# Chapter 7

## Semiconductor device operation under a high magnetic field

### 7.1 Introduction

The III-V semiconductors have been used to fabricate optoelectronic devices for a wide range of applications requiring the source and detection of UV-VIS-IR light. The development of light-emitting diodes and semiconductor lasers remains in the focus of research for their utilization in telecommunication systems, materials processing, medical applications, spectroscopic measurements, pumping of solid-state lasers, etc.[275, 276] A considerable amount of research has been put to develop highly efficient, tunable-wavelength, and low-divergent light sources by semiconductor quantum structures.[277, 278, 279] Similar to this, an extensive amount of research has also been performed to develop high-responsivity photo-detectors with ultra-low dark current, which can be operated in the harsh environment of radiation.[280, 281, 282] Over the past few decades, the impact of magnetic field on the spectral linewidth, output power, and energy eigenstates of light-emitting devices has been extensively investigated by many authors.[283, 284, 285] It has been shown that the magnetic field-driven spatial confinement of charge carriers alters the inter-subband and inter-band electronic transitions, which can enhance the photon-flux and operating temperature of quantum cascade lasers (QCLs).[54, 286, 287] The operation of such devices under a high magnetic field can provide crucial information related to the scattering of charges



and electron-phonon interaction underlying the device efficiency.[288] Also, it has been demonstrated that the response of a photo-detector can be dramatically enhanced by almost 25 times when subject to a strong magnetic field.[289] In addition to this, it is extremely important to study the performance of semiconductor devices under a strong magnetic field, especially for critical scientific experiments and medical applications. With this in mind, the impact of magnetic field on semiconductor detectors operating in large hadron collider,[290] time of flight measurements,[291] and magnetic resonance imaging[292] was investigated by many groups. More recently, the role of a magnetic field on the performance of single-photon devices and applications related to the quantum computer is investigated. It has been found that the sensitivity of single-photon detectors increases by nearly four orders of magnitude under a high field.[293] The magnetic field along different directions can also control the spin-orbit interaction and Zeeman energy, which is often desired in quantum qubits and quantum information processing.[294, 295, 296]

Note that the development of those novel devices and their operation under a high magnetic field requires an involved study, which is beyond the scope of the present thesis. The main objective of this chapter is to validate our theoretical and experimental findings of magneto-optical spectroscopy during the device operation. Experiments are performed on the QW-based laser diodes and photo-detectors under similar conditions. The edge-emitting diode-lasers with a considerable number of disorders and a p-i-n photo-detector are developed. The impact of carrier localization on the performance of these devices is investigated at different temperatures. Finally, the role of magnetic perturbation on the lasing characteristics and spectral response of the detector is investigated at a low-temperature. Further studies in this direction would be beneficial to realize novel optoelectronic devices related to the quantum technology and information processing.

## 7.2 Sample details and experimental procedure

For this study, InGaAs/GaAs/AlGaAs-based laser-structures are grown on  $n^+$  GaAs substrates at 670 °C. The structures have consisted of two compressively strained  $\text{In}_{0.2}\text{Ga}_{0.8}\text{As}$  QWs of 80 Å thickness. The waveguide and clad regions are formed by  $\text{Al}_{0.15}\text{Ga}_{0.85}\text{As}$  and  $\text{Al}_{0.5}\text{Ga}_{0.5}\text{As}$  alloys respectively, where n and p-type doping is performed by silane and diethylzinc precursors. A schematic diagram of the laser-structure and theoretically computed energy-band profile are shown in Figs. 7.1a and 7.1b. The lasers are operated by ILX Lightwave LDP-3840B pulsed current source, where pulse-width ( $P_F$ ), pulse repetition interval (PRI), and applied current can be varied in the range of 0.1-100  $\mu\text{s}$ , 0.04-100 ms, and 0-3 A, respectively. In addition to this, a GaAs/AlGaAs p-i-n detector structure is grown on  $n^+$  GaAs substrate at

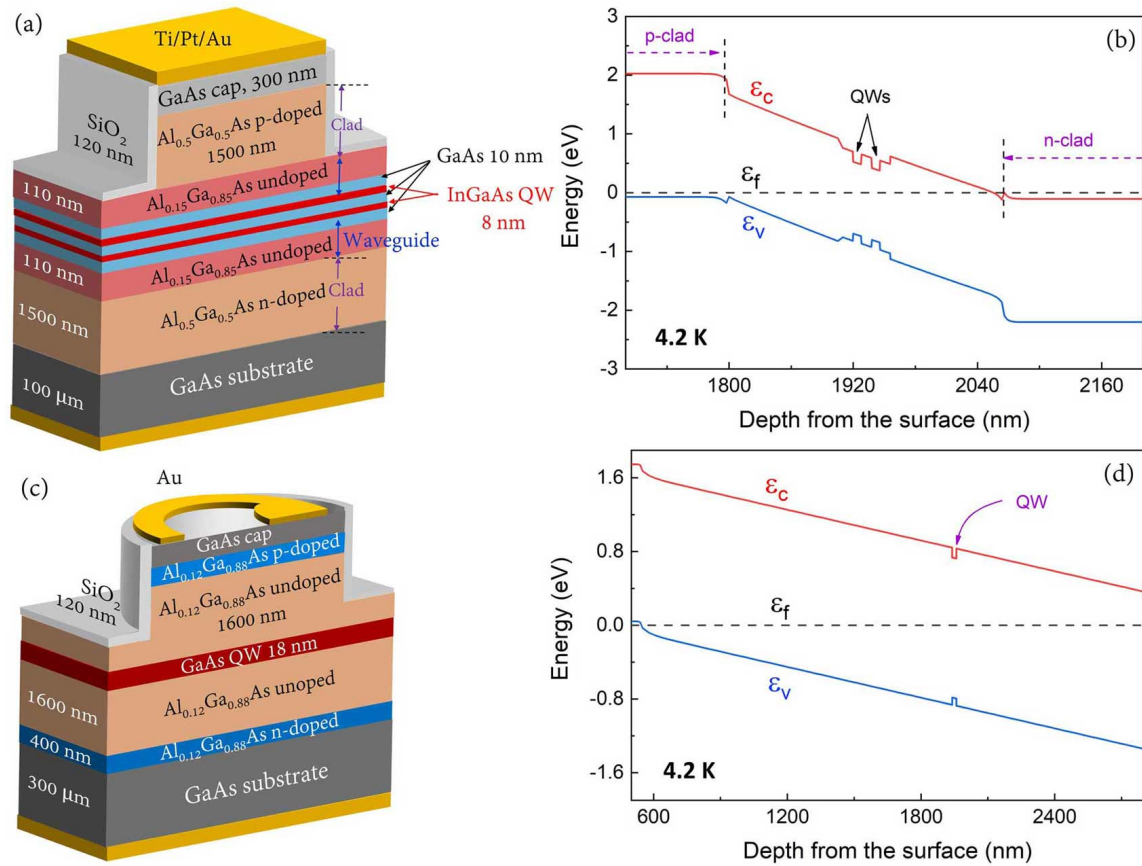


Figure 7.1: (a) Schematic and (b) energy band-profile of the InGaAs/GaAs laser structure. (c) Layer details and (d) band-profile of a GaAs/AlGaAs p-i-n detector structure.

730 °C. Here, a shallow GaAs QW of thickness 180 Å is embedded in the p-i-n structure, which is surrounded by p and n-Al<sub>0.12</sub>Ga<sub>0.88</sub>As layers (see, Fig. 7.1c). Figure 7.1d shows the energy band profile of the QW-based photo-detector. The barrier height being very small,  $\Delta\varepsilon_c \approx 97$  meV and  $\Delta\varepsilon_v \approx 76$  meV, perturbation due to a magnetic field or thermal energy may influence the carrier escape probability in the QW. The steps involved in the processing of edge-emitting laser-diodes and photo-detector by the maskless-photolithography system are described in Sections 2.7.1 and 2.7.2. The laser and detector are operated at LHe temperature under a magnetic field perpendicular to the QW-plane.

### 7.3 Edge-emitting diode lasers

In order to investigate the impact of a magnetic field on the lasing characteristics, few laser diode devices are fabricated on InGaAs/GaAs QW-based structures. These structures are grown by different indium-sources with slight variations in QW thickness and different aluminum composition in waveguides. Among these devices, the laser diode with a considerable number of defects are investigated in the present work so that the impact of magnetic field on the disorder related feature can be distinctly observed. Figures 7.2a and 7.2b show the light output power-current characteristics and laser emission spectra at room temperature under  $P_\Gamma = 4 \mu\text{s}$  and PRI = 0.5 ms. During the room temperature operation, laser diodes were kept on a Peltier-cooled metal plate to reduce the heat-load in the device, and a needle-shaped contact is used for a single element lasing operation. A considerable rise in laser-power is observed with increasing the current up to 2.5 A, where the peak power is calculated by  $p'_{peak} = (p'_{av} - p'_{dark}) \times \text{PRI}/P_\Gamma$ . The symbols  $p'_{av}$  and  $p'_{dark}$  denote the average laser power and the background light-signal measured by a power meter. It is observed that the emission spectra convolutes two partially merged lasing features, which are marked as  $L_1$  and  $L_2$  in Fig. 7.2b. With our previous understanding of PL-measurements, the origin of  $L_2$  (at lower-energy) is understood by the electron-hole recombination

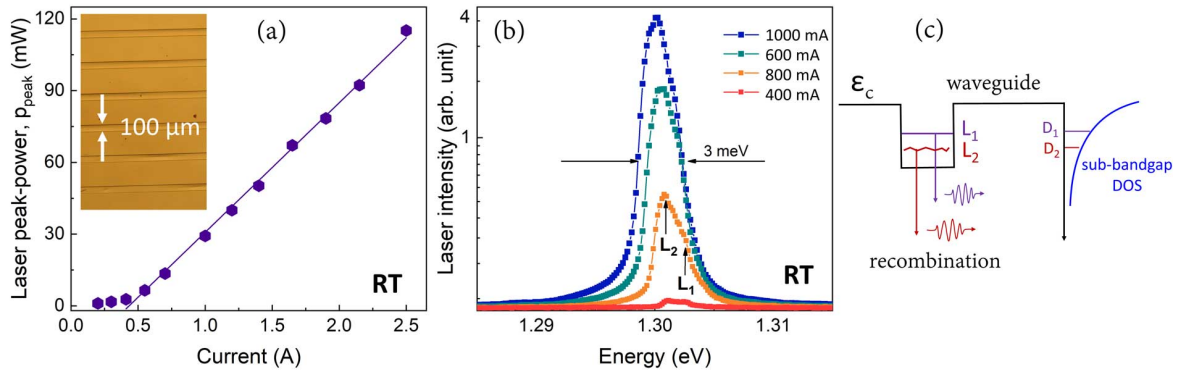


Figure 7.2: (a) light output power-current characteristics, (b) emission spectra of the laser at room temperature, and (c) schematic diagram showing the band-to-band and defect-related recombination in the active layer. The inset of figure (a) shows the photograph of the laser diode array.

via localization states (Fig. 7.2c). These localization potentials might be originated by indium-rich valleys and defects acquainted in the InGaAs QW.[105] A strong lasing intensity related to the BX feature ( $L_2$ ) indicates that the carriers in the QW are highly susceptible to be captured by defect states. The efficiency of this laser diode is found to be lower as compared to other high-quality lasers (a few Watts of peak power), which was reported in Refs. [87, 297]. The laser power is mainly constrained by the localization of charges in the active layer, series resistance in the device, and the quality of mirror-facets.

Thereafter, the laser diodes are operated at 4.2 K under a magnetic field perpendicular to the QW-plane. The design of the sample stage for the operation of diode lasers in LHe cooled Dewar is schematically depicted in Fig. 7.3a. The laser diodes are operated at 340 mA pulsed current condition with  $P_{\Gamma} = 4 \mu\text{s}$ ,  $\text{PRI} = 0.5 \text{ ms}$ . From the experimental perspective, the operation of diode lasers in a very small area inside the LHe cooled Dewar and collection of light by the optical fiber are the major difficulties. In order to improve light collection efficiency, two-laser diode elements are simultaneously operated for a given current, which may enhance the broadening of the recorded spectra. Figure 7.3b shows the emission spectra of the laser diode as a function of the magnetic field. Similar to the room temperature operation, the emission spectra at a

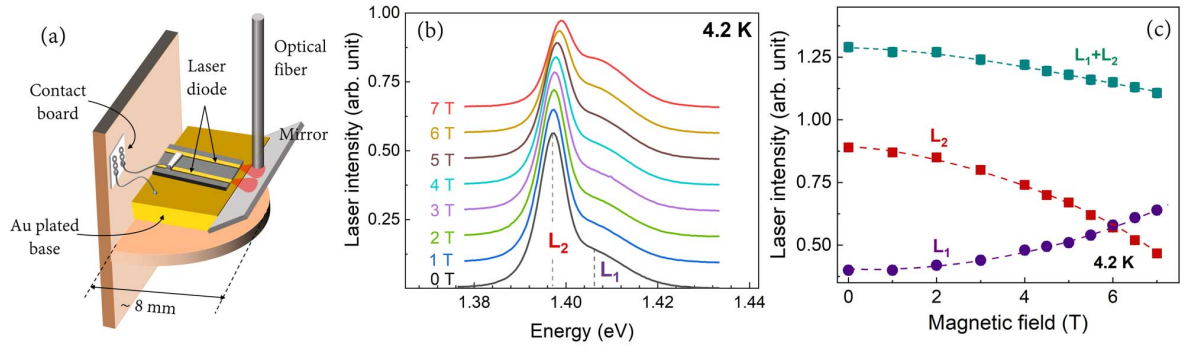


Figure 7.3: (a) Sample stage design for the operation of laser under a high magnetic field, (b) the emission spectra of the diode laser, and (c) laser intensity as a function of the magnetic field at 4.2 K.

low-temperature are contributed by  $L_1$  and  $L_2$ . It is observed that the intensity of  $L_2$  drastically reduces with an increase in the magnetic field, Fig. 7.3b. The reduction of  $L_2$  can be attributed to the in-plane confinement of charge carriers, i.e., carriers in the QW experience a less number of defects under a high field (see, Chapter 4). At the same time, the intensity of  $L_1$  increases because the oscillator strength of FX transition enhances by confining two-oppositely charged particles closer together. As a result of this, the laser intensity corresponding to  $L_1$  becomes dominant under  $B \geq 6$  T. It is found that the total lasing intensity (i.e.,  $L_1 + L_2$ ) gradually decreases with an increase in magnetic field (Fig. 7.3c), which is contradictory to our previous observation on magneto-PL spectra of QWs. The additional contribution in the present study arises due to (a) the injection of electrical current and (b) gain mechanism associated to lasing operation. At the threshold condition, the loss of photons should be equal (or lower) to the gain in the optical medium ( $g_{\text{modal}} = \alpha_i^* + \alpha_{\text{mirror}}^*$ ), which may largely vary for different energy eigenstates of a QW.[69] Here,  $\alpha_i^*$  denotes the intrinsic loss and  $\alpha_{\text{mirror}}^* = 1/2l_r \times \ln(1/R_1^*R_2^*)$  symbolizes the mirror loss, where  $l_r$  is the length of the resonator and  $R_1^*/R_2^*$  are the reflectivity of the mirrors. In particular, the absorption losses in AlGaAs waveguide increases with increasing the photon energy of the laser beam. This is because the density of defects in the sub-bandgap region of semiconductors exponentially increases towards the band-edge [ $\alpha_{\text{subbandgap}}^* \sim \exp\{-s_t(\varepsilon_g - \varepsilon)/k_B T\}$ ],[298]

as shown in Fig. 7.2c. Here,  $s_t$  denotes the steepness parameter. Therefore, when the lasing emission shifts from  $L_2$  to  $L_1$  and also due to the Landau diamagnetic energy, intrinsic loss of photons in the waveguide medium increases. This might be the reason that the  $L_1 + L_2$  gradually decreases under a high magnetic field, even though the modal gain of the system (Eq. 2.24) increases due to the Landau state formation. Note that, under a higher injection current, the impact of device-heating on the boiling rate of LHe becomes severe. Therefore, laser diodes in the present study could not be operated by varying the injection current.

In summary, an external magnetic field can be beneficial to suppress lasing emission via defect states, which may also offer a tunability in lasing wavelength. The magnetic field being solely responsible for the change in lasing wavelength at a given current, such an effect would be useful to realize fundamental mechanisms underlying the wavelength tunability in asymmetric waveguide lasers.[277, 299] A further study in this direction needs to be performed by varying the injection current, QW-thickness, and modification of waveguide structure.

## 7.4 Photo-detectors

Figure 7.4a shows the photograph of the fabricated detector, and its current-voltage characteristics in dark and light illuminated ( $\lambda = 730$  nm) conditions at 4.2 K are shown in Fig. 7.4b. In this measurement, a broad-spectrum of a QTH lamp is monochromatized by iHR-320 monochromator, and the power of the excitation light is controlled by a neutral-density filter. The dark current ( $i_{dark}$ ) of the photo-detector is found to be  $10 \pm 5$  pA (at -2 V), where this lower value of  $i_{dark}$  can be explained by the accumulation of background charges into the QW-region, which acts as an artificial trap center. However, the dark current of the devices considerably increases under the reverse bias voltage higher than -2 V (Fig. 7.4a), which indicates the tunneling of charges from the QW. Similar to this, the photo-current density of the device exhibits a step like enhancement near -2 V reverse bias voltage. The responsivity of a photo-diode

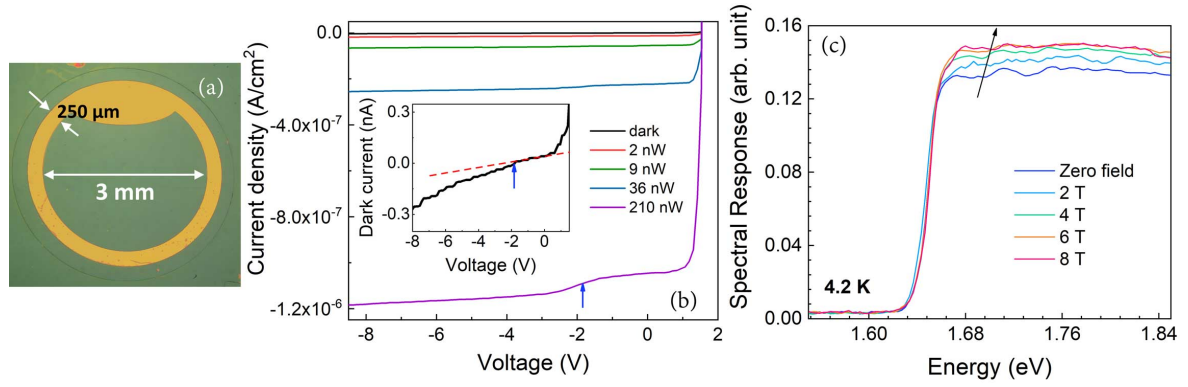


Figure 7.4: (a) Photograph of the photo-detector, (b) current-voltage characteristics under different excitation powers, and (c) spectral-response as a function of magnetic field.

can be estimated by the following relation,[300]

$$\mathfrak{R} = \frac{JA_p}{p'} \quad (7.1)$$

where  $A_p$  is the active area of the detector (diameter 3 mm), and  $p'$  is the power of the incident light. The responsivity estimated at the reverse bias voltage of -6 V is summarized in Table 7.1. Also, the specific detectivity  $D^* = \mathfrak{R}\sqrt{1/(4k_B T/RA_e + 2eJ_{dark})}$  and quantum efficiency  $\eta^* = \mathfrak{R}hc/e\lambda$  of the device are evaluated with the help of  $\mathfrak{R}$ , [301, 302] where  $RA_e$  is the dynamic resistance-area product and  $A_e$  being the area of electric current. The estimated  $D^*$  and  $\eta^*$  at 4.2 K are summarized in Table 7.1. A slight decrease in  $\mathfrak{R}$  at higher excitation power (Table 7.1) suggests the light-induced decrease in band-bending and the localization of charges due to the carrier-carrier interaction (see, Chapter 3). Therefore, the drift velocity of charge carriers decreases, and migration of charges along the growth direction is affected. Additionally, in a separate set of measurement at 83 K, the detector parameters at 210 nW power are estimated to be  $\mathfrak{R} = 0.53$  A/W,  $D^* = 1.2 \times 10^{13}$  cmHz<sup>1/2</sup>W<sup>-1</sup>,  $\eta^* = 0.89$  and  $i_{dark} = 0.5$  nA. Therefore, a slight increase in  $\mathfrak{R}$  and  $\eta^*$  at 83 K can be explained by the emission of charge carriers that were captured by defect states and due to an enhancement of  $\tau_r$  (Chapter 3).

The spectral response of the photo-detector with increasing the magnetic field up



Table 7.1: The estimated responsivity, specific detectivity, and quantum efficiency of the detector at 4.2 K.

illumination power (nW)	responsivity (A/W)	specific detectivity $\times 10^{13}(\text{cmHz}^{1/2}\text{W}^{-1})$	quantum efficiency
2	0.49	2.1	0.83
9	0.45	2.0	0.77
36	0.50	2.2	0.84
210	0.39	1.7	0.66

to 8 T is plotted in Fig. 7.4b. Due to the radiative recombination of charges, a distinct spectral feature related to the QW transition could not be recorded at 4.2 K.<sup>1</sup> On the other hand, the spectral-response in the above-bandgap region of  $\text{Al}_{0.12}\text{Ga}_{0.88}\text{As}$  increases by 13 % under the magnetic field up to 8 T. Such an observation can be explained by the following possibilities,

(i) diffusion of photo-generated charge carriers in the x-y plane is restricted by the applied magnetic field perpendicular to the sample surface. Therefore, the in-plane diffusion followed by the localization of photo-generated charge carriers in the AlGaAs layer decreases under a high magnetic field. In this condition, the number of charge carriers which is flowing along the z-direction of the p-i-n structure increases, which enhances the spectral response.

(ii) Probability of carrier escape from the QW increases due to magnetic field-driven lowering in barrier height,  $\varepsilon_{esc}^{e/v} \approx \Delta\varepsilon_{c/h} - (j + 1/2)\hbar eB/m_{e/h}^*$  (see, Section 4.4.1). These charge carriers then move according to the built-in electric field to enhance the spectral response of the detector.

#### 7.4.1 Magneto-PL of the detector sample

To probe the magnetic field-driven flow of charges along the z-direction and their accumulation in QW, magneto-PL spectra of the detector sample are also recorded at 4.2 K (Fig. 7.5a). In the PL spectra, two distinct PL features related to the indirect excitons (IX) and FX transition are observed, Figs. 7.5a and 7.5b. This IX transition could be contriuted by the recombination of charges, which are drifted by built-in

<sup>1</sup>See the results obtained by temperature-dependent PL and SPV measurements in Chapter 3



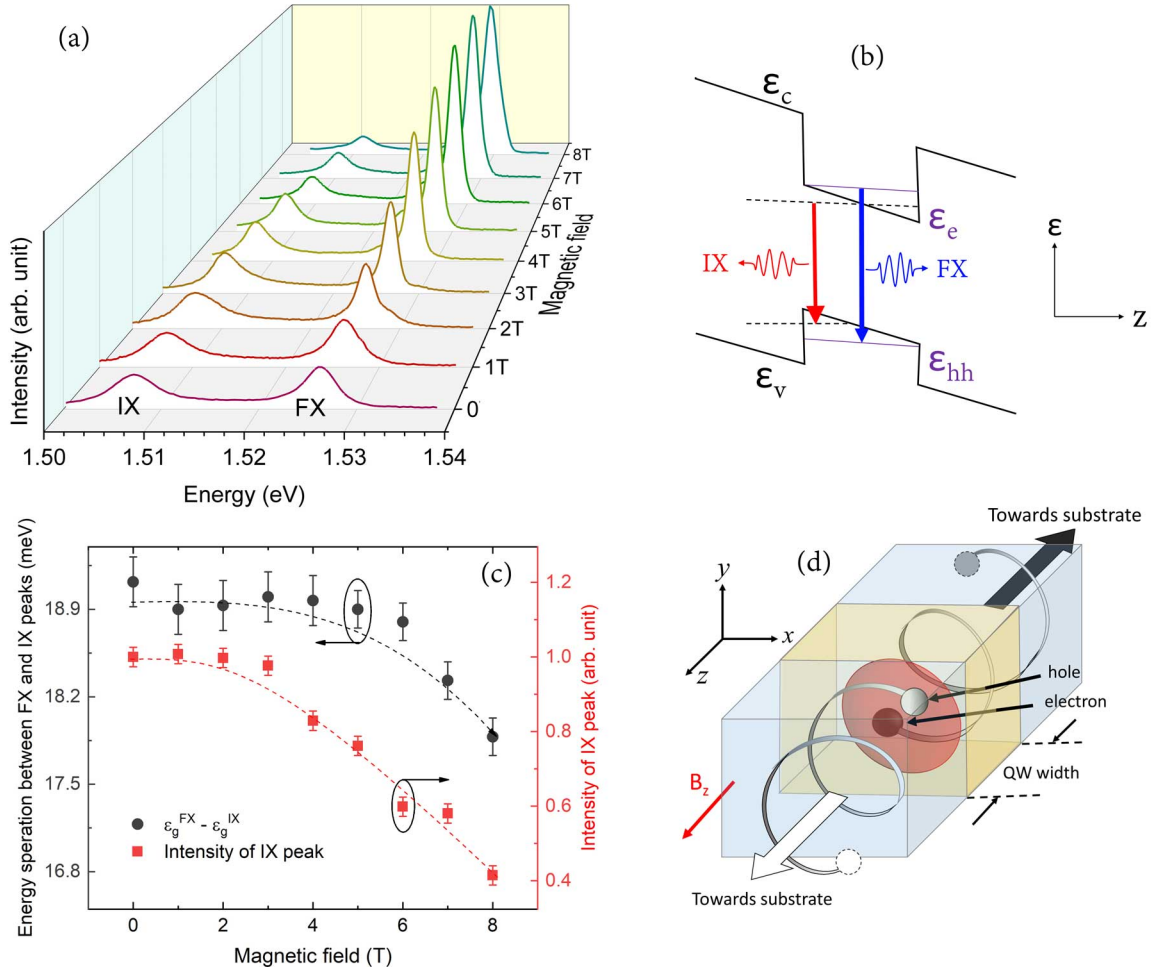


Figure 7.5: (a) Magneto-PL spectra of the p-i-n detector structure, (b) schematic diagram showing the direct and indirect excitonic transitions, and (c) energy separation between IX - FX peaks and PL intensity of IX transition as a function of magnetic field. (d) Magnetic field driven in-plane confinement of charges and their drift due to the structural electric field are schematically illustrated.

electric field and are captured by opposite interfaces of the QW (see, dotted lines). It is observed that the separation between FX and IX peaks (i.e.,  $\epsilon_g^{FX} - \epsilon_g^{IX}$ ) decreases with an increase in the magnetic field (Fig. 7.5c). Also, the intensity of the IX feature significantly decreases under a high magnetic field (Fig. 7.5c). The magnetic field driven decrease in IX PL intensity can be explained by this reduction of band-bending, which could be due to an enhancement in carrier accumulation inside the QW. This is because the magnetic field restricts the in-plane migration of charge carriers followed by their localization in barrier layers, which help in drifting the charges according to the built-in

electric field (z-direction), as shown in Fig. 7.5d. In this process, a significant number of carriers are also captured by the QW layer. Nonetheless, a large fraction of these charge carriers escape from the QW due to the magnetic field driven lowering in barrier height (see Chapter 4), which enhances the spectral response of the photo-detector.

## 7.5 Conclusion

In conclusion, edge-emitting laser diodes and photo-detector are developed, and the impact of carrier localization on the performance of these devices is investigated. The lasing characteristics of a QW-based diode laser with a considerable number of defects are investigated. It is observed that the contribution of defect states on the lasing emission can be suppressed by an external magnetic field, which also offers a tunability in laser wavelength. Such an effect can be used to understand gain mechanics of tunable wavelength lasers, which need further investigation. On the other hand, localization of charges within a QW helps in reducing the dark current of a photo-detector. It is observed that the responsivity of the detector decreases with increasing the light illumination power, which can be explained by the reduction of band-bending and enhancement of carrier localization at the hetero-interfaces. Under a high magnetic field, the in-plane diffusion of photo-generated charge carriers is restricted, and therefore, the in-plane migration followed by the capture of charge carriers by defects becomes feeble. Moreover, a significant number of electron and hole escape from the QW due to the magnetic field-driven lowering of barrier height. As a result of this, the spectral response of the photodetector increases with the strength of a magnetic field. The magnetic field-assisted flow of charges along the growth direction of the p-i-n structure and reduction of band-bending are also probed by magneto-PL spectroscopy of the detector structure.

## Thesis Highlight

**Name of the Student:** Subhomoy Halder

**Enrollment No.:** PHYS03201404012

**Name of the CI/OCC:** Raja Ramanna Centre for Advanced Technology, Indore.

**Thesis Title:** Magneto-optical transport studies on ultra-low disordered semiconductor quantum wells grown by MOVPE.

**Discipline:** Physical Sciences

**Sub-area of the discipline:** Semiconductor Physics

**Date of Viva Voce:** 02/07/2020

Over the past few decades, optical and transport properties of III-V semiconductors have been extensively investigated for the development of numerous optoelectronic devices. In particular, the excellent electro-optical properties of ultralow-disordered quantum structures are beneficial in high-efficiency optical-emitters, photovoltaics, sensors, and high-mobility devices. Additionally, radiative recombination efficiency of the material system can be enhanced by a magnetic field driven spatial confinement of excitons. The motivation of the present thesis is to utilize the 'magnetic field' as a unique tool to control recombination, transport, and magnetic properties of charge carriers. The thesis deals with novel methodologies of spectroscopic and transport measurements on GaAs quantum wells (QWs). The role of quantum confinement on the excitonic recombination and effective mass of charge carriers is investigated by magneto-optical spectroscopy (Fig. 1a). It is found that the effective mass of excitons significantly increases with a reduction in QW thickness. The foremost reason behind such an observation is found to be the non-parabolicity of bands, which becomes dominant when the energy eigenstate is at higher ( $E, k$ ). It is observed that the PL intensity related to disorder bound excitons decreases under a high magnetic field. A phenomenological model of magneto-excitons is developed (Fig. 1b), where the magnetic field-driven reduction in bound-exciton PL is used to estimate point defect density in QWs. Results obtained by magneto-optical spectroscopy are also correlated with that of the quantum Hall measurements (Fig. 1c). It is shown that magneto-optical spectroscopy with a rate equation analysis can provide detailed information on competitive electro-optical processes in quantum structures. Such an investigation would be beneficial, particularly when a contact-based measurement is not feasible. Also, it is found that the electron-hole pairs in a QW can be separated by a magnetic field parallel to the QW plane, which reduces the PL intensity and develops an in-plane photo-voltage signal (Fig. 1d). To fabricate semiconductor devices, a simple maskless-photolithography system is also developed (Fig. 1e). Finally, it is shown that the carrier recombination and redistribution processes in semiconductor devices can be controlled by a magnetic field, which offers tunability in lasing wavelength and enhances the charge collection efficiency in photodetectors. Besides the physics of magneto-excitons, the present thesis provides clear guidelines for magnetic field controlled advanced electro-optical devices development.

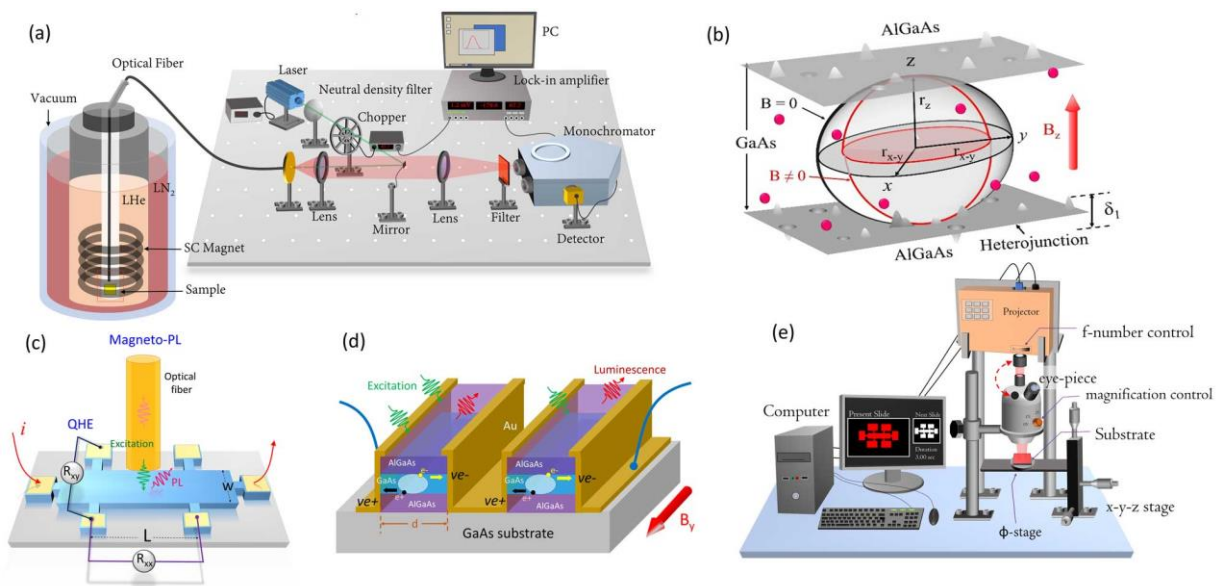


**Figure 1** (a) Schematic of the experimental setup for magneto-optical measurements and (b) magnetic field-driven spatial confinement of excitons in a QW. (c) Simultaneous measurement of magneto-PL and quantum Hall, (d) measurements of in-plane charge separation under a parallel magnetic field, and (e) schematic of the maskless-photolithography setup.

# Bibliography

- [1] N. Li, K. Han, W. Spratt, S. Bedell, J. Ott, M. Hopstaken, F. Libsch, Q. Li, and D. Sadana, *Nat. Photonics* **13**, 588 (2019).
- [2] G. C. Gardner, S. Fallahi, J. D. Watson, and M. J. Manfra, *Journal of Crystal Growth* **441**, 71 (2016).
- [3] S. Chen, W. Li, J. Wu, Q. Jiang, M. Tang, S. Shutts, S. N. Elliott, A. Sobiesierski, u. J. Seeds, I. Ross, et al., *Nat. Photonics* **10**, 307 (2016).
- [4] S. Bagheri, R. Talebzadeh, B. Sardari, and F. Mehdizadeh, *Optik* **199**, 163315 (2019).
- [5] B. M. Arora, A. Majumdar, A. P. Shah, M. Gokhale, S. Ghosh, A. Bhattacharya, and D. Sengupta, *Infrared physics & technology* **50**, 206 (2007).
- [6] Z. Wan, u. Kazakov, M. J. Manfra, L. N. Pfeiffer, K. W. West, and L. P. Rokhinson, *Nat. Commun.* **6**, 7426 (2015).
- [7] S. Saberi-Pouya, S. Conti, A. Perali, A. F. Croxall, u. R. Hamilton, F. M. Peeters, and D. Neilson, *arXiv preprint arXiv:1910.06631* (2019).
- [8] M. Lindemann, u. Xu, T. Pusch, R. Michalzik, M. R. Hofmann, I. Žutić, and N. C. Gerhardt, *Nature* **568**, 212 (2019).
- [9] C. Jones, M. A. Fogarty, A. Morello, M. F. Gyure, A. S. Dzurak, and T. D. Ladd, *Phys. Rev. X* **8**, 021058 (2018).
- [10] S. Prabhakar and R. Melnik, in *Nanomaterials for Security* (Springer, 2016), pp. 25–33.
- [11] T. Wagner, P. Strasberg, J. C. Bayer, E. P. Rugeramigabo, T. Brandes, and R. J. Haug, *Nat. Nanotechnol.* **12**, 218 (2017).
- [12] H. Wang, Z. C. Duan, Y. H. Li, S. Chen, J. P. Li, Y.-M. He, M. C. Chen, Y. He, X. Ding, C.-Z. Peng, et al., *Phys. Rev. Lett.* **116**, 213601 (2016).
- [13] D. Huber, M. Reindl, Y. Huo, H. Huang, J. S. Wildmann, O. G. Schmidt, A. Rastelli, and R. Trotta, *Nat. Commun.* **8**, 15506 (2017).

- [14] M. Rispler, P. Cerfontaine, V. Langrock, and B. M. Terhal, arXiv preprint arXiv:2002.05136 (2020).
- [15] M. A. Tito and Y. A. Pusep, J. Phys. D: Appl. Phys. **51**, 015304 (2017).
- [16] H. Dakhlaoui and M. Nefzi, Superlattices Microstruct. **136**, 106292 (2019).
- [17] F. Dybala, J. Kopaczek, M. Gladysiewicz, E.-M. Pavelescu, C. Romanitan, O. Ligor, A. Arnoult, C. Fontaine, and R. Kudrawiec, Appl. Phys. Lett. **111**, 192104 (2017).
- [18] Y. V. Terent'ev, S. Danilov, M. Durnev, J. Loher, D. Schuh, D. Bougeard, S. Ivanov, and S. Ganichev, J. Appl. Phys. **121**, 053904 (2017).
- [19] S. Harrison, M. P. Young, P. D. Hodgson, R. J. Young, M. Hayne, L. Danos, A. Schliwa, A. Strittmatter, A. Lenz, H. Eisele, et al., Phys. Rev. B **93**, 085302 (2016).
- [20] A. Arora, A. Mandal, S. Chakrabarti, and S. Ghosh, J. Appl. Phys. **113**, 213505 (2013).
- [21] S. Adachi, J. Appl. Phys. **58**, R1 (1985).
- [22] M. Levinshtein, *Handbook series on semiconductor parameters*, vol. 1 (World Scientific, 1997).
- [23] R. S. Knox, *Theory of excitons* (Academic Press, 1963).
- [24] J. Singh, *Excitation energy transfer processes in condensed matter: theory and applications* (Springer Science & Business Media, 2013).
- [25] L. C. L. Y. Voon and M. Willatzen, *The kp method: electronic properties of semiconductors* (Springer Science & Business Media, 2009).
- [26] L. C. Andreani and u. Pasquarello, Phys. Rev. B **42**, 8928 (1990).
- [27] A. Tiutiunnyk, I. Pérez-Quintana, D. Laroze, C. A. Duque, and M. E. Mora-Ramos, Appl. Phys. A **126**, 23 (2020).
- [28] A. Tiutiunnyk, I. Pérez-Quintana, D. Laroze, C. A. Duque, and M. E. Mora-Ramos, Appl. Phys. A **126**, 23 (2020).
- [29] Z.-H. Zhang, J.-H. Yuan, K.-X. Guo, and E. Feddi, Materials **12**, 78 (2019).
- [30] J. I. Pankove, *Optical processes in semiconductors* (Courier Corporation, 1975).
- [31] B. G. Streetman and S. K. Banerjee, *Solid state electronic devices* (Prentice-Hall, 2005).
- [32] G. H. Wannier, Phys. Rev. **52**, 191 (1937).
- [33] J. A. Frenkel, Phys. Rev. **37**, 1276 (1931).

- [34] J. Ding, M. Hagerott, P. Kelkar, A. V. Nurmikko, D. C. Grillo, L. He, J. Han, and R. L. Gunshor, Phys. Rev. B **50**, 5787 (1994).
- [35] E. Göbel, H. Herzog, M. H. Pilkuhn, and K. H. Zschauer, Solid State Commun. **13**, 719 (1973).
- [36] G. Grosso, J. Graves, A. T. Hammack, A. A. High, L. V. Butov, M. Hanson, and A. C. Gossard, Nat. Photon. **3**, 577 (2009).
- [37] Y. H. Huo, V. Křápek, O. G. Schmidt, and A. Rastelli, Phys. Rev. B **95**, 165304 (2017).
- [38] E. Poem, Y. Kodriano, C. Tradonsky, N. H. Lindner, B. D. Gerardot, P. M. Petroff, and D. Gershoni, Nat. Phys. **6**, 993 (2010).
- [39] I. Schwartz, E. Schmidgall, L. Gantz, D. Cogan, E. Bordo, Y. Don, M. Zielinski, and D. Gershoni, Phys. Rev. X **5**, 011009 (2015).
- [40] A. V. Trifonov, E. S. Khrantsov, K. V. Kavokin, I. V. Ignatiev, A. V. Kavokin, Y. P. Efimov, S. A. Eliseev, P. Y. Shapochkin, and M. Bayer, Phys. Rev. Lett. **122**, 147401 (2019).
- [41] R. Tempelaar and T. C. Berkelbach, Nat. Commun. **10**, 1 (2019).
- [42] H. Mathieu, P. Lefebvre, and P. Christol, Phys. Rev. B **46**, 4092 (1992).
- [43] D. J. Griffiths and D. F. Schroeter, *Introduction to quantum mechanics* (Cambridge University Press, 2018).
- [44] S. M. Sze and K. K. Ng, *Physics of semiconductor devices* (John Wiley & sons, 2006).
- [45] J. H. Davies, *The physics of low-dimensional semiconductors: an introduction* (Cambridge university press, 1998).
- [46] W. T. Masselink, P. J. Pearah, J. Klem, C. Peng, H. Morkoc, G. D. Sanders, and Y.-C. Chang, Phys. Rev. B **32**, 8027 (1985).
- [47] M. Fox, *Optical properties of solids* (2001).
- [48] M. Sugawara, N. Okazaki, T. Fujii, and S. Yamazaki, Phys. Rev. B **48**, 8848 (1993).
- [49] V. Voliotis, R. Grousson, P. Lavallard, and R. Planel, Phys. Rev. B **52**, 10725 (1995).
- [50] S. Das Sarma, R. Jalabert, and S. R. E. Yang, Phys. Rev. B **39**, 5516 (1989).
- [51] R. Pässler, Phys. Rev. B **66**, 085201 (2002).
- [52] N. Miura, *Physics of semiconductors in high magnetic fields*, vol. 15 (Oxford University Press, 2008).

- [53] G. Landwehr, *High Magnetic Fields in Semiconductor Physics: Proceedings of the International Conference, Würzburg, Fed. Rep. of Germany, August 18–22, 1986*, vol. 71 (Springer Science & Business Media, 2012).
- [54] T. JOUR, Wade, , G. Fedorov, D. Smirnov, S. Kumar, B. S. Williams, Q. Hu, and J. L. Reno, *Nat Photon* **3**, 41 (2009).
- [55] F. Valmorra, G. Scalari, K. Ohtani, M. Beck, and J. Faist, *New Journal of Physics* **17**, 023050 (2015).
- [56] K. Von Klitzing, *Rev. Mod. Phys.* **58**, 519 (1986).
- [57] F. Lafont, A. Rosenblatt, M. Heiblum, and V. Umansky, *Science* **363**, 54 (2019).
- [58] L. Du, I. Knez, G. Sullivan, and R.-R. Du, *Phys. Rev. Lett.* **114**, 096802 (2015).
- [59] G. B. Stringfellow, *Organometallic vapor-phase epitaxy: theory and practice* (Elsevier, 1999).
- [60] B. D. Cullity and S. R. Stock, *Elements of X-ray Diffraction*, vol. 3 (Prentice hall New Jersey, 2001).
- [61] J. Feldmann, G. Peter, E. O. Göbel, P. Dawson, K. Moore, C. Foxon, and R. J. Elliott, *Phys. Rev. Lett.* **59**, 2337 (1987).
- [62] H. Kawai, K. Kaneko, and N. Watanabe, *J. Appl. Phys.* **56**, 463 (1984).
- [63] L. Kronik and Y. Shapira, *Surface and Interface Analysis: An International Journal devoted to the development and application of techniques for the analysis of surfaces, interfaces and thin films* **31**, 954 (2001).
- [64] V. Donchev, K. Kirilov, T. Ivanov, and K. Germanova, *Materials Science and Engineering: B* **129**, 186 (2006).
- [65] T. K. Sharma and S. Kumar, *Appl. Phys. Lett.* **79**, 1715 (2001).
- [66] S. Datta, S. Ghosh, and B. M. Arora, *Review of Scientific Instruments* **72**, 177 (2001).
- [67] V. R. V. Pillai, S. K. Khamari, V. K. Dixit, T. Ganguli, S. Kher, and S. M. Oak, *Nuclear Instruments and Methods in Physics Research Section A: Accelerators, Spectrometers, Detectors and Associated Equipment* **685**, 41 (2012).
- [68] G. Brammertz, K. Martens, S. Sioncke, A. Delabie, M. Caymax, M. Meuris, and M. Heyns, *Appl. Phys. Lett.* **91**, 133510 (2007).
- [69] R. D. Diehl and R. L. Diehl, *High-power diode lasers: fundamentals, technology, applications*, vol. 78 (Springer Science & Business Media, 2000).

- [70] V. K. Dixit, S. K. Khamari, C. Tyagi, S. D. Singh, S. Porwal, R. Kumar, C. Mukherjee, P. Mondal, A. K. Srivastava, T. K. Sharma, et al., J. Phys. D: Appl. Phys. **45**, 365104 (2012).
- [71] S. K. Khamari, V. K. Dixit, T. Ganguli, S. Porwal, S. D. Singh, S. Kher, R. K. Sharma, and S. M. Oak, "Nucl. Instrum. Methods Phys. Res. B **269**, 272 (2011).
- [72] E. Peiner, A. Schlachetzki, and D. Krüger, Journal of the Electrochemical Society **142**, 576 (1995).
- [73] H. H. Wieder, *Laboratory Notes on Electrical and Galvanomagnetic Measurements. (Materials Science Monographs, 2.)* (Elsevier Scientific Publishing Co., 1979).
- [74] R. W. Shaw and D. E. Hill, Phys. Rev. B **1**, 658 (1970).
- [75] K. Y. Chen, C. T. Liang, D. R. Hang, L.-H. Lin, C. F. Huang, Y. H. Chang, C.-Y. Huang, J. C. Chen, C.-C. Tang, S.-F. Chen, et al., Physica E Low Dimens. Syst. Nanostruct. **44**, 1558 (2012).
- [76] R. Dingle, Proc. R. Soc. Lond. A **211**, 517 (1952).
- [77] K. Von Klitzing, Reviews of Modern Physics **58**, 519 (1986).
- [78] D. Tong, Centre for Mathematical Sciences, Cambridge (2016).
- [79] C. Vieu, F. Carcenac, A. Pepin, Y. Chen, M. Mejias, A. Lebib, L. Manin-Ferlazzo, L. Couraud, and H. Launois, Applied surface science **164**, 111 (2000).
- [80] E. Spille and R. Feder, in *X-ray Optics* (Springer, 1977), pp. 35–92.
- [81] R. G. Woodham, R. M. Jones, D. G. Hasko, J. R. A. Cleaver, and H. Ahmed, Micro-electronic Engineering **17**, 563 (1992).
- [82] H. I. Smith, R. Menon, A. Patel, D. Chao, M. Walsh, and G. Barbastathis, Microelectronic engineering **83**, 956 (2006).
- [83] A. Rodriguez, M. Echeverría, M. Ellman, N. Perez, Y. K. Verevkin, C. S. Peng, T. Berthou, Z. Wang, I. Ayerdi, J. Savall, et al., Microelectronic Engineering **86**, 937 (2009).
- [84] J. D. Musgraves, B. T. Close, and D. M. Tanenbaum, American journal of physics **73**, 980 (2005).
- [85] J. D. Musgraves, *Maskless Projection Lithography* (Pomona College, 2003).
- [86] K. Lambert, *A Maskless Photolithography Apparatus for the Microfabrication of Electrical Leads* (Linfield college, 2012).



- [87] V. K. Dixit, S. K. Khamari, S. Porwal, A. Chatterjee, G. Vashisht, S. Halder, A. Khakha, V. Agnihotri, R. Kumar, T. K. Sharma, et al., *Kiran* **27** (2016).
- [88] G. Vashisht, V. K. Dixit, S. Porwal, R. Kumar, T. K. Sharma, and S. M. Oak, *J. Appl. Phys.* **119**, 095708 (2016).
- [89] L. Kronik, L. Burstein, Y. Shapira, and M. Oron, *Appl. Phys. Lett.* **63**, 60 (1993).
- [90] J. Singh, K. K. Bajaj, and S. Chaudhuri, *Appl. Phys. Lett.* **44**, 805 (1984).
- [91] B. Bansal, M. Hayne, B. M. Arora, and V. V. Moshchalkov, *Appl. Phys. Lett.* **91**, 251108 (2007).
- [92] J. De Oliveira, E. A. Meneses, and E. Da Silva, *Phys. Rev. B* **60**, 1519 (1999).
- [93] I. Aksenov, J. Kusano, Y. Aoyagi, T. Sugano, T. Yasuda, and Y. Segawa, *Phys. Rev. B* **51**, 4278 (1995).
- [94] J. Singh, K. Bajaj, and S. Chaudhuri, *Appl. Phys. Lett.* **44**, 805 (1984).
- [95] J. Singh and K. Bajaj, *J. Appl. Phys.* **57**, 5433 (1985).
- [96] K. Akiyama, N. Tomita, Y. Nomura, and T. Isu, *Appl. Phys. Lett.* **75**, 475 (1999).
- [97] D. F. Nelson, R. C. Miller, and D. A. Kleinman, *Phys. Rev. B* **35**, 7770 (1987).
- [98] G. Pettinari, O. Drachenko, R. B. Lewis, and T. Tiedje, *Phys. Rev. B* **94**, 235204 (2016).
- [99] H. Zhu, K. Lai, D. C. Tsui, S. P. Bayrakci, N. P. Ong, M. Manfra, L. Pfeiffer, and K. West, *Solid State Commun.* **141**, 510 (2007).
- [100] J. Martinez-Pastor, A. Vinattieri, L. Carraresi, M. Colocci, P. Roussignol, and G. Weimann, *Phys. Rev. B* **47**, 10456 (1993).
- [101] Y. P. Varshni, *Physica* **34**, 149 (1967).
- [102] I. A. Vainshtein, A. F. Zatsepin, and V. S. Kortov, *Physics of the Solid State* **41**, 905 (1999).
- [103] U. Piespergen, in *Semiconductors and semimetals* (Elsevier, 1966), vol. 2, pp. 49–60.
- [104] Q. Li, S. J. Xu, M. H. Xie, and S. Y. Tong, *J. Phys. Condens. Matter* **17**, 4853 (2005).
- [105] V. K. Dixit, S. Porwal, S. D. Singh, T. K. Sharma, S. Ghosh, and S. M. Oak, *J. Phys. D Appl. Phys.* **47**, 065103 (2014).
- [106] R. Khordad and H. Bahramiyan, *J. Appl. Phys.* **115**, 124314 (2014).

- [107] E. M. Lopes, J. L. Duarte, I. Dias, E. Laureto, P. Guimaraes, A. Subtil, and u. A. Quivy, *J. Lumin.* **132**, 1183 (2012).
- [108] E. F. Schubert, E. O. Göbel, Y. Horikoshi, K. Ploog, and H. J. Queisser, *Phys. Rev. B* **30**, 813 (1984).
- [109] F. Adler, M. Geiger, A. Bauknecht, F. Scholz, H. Schweizer, M. Pilkuhn, B. Ohnesorge, and A. Forchel, *J. Appl. Phys.* **80**, 4019 (1996).
- [110] J. Christen, M. Grundmann, E. Kapon, E. Colas, D. Hwang, and D. Bimberg, *Appl. Phys. Lett.* **61**, 67 (1992).
- [111] B. Deveaud, F. Clérot, N. Roy, K. Satzke, B. Sermage, and D. S. Katzer, *Phys. Rev. Lett.* **67**, 2355 (1991).
- [112] I. Vurgaftman, J. R. Meyer, and L. R. Ram-Mohan, *J. Appl. Phys.* **89**, 5815 (2001).
- [113] M. B. Johnson, O. Albrechtsen, R. M. Feenstra, and H. W. M. Salemink, *Appl. Phys. Lett.* **63**, 2923 (1993).
- [114] M. B. Johnson, U. Maier, H.-P. Meier, and H. W. M. Salemink, *Appl. Phys. Lett.* **63**, 1273 (1993).
- [115] O. Albrechtsen, D. J. Arent, H. P. Meier, and H. W. M. Salemink, *Appl. Phys. Lett.* **57**, 31 (1990).
- [116] S. Gwo, K. J. Chao, and C. K. Shih, *Appl. Phys. Lett.* **64**, 493 (1994).
- [117] S. K. Lyo, E. D. Jones, and S. R. Kurtz, *J. Lumin.* **60**, 409 (1994).
- [118] C. He, Z. Qin, F. Xu, M. Hou, S. Zhang, L. Zhang, X. Wang, W. Ge, and B. Shen, *Sci. Rep.* **5** (2015).
- [119] T. Schmidt, K. Lischka, and W. Zulehner, *Phys. Rev. B* **45**, 8989 (1992).
- [120] S. Jin and A. Li, *J. Appl. Phys.* **81**, 7357 (1997).
- [121] M. Mosko, A. Moskova, and V. Cambel, *Phys. Rev. B* **51**, 16860 (1995).
- [122] S. Datta, B. M. Arora, and S. Kumar, *Phys. Rev. B* **62**, 13604 (2000).
- [123] S. Kumar, T. Ganguli, P. Bhattacharya, U. N. Roy, S. S. Chandvankar, and B. M. Arora, *Appl. Phys. Lett.* **72**, 3020 (1998).
- [124] T. Ivanov, V. Donchev, K. Germanova, and K. Kirilov, *J. Phys. D Appl. Phys.* **42**, 135302 (2009).
- [125] T. K. Sharma, S. Kumar, and K. C. Rustagi, *J. Appl. Phys.* **92**, 5959 (2002).

- [126] R. Roychowdhury, V. K. Dixit, G. Vashisht, T. K. Sharma, C. Mukherjee, S. K. Rai, and S. Kumar, *Applied Surface Science* **476**, 615 (2019).
- [127] M. Group, *Band engineering*, <http://my.ece.ucsb.edu/mgrundmann/bandeng.htm>.
- [128] W.-C. Liu, *J. Mater. Sci.* **25**, 1765 (1990).
- [129] L. Kronik and Y. Shapira, *Surface science reports* **37**, 1 (1999).
- [130] V. Donchev, K. Kirilov, T. Ivanov, and K. Germanova, *Materials Science and Engineering: B* **129**, 186 (2006).
- [131] S. Halder, V. K. Dixit, G. Vashisht, S. Porwal, and T. K. Sharma, *J. Appl. Phys.* **124**, 055704 (2018).
- [132] B. M. Arora, S. Ghosh, S. Datta, and S. Kumar, *Mater. Sci. Semicond. Process.* **4**, 489 (2001).
- [133] Y. Fang, L. Wang, Q. Sun, T. Lu, Z. Deng, Z. Ma, Y. Jiang, H. Jia, W. Wang, J. Zhou, et al., *Sci. Rep.* **5**, 12718 (2015).
- [134] T. K. Sharma, S. Kumar, and K. C. Rustagi, *J. Appl. Phys.* **92**, 5959 (2002).
- [135] I. T. Jeong, S. Ahn, D. H. Kim, J. C. Woo, and S. J. Rhee, *J. Korean. Phys. Soc.* **45**, 1181 (2004).
- [136] M. Hayne and B. Bansal, *Luminescence* **27**, 179 (2012).
- [137] R. L. Greene and K. K. Bajaj, *Solid State Commun* **45**, 831 (1983).
- [138] D. C. Rogers, J. Singleton, R. J. Nicholas, C. T. Foxon, and K. Woodbridge, *Phys. Rev. B* **34**, 4002 (1986).
- [139] J. C. Maan, G. Belle, A. Fasolino, M. Altarelli, and K. Ploog, *Phys. Rev. B* **30**, 2253 (1984).
- [140] R. C. Miller, D. A. Kleinman, and A. C. Gossard, *Phys. Rev. B* **29**, 7085 (1984).
- [141] S. S. Dosanjh, E. F. Bowser, and J. J. Harris, *Appl. Phys. Lett.* **64**, 2142 (1994).
- [142] S. N. Chaudhuri and K. K. Bajaj, *Phys. Rev. B* **29**, 1803 (1984).
- [143] T. Hiroshima and R. Lang, *Appl. Phys. Lett.* **49**, 456 (1986).
- [144] K. H. Yoo, L. R. Ram-Mohan, and D. F. Nelson, *Phys. Rev. B* **39**, 12808 (1989).
- [145] M. de Dios-Leyva, E. Reyes-Gómez, C. A. Perdomo-Leiva, and L. E. Oliveira, *Phys. Rev. B* **73**, 085316 (2006).

- [146] V. G. Golubev, V. I. Ivanov-Omskii, I. G. Minervin, A. Osutin, and D. Polyakov, *Sov. Phys. JETP* **88**, 2052 (1985).
- [147] B. D. McCombe, *Phys. Rev.* **181**, 1206 (1969).
- [148] G. Bastard, *Phys. Rev. B* **24**, 5693 (1981).
- [149] N. Kotera, *J. Appl. Phys.* **113**, 234314 (2013).
- [150] J. Lee, E. S. Koteles, and M. Vassell, *Phys. Rev. B* **33**, 5512 (1986).
- [151] A. Persson and R. M. Cohen, *Phys. Rev. B* **38**, 5568 (1988).
- [152] U. Ekenberg, *Phys. Rev. B* **40**, 7714 (1989).
- [153] A. Raymond, J. L. Robert, and C. Bernard, *J. Phys. C* **12**, 2289 (1979).
- [154] C. R. Pidgeon and R. N. Brown, *Phys. Rev.* **146**, 575 (1966).
- [155] G. C. La Rocca and M. Cardona, *Physica status solidi (b)* **167**, 115 (1991).
- [156] E. Ivchenko, A. Y. Kaminski, and U. Rössler, *Phys. Rev. B* **54**, 5852 (1996).
- [157] J. Singh and K. K. Bajaj, *J. Appl. Phys.* **57**, 5433 (1985).
- [158] S. Halder, V. K. Dixit, G. Vashisht, S. K. Khamari, S. Porwal, T. K. Sharma, and S. M. Oak, *Sci. Rep.* **7**, 4905 (2017).
- [159] M. Kozhevnikov, B. Ashkinadze, E. Cohen, and A. Ron, *Phys. Rev. B* **52**, 17165 (1995).
- [160] B. Shojaei, A. C. C. Drachmann, M. Pendharkar, D. J. Pennachio, M. P. Echlin, P. G. Callahan, S. Kraemer, T. M. Pollock, C. M. Marcus, and C. J. Palmstrøm, *Phys. Rev. B* **94**, 245306 (2016).
- [161] G. Vashisht, V. K. Dixit, S. Halder, and T. K. Sharma, *J. Lumin.* **206**, 342 (2019).
- [162] T. S. Shamirzaev, J. Debus, D. R. Yakovlev, M. M. Glazov, E. L. Ivchenko, and M. Bayer, *Phys. Rev. B* **94**, 045411 (2016).
- [163] J. Shao, Z. Qi, H. Zhao, L. Zhu, Y. Song, X. Chen, F.-X. Zha, S. Guo, and S. M. Wang, *J. Appl. Phys.* **118**, 165305 (2015).
- [164] Y. I. Mazur, M. D. Teodoro, L. Dias de Souza, M. E. Ware, D. Fan, S.-Q. Yu, G. G. Tarasov, G. E. Marques, and G. J. Salamo, *J. Appl. Phys.* **115**, 123518 (2014).
- [165] A. Hatke, M. A. Zudov, J. D. Watson, M. J. Manfra, L. N. Pfeiffer, and K. W. West, *Phys. Rev. B* **87**, 161307 (2013).

- [166] S. Haldar, V. K. Dixit, G. Vashisht, S. Porwal, and T. K. Sharma, *J. Phys. D: Appl. Phys.* **50**, 335107 (2017).
- [167] M. Sugawara, *Phys. Rev. B* **45**, 11423 (1992).
- [168] M. J. Manfra, *Annu. Rev. Condens. Matter Phys.* **5**, 347 (2014).
- [169] T. Damen, J. Shah, D. Oberli, D. Chemla, J. Cunningham, and J. Kuo, *Phys. Rev. B* **42**, 7434 (1990).
- [170] M. Gulia, F. Rossi, E. Molinari, P. E. Selbmann, and P. Lugli, *Phys. Rev. B* **55**, R16049 (1997).
- [171] B. Monemar, H. Kalt, C. Harris, J. P. Bergman, P. O. Holtz, M. Sundaram, J. L. Merz, A. C. Gossard, K. Köhler, and T. Schweizer, *Superlattices Microstruct.* **9**, 281 (1991).
- [172] J. P. Eisenstein, H. L. Stormer, V. Narayanamurti, A. Y. Cho, A. C. Gossard, and C. W. Tu, *Phys. Rev. Lett.* **55**, 875 (1985).
- [173] M. E. Raikh and T. V. Shahbazyan, *Phys. Rev. B* **47**, 1522 (1993).
- [174] J. F. Ryan, *Physica B+ C* **134**, 403 (1985).
- [175] X. Yao and u. Belyanin, *Journal of Physics: Condensed Matter* **25**, 054203 (2013).
- [176] K. Mukai, N. Ohtsuka, H. Shoji, and M. Sugawara, *Appl. Phys. Lett.* **68**, 3013 (1996).
- [177] M. Grundmann and D. Bimberg, *Phys. Rev. B* **55**, 9740 (1997).
- [178] T. A. Vaughan, R. J. Nicholas, C. Langerak, B. N. Murdin, C. R. Pidgeon, N. J. Mason, and P. J. Walker, *Phys. Rev. B* **53**, 16481 (1996).
- [179] C. Becker, A. Vasanelli, C. Sirtori, and G. Bastard, *Phys. Rev. B* **69**, 115328 (2004).
- [180] M. Dahl, D. Heiman, A. Pinczuk, B. B. Goldberg, L. N. Pfeiffer, and K. W. West, *Phys. Rev. B* **45**, 6957 (1992).
- [181] B. Tavares, M. Tito, and Y. A. Pusep, *J. Appl. Phys.* **119**, 234305 (2016).
- [182] T. R. Merritt, M. A. Meeker, B. A. Magill, G. A. Khodaparast, S. McGill, J. G. Tischler, S. G. Choi, and C. J. Palmstrøm, *J. Appl. Phys.* **115**, 193503 (2014).
- [183] L. Sapienza, R. Al Khuzheyri, A. Dada, A. Griffiths, E. Clarke, and B. D. Gerardot, *Phys. Rev. B* **93**, 155301 (2016).
- [184] J. Bellessa, V. Voliotis, R. Grousson, X. Wang, M. Ogura, and H. Matsuhata, *Phys. Rev. B* **58**, 9933 (1998).

- [185] D. C. Rogers, J. Singleton, R. J. Nicholas, C. T. Foxon, and K. Woodbridge, *Phys. Rev. B* **34**, 4002 (1986).
- [186] W. Van der Poel, L. W. Molenkamp, C. T. Foxon, and Others, *Phys. Rev. B* **35**, 8281 (1987).
- [187] A. Higo, T. Kiba, Y. Tamura, C. Thomas, J. Takayama, Y. Wang, H. Sodabanlu, M. Sugiyama, Y. Nakano, I. Yamashita, et al., *Sci. Rep.* **5**, 9371 (2015).
- [188] J. D. Lambkin, D. J. Dunstan, K. P. Homewood, L. K. Howard, and M. T. Emeny, *Appl. Phys. Lett.* **57**, 1986 (1990).
- [189] G. Bacher, H. Schweizer, J. Kovac, A. Forchel, H. Nickel, W. Schlapp, and R. Lösch, *Phys. Rev. B* **43**, 9312 (1991).
- [190] D. J. Moss, T. Ido, and H. Sano, *IEEE journal of quantum electronics* **30**, 1015 (1994).
- [191] M. Gurioli, A. Vinattieri, M. Colocci, C. Deparis, J. Massies, G. Neu, A. Bosacchi, and S. Franchi, *Phys. Rev. B* **44**, 3115 (1991).
- [192] B. Ridley, *Phys. Rev. B* **41**, 12190 (1990).
- [193] P. Wang, K. K. Lee, G. Yao, Y. C. Chen, and R. G. Waters, *Appl. Phys. Lett.* **56**, 2083 (1990).
- [194] R. Steed, M. Matthews, J. Plumridge, M. Frogley, C. Phillips, Z. Ikonc, P. Harrison, O. Malis, L. N. Pfeiffer, and K. W. West, *Appl. Phys. Lett.* **92**, 183104 (2008).
- [195] L. Hrivnák, *Appl. Phys. Lett.* **56**, 2425 (1990).
- [196] Y. Kajikawa, M. Hata, N. Sugiyama, and Y. Katayama, *Phys. Rev. B* **42**, 9540 (1990).
- [197] C. Jiang, W. Xu, A. Rasmita, Z. Huang, K. Li, Q. Xiong, and W.-b. Gao, *Nature commun.* **9**, 753 (2018).
- [198] R. Shen, H. Mino, G. Karczewski, T. Wojtowicz, J. Kossut, and S. Takeyama, *J Lumin.* **112**, 204 (2005).
- [199] J.-W. Wang and S.-S. Li, *Appl. Phys. Lett.* **92**, 012106 (2008).
- [200] M. Fritze, I. E. Perakis, A. Getter, W. Knox, K. W. Goossen, J. E. Cunningham, and S. Jackson, *Phys. Rev. Lett.* **76**, 106 (1996).
- [201] K. Chang and F. M. Peeters, *Phys. Rev. B* **63**, 153307 (2001).
- [202] S.-L. Tyan, P. A. Shields, R. J. Nicholas, F.-Y. Tsai, and C.-P. Lee, *Japanese J. Appl. Phys.* **39**, 3286 (2000).

- [203] S. Y. Bodnar, P. Grigoryev, D. K. Loginov, V. G. Davydov, Y. P. Efimov, S. A. Eliseev, V. A. Lovtcius, E. V. Ubyivovk, V. Y. Mikhailovskii, and I. V. Ignatiev, *Phys. Rev. B* **95**, 195311 (2017).
- [204] A. Fasolino, G. Platero, M. Potemski, J. C. Maan, K. Ploog, and G. Weimann, *Surf. Sci.* **267**, 509 (1992).
- [205] J.-B. Xia and W.-J. Fan, *Phys. Rev. B* **40**, 8508 (1989).
- [206] L. V. Butov, A. V. Mintsev, Y. E. Lozovik, K. L. Campman, and G. A. C, *Phys. Rev. B* **62**, 1548 (2000).
- [207] B. L. V., L. C. W., C. D. S., Lozovik, Y. E., C. K. L., and G. A. C., *Phys. Rev. Lett.* **87**, 216804 (2001).
- [208] Y. Sidor, B. Partoens, and F. M. Peeters, *Phys. Rev. B* **71**, 165323 (2005).
- [209] A. Ney, J. S. Harris, and S. S. P. Parkin, *J. Phys. Condens. Matter* **18**, 4397 (2006).
- [210] I. Žutić, J. Fabian, and S. D. Sarma, *Rev. Mod. Phys.* **76**, 323 (2004).
- [211] H. Yu and W. Yao, *Nat. Mater.* **16**, 876 (2017).
- [212] T. Frey, M. Maier, J. Schneider, and M. Gehrke, *Journal of Physics C: Solid State Physics* **21**, 5539 (1988).
- [213] T. Hesjedal, U. Kretzer, and A. Ney, *Semicond. Sci. Technol.* **27**, 055018 (2012).
- [214] E. Kilicarslan, S. Sakiroglu, M. Koksall, H. Sari, and I. Sokmen, *Physica E Low Dimens Syst Nanostruct.* **42**, 1531 (2010).
- [215] N. M. Irulayee and K. N. Krishnan, *Physica E Low Dimens Syst Nanostruct.* **41**, 193 (2008).
- [216] M. Wilde, J. Springborn, C. Heyn, D. Heitmann, and D. Grundler, *Physica E Low Dimens. Syst. Nanostruct.* **22**, 729 (2004).
- [217] A. K. Pramanik and A. Banerjee, *J. Phys. Condens. Matter* **28**, 35LT02 (2016).
- [218] Y. Sidor, B. Partoens, F. M. Peeters, J. Maes, M. Hayne, D. Fuster, Y. Gonzalez, L. Gonzalez, and V. V. Moshchalkov, *Phys. Rev. B* **76**, 195320 (2007).
- [219] A. N. Priest, R. J. Nicholas, S. P. Najda, G. Duggan, and A. H. Kean, *Physica E Low Dimens. Syst. Nanostruct.* **2**, 237 (1998).
- [220] P. Le Jeune, D. Robart, X. Marie, T. Amand, M. Brousseau, J. Barrau, V. Kalevich, and D. Rodichev, *Semicond. Sci. Technol.* **12**, 380 (1997).

- [221] M. J. Snelling, E. Blackwood, C. J. McDonagh, R. T. Harley, and C. T. B. Foxon, Phys. Rev. B **45**, 3922 (1992).
- [222] I. V. Lerner and Y. E. Lozovik, Sov. Phys. JETP, **51**, 588 (1980).
- [223] S. Harrison, M. P. Young, P. D. Hodgson, R. J. Young, M. Hayne, L. Danos, A. Schliwa, A. Strittmatter, A. Lenz, H. Eisele, et al., Phys. Rev. B **93**, 085302 (2016).
- [224] J. C. Maan, G. Belle, A. Fasolino, M. Altarelli, and K. Ploog, Phys. Rev. B **30**, 2253 (1984).
- [225] C. Y.-P. Chao and S. L. Chuang, Phys. Rev. B **48**, 8210 (1993).
- [226] X. Yin, H.-M. Chen, F. H. Pollak, Y. Chan, P. A. Montano, P. D. Kirchner, G. D. Pettit, and J. Woodall, Appl. Phys. Lett. **58**, 260 (1991).
- [227] S. Halder, V. K. Dixit, G. Vashisht, S. Porwal, and T. K. Sharma, J. Appl. Phys. **124**, 055704 (2018).
- [228] V. K. Dixit, S. D. Singh, T. K. Sharma, T. Ganguli, R. Jangir, S. Pal, B. Q. Khattak, A. K. Srivastava, H. Srivastava, and S. M. Oak, in *Physics of Semiconductor Devices, 2007. IWPSD 2007. International Workshop on* (IEEE, 2007), pp. 355–358.
- [229] K. M. Yu, W. Walukiewicz, T. Wojtowicz, W. L. Lim, X. Liu, Y. Sasaki, M. Dobrowolska, and J. K. Furdyna, Appl. Phys. Lett. **81**, 844 (2002).
- [230] S. Hudgens, M. Kastner, and H. Fritzsche, Phys. Rev. Lett. **33**, 1552 (1974).
- [231] P. Nithiananthi and K. Jayakumar, Solid State Commun. **137**, 427 (2006).
- [232] X. L. Zheng, D. Heiman, and B. Lax, Phys. Rev. B **40**, 10523 (1989).
- [233] D. Chadi, R. White, and W. Harrison, Phys. Rev. Lett. **35**, 1372 (1975).
- [234] R. L. Samaraweera, H.-C. Liu, B. Gunawardana, A. Kriisa, C. Reichl, W. Wegscheider, and R. G. Mani, Sci. Rep. **8**, 10061 (2018).
- [235] L. C. Tung, X. G. Wu, L. N. Pfeiffer, K. W. West, and Y. J. Wang, J. Appl. Phys. **108**, 083502 (2010).
- [236] V. V. Vainberg, A. S. Pylypchuk, V. N. Poroshin, O. G. Sarbey, N. V. Baidus, and A. A. Biryukov, Physica E Low Dimens. Syst. Nanostruct. **60**, 31 (2014).
- [237] T. Chakraborty and P. Pietiläinen, *The quantum Hall effects: integral and fractional*, vol. 85 (Springer Science & Business Media, 2013).



- [238] S. Y. Chou, D. A. Antoniadis, and H. I. Smith, IEEE Transactions on Electron Devices **34**, 883 (1987).
- [239] M. J. Kane, N. Apsley, D. A. Anderson, L. L. Taylor, and T. Kerr, J Physics C: Solid State Physics **18**, 5629 (1985).
- [240] M. Grayson and F. Fischer, J. Appl. Phys. **98**, 013709 (2005).
- [241] D. A. Syphers, K. P. Martin, and R. J. Higgins, Appl. Phys. Lett. **49**, 534 (1986).
- [242] V. K. Dixit, T. K. Sharma, T. Ganguli, S. D. Singh, R. Kumar, S. Porwal, A. K. Nath, B. Karmakar, A. P. Shah, and B. M. Arora, in *Proceedings of the DAE solid state physics symposium. V. 51* (2006), vol. 38.
- [243] A. F. Bangura, J. D. Fletcher, A. Carrington, J. Levallois, M. Nardone, B. Vignolle, P. J. Heard, N. Doiron-Leyraud, D. LeBoeuf, L. Taillefer, et al., Phys. Rev. Lett. **100**, 047004 (2008).
- [244] I. V. Soldatov, A. V. Germanenko, and N. Kozlova, Physica E Low Dimens. Syst. Nanostruct. **57**, 193 (2014).
- [245] S. Peters, L. Tiemann, C. Reichl, and W. Wegscheider, Phys. Rev. B **94**, 045304 (2016).
- [246] L. J. Cui, Y. P. Zeng, Y. Zhang, W. Z. Zhou, L. Y. Shang, T. Lin, and J. H. Chu, Physica E Low Dimens. Syst. Nanostruct. **83**, 114 (2016).
- [247] J. C. Blancon, A. V. Stier, H. Tsai, W. Nie, C. C. Stoumpos, B. Traoré, L. Pedesseau, M. Kepenekian, F. Katsutani, G. T. Noe, et al., Nat. Commun. **9**, 2254 (2018).
- [248] M. Zybert, M. Marchewka, E. M. Sheregii, D. G. Rickel, J. B. Betts, F. F. Balakirev, M. Gordon, A. V. Stier, C. H. Mielke, P. Pfeffer, et al., Phys. Rev. B **95**, 115432 (2017).
- [249] B. B. Goldberg, D. Heiman, A. Pinczuk, C. W. Tu, A. C. Gossard, and J. H. English, Surf. Sci. **196**, 209 (1988).
- [250] I. V. Kukushkin, K. v. Klitzing, and K. Ploog, Phys. Rev. B **37**, 8509 (1988).
- [251] D. J. Lockwood and A. Pinczuk, *Optical phenomena in semiconductor structures of reduced dimensions*, vol. 248 (Springer Science & Business Media, 2012).
- [252] G. R. Johnson, B. Cavenett, A. Kana'ah, E. J. Pakulis, and W. I. Wang, Appl. Phys. Lett. **50**, 1512 (1987).
- [253] M. Dahl, D. Heiman, A. Pinczuk, B. Goldberg, L. N. Pfeiffer, and K. West, Surf. Sci. **263**, 638 (1992).

- [254] H. A. Zarem, P. C. Sercel, J. A. Lebens, L. E. Eng, A. Yariv, and K. J. Vahala, *Appl. Phys. Lett.* **55**, 1647 (1989).
- [255] P. C. Sercel, H. A. Zarem, J. A. Lebens, L. E. Eng, A. Yariv, and K. J. Vahala, in *International Technical Digest on Electron Devices Meeting* (IEEE, 1989), pp. 285–288.
- [256] J. Nakamura, S. Fallahi, H. Sahasrabudhe, R. Rahman, S. Liang, G. C. Gardner, and M. J. Manfra, *Nat. Phys.* (2019).
- [257] V. K. Dixit, S. D. Singh, S. Porwal, R. Kumar, T. Ganguli, A. K. Srivastava, and S. M. Oak, *J. Appl. Phys.* **109**, 083702 (2011).
- [258] S. Halder, G. Vashisht, U. K. Ghosh, Ghosh, A. K. Jaiswal, S. Porwal, A. Khakha, T. K. Sharma, and V. K. Dixit, *DAE-SSPS AIP Conf. Proc.* **2115**, 030219 (2019).
- [259] N. Tang, B. Shen, Z. W. Zheng, J. Liu, D. Chen, J. Lu, R. Zhang, Y. Shi, Y. D. Zheng, Y. S. Gui, et al., *J. Appl. Phys.* **94**, 5420 (2003).
- [260] D. Y. Oberli, M. V. Klein, T. Henderson, D. R. Wake, and H. Morkoç, in *Hot Carriers in Semiconductors* (Elsevier, 1988), pp. 413–418.
- [261] A. Seilmeier, M. Wörner, G. Abstreiter, G. Weimann, and W. Schlapp, *Superlattices Microstruct.* **5**, 569 (1989).
- [262] S. Hunsche, K. Leo, H. Kurz, and K. Köhler, *Phys. Rev. B* **50**, 5791 (1994).
- [263] I. Lo, M. J. Kao, W. C. Hsu, K. K. Kuo, Y. C. Chang, H. M. Weng, J.-C. Chiang, and S.-F. Tsay, *Phys. Rev. B* **54**, 4774 (1996).
- [264] S. J. MacLeod, K. Chan, T. P. Martin, A. R. Hamilton, A. See, A. P. Micolich, M. Aagesen, and P. E. Lindelof, *Phys. Rev. B* **80**, 035310 (2009).
- [265] D. Reuter, M. Versen, M. D. Schneider, and A. D. Wieck, *J. Appl. Phys.* **88**, 321 (2000).
- [266] E. H. Hwang and S. D. Sarma, *Phys. Rev. B* **77**, 235437 (2008).
- [267] F. Stern and S. D. Sarma, *Phys. Rev. B* **30**, 840 (1984).
- [268] S. Mori and T. Ando, *Phys. Rev. B* **19**, 6433 (1979).
- [269] M. Hartig, J. D. Ganiere, P. E. Selbmann, B. Deveaud, and L. Rota, *Phys. Rev. B* **60**, 1500 (1999).
- [270] E. H. Hwang and S. D. Sarma, *Phys. Rev. B* **77**, 235437 (2008).
- [271] V. T. Renard, I. V. Gornyi, O. A. Tkachenko, V. A. Tkachenko, Z. D. Kvon, E. B. Olshanetsky, A. I. Toropov, and J. C. Portal, *Phys. Rev. B* **72**, 075313 (2005).

- [272] A. P. Dmitriev, V. Y. Kachorovskii, and I. V. Gornyi, *Phys. Rev. B* **56**, 9910 (1997).
- [273] D. C. Rogers, J. Singleton, R. J. Nicholas, C. T. Foxon, and K. Woodbridge, *Phys. Rev. B* **34**, 4002 (1986).
- [274] K. Betzler, B. Zhurkin, and A. Karuzskii, *Solid State Commun.* **17**, 577 (1975).
- [275] R. L. Byer, *Science* **239**, 742 (1988).
- [276] A. Castellano, L. Cerutti, J. B. Rodriguez, G. Narcy, A. Garreau, F. Lelarge, and E. Tournié, *APL Photonics* **2**, 061301 (2017).
- [277] D. A. Veselov, K. R. Ayusheva, N. A. Pikhtin, A. V. Lyutetskiy, S. O. Slipchenko, and I. S. Tarasov, *J. Appl. Phys.* **121**, 163101 (2017).
- [278] A. F. Castiglia, M. Rossetti, D. Marcus, and C. Velez, *Low power edge-emitting laser diode and laser diode module* (2019), uS Patent 10,193,310.
- [279] S. Li, Q. Gong, C. Cao, X. Wang, L. Yue, Y. Wang, and H. Wang, *Superlattices Microstruct.* **59**, 97 (2013).
- [280] R. M. France, P. Espinet-Gonzalez, B. B. Haidet, K. Mukherjee, H. L. Guthrey, H. A. Atwater, and D. Walker, *IEEE Journal of Photovoltaics* **10**, 103 (2019).
- [281] Geetanjali, S. Porwal, R. Kumar, V. K. Dixit, T. K. Sharma, and S. M. Oak, in *AIP Conference Proceedings* (AIP Publishing LLC, 2016), vol. 1731, p. 120033.
- [282] V. K. Dixit, A. Marathe, G. Bhatt, S. K. Khamari, K. Rajiv, R. Kumar, C. Mukherjee, C. J. Panchal, T. K. Sharma, and S. M. Oak, *J. Phys. D: Appl. Phys.* **48**, 105102 (2015).
- [283] Y. Arakawa, K. Vahala, A. Yariv, and K. Lau, *Appl. Phys. Lett.* **48**, 384 (1986).
- [284] D. Beznosko, G. Blazey, A. Dyshkant, V. Rykalin, and V. Zutshi, *Nuclear Instruments and Methods in Physics Research Section A: Accelerators, Spectrometers, Detectors and Associated Equipment* **553**, 438 (2005).
- [285] K. L. Jahan, A. Boda, I. Shankar, C. N. Raju, and A. Chatterjee, *Sci. Rep.* **8**, 1 (2018).
- [286] H. Takahashi, A. Quema, R. Yoshioka, S. Ono, and N. Sarukura, *Appl. Phys. Lett.* **83**, 1068 (2003).
- [287] A. Danicc, J. Radovanovic, V. Milanovic, D. Indjin, and Z. Ikonic, *Physica E: Low-dimensional Systems and Nanostructures* **81**, 275 (2016).
- [288] A. Leuliet, A. Vasanelli, A. Wade, G. Fedorov, D. Smirnov, G. Bastard, and C. Sirtori, *Phys. Rev. B* **73**, 085311 (2006).

- [289] C. Yu, L. Li, T. F. Xu, B. Zhang, X. Luo, and W. Lu, *AIP Advances* **8**, 125014 (2018).
- [290] R. Cardinale, C. D'Ambrosio, R. Forty, C. Frei, T. Gys, A. Petrolini, D. Piedigrossi, B. Storaci, and M. Villa, *Journal of Instrumentation* **6**, P06010 (2011).
- [291] M. Bonesini, F. Strati, G. Baccaglioni, F. Broggi, G. Volpini, G. Cecchet, A. DeBari, R. Nardo, M. Rossella, S. Dussoni, et al., *Nuclear Instruments and Methods in Physics Research Section A: Accelerators, Spectrometers, Detectors and Associated Equipment* **567**, 200 (2006).
- [292] R. Hawkes, A. Lucas, J. Stevick, G. Llosa, S. Marcatili, C. Piemonte, A. Del Guerra, and T. A. Carpenter, in *2007 IEEE Nuclear Science Symposium Conference Record* (IEEE, 2007), vol. 5, pp. 3400–3403.
- [293] S. Komiyama, O. Astafiev, V. Antonov, T. Kutsuwa, and H. Hirai, *Nature* **403**, 405 (2000).
- [294] L. R. Schreiber and H. Bluhm, *Science* **359**, 393 (2018).
- [295] T. Tanttu, B. Hensen, K. W. Chan, C. H. Yang, W. W. Huang, M. Fogarty, F. Hudson, K. Itoh, D. Culcer, A. Laucht, et al., *Phys. Rev. X* **9**, 021028 (2019).
- [296] R. de Sousa, X. Hu, and S. D. Sarma, *Phys. Rev. A* **64**, 042307 (2001).
- [297] T. K. Sharma, T. Ganguli, V. K. Dixit, S. D. Singh, S. Pal, S. Porwal, R. Kumar, A. Khakha, R. Jangir, V. Kheraj, et al., *arXiv preprint arXiv:1412.1568* (2014).
- [298] I. Bonalde, E. Medina, M. Rodriguez, S. Wasim, G. Marin, C. Rincón, A. Rincón, and C. Torres, *Phys. Rev. B* **69**, 195201 (2004).
- [299] B. S. Ryvkin and E. A. Avrutin, *J. Appl. Phys.* **98**, 026107 (2005).
- [300] M. K. Das and N. Das, *J. Appl. Phys.* **105**, 093118 (2009).
- [301] P. Martyniuk, D. Benyahia, A. Kowalewski, L. Kubiszyn, D. Stepien, W. Gawron, and A. Rogalski, *Solid-State Electronics* **119**, 1 (2016).
- [302] A. Dwivedi, *J. Appl. Phys.* **110**, 043101 (2011).

# Appendix A

In this study, excitation power-dependent magneto-PL spectroscopy is performed on a 150 Å thick GaAs/AlGaAs modulation-doped QW. The silane precursor is used to dope Si atoms in AlGaAs barriers, with a typical donor density of  $\sim 1 \times 10^{17} \text{ cm}^{-3}$ . The separation between the doped AlGaAs layers and the GaAs-QW is kept approximately 1100 Å, which help in reducing the ionized donor scattering. The electrons from the doped AlGaAs diffuse in the neighboring layers and accumulate in the QW region. The energy-band diagram of the sample is evaluated by solving the Schrödinger-Poisson equation, Fig. 1a. Figure 1b shows the PL spectra of the QW under two different laser excitation power densities ( $p_{exc}$ ), i.e., 0.5 and 2 W/cm<sup>2</sup>. It is observed that the spectral line-shape is convoluted with two partially merged PL features. The PL peak at higher energy side of the spectra is assigned to the electron-heavy hole excitonic recombination ( $FX_{HH}$ ), whereas the peak at lower energy side is contributed by the recombination of negatively charged excitons, i.e., trions ( $X_{HH}^-$ ), Fig. 1b. The separation between  $FX_{HH}$  and  $X_{HH}^-$  is found to be  $\sim 1.6 \text{ meV}$ , which is the measure of binding energy of

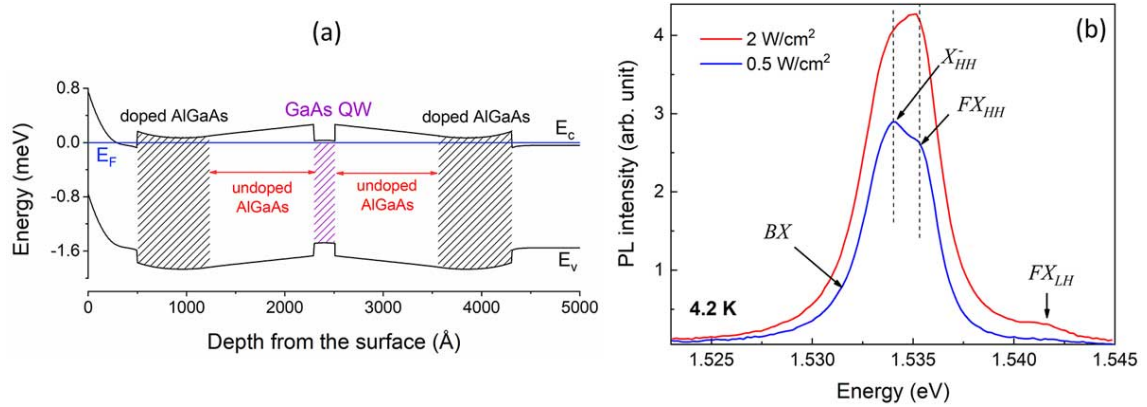


Figure 1: (a) Energy-band structure of the modulation-doped QW and (b) PL spectra of the QW under two different excitation power densities at 4.2 K.

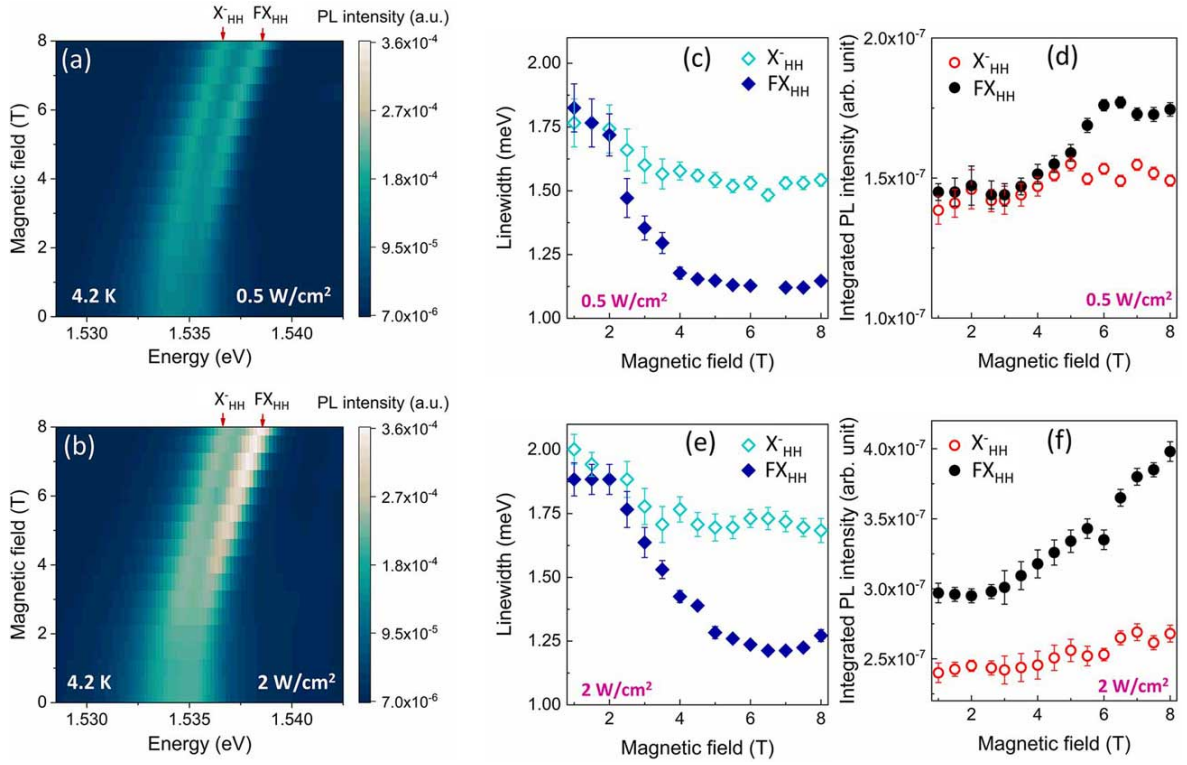


Figure 2: Magneto-PL spectra under two different excitation powers, (a) 0.5 and (b) 2 W/cm<sup>2</sup>. (c) The linewidth and (d) intensity of  $FX_{HH}$  and  $X_{HH}^-$  transitions as a function of the magnetic field under  $p_{exc} = 0.5$  W/cm<sup>2</sup>. The variations of PL linewidth and intensity related to the two features under  $p_{exc} = 2$  W/cm<sup>2</sup> are plotted in figure (e) and (f).

trions. In past, a similar order of  $\varepsilon_b$  of trions for a GaAs QW has been theoretically and experimentally estimated by many groups [Phys. Rev. B **53**, R1709 (1996)][Physica status solidi (b) **221**, 281 (2000)]. Note that Si atoms being remotely doped in AlGaAs layers (Fig. 1a), the observed PL features corresponding to the QW can not be influenced by ionized donor states. It is observed that the PL intensity related to  $FX_{HH}$  and  $X_{HH}^-$  transitions increases with an enhancement of  $p_{exc}$ . However, increase of PL intensity with  $p_{exc}$  is found to be significant for  $FX_{HH}$  transition as compared to the  $X_{HH}^-$  feature. Such an observation indicates that the formation of excitons largely depends on the photo-generated electron-hole pair density in the QW. On the contrary, the intrinsic carrier density in the QW decides the formation of trions and their radiative recombination efficiency.

To realize the optical response and stability of excitonic quasi-particles under an

external perturbation, magneto-PL spectroscopy is performed under the same excitation powers of laser light, Figs. 2a and 2b. The variations of PL linewidth and intensity of  $FX_{HH}$  and  $X_{HH}^-$  transitions as a function of the magnetic field are plotted in Figs. 2(c-f). At  $p_{exc} = 0.5 \text{ W/cm}^2$ , it is observed that the magnetic field driven enhancement of PL intensity and decrease in PL linewidth are feeble for  $X_{HH}^-$  transition than the  $FX_{HH}$  feature (Figs. 2c and 2d). Such a variation becomes even more distinct under a high power light illumination ( $2 \text{ W/cm}^2$ ) when a dramatic enhancement of  $FX_{HH}$  PL intensity is observed with an increase in the magnetic field. On the contrary, in the case of  $X_{HH}^-$  transition, the magnetic field driven enhancement of PL intensity and reduction of PL linewidth is found to be invariant under the two excitation powers (Figs. 2d and 2f).

The magnetic field driven shift in PL peaks are also estimated by the use of Figs. 2a and b, which is then plotted in Fig. 3. Careful observation shows that the diamagnetic shift of  $FX_{HH}$  peak slightly varies under the two-excitation powers (Fig. 3). However, such a variation could not be observed for the diamagnetic shift of  $X_{HH}^-$  transition. In summary, the results obtained by excitation power-dependent magneto-PL spectroscopy suggest that optical and fundamental properties of trions primarily depend on the intrinsic carrier density in the QW, which are stable under an external perturba-

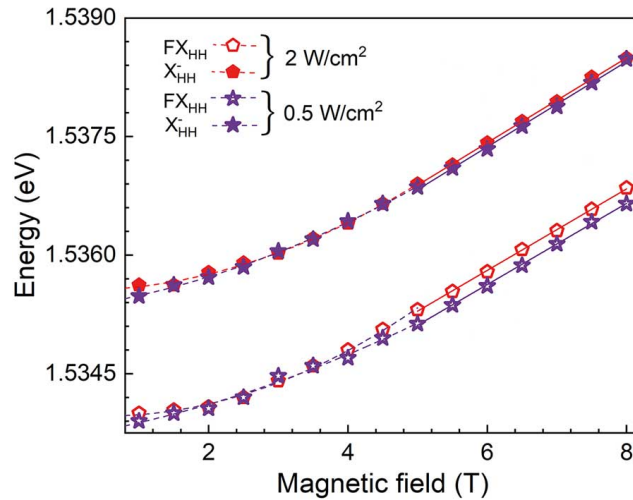


Figure 3: Diamagnetic shift of  $FX_{HH}$  and  $X_{HH}^-$  transitions as a function of the magnetic field.

tion. This could be because the additional electron in the trion help to screen external perturbations like carrier-carrier interaction and magnetic confinement effects. On the contrary, the formation of excitons and their optical properties strongly depend on the photo-generated carrier density, which are sensitive to carrier-carrier interactions and basic properties of the material system.

## Appendix B

Table 1: Layer details of samples  $S_1$ ,  $S_2$ , and  $S_3$  that are used for magneto-PL, magneto-PV and magnetic susceptibility measurements in Chapter 5

Sample name	Details of the QW and barrier layers	Growth conditions
$S_1$	GaAs/Al <sub>0.64</sub> Ga <sub>0.36</sub> As four-QWs QW thicknesses: 190, 100, 50, and 30 Å 980 Å thick barrier QWs and barriers are undoped	Grown at 730 °C, 50 mbar, on n <sup>+</sup> GaAs substrate
$S_2$	GaAs/Al <sub>0.45</sub> Ga <sub>0.55</sub> As single-QW QW thickness: 48 Å 2670 Å thick barrier QW and barrier are undoped	Grown at 730 °C, 50 mbar, on n <sup>+</sup> GaAs substrate
$S_3$	GaAs/Al <sub>0.27</sub> Ga <sub>0.63</sub> As 50-QWs QW thickness: 75 Å each 210 Å thick barrier QWs are doped with Si (10 <sup>18</sup> cm <sup>-3</sup> )	Grown at 730 °C, 50 mbar, on n <sup>+</sup> GaAs substrate



# Appendix C

The magneto-resistance measurements on the Hall bar device are performed under perpendicular and parallel magnetic field configurations, and the results obtained by this measurements are shown in Figs. 4a and 4b. Measurements are performed by Keithley source measuring unit at 4.2 K without illuminating a light. The distinct oscillations in longitudinal magneto-resistance  $R_{xx}$  and quantized variations in Hall resistance  $R_{xy}$  are observed under the perpendicular magnetic field configuration (Fig. 4a). However, the magnetic field driven enhancement of  $R_{xy}$  and oscillations in  $R_{xx}$  is found to be feeble under the magnetic field parallel to the QW plane (Fig. 4b). Unlike the perpendicular magnetic field case, it is observed that the  $R_{xx}$  gradually decreases with an increase of  $B_y$  in a low-field regime and oscillations are only observed above  $\sim 4$  T.

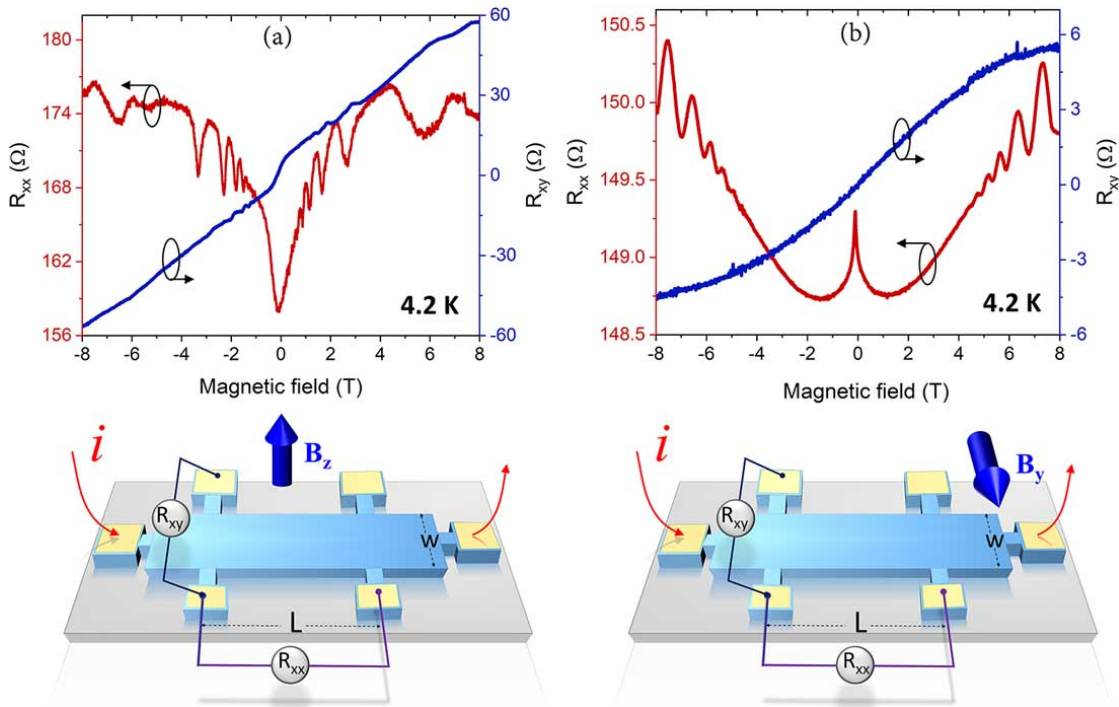


Figure 4: The longitudinal magneto-resistance and Hall resistance of the modulation-doped QW sample under the (a) perpendicular and (b) parallel magnetic field configurations at 4.2 K.

Such observations can be explained by the theoretical and experimental understanding developed in Chapter 5. The oscillatory variations of  $R_{xx}$  under the Voigt configuration confirms that the charge carriers in the QW are confined in the z-direction. Since, the charge carriers are already confined in this direction by the barrier potential, the quantization of energy state and its impact on  $R_{xx}$  is only observed under strong magnetic field. Moreover, with the carriers under  $B_y$  move in the x-direction,  $R_{xx}$  initially decreases with increasing the  $B_y$ . Further investigation to identify the filling ratio of Landau states corresponding to the  $R_{xx}$  oscillations and variation of  $R_{xy}$  as a function of  $B_y$  need to be performed, which is not reported in the literature.